Winter 2015

Structure-thermal coupling in viscoelastic material in rubber bushing of vehicle system

Zhengui Zhang
Purdue University

Graduate School Form 30
(Updated 11/20/2014)

PURDUE UNIVERSITY
GRADUATE SCHOOL
Thesis/Dissertation Acceptance

This is to certify that the thesis/dissertation prepared

By Zhengui Zhang

Entitled
STRUCTURE-THERMAL COUPLING IN VISCOELASTIC MATERIAL IN RUBBER BUSHING OF VEHICLE SYSTEM

For the degree of Doctor of Philosophy

Is approved by the final examining committee:

Haiyan H Zhang

Qingyou Han

Richard Mark French

Xiuming Diao

To the best of my knowledge and as understood by the student in the Thesis/Dissertation Agreement, Publication Delay, and Certification/Disclaimer (Graduate School Form 32), this thesis/dissertation adheres to the provisions of Purdue University's "Policy on Integrity in Research" and the use of copyrighted material.

Haiyan H Zhang

Approved by Major Professor(s): _____

_____

Approved by: Kathryne A. Newton 02/14/2015

Head of the Department Graduate Program Date

STRUCTURE-THERMAL COUPLING IN VISCOELASTIC MATERIAL IN RUBBER BUSHING OF VEHICLE SYSTEM

A Dissertation

Submitted to the Faculty

of

Purdue University

by

Zhengui Zhang

In Partial Fulfillment of the

Requirements for the Degree

of

Doctor of Philosophy

May 2015

Purdue University

West Lafayette, Indiana

Dedicated this dissertation to
my family and my love Tengfei Long
for their understanding, patience and encouragement

ACKNOWLEDGMENTS

I would like to present my heartfelt appreciation and gratitude to Dr. Haiyan H. Zhang. He guided me in patience and without reservation to help me to complete my Ph.D dissertation at Purdue University. I was deeply inspired by Dr. Zhang′s richness in knowledge in multiple disciplines. He can always give me suggestions about how to solve those tricky problems in my research. Dr. Zhang′s personal characters, such as humbleness, enthusiasm, diligence and warm heart also greatly affected my view points on research and life. Without his encouragement and support, the accomplishment of this dissertation is almost impossible. It is fortunate to have Dr. Zhang as my advisor in those years.

Thanks Prof. Doyle in school of Aeronautics and Astronautics at Purdue. He gave me intensive and comprehensive FEA and dynamic analysis training each week in person. Prof. Doyle shared his FORTRAN source code with me and guided me to do the dynamic structure analysis with FFT spectral analysis and FEA method. I am equally thankful for Dr. French and Dr. Diao for serving on my committee. I also would like to thank Prof. Erk, Prof. Olek, Prof. Pourpoint, Prof. Dyke, Prof. Sadeghi and technical manager Sherwood, who allowed me to access their laboratories to carry out all those tests and experiments for my dissertation. The last but not the least, thanks to the MDL group members. All of them are awesome! Especially, Dr Yueen Li taught me exclusively in how to write and layout a dissertation and Cong Liao helped me to design the fixture for rubber bushing dynamic test.

TABLE OF CONTENTS

LIST OF TABLES

LIST OF FIGURES

Figure Page

ABSTRACT

Zhang, Zhengui Ph.D., Purdue University, May 2015. Structure-Thermal Coupling in Viscoelastic Material in Rubber Bushing of Vehicle System. Major Professor: Haiyan H. Zhang.

The objective of this research is to utilize the frequency-dependent viscoelastic material model and characterize the dynamic response of rubber bushing under external excitation. Furthermore, with appropriate modeling, two heat generation mechanisms of rubber bushing are explored and their thermal fields are investigated. Due to the nonlinear force-deflection relationship of the viscoelastic material, finding satisfactory mechanical properties of rubber components still poses a great challenge. However, industry nowadays is in urgent demand for precise finite element analysis(FEA) modeling of rubber components. For example, a proper constitutive relationship of rubber components is critical to providing a reliable and trustable simulation of vehicle suspension systems. As for current FEA commercial software, the frequency-dependent modulus of viscoelastic material hasn′t been well presented and they have failed to provide satisfactory results. Therefore, two approaches, FEA and the multi-body dynamic analysis have been selected together to give a more comprehensive and credible prediction of suspension system′s performance in different working conditions. The FEA approach evaluated the stability of rubber bushing in view of the dynamic response and temperature distribution under high frequency excitation. With these results, the life prediction of rubber bushing becomes more feasible. The multi-body dynamic analysis explores the structure instability of rubber bushing when exposed to extremely high frequency and estimates the dissipation energy in the rubber core.

The key innovations of this paper can be classified into four aspects. The first one is the application of multi-body dynamics in the dynamic analysis of rubber bushing. Based on experimental modal analysis, the sandwich cylindrical rubber bushing is treated as multi-body. With the multi-body model, the transfer function of the rubber bushing is calculated in order to estimate the dynamic response. The second innovation comes from the development of the FORTRAN program to solve the system transfer function of the structure made of viscoelastic material. Since the geometry and boundary conditions are amenable in FEA compared with the experimental modal testing, this approach is not just applicable in rubber bushing dynamic analysis, but also useful in dynamic analysis of different rubber components. The third innovative contribution of this research is connecting the multi-body analysis with continuum mechanics to evaluate the mechanical properties of rubber bushing. The last innovation is the structure-thermal coupling of rubber bushing to predict its temperature distribution based on the heat source calculated from the FEA simulation. The finite volume method (FVM) is applied using MATLAB in the simulation of temperature distribution. In this research, the classical standard linear model is applied in the FEA program to characterize the variation of viscoelastic material in the frequency domain. The three parameters of this model have been identified with the batch data measurement using dynamic mechanical analysis equipment (DMA). Specially, two heat generation mechanisms are explored to emphasize the friction-induced hysteresis damping except for the commonly discussed viscous damping. As complementation of FORTRAN program simulation in the frequency domain, the multi-physics commercial software COMSOL is employed to estimate the dynamic response of rubber bushing and temperature distribution in the time domain. To verify the results of FEA and multi-body dynamic approach in the dynamic and thermal analysis of rubber bushing, dynamic tests have been carried out using torsion and tensile testing machines. The experimental temperature distribution is in good agreement with the simulation results, which indicated the feasibility of the FEA method.

However, due to the limited experience and complicated constitutive relationship of the viscoelastic material, the standard linear viscoelastic model is chosen to simulate the heat dissipation mechanism of rubber core. The high-frequency or high-temperature dynamic testing are almost impossible because of the experiment equipments′ range of service. As the first step of predicting the dissipation energy density and temperature distribution of rubber components, the initial explorations are significant and provide a proper guidance for further predictions about life expectation.

CHAPTER 1. INTRODUCTION

This chapter begins with the motivation of this research by presenting the current demands and challenges in the simulation of vehicle′ dynamic performance, especially given that the current commercial software is not sufficient to predict precise heat generation rate and temperature distribution of rubber bushing. To start, the background and research interests about rubber bushing are thoroughly assessed and summarized. With a thorough understanding of this material, the assumption, limitation and objectives of this research are stated.

1.1 Motivation of the Research

Rubber bushings/mountings are widely installed on vehicle systems and they can reduce the vibration, noise in the vehicles and also absorb shocks from the environment. Generally speaking, rubber bushing with longer lift time is one of the advantages of vehicle systems in the globally competitive market. However, to reach this goal, several technical challenges should be solved. This research is also inspired by this goal and the motivation is the quantitative description of rubber bushings/mountings dynamic characterization and its modeling for elastomeric cylindrical bushing. Viable elastomeric measurement methodology for modeling and analysis of elastomeric cylindrical bushing used in the chassis structure is needed.

Rubber has higher yield strain and lower Young′s modulus compared with other metal materials used in the vehicles. It is indispensible material in view of its flexibility, extensibility, resiliency and durability, especially, the non permanent deformation or fracture is still permissible at larger strain(Harper, 2006). However, the nonlinear stress and strain relationship leads to the accumulation of dissipation energy inside the rubber component. The mechanical properties of rubber material

are sensitive to the change of temperature. Beside of this, the strain rate of rubber also affects it viscoelastic behaviors. Because of the complexity, the proper constitutive model to represent viscoelastic material is still a great challenge compared with other engineering materials (Whibley, Cutts, Phillip, & Pearce, 2005).

Although the FEA is a fairly difficult task for the viscoelastic material, should proper analytical methods be adopted, the numerical estimation errors can be less than 10%. The input to the viscoelastic bushings/mountings structure produces four types of variables, which are the instantaneous strain, the instantaneous mass motions, viscous damping dissipation, and hysteretic energy accumulation. The relationship of these four variables can be used to derive/ form an index for elastomeric cylindrical bushing durability. It can also be used to obtain the design specifications.

Currently, constitutive models of viscoelastic material in FEA commercial software couldn′t provide satisfactory and effective simulation models for elastic response of rubber components at low strains (i.e. in 1-20% range). Vehicle handling and ride quality are most probably related to this low strain level, which still displays nonlinearity. Unfortunately, that is not captured in existing commercial material models (i.e. in Abaqus FEA). In sum, the biggest roadblocks to reaching more effective and widespread rubber computer-aided engineering (CAE) are two aspects; 1) obtain more reliable and proper material data to populate or optimize the existing material models and 2) gain ability to predict serving life of rubber components.

1.2 Background of Rubber Bushing

Most of current researched rubber bushings/mountings are installed on the suspension system of the vehicle system. For more widely-spread applications of current work in the vehicle industry, similar rubber components are used in the

following investigation. The literature review about rubber bushing is presented in three parts: the structure and working principle of rubber bushing, the heat generation and its accumulation mechanism, and the existing challenges in the research about rubber bushing.

1.2.1 Structure and Mechanical Behavior of Rubber Bushing

Rubber bushing is an isolator to reduce the vibration or noise because of the intermediate damping through the energy transmission to the chassis of the vehicle. Besides of this, the rubber bushings installed on the suspension systems separates metal parts on the vehicle and allows certain movement. Those small parts of the vehicle, such as tie bar and lower arm can be connected using the rubber bushing. It is the viscoelastic material minimizing the transmission of vibration and noise across the connecting components (Kadlowec, Wineman, & Hulbert, 2003).

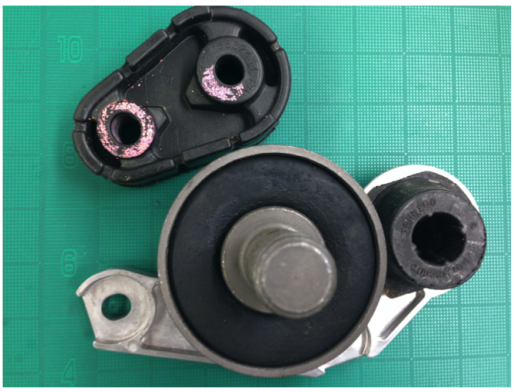

Figure 1.1.: Bushings used for vehicles.

The commonly used rubber bushing is composed of three parts, a hollow rubber core and two cylindrical steel sleeves encompassing the rubber core, that structure possesses high damping capacity and durability(Fujiwara, Tanuma, & Yoda, 1992). The metallic cylindrical envelope made of steel can distribute the external load on the rubber component. Figure 1.1 provides some examples of common commercial rubber bushing.

The cylindrical rubber core is inserted between the two layers of metal shell, which are kept concentric with the rubber layer. The method most commonly used to combine rubber and metallic or non-metallic components is the use of adhesive cements. Prior to the use of these special adhesives, the surface of the insert must be clean and free of contamination (Blaurock, 1955) and (Harold, 1933). Besides of clearness of surface of the steel sleeves before the chemically vulcanized bonding, special preparation like degreasing, blasting, and/or a suitable chemical treatment are needed. The expected adhesion of bonding is obtained by vulcanizing the rubber core to the steel sleeve and the cure of rubber happens during the vulcanization. Radial compressive stress is introduced after pushing the two metal shells to each other and the good assembly should make sure the uniformly distributed stresses. As the request of the product design or application scope, adhesion measurement is commonly done to guarantee the bond strength of molds after vulcanized bonding, that testing methods or instructions can be referenced from the ASTM testing standard D429.

Rubber bushings installed on the automotive suspension system play a more and more important and critical role because of its elasticity and inherent damping, especially, engineering rubbers with fillers (e.t, many kinds of carbon black). The roadblock of proper prediction about the frequency and amplitude dependent of the dynamic behaviors of rubber components is the complex properties of this material(García Tárrago, Kari, Vinolas, & Gil-Negrete, 2007). The nonlinear stress and strain relationship of rubber attracted many researchers. The interactions between the filler and the polymer matrix and also the interactions within the fillers lead to a lager shear modulus magnitude even at small amplitude. The mechanism of frictional behavior, breaking of filler structure and loss factor have been investigated intensively (Medalia, 1978), and (Kraus, 1978). Dynamic measurements and finite element simulation are also carried out by some researchers while the non-homogeneous strain state inside the rubber bushing causes the

trouble to estimate dynamic stiffness using the existing material model (Austrell, Olsson, & Jonsson, 2001), and (Olsson & Austrell, 2003).

During normal service, the automotive suspension system is under radial, torsional and combined radial-torsional loading (Figure 1.2). Radial mode is the translation movement of one sleeve relative to the other sleeve while the torsional mode is the rotation of one to the other about the centerline. Besides of the complicated coupling of the two different modes of deformation the responses of displacements and rotations to forces and moments are nonlinear and time-dependent. Attribute to those characters, reliable finite element analysis is facing great challenge. The bushing research has attracted lots of attention in recent, however, the material parameters is still empirical and experimental dependent, such as tension, compression, equibiaxial tension or pure shear tests. Test procedures, range of deformation and deformation histories are quite complex and affect the response of rubber bushing. To achieve desired objectives of isolators, a comprehensive understanding of viscoelastic material is necessary. As the primary material working as automotive vibration isolators, rubber have several special attributes (Lewitzke & Lee, 2001). Rubber has good resilience and high energy storage capability, and good recovery ability even from large deformation under cycle loading. In extreme working condition, elongation up to 1000% is possible to happen on rubber and the required stress is low because of the rather low modulus of this material.

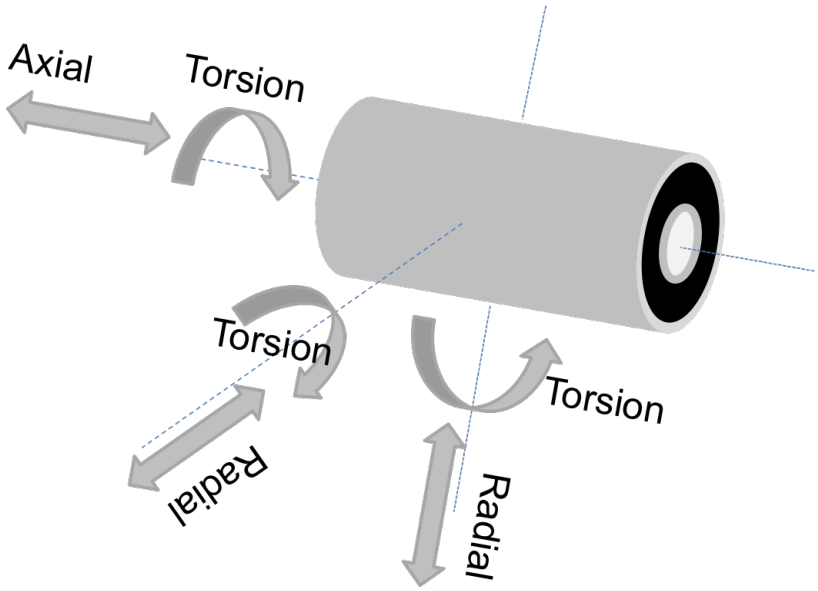

Figure 1.2.: Rubber bushing under combined loading.

The mechanism of carbon black working as reinforcement fillers in elastomers is discussed for hundred years (Kraus, 1971). The inclusion of carbon black in rubber can greatly improve abrasion resistance, tear and tensile strength but some undesirable effects can accompany, such as relaxation rates and hysteresis. With the increasing pronounced reinforcing ability of filler, the hysteresis heat built up in rubber attracts more attention. Hysteresis is usually measured at low-amplitude oscillations test to record the out of phase between input load and output displacement. The tangent of loss angle ($\tan\delta$) is usually measured as a better indicator of the capability of hysteresis. The loss modulus and $\tan\delta$ may increase along with the increase of carbon black fraction. Crystallization and network structure reorganization are two dominate reasons for hysteresis in filled rubbers (A. Payne & Whittaker, 1971). The presence of filler may increase the viscoelasticity and correspondingly increase of the hysteresis. It is still debatable about filler′s effect, since in the highly restrained mobility of occluded rubber, fillers may be not able to develop hysteresis that much.

Dynamic properties of rubber mean respond to transient or steady loading without leading to permanent deformation or damage, especially, the deformation under usually under 25%. The mechanical properties of rubber covered in this article are important in designing rubber components to be used under dynamic conditions, such as tires, power transmission belts, vibration isolation mountings, etc. To help readers get familiar with the rubber, a certain amount of background is given in the following. The first step begins with the definition of those terms used in describing dynamic properties. The nature of carbon black is reviewed and later, those methods and instruments used to measure the physical and mechanical properties are described briefly. Finally, some classical models are given, together with the dynamic behavior of typical models, as a preface to the review of more recent work in this field.

In filled rubber, several mechanisms result in dissipation energy accumulated in rubber components. Low strain hysteresis mechanisms include filler-induced, rate independent hysteresis and viscoelasticity of rubber. Hysteresis is small at low strain and displays primarily at high strain levels. Mullins effect and strain-crystallization are two reasons accounting for the high strain hysteresis mechanisms. A brief description of each mechanism follows.

The Mullins effect describes initial transient softening of rubber shown in the stress-strain curve and mainly presents in the fillers polymers(Diani, Fayolle, & Gilormini, 2009), (Mullins, 1969), and (Roland, 1989). The stiffness displayed in the first loading is much higher than the following equal or lesser loading and the subsequent loadings presents a steady state and nonlinear behavior. Fatigue properties improvement in filled, non strain crystallizing rubber compared with unfilled, non strain crystallizing rubber. This is attributed to dissipative mechanism, which is discussed later.

Compared with Mullins effect, crystallization takes place at higher strain as to elastomers, as a result, the phenomenon of strain crystallization contributes to another mechanism of hysteresis at higher strain (Mars & Fatemi, 2004). Without

deformation, the polymer network chains in the rubber are in disorder and form an amorphous state. With the increase of strain, those chains are stretched straightly, become highly ordered and turn to crystalline state. This time dependent phase change is reversible since the crystallized state can disappear after release of strain. Furthermore, the increased stiffness and hysteresis induced by strain crystallization will not be affected by the further cycle loading. Besides of the influence on the hysteresis, strain crystallization also assists in preventing the crack growth, which exhibits better fatigue properties if the strain merely increases at small range.

The crystallization induced hysteresis is time dependent, while another also commonly observed hysteresis is rate independent hysteresis, especially when the strain is in small range. Many researchers have recently developed models to characterize the behaviors of rate-independent behavior since the traditional linear viscoelasticity models couldn′t approximate the properties concisely. Compared with the hysteresis loss contributed by Mullins effects and crystallization, the proportion caused by rate-independent hysteresis is much smaller. Further research indicates that the hysteresis is dependent on strain amplitude, strain temperature and average strain range (Luchini, Peters, & Arthur, 1994).

The crystallization induced hysteresis is time dependent, while another also commonly observed hysteresis is rate independent hysteresis, especially when the strain is in small range. Many researchers have recently developed models to characterize the behaviors of rate-independent behavior since the traditional linear viscoelasticity models couldn′t approximate the properties concisely. Compared with the hysteresis loss contributed by Mullins effects and crystallization, the proportion caused by rate-independent hysteresis is much smaller. Further research indicates that the hysteresis is dependent on strain amplitude, strain temperature and average strain range (Luchini et al., 1994).

1.2.2 General Constitutive Models of Rubber

For rubber materials, the stress and strain are nonlinear, which makes the often used linear elastic not appropriate to characterize the mechanical relationship of rubber. To study the behavior of large deformation in rubber with the finite element method, the proper constitutive relationship of rubber is necessary (Ali, Hosseini, & Sahari, 2010). Many models are developed to embody the nonlinear, isotropic, incompressible and nearly rate-independent viscoelastic materials. Rubber materials usually are associated to the elastomers, while the later shows almost elastic response. Those types of elastic behaviors of elastomers are usually represented with hyperelastic behaviors. Rubber materials′ mechanical properties are temperature dependent, which illustrates softening with the rising temperature. The coexisting of elastic and viscous properties is generally approximated with viscoelastic constitutive models.

1.2.2.1. Hyperelastic Model

(a) Phenomenological Theories

Rubber can be approximated as linearly elastic materials at low load or small strain, however, the traditional elastic theory applied for most engineering materials is not applicable. As hyper-elastic materials, rubber can be described using stored energy function. Commonly, simple mechanical tests, like uniaxial, biaxial and shear test data are applied to identify those parameters in constitutive models. Constitutive models of rubber and rubber-like materials has been characterized by many researchers. Strain energy function is the starting point to start modeling of rubber material. Hyper-elastic orthotropic mechanical behavior focusing on entropy change and strain energy change are derived from deformation of constitute macromolecules and representative orthotropic unit cell (Bischoff, Arruda, & Grosh, 2002). Rivlin′s phenomenological theories are developed to define the isotropic elastic behavior of elastomers (Barenblatt & Joseph, 1997). This method imports

continuum mechanics and provides a mathematical framework to describe rubber. Three strain invariants I_1, I_2 and I_3 are introduced to represent strain energy function,

$$W = f(I_1, I_2, I_3) \tag{1.1}$$

Where W is strain energy function or stored energy function per unit volume, and I_1, I_2 and I_3 are invariants of the green strain tensor derived from principle extension rations λ_1, λ_2 and λ_3, which are defined as,

$$I_1 = {\lambda_1}^2 + {\lambda_2}^2 + {\lambda_3}^2 \tag{1.2}$$

$$I_2 = {\lambda_1}^2{\lambda_2}^2 + {\lambda_2}^2{\lambda_3}^2 + {\lambda_3}^2{\lambda_1}^2 \tag{1.3}$$

$$I_3 = {\lambda_1}^2{\lambda_2}^2{\lambda_3}^2 \tag{1.4}$$

Then, strain energy, W can be rewritten as,

$$W = \sum_{i+j+k=1}^{\infty} C_{ij}(I_1 - 3)^i(I_2 - 3)^j(I_3 - 1)^k \tag{1.5}$$

As to incompressible materials, $I_3 = 1$ is assumed. Then,W in Equation (1.5) can be simplified again,

$$W = \sum_{i+j=1}^{\infty} C_{ijk}(I_1 - 3)^i(I_2 - 3)^j \tag{1.6}$$

A considerable amount of models are published to describe the hyperelastic, and the correct representation of those models should follow several provisions: 1) The response of rubbers can be exactly reproduced; 2) Model can be applied at various deformation modes; 3) Small number of fitting material parameters to simplify measurements; 4) Simple and easy operation to derive the mathematical formulation (Chagnon, Marckmann, & Verron, 2004). Several acceptable and practicable models used in commercial finite element software are presented in the following. Polynomial model in the compressible form is introduced to represent the stress-strain behavior of filled elastomers (Forni, Martelli, & Dusi, 1999),

$$W = \sum_{i+j=1}^{\infty} C_{ijk}(\bar{I}_1 - 3)^i(\bar{I}_2 - 3)^j + \sum_{i=1}^{N} \frac{1}{D_i}(J_{el} - 1)^{2i} \tag{1.7}$$

Where W is strain energy density or potential energy per unit volume. $\bar{I}_1$ and $\bar{I}_2$ are 1^{st} and 2^{nd} invariants of the deviatoric Cauchy-Green tensor. J_{el} is the elastic volume ratio. C_{ij} and D_i are material constants. C_{ij} stands for the shear behavior. D_i is related with compressibility, which is zero for totally incompressible materials. A more commonly used and computationally intensive model is Ogden′s energy function, which is more accurate in fitting experiment tests compared with polynomial model(Ogden, 1972),

$$W = \sum_{i=1}^{N} \frac{2\mu_i}{{\alpha_i}^2}(\bar{\lambda_1}^{\alpha_i} + \bar{\lambda_2}^{\alpha_i} + \bar{\lambda_3}^{\alpha_i} - 3) + \sum_{i=1}^{N} \frac{1}{D_i}(J_{el} - 1)^{2i} \tag{1.8}$$

Where $\bar{\lambda_1} = J^{-\frac{1}{3}}\lambda_i$. $J = \lambda_1\lambda_2\lambda_3$ and J is the Jacobean determinant. The constant μ_i and λ_i are introduced here to describe the rubbers shear behavior. Another most favorite constitutive model is Mooney-Rivlin models (Mooney, 2004), and (R. Rivlin, 1948),

$$W = \sum_{i=1}^{N} C_{ij}(\bar{I}_1 - 3)^i + (\bar{I}_2 - 3)^j) + \sum_{i=1}^{N} \frac{1}{D_i}(J_{el} - 1)^{2i} \tag{1.9}$$

When the C_{00} is 0 and then the first order of incompressible materials is simplified as,

$$W = C_{10}(\bar{I}_1 - 3) + C_01(\bar{I}_2 - 3) \tag{1.10}$$

This equation can be rewritten by setting $N = 0$, $\alpha_1 = 0$, $\alpha_2 = -2$, $C_{10} = \frac{\mu_1}{2}$ and $C_{01} = -\frac{\mu_2}{2}$ to get,

$$W = \frac{\mu_1}{2}(\bar{\lambda_1}^2 + \bar{\lambda_2}^2 + \bar{\lambda_3}^2 - 3) - \frac{\mu_2}{2}(\bar{\lambda_1}^{-2} + \bar{\lambda_2}^{-2} + \bar{\lambda_3}^{-2} - 3) \tag{1.11}$$

There is another model Neo-Hookean, which has been pre-programmed into Abaqus FEA package. Defining $N = 1$ in the reduced polynomial model, the Neo-Hookean model is given as,

$$w = C_{10}(\bar{I}_1 - 3) + \frac{1}{D_1}(J_{el} - 1)^2 \tag{1.12}$$

Similarly, the Neo-Hookean model can be offered by setting $N = 1$, $\alpha_1 = 2$ in the Ogden model,

$$W = \frac{\mu_1}{2}(\bar{\lambda_1}^2 + \bar{\lambda_2}^2 + \bar{\lambda_3}^2 - 3) = C_{10}(I_1 - 3) \tag{1.13}$$

This model is recommended because it includes the statistical theory of rubber elasticity,

$$W = \frac{1}{2}NKT(I_1 - 3) \tag{1.14}$$

Where, N is the number of network per unit volume. K is the Boltzmann constant and T is the absolute temperature. When $N = 3$ in the polynomial model, it becomes more applicable for wider range of deformation and be able to predict different deformation modes from a simple data test. The new model is named as Yeoh model(Peeters & Kussner, 1999),

$$w = \sum_{i=1}^{3} C_{i0}(I_1 \bar{} - 3)^i + \sum_{i=1}^{3} \frac{1}{D_i}(J_{el} - 1)^{2i} \tag{1.15}$$

Where $\mu_0 = 2C_{10}$ and $K_0 = \frac{2}{D_1}$ are initial shear modulus and bulk modulus. Besides of those discussed models, there are some other important models, such as Van der Waals models. Because of the limited space of this dissertation, detailed introduction of those models will not be listed here.

(b) Statistical Mechanics Treatments

Besides of those model derived from phenomenological theories, another important branch targeting at accurate distribution of rubber elasticity is statistical mechanical treatments (Boyce & Arruda, 2000), and (Treloar, 1975). The basic structure of rubber is defined as randomly oriented long molecular chains. The end to end length r of chain′s distribution is obtained from Gaussian treatment,

$$p(r) = 4\pi(\frac{3}{2\pi nl^2})^{\frac{3}{2}} r^2 exp(-\frac{3r^2}{2nl^2}) \tag{1.16}$$

Where l is the length of each link and n is the number of links in a chain. The average initial chain length is given by,

$$L_0 = (\bar{r^2})^{\frac{1}{2}} = (nl^2)^{\frac{1}{2}} = \sqrt{nl} \tag{1.17}$$

The elastic strain energy function W can be obtained by considering the configurational entropy change when the chain structure is stretched or compressed. The energy is represented as,

$$w = \frac{1}{2}NK\theta({\lambda_1}^2 + {\lambda_2}^2 + {\lambda_3}^2 - 3) \tag{1.18}$$

Where k is Boltzmann constant and θ is of absolute temperature. While this is applicable only when the deformation is limited, and chain is not fully extended. In the case of lager deformation, for example, r/nl approaching to 0.4, non-Guassian nature should be taken into account to describe the chain stretch model. Kuhn and Grun (Kuhn & Grün, 1946) have the non-Gaussian force elongation for a chain and inverse Langevin function as,

$$f = \frac{k\theta}{l} L^{-1}(\frac{r}{nl}) = \frac{k\theta}{l} L^{-1}(\frac{\lambda}{\sqrt{n}}) \tag{1.19}$$

$$\frac{r}{nl} = coth(\beta) - \frac{1}{beta} = L(\beta) \tag{1.20}$$

$$\beta = L^{-1}(\frac{r}{nl}) \tag{1.21}$$

To figure out the connection between stretches of individual chains to the deformation of the material, some representative network structures are proposed. Arruda and Boyce (Arruda & Boyce, 1993) presented a 8-chain model to derive the strain energy function. The stretch of each chain is characterized as, $\lambda_{chain} = (\frac{1}{3}({\lambda_1}^2 + {\lambda_2}^2 + {\lambda_3}^2))^{\frac{1}{2}}$, and the strain energy function is formulated as,

$$W_{8ch} = NK\theta\sqrt{n}[\beta_{chain}\lambda_{chain} + \sqrt{n}ln(\frac{\beta_{chain}}{sinh(\beta_{chain})})] \tag{1.22}$$

Where $\beta_{chain} = L^{-1}(\frac{\lambda_{chain}}{\sqrt{n}})$. The 8-chains model can capture the complicated network respond in a simple way and can predict the biaxial data than the full network model. However, the 8-chians model does not assure affine deformation.

1.2.2.2. Viscoelastic Model

(a) Three Classical Models

Before the discussion about the standard three parameters model, it is better to introduce two basic and classic viscoelastic material models. The first one is the Maxwell model, which is proposed by James Clerk Maxwell in 1867 to describe the elasticity and viscoelastic of those viscoelastic materials (Roylance, 2001). In the Maxwell model, the material is simulated with a spring and a dashpot in series

connection (Figure 1.3(a)), which indicates that the two elements are under same stress and the total strain comes from the total contribution.

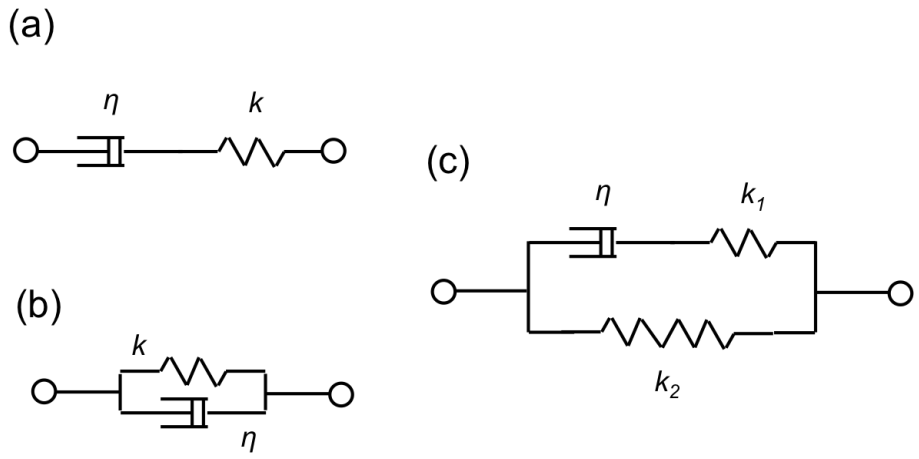

Figure 1.3.: (a) Maxwell model; (b) Voigt model; (c) the standard linear model.

The derivative of strain over time is composed of two parts, spring element and dashpot, that give the time dependent strain as,

$$\frac{d\epsilon}{dt} = \frac{d\epsilon_\eta}{dt} + \frac{d\epsilon_s}{dt} = \frac{\sigma}{\eta} + \frac{1}{k}\frac{d\sigma}{dt} \quad \text{and} \quad \epsilon(0) = \frac{\sigma(0)}{k} \tag{1.23}$$

Where η is the coefficient of viscosity and k is the stiffness of the spring element. Voigt model or Kelvin-Voigt model is similar to the Maxwell model but the two elements are in parallel connection (Figure 1.3(b)). That combination indicates the two elements sharing the external load and displaying the same strain (Meyers & Chawla, 1991). The time dependent stress and strain relationship is given as,

$$\sigma(t) = k\epsilon(t) + \eta\frac{d\epsilon(t)}{dt} \quad \text{and} \quad \dot{\epsilon}(0) = 0 \tag{1.24}$$

Where $\sigma(t)$ and $\epsilon(t)$ are stress and strain at time t. The three parameters model is also named as standard linear solid model, which is similar to a combination of Maxwell and Voigt model (Figure 1.3(c)). Since Maxwell model doesn′t give satisfactory description of creep or recovery and Kelvin-Voigt model doesn′t give satisfying stress relaxation, the superposition of the two models in the standard

model can reproduce the comprehensive mechanical properties in the most satisfaction. The physical relations of this model in Figure 1.3(c) are more complicated than the other two models, which are written as,

$$\sigma = \sigma_1 + \sigma_2 \quad \text{and} \quad \epsilon = \epsilon_1 = \epsilon_2 \tag{1.25}$$

The time derivative of the three parameters model can be formulated as,

$$\frac{d\epsilon}{dt} = \frac{k_2}{\eta}\frac{1}{k_1 + k_2}(\frac{\eta}{k_2}\frac{d\sigma}{dt} + \sigma - k_1\epsilon) = \frac{1}{\tau}\frac{1}{k_1 + k_2}(\frac{1}{\tau}\frac{d\sigma}{dt} + \sigma - k_1\epsilon) \tag{1.26}$$

Where $\frac{\eta}{k_2} = \tau$ defines the relaxation time.

(b) Generalized Maxwell Model

The generalized Maxwell model is composed of several Maxwell models and one spring element. Those Maxwell models are connected in parallel (Rosen, 1982). This model is shown in Figure 1.4,

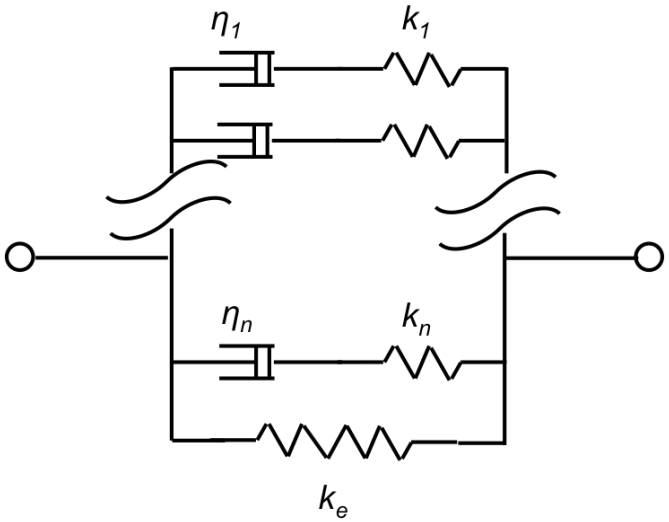

Figure 1.4.: General Maxwell model.

The time-dependent stress and strain relationship of this model is given as,

$$E(t) = \frac{\sigma(t)}{\epsilon_0} = \int_0^\infty E(\tau)exp(-\frac{t}{\tau})d\lambda \tag{1.27}$$

Where ϵ_0 is the initial imposed strain and the continuous distribution $E(\tau)$ is a function of relaxation time, which is also determined by the specific elements of the generalized Maxwell model. The generalized Maxwell model is mostly employed in the commercial software to simulate the mechanical properties of viscoelastic material such as Abaqus FEA.

(c) Berg′s Model

Figure 1.5 shows a nonlinear, dynamic rubber spring model, which is composed of elastic force(spring components), friction force(non linear behavior) and viscous force(energy loss mechanism) (Berg, 1998). The friction force is included to represent the rate-independent hysteresis and increased stiffness at small displacement amplitudes. With this model, detailed expression of steady state force amplitude and energy loss at each cycle can be estimated(Berg, 1997). This model provides a reasonable tool simulating the dynamic analysis of rail vehicle. Friction hysteresis is affected by fillers characteristic, rubber′s dimension and excitation direction. Specially, hysteresis in rolling rubber may be more distinguished because of the additional sliding friction. In this model, viscous force is represented by a linear viscous damper and a linear spring.

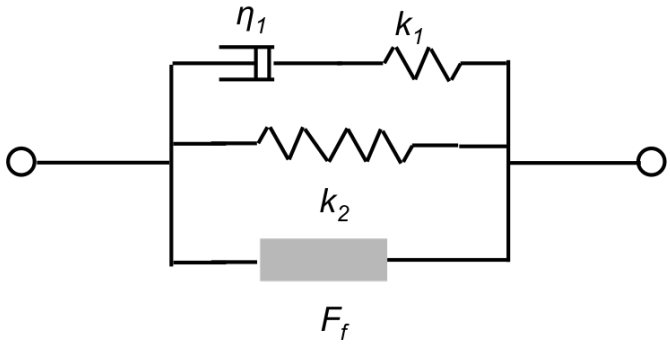

Figure 1.5.: Berg′s model.

In Berg′s model, the force applied on the rubber components is share by three parts. Besides of the friction, this elastic part is presented as $F_e = K_e x$, and the viscous force model comes from the Maxwell model. The main contribution of

this model lies in the inclusion and skillfully calculation about the friction forces, which is highly credited by later researchers. In this model, energy loss caused by the friction force are determined by the external force at the maximum deformation and the location when the friction force reaches to half of the maximum deformation F_{max}, that definition gives the energy loss and damping as,

$$E_f = 2F_{fmax}\left(2x_0 - x_0(1+a_0)^2 ln\frac{x_2(1+a_0)+2x_0}{x_2(1+a_0)}\right) \tag{1.28}$$

$$D_f = \frac{E_f}{F_{f0}x_0} = \frac{2F_{fmax}}{a_0 x_0}\left(2x_0 - x_0(1+a_0)^2 ln\frac{x_2(1+a_0)+2x_0}{x_2(1+a_0)}\right) \tag{1.29}$$

Similar to Berg′s model, Stawomir (Dzierzek, 2000) proposed a model based on experiment to describe the typical cylindrical rubber bushing. This model is decomposed into five parts to analysis the hysteresis curve obtained from tests. The restoring force element is emulated as a tangent spring, $F_g = k_t\frac{2d_t}{\pi}\tan\frac{\pi x}{2d_t}$, where x is linear displacement in axial or radial direction, K_t is stiffness coefficient, coming from the inclination of curve at $X = 0$ position, dt is the characteristic thickness of the bushing. Because dt approximates to zero in radial test and is infinite in the axial test according to the physical limits of rubber bushing. The restoring force in axial direction can be derived as $d_t = K_t$x. The remaining model standing for dissipative force includes elastic springs, viscous dampers and frictional dampers. The frictional element is kind of intricate as shown in Equation 1.30,

$$F_f = \left[c_3(\frac{2d_t}{\pi}\tan\frac{\pi x}{2d_t} - k_t x)^{(c_4)} + c_5\right]\frac{\dot{x}}{\sqrt{|\dot{x}^2 - x\ddot{x}|}} \tag{1.30}$$

Where C_3 and C_4 are dimensionless coefficients of friction. Exponential friction damping affects the radial tests, especially the non-linear hysteresis curve. Further, deformation speed profile also affects frictional damping. That explains the complicated description of non linear friction element (F_f). Parameter identification prefers affordable amount of measurement and simple computation is enable to be handled using MATLAB.

1.2.3 Heat Generation and Accumulation

1.2.3.1. Influence of Thermal on Properties of Rubber

Compared with many other metal material used in the vehicle systems, the energy storage capacity of rubber is much higher. The static friction between components can be minimized through rubber components to improve the riding comfort by reducing the harshness. Compression, tension and shear are three major loading deformations experienced by rubber bushing (Heldt, 1948). As the main component installed on the suspension system, the rubber bushing is expected to be stiff enough to support certain loading, and have high hysteresis to absorb vibration and noise. While lower heat generation is pursued for rubber components, which conflicts with expectation about high hysteresis. Rubber fatigue is one of the basic disadvantages of rubber components, which leads to unsatisfactory service life. The force-displacement curve of rubber components plots hysteretic loop after cycle loading because of the nonlinear behavior of this material. The area inside the loop is the dissipation energy attributed to the heat accumulation in the rubber components (Johnson & Chen, 2005). This dissipation energy is converted to heat and accounts for the rubber fatigue. The temperature of rubber also increases under cycle loading as the dissipation energy and the much slower heat transfer conductivity of rubber. The initial step to estimate the dissipation energy and heat accumulation in the rubber components is to obtain the proper constitutive model to characterize the material. That step is complicated as composition of rubber affects its mechanical behaviors, for example, the stress and strain curve is associated with the change of carbon black fillers supplies or percentage(Ebbott, Hohman, Jeusette, & Kerchman, 1999). Furthermore, the strain rate, interaction between carbon black and polymer, and environment temperature affect the dissipation energy in rubber(Park, Hong, Kim, & Kim, 2000). The influence of composition isn′t covered in this research, which is dedicated to the mechanism of

dissipation energy. In sum, the heat built-up in rubber deteriorated the physical, chemical and mechanical properties, especially the aging process is promoted and life expectation is shorted(Woo & Park, 2011).

It is desirable to improve the life expectation by reducing the accumulated heat in rubber. Thus, to explore the lifetime of rubber considering the heat generation, many researchers have investigated the influence of mechanical properties on the thermal mechanism and service life. FEA is one of the powerful and widely-used approaches to analysis the structure and heat transfer of rubber components in recent decades.

The heat generation rate is prerequisite of heat transfer analysis in prediction of temperature rising. In this research, loading frequency of rubber bushing installed on the suspension system of the vehicles can be approximated with the rotation frequency of tires, which is depended on the driving speed of vehicles and radius of tires. The general frequency of excitation derived from the driving speed is $f = V_c/L_r = V_c/(2\pi R_r)$, where V_c is the speed, and L_r and R_r are the rolling tire′ circumferential length and radius(Y.-J. Lin & Hwang, 2004). The heat generation rate HG can be estimated with $HG = (loss\ used) \times f = (loss\ used)/(unit\ time)$, where unit time is the time need for one cycle of tire rolling. With the heat source calculated from the heat generation rate, the steady state or transient heat transfer analysis of rubber bushing can be simulated. Then, the prediction about temperature distribution and rising rate becomes possible.

Relationship between hysteresis and rubber fatigue has been investigated by many researchers. Sudden fracture can occurs in a material without hysteresis since the crack growth rate is associated with the hysteresis behaviors (Mars & Fatemi, 2004). The rubber′nucleation life of crack and growth rate of fatigue crack are affected by rising temperature, and the temperature dependence is slightly related with the percentage of fillers. Furthermore, the change of chemical properties or aging at higher temperature may lead to continued vulcanization. As a result, the

lift expectation of rubber components is shortened even more at elevated temperature.

1.2.3.2. Time-Temperature Effect of Rubber

Besides of the time and frequency-dependence of viscoelastic mechanical properties, the dependence of mechanical properties on the temperature and pressure has been thoroughly investigated by many researchers (Ferry, 1980). For the rubber bushing installed on the suspension system of the vehicle, the effect of pressure is negligible but the influence of temperature is tremendous in changing the viscoelastic properties of rubber components. Especially, the sensitive temperature range is merely a little bit higher than the room temperature. Another temperature related research is the glass transformation temperature, which has explicit research publications. Compared with that one, the investigation about the temperature effect on viscoelastic properties deserves more attention, even though it can be observed from the qualitatively viscoelastic mechanical analysis, such as creep and relaxations. The previous review has mentioned the change of rubber′s states from glass to viscoelastic, rubber and then rheological behavior. The relaxation and creep modulus are highly time dependent at viscoelastic state. For certain viscoelastic materials, the molecular constitution and structure are critical to determine those parameters characterizing the temperature effect. With the comprehensive understanding of temperature and time effect, the relaxation modulus at lower temperature can extrapolate the modulus at higher temperature. A shift factor is introduced to describe the shift of relaxation curve versus the temperature. An empirical equation to format the temperature dependence was constructed by Williams, Landel and Ferry (WLF) Equation (Gabbott, 2008). Figure 1.6 is the example of temperature effect on the elastic relaxation modulus, T_0 is the reference temperature and the remaining temperatures are higher than T_0.

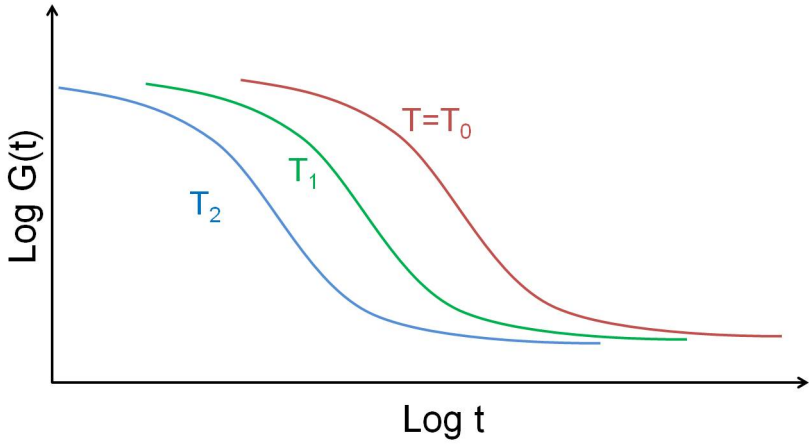

Figure 1.6.: Temperature dependence of elastic relaxation modulus.

Williams-Landell-Ferry (WLF) Equation is built on the basis of Dolittle equation and the universal form is given as,

$$log(\alpha_T) = \frac{-C_1(T - T_0)}{C_2 + (T - T_0)} \tag{1.31}$$

Where α is a shift factor or superposition parameter, T is selected temperature and T_0 is the reference temperature or glass transition temperature. The constant C_1 implicates the free volume and the constant C_2 is related with the thermal expansion during the glass transition (Ferry, 1980). The reduced variables method or time-temperature superposition method is applied here to extrapolate the two constants. The reduced variables approach is widely applied in many fields, such as mechanical, magnetic and dielectric with time-dependent relaxation. The time-temperature superposition is similar to the extrapolate approach, which predicts the unknown properties from the known data. With the extracted constants from experiential testing, the shift curve representing the variation of shift factor on the temperature spectrum is constructed. This master curve facilities the prediction of temperature shift factor at other temperature. One of the drawbacks of this WFL equation is that its application temperature range should be higher than the reference temperature. Prediction at lower temperature may cause some

exceptions and is not reliable (Sullivan, 1990), while the WFL equation will regress to the Arrhenius law.

1.2.3.3. Heat Transfer Principles in the Solid

(a) The First Law of Thermal Dynamics

Taking ΔU as the change of internal energy in a infinitesimal element in continuous, at quasi static, it is written as,

$$\Delta U = Q - W \tag{1.32}$$

Where Q is quantity of heat supplied to the element by its surroundings and W is external work done to the system. The law of conservation of energy is listed as,

$$\delta W + \delta Q = dE + dK \tag{1.33}$$

In that closed system, external work and heat equal to inner energy and kinetic energy. Do derivative over time of Equation 1.33 and get,

$$\dot{W} + \dot{Q} = \dot{E} + \dot{K} \tag{1.34}$$

Where $\dot{E} = \rho\dot{e}$, e is the internal energy in unit mass, $\dot{K} = \rho\nu\dot{\nu}$ and $\dot{Q} = -\nabla.h + \rho\gamma$, then, the external work becomes,

$$\dot{W} = \nabla.(\sigma.\nu) + \rho\nu.f \tag{1.35}$$

And the Equation 1.34 can be rewritten as,

$$\rho\dot{e} - \sigma_{ij}\dot{\epsilon_{ij}} + h_{ij} - \rho\gamma = 0 \tag{1.36}$$

This is energy equilibrium of a closed system.

(b) Constitutive Equation of Isotropic Thermo-Elastic Material

Define lame constant λ and μ, coefficient of thermal expansion α and temperature change $\Delta\theta$. The stress and strain relationship considering the thermal effect can be given as,

$$\sigma_{ij} = C_{ijkl}(\epsilon_{kl} - \alpha\Delta\theta\delta_{kl}) \tag{1.37}$$

This is the linear elastic isotropic constitutive equation. The C_{ijkl} is the elastic modulus tensor and often expressed as,

$$C_{ijkl} = \lambda\delta_{ij}\delta_{kl} + \mu(\delta_{ik}\delta_{jl} + \delta_{ij}\delta_{jk}); \quad and \quad C_{ijkl}\epsilon_{kl} = \lambda\epsilon_{kk}\delta_{ij} + 2\mu\epsilon_{ik} \tag{1.38}$$

With those constitutive equations, it is easy to derive the temperature dependent stress,

$$\sigma_{ij} = \lambda(\epsilon_{kk} - 3\alpha\Delta\theta)\delta_{ij} + 2\mu(\epsilon_{ij} - \alpha\Delta\theta\delta_{ij}) \tag{1.39}$$

As to the thermal viscoelasticity materials, the constitutive equation is dependent on the history of strain and temperature, which is generally represented as,

$$\begin{cases} \sigma(t) = \sigma(\epsilon^t(S), T^t(S)) \\ \eta(t) = \eta(\epsilon^t(S), T^t(S)) \end{cases} \tag{1.40}$$

Where η is the entropy of unit mass, t is the current time, S is the symbolic of Laplace transformation. The Equation (1.40) is applicable at small strain range and small temperature variation. The stress merely relays on the reference temperature and time. For more rigorous discussion, the materials′ mechanical properties are also affected by the bias of real time temperature to the reference temperature. The new coupling relationship includes the influence of temperature and time, which introduce stress based on the current and history function,

$$\sigma(t) = \sigma(\epsilon(t-s), T(t-s), \epsilon(t), T(t)) \tag{1.41}$$

Where s is the time gap from current to the past and define $\tau = t - s$. To solve the equation, the WFL equation is servable, which is expedient to estimate the relaxation function $\tau = t - s$ of any temperature from the reference temperature using the shift factor. The one dimensional stress and strain relationship of thermal-viscoelastic materials is rewritten as,

$$\sigma(t) = \int_{-\infty}^{t} Y(T, \xi_1 - \xi_2)\frac{\partial(\epsilon - \alpha(T(\tau)))}{\partial\tau}d\tau \tag{1.42}$$

The deformation and energy loss of incompressible viscoelastic materials coming from the torsional deformation have been researched for many decades. Specifically,

most of those studied models are cylindrical components, which give us appropriate insights. Batra and Yu analyzed the response of isotropic viscoelastic materials upon the torsional dynamic deformations with the developed material constitutive relationships considering the second Piola-Kirchhoff stress tensor and deviatoric Cauchy stress tensor (Batra & Yu, 2000), and (Batra & Yu, 1999). Feng coupled the torsion with extension and gave the theoretical solution with the experiment verification. That research was more realistic to predict the deformation of cylindrical components made with viscoelastic materials (Feng, Hung, & Chang, 1992). Similarly, the coupling of tension and torque has been studied by Mackenna and Zapas to emphasis the response of poly tubes to the variation of time and deformation (McKenna & Zapas, 1979). Extension or compression is usually accompanying with torsion in the theoretical analysis of cylindrical rubber, that is attributed to the impossible torsion alone deformation and surface tractions needed to keep the position of free ends (R. S. Rivlin, 2004). On the basis of three parameters model, Hausler developed a theory about the constitutive relations and experimentally tested it on the simple torsion loaded cylindrical component (Hausler & Sayir, 1995).

Many researchers investigated the temperature distribution in the rubber components with heat flow governing equations. Clark proposed a one dimensional model to build a temperature rising model and solved the required thermal equilibrium time (S. K. Clark, 1976). Yeow developed a three dimensional model and used the finite difference method to calculate the temperature distribution of rubber components on the influence of various parameters (Yeow, El-Sherbiny, & Newcomb, 1978). Becher built a generalized model combining the viscous Maxwell elements and plastic Prandtl elements simulating the hysteresis behavior and giving a dissipation and temperature distribution of the rubber components (Becker, Dorsch, Kaliske, & Rothert, 1998). To estimate the temperature distribution of the rubber component in the dynamic situation, bi-directional iteration was proposed by Whicker to include the effect of structure deformation to the temperature and again

the effect of temperature to the structure deformation (Whicker, Browne, Segalman, & Wickliffe, 1981), (Whicker, Browne, & Segalman, 1981), and (Whicker, Browne, Segalman, Whicker, & Rohde, 1981). That strategy to solve the temperature filed of rubber components has been widely accepted by many researchers. Then, the heat transfer model was employed to predict the temperature distribution by taking the dissipated energy as the heat source of rubber bushing. In sum, the mechanisms of heat generation in the viscoelastic material were discussed in many publications, and so as to the static external excitation induced hysteresis damping (Jones, 2001).

(c) Heat transfer coefficients

The temperature distribution plotted from the analytical solution of heat transfer indicates thermal equilibrium of rubber components, and after this period, the heat generated from the damping can completely diffuse to the ambient. With this assumption, Schuring (Schuring, 1980) derived a thermal equilibrium equation to describe the equal power between rolling resistance and heat transferred to the environment. Furthermore, the loading is proportional with the rolling resistance, then, the convection heat transfer of tire is dependent on the driving speed of tire and written in an empirical formula as $h = C.V^{0.52}$, where the constant C is experiment determined. It is important to point out that the coefficient is an equilibrium value describing the entire surface rather than filed function. Some researchers take the coefficient as radial distribution considering the geometry of tire, while in current research, the profile of rubber bushing is commonly cylindrical and the coefficient about tire in radius direction is not appropriate (Mc Allen, Cuitino, & Sernas, 1996) and (Popiel & Bogusławski, 1975). More depth research founds the coefficient is both radius and curvature-dependent. Besides of this, the heat transfer coefficient is inversed from the surface temperature of rolling tire, the inverse method is more close to the analysis results of tire distribution (Ebbott et al., 1999) and (Mc Allen et al., 1996). However, inverse method isn′t economical efficient considering the design optimization of rubber elements.

Smooth convex of revolving curved surface about the convection heat transfer coefficient in air or flow is an important topic, which has been discussed for hundreds of years and grabs many attentions. The heat transfer characteristics are considerable complicated since they are determined by many factors, such as centrifugal force, coriolis force. There are three typical models to specify the coefficient. The earliest model deduced the surface heat transfer coefficient (HTC) with the rotating disk (Popiel & Bogusławski, 1975). Later, more researchers have been carried out on the rotating corns (Tien & Campbell, 1963). Most of those researchers started from setting up experiment and then analysis the relationship between temperature and thermal transfer. For the rotating disk and corn model about heat transfer, the effect of surface curvature was weakened. To pursue more representative expression, Kreith (Kreith, 1968) summarized the convection heat transfer in various rotating geometry and medium. Considering the high speed of driving vehicles, air flow was commonly taken as turbulence rather than laminar flow. Kreith presented the heat transfer of turbulence flow through the smooth convex rotating system surface as,

$$Nu_x = B_2.{Re_x}^{0.8} \tag{1.43}$$

Where B_2 is constant, $Nu_x = \frac{h(x).x}{k_{air}}$, $Re_x = \frac{\omega r x}{V_{air}}$ are local Nusselt number and Reynolds number of the smooth convex rotating surface. $h(x)$ is the local heat transfer coefficient, r is the radius and x is the curvilinear coordinates, K_{air} is the heat conductivity of air, V_{air} is the kinematic viscosity, ω is the rotating angular velocity. Since the smooth convex rotating surface can embody the effect of curvature on the convection heat transfer, furthermore, the cylindrical rubber bushing is of rotating system, thus, the third model is the most representative and most applicable to current case.

For the contact flat surface of the random nominally roughness, the profilometer traces of all flat surface shows the same statistical variations and gives

the same pattern (Cooper, Mikic, & Yovanovich, 1969), and (Mikić, 1974). Mikic derived an equation to estimate the contact resistance of such nominally flat surface,

$$h_c = 1.55\frac{\bar{k}\tan\theta}{\sigma}(\frac{\bar{p}\sqrt{2}}{\bar{E}\tan\theta})^{0.94} \tag{1.44}$$

Where $1/\bar{k} = 0.5(1/k_1 + 1/k_2)$ and $\bar{E} = E_1E_2/(E_1(1-{v_1}^2) + E_2(1-{v_2}^2))$. $\bar{p}$ is the mean contact pressure, $\tan\theta$ and σ are parameters charactering the roughness of contact surface, $\bar{E}$ and $\bar{k}$ are equivalent elastic modulus and equivalent heat conductivity separately.

The Reynolds of air flow for the driving truck is available with the abundant experiment data in publications, which are around 2×10^5. With the Reynolds coefficient, the heat transfer convection coefficient can be givens as,

$$h_a(x) = B_2\frac{k_{air}r^{0.8}{\omega_c}^{0.8}}{V_{air}^{0.8}} \tag{1.45}$$

Where r is the radius coordinates and x is the curvilinear coordinates from the outer surface. K is the contact heat conductivity. Rubber bushing is installed on the stabilizing bar and gap may exist between the two surfaces during the driving. But the air flow existing in the gap is poor to conduct the heat transfer, which leads to extra thermal resistance. The temperature jump will happen at the two materials because the thermal resistance. In current case, if the temperature of stabilizing bar is room temperature, then, the surface of the inner surface maybe a little bit higher than room temperature. The heat flux rate can be given as,

$$q = \frac{T_1 - T_2}{R_c} = h_c(T_1 - T_2) \tag{1.46}$$

When radial load applies on the rubber bushing, the top and bottom part of the rubber bushing experience different stress, furthermore, the contact pressure affects the contact thermal conductivity.

All in all, the heat transfer coefficients are estimated mainly from the experiment measurements. The following are some procedures suggested. Firstly, measure the equilibrium temperature of the outer sleeves and set it as the known

temperature. Secondly, set the initial value of the heat transfer coefficients. Thirdly, calculate the equilibrium temperature distribution with analytical solution or numerical solutions. Fourthly, compare the experimental measured temperature with the estimated temperature to adjust the initial value. Thermal infrared imager is commonly applied in experiment to measure the surface temperature of rubber components. Calibration and initial value of heat generation rate should be set before the testing. The heat generation rate of rubber core is temperature-dependent. It is important to notice that rubber components are commonly composed of steel and rubber and the heat transfer rate of steel is higher than that of rubber. In their measurement, the thermal infrared imager is fixed the in front of the rubber products and test twice for the outer surface and end surface of rubber components. Temperature over time is record until the stable temperature distribution is reached.

1.2.4 Challenge of Rubber Bushing Research

In order to predict performance of vehicle under a wide variety of driving conditions, one of the key components is the constitutive relationship of rubber. It is significant to the simulation of suspension system. However, the modeling of rubber components still faces great technical challenges and the following parts describe that challenges.

- The first one is the nonlinearity of mechanical properties of rubber, even though at relatively small strain. Especially, those rubbers contain particulate fillers.
- The dynamic application of bushing as the loading histories is complex, including both step/impulse transient loading and multi-frequency sinusoidal loading. Thus, it is difficult to predict the effect of complex loading histories on the nonlinear, time-dependent material.

- One of the commonly underestimated characters of elastomers is hysteresis upon loading and consequently generated heat upon deformation. Viscoelastic response of elastomers can be affected because the heat will raise the temperature of bushing.

- Time-dependent behavior of rubber bushing is complex, which embodies in both shear and volumetric deformation.

- Complex mixtures of an elastomer base resin, particulate fillers like carbon black and/or fumed silica, etc, as well as the part of manufacturing process affects the performance of the engineering rubber. Slight change of rubber supply, formulations may affect the performance of rubber, while those changes may not attract the attention of suppliers

The temperature gradient of rubber is much larger than steel due to the much lower heat transfer rate. The effect of temperature has very limited effect on the variation of conductivity and specific heat of rubber. Thus, in current research, those parameters are defined as constant and applied for the entire time range (Ebbott et al., 1999),and (Oh, Kim, Kim, Moon, & Park, 1995).

Approximated estimation of heat transfer coefficients is important. Actually, the heat transfer coefficient is a function of composition and velocity of air flow. That means the increase of driving speed of vehicles is corresponding to higher heat transfer coefficient (S. K. Clark, 1976). Usually, it is three to four hours for a truck tire to reach temperature equilibrium. For the rubber components, the barrier to quickly reach the balance is the much slower thermal conductivity of rubber compared with steel. Even though, the speed affects the heat transfer coefficient, but the influence is not so primary. Thus, in order to control the temperature rising time without changing other parameters of rubber bushing, the geometry of rubber should be critical to reach the achievement.

1.3 Objectives

Fatigue of rubber components used in vehicle application is highly related to the Mullin effect, which is known as softening effect, especially during the initial loading cycles (Chagnon et al., 2004). Thus, in order to evaluate the life of rubber components, it is necessary to consider Mullins effect. With the development of the powerful calculation ability of computer, simulation using commercial software becomes more and more predominant nowadays. In view of the important role of suspension system in the vehicle simulation, the transmission of external force and torque through suspension system demands precise formulation. Thus, the first critical problem is the rubber bushing′s dynamic mechanical behaviors when the external force and torque induce translations and rotations of rubber components. The second problem is the rubber′s constitutive equation and its corresponding models to credibly describe the dynamic response of rubber, which can be used in the FEA simulation. Besides, the damping of rubber should be thoroughly analyzed to include the hysteresis and viscous damping, in return, the heat generation mechanism can be derived. Possibility, the life expectation can be estimated considering the aging speed up due to the higher temperature of the rubber components subjected to external harmonic excitation. FEM analysis should be carried out to simulate the heat generation and estimate the dissipation energy distribution. With this higher temperature indication, the possible strategy to reduce the heat accumulation at lower temperature can be proposed, which may bring great business benefit if the life expectation of rubber bushing can be elongated.

1.4 Outline of Dissertation

The layout of the dissertation is given as follows. Chapter one initializes the motivation of this research, which is followed by the background and interest points of rubber bushing. A brief description of rubber bushing has been presented to

point out the service condition of rubber bushing and its function in the suspension system of the vehicle. Then, the complex properties of rubber materials are elaborated to present those challenges expected in the current rubber bushing research. Chapter one explains the necessity and difficulties of this research and emphasizes the significant to solve those problems in this research. The following work can be clearly presented in Figure 1.7.

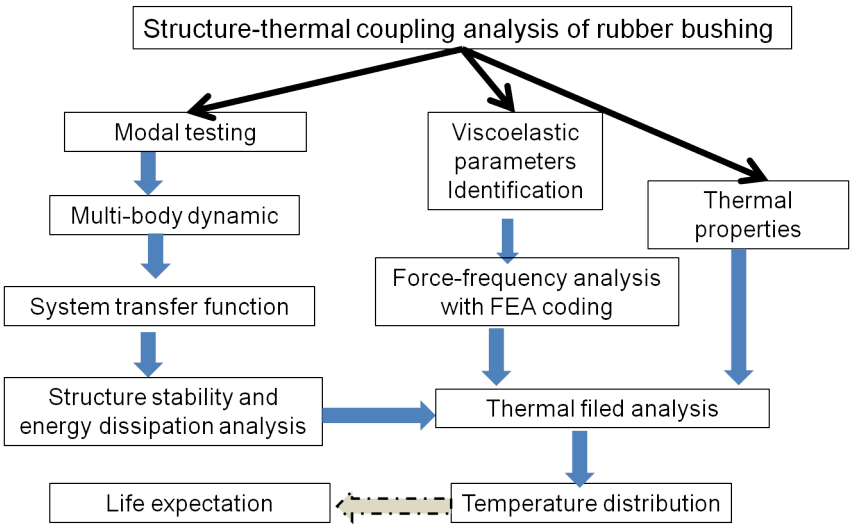

Figure 1.7.: Flowchart of research.

Chapter two begins with the definition and application of multi-body dynamic mechanism, which is commonly used in the dynamic analysis of vehicle. This method is employed to investigate the dynamic behaviors of rubber bushings installed on the suspension system. Hammer impact modal testing is carried out to get transfer function of the rubber bushing system, which is simplified as multi-body later. The energy dissipation of the rubber bushing system is also estimated with the fitted transfer function on the basis of multi-body analysis.

To achieve reliable simulation of the transmission of rubber bushing, the constitutive equation of rubber bushing is required and presented in Chapter three. The complicated mechanical properties of rubber indicate the importance to build a reliable rubber bushing model while without bringing in too much calculation

burden. This chapter gives a detailed comparison about those classical constitutive viscoelastic models in time domain and frequency domain and then determines the standard linear model as the simplest credible material model to describe the mechanical behaviors of rubber. Spectrum analysis is employed to deal with the problem in time domain, especially the problem with arbitrary loading history. Two factors contributing to the heat generation in the viscoelastic material under dynamic loading are considered. Hysteresis effect is characterized with a three-linear model to describe the friction between molecular chains and carbon black particles. Constitutive equation presenting the viscoelastic properties has been derived on the basis of Laplace transformation. MTS and DMA tests are carried out to obtain enough data to identify the parameters for further analysis in FEA. Multivariable-constrained optimization method is applied to estimate the parameters in the standard liner viscoelastic model using MATLAB with the massive data from the DMA test.

Chapter four begins with the preprocessing and post-processing of force-frequency FORTRAN program. The static simulation results are contrasted with the frequency scan analysis to evaluate the programming with complex variables. To verify the reliability and demonstrate the capability of the program, the testing on elastic structure with damping and viscoelastic structure are carried out separately. The calculated results from the FORTRAN program include displacement, strain, stress and energy dissipation of each cycle at different excitation frequency. Besides, the response of blast loading on viscoelastic beam is investigated to examine the application of spectrum analysis and FEA on the problem in time domain. More important, the approaches to develop the dissipation energy using FEA and the density of dissipation energy in the rubber core are presented in this part.

Chapter five measures the density and thermal properties of rubber material and specifies the boundary conditions of the rubber bushing. Analytical solution is approached to explore the steady and transient temperature distribution assuming

the constant hear source. MATLAB is employed to develop the FVM procedures to simulate the heat transfer in the three layered structure of rubber bushing. The temperature distribution of rubber core at different loading frequency and amplitude is accomplished based on the heat source generated from the FORTRAN program.

Finally, in chapter six, using the commercial software multi-physics COMSOL, the heat generation and temperature distribution of rubber bushing under the external harmonic excitation are calculated. In this simulation, the Prony series coefficients are applied in the COMSOL to represent the viscoelastic material mechanical properties. The MTS dynamic torsion and radial tests are carried out at quasi-static and higher frequency range. The temperature distribution at different frequency and amplitude range is recorded with thermal imager. The temperature rising rate and distribution obtained from the simulation and experiment are compared, that result confirms the success of force-frequency and heat transfer program.

CHAPTER 2. MULTI-BODY DYNAMIC ANALYSIS OF RUBBER BUSHING

There are still great demands to decrease repeating errors occurred decades in vehicle dynamic design and many areas are eager to be improved even though the mathematical tool and computing capability have greatly accelerated the development of technologies (Blundell, Harty, et al., 2004). Isolation and control are two major factors affecting the dynamic performance of vehicle. Isolation concerns about avoiding those disturbances, which are caused by the operation of the vehicles. These types of disturbances partially come from the working vehicle, such as vibration and noise. Besides of this, the external environment also imposes certain disturbances. Control is about the response of vehicle subjected to the demands of driver. The skill and capability of drives are important to control the performance of the vehicle while that work load at critical times may be beyond the controllable scope and failure to be operated properly. To keep the risk at lowest probability, more optimized dynamic design of vehicle system may give a controllable behavior of vehicles. Extended displacement and nonlinearly in space commonly occur to those parts in the complicated vehicle systems. Heavy algebra and calculus are expected to construct the kinematic or dynamic equation of vehicle system, as a result, the closed form analytical solutions maybe unreachable since the nonlinearity and complexity. Facing this critical challenge, multi-body dynamic analysis is developed to analysis the complicated suspension system of vehicle and the corresponding kinematic and dynamic behaviors.

Kinematics and Compliance (K&C) of suspension system are constantly investigated by researchers in the field of vehicle. The proper designed rubber bushings used in the suspension system contribute to achieve desirable properties, such as efficiently isolate high frequency vibration from the environment. To evaluate the behavior of suspension, K&C test or characteristics are good

indicators, which can reflect the design and characteristics of many important parts and overall structure. As a widely and commonly used part in the suspension, bushings behaviors are critical to the performance of K&C under nearly cycle loading, especially the influence on compliance is pretty obvious. During rolling or traveling, force equilibrium on the suspension system will be rebuilt, which will lead to corresponding redistribution of force and change of deformation on rubber bushing. There are many bushings installed on the suspension system, which are different in the installation locations and positions, and then stiffness of bushings is different according to its purpose. The higher force applied on the axis direction of the bushing can cause larger deformation, and the bushings′ stiffness in this direction is decisive in determining the compliance of suspension and wheel attitude, even the vehicle driving performance (Song, Chen, Lin, & Ma, 2012). Considering the important role of bushing playing in the suspension system, even the full vehicle, lots of researches strive to explore the effect of bushings′ characteristics on the performance of suspension system. Bushing usually plays dominate role merely in one direction according to its specific installation location and orientations, while in this chapter, the initial exploration using multi-body analysis begins with translation movements. There are many approaches to develop the multi-body analysis. In the early research, Newton-Euler has been commonly used in satellites dynamic analysis and on the basis of that principle, many methods are developed (Andrews & Kesavan, 1978), and (Hooker & Margulies, 1965). Lagrange equation is another approach widely used in the multi-body dynamics analysis, and computer program ADAMS and DADS are developed to proceed the dynamic calculation and produce many representative work (Chace, 1984), (Haug, 1984), and (Haug, 1989). The symbolical theory is employed by Roberson and Wittenbury to describe the characteristics of multi-body and they also develop the computer program MESA VERDE (Roberson & Wittenburg, 1966), and (Wittenburg & Schmidt, 1990). On the basis of multiple degree of freedom and discrete system, Kane method is introduced to characterize the dynamic behaviors using the

pseudo-velocity as dependent variant (Kane & Levinson, 1985), and (Kane, Likins, & Levinson, 1983). In the current research, for the clear description with tree structure, Wittenbury method is employed to characterize the dynamic behaviors of rubber bushing installed on the suspension system of vehicle.

2.1 Mathematic Notation

Vector, tensor and matrices are the carriers of multi-body mechanics. The following discussion will briefly describe the mathematic notations used in the dynamic analysis on the basis of right handed Cartesian coordinates (Wittenburg, 2007). Vector v is composed of three unit base vectors e_1, e_2 and e_3, which are orthogonal to each other and satisfy the right handedness conditions,

$$\begin{aligned} V &= v_1 e_1 + v_2 e_2 + v_3 e_3 \\ e_i \cdot e_j &= \delta_{ij} (i, j = 1, 2, 3) \\ e_1 \cdot e_2 \times e_3 &= +1 \end{aligned} \tag{2.1}$$

where v_1 , v_2 and v_3 are scalar quantities of coordinates in vector v. Define ${e^1}_i (i = 1, 2, 3)$ as the base vectors of base 1 and ${e^2}_i (i = 1, 2, 3)$ as the base vectors of base 2. ${e^2}_i$ can be represented in ${e^1}_i$ using the scalars ${\alpha^{21}}_{ij}$, which is the cosine angle of the two base vectors. That transformation can be written in matrix with the direction cosine matrix, $\underline{e^2} = \underline{A^{21} e^1}$. Furthermore, the scalar product of any two rows or columns elements in the cosine matrix is equal to the Kronecker delta,

$${e^2}_i = \sum_{j=1}^{3} {\alpha_{ij}}^{21} {e^1}_j (i = 1, 2, 3) \tag{2.2}$$

$$\sum_{k=1}^{3} {\alpha_{ik}}^{21} {\alpha^{21}}_{jk} = \sum_{k=1}^{3} {\alpha_{ki}}^{21} {\alpha^{21}}_{kj} = \delta_{i,j} (i, j = 1, 2, 3) \tag{2.3}$$

The Equation (2.2) describes the relationship of vector coordinates with respect to different bases, which is important to connect the independent coordinate system with the general coordinate systems in multi-body analysis. The tensor D is another very important notation used in multi-body dynamic analysis. It is defined

as the summation of two vectors′ dyadic products. Swapping the two vectors in the dyadic product will give a conjugate of D,

$$D = a_1 b_1 + a_2 b_2 + a_3 b_3 + ... \tag{2.4}$$

$$\bar{D} = b_1 a_! + b_2 a_2 + b_3 a_3 + ... \tag{2.5}$$

where the tensor D is commonly expressed in matrix after decomposing the vectors on the base $\underline{e_i}$ and regrouping it on coordinate scalars D_{ij}. Similarly, if the tensor D is decomposed on another base $\underline{e_j}$, the coordinate matrices $\underline{D^1}$ and $\underline{D^2}$ of the two bases can transform with each other,

$$\begin{aligned} D &= \sum_{i=3}^{3} \sum_{j=1}^{3} D_{ij} e_i e_j = \underline{e^T D e} \\ D &= \underline{e^{2^T} D^2 e^2} = \underline{e^{1^T} D^1 e^1} \\ \underline{D^2} &= \underline{A^{21} D^2 A^{12}} \end{aligned} \tag{2.6}$$

Vector cross product is used to describe the tenors with skew-symmetric coordinate matrix, thus, it is important to get familiar with the cross product of vectors,

$$a \times b \times v = ba \cdot v - ab \cdot v = ba - ab \cdot v \tag{2.7}$$

Where the tensor $(ba - ab)$ can be decomposed in a specified base, which displays in a skew-symmetric coordinate matrix in Equation 2.8. $C_i (i = 1, 2, 3)$ are the coordinates of C. The symbol $\widetilde{\underline{c}}$ is introduced to simplify those equations from vectors to scalars,

$$(ba - ab) = \widetilde{c} = \begin{bmatrix} 0 & -c_3 & c_2 \\ c_3 & 0 & -c_1 \\ -c_2 & c_1 & 0 \end{bmatrix} \tag{2.8}$$

$$c = \sum_{i=1}^{n} \sum_{j=1}^{n} a_i D_{ij} b_j = \underline{a^T} D \underline{b} \tag{2.9}$$

Equation 2.9 shows the transformation from tensor scalar by left multiplication with a_i and right multiplication with b_j when numerical calculation is more convenient than matrix expression.

2.2 Kinematic and Dynamic Analysis of Rubber Bushing

This part talks about the development of kinematic and dynamic analysis of rubber bushing using the Wittenbury approach. For the dynamic analysis, the kinematic relationship of kinematic is discussed in front of the dynamic analysis as the later is analyzed on the basis of the former. A single rigid body is set as example in the first step to introduce the concepts and methods used in the multi-body analysis. The second step is the kinematic relationship of rubber bushing after building the tree structure to describe the connections between bodies. The third step is the dynamic analysis on the basis of kinematic results.

2.2.1 Kinematic Analysis of Single Rigid Body

Symbolic graph and tree structure are employed here to describe the connection of multi-body. Figure 2.1 gives a simple example of rigid body. Assuming the external force F_i and torque M_i are applied on a rigid body S_i, and the external force F_i is applied on the mass center C_i. The internal force ${X^c}_a$ and internal torque Y_a apply on the joint u_a, where c refers to the constraining anti-force. An incidence matrix S_{ia} is introduced here to describe the tree structure consisting of arc and vertices. Matrix $S_{ia}(i = 0, ..., n; a = 1, ..., m)$ are defined according to the following rules: $S_{ia} = 1$ if the arc a is the joint of body i and pointing away from the body i; $S_{ia} = -1$ if the arc a is of the joint i and pointing toward the body i; $S_{ia} = 0$ if none the two cases is satisfied. With the definition of locations and loadings, the force and moment equilibrium equation can be written as,

$$m_i {r''}_i = F_i + \sum_{a=1}^{n} S_{ia} {X_a}^c, (i = 1, ..., n) \tag{2.10}$$

Where, r_i is the radius vector from the inertial space to the mass center C_i. Define the arm of internal force from joints as C_{ib} and C_{ic}, then, the coupling moment on the mass center C_i can be represented as,

$$(c_{ib} \times {X_b}^c + Y_b) - (c_{ic} \times {X_c}^c + Y_c) \tag{2.11}$$

The moment of momentum is,

$$L'_i = M_i + \sum_{a=1}^{n} S_{ia}(c_{ia} \times X_a{}^c + Y_a), (i = 1, ..., n)$$
$$\text{or in matrix} \quad [L'] = [M] + [C][X^c] + [S][Y] \tag{2.12}$$

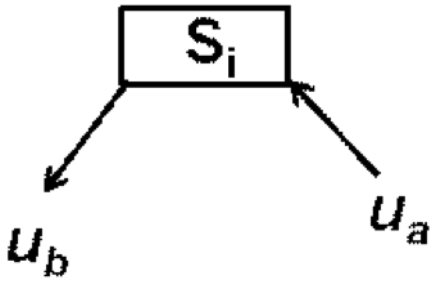

Figure 2.1.: Sketch of two joints connected on the rigid body.

As to the mechanic behavior of entire system, the internal force $X_a{}^c$ is merely intermediate variable and can be derived by pre-multiply $[T]$ with force equilibrium in Equation 2.10. After elimination of variable $X_a{}^c$, the moment of momentum can be rewritten as,

$$[L'] - [C][T] \times ([m][r''] - [F]) = [M] + [S][Y] \tag{2.13}$$

$$[X^c] = [T]([m][r''] - [F]) \tag{2.14}$$

Where m, S and $[T]$ are scalars. In the current expression, moment of momentum is given in local coordinates, in the next step, radius vector r_i in general coordinates will be introduced. Figure 2.2 displays the radius vector of three rigid bodies. Setting the C_0 is located at the joint u_i and the vector $C_{01} = 0$. C_0 is not incident with other vertices, thus, it is reasonable to define $c_{0a} = 0(a = 1, \ldots, n)$. The radius vectors of B_1 and B_2 in the Figure 2.2 can be described as,

$$r_i + c_{11} = r_2 + c_{12} \tag{2.15}$$

For the tree structure described rigid bodies, the radius vector can be represented using the time-dependent $r_0(t)$ and incident matrix as,

$$r_0[S_0]^T + [S]^T[r] + [C]^T[1_n] = 0 \tag{2.16}$$

Where, $C = S_{ia}c_{ia}$. Left multiply the equation and using the relationship between $[T]$ and $[S]$ to get,

$$[r] = r_0[1_n] - ([C][T])^T[1_n] \tag{2.17}$$

Where, $d_{ij} = ([C][T])_{ij} = \sum_{a=1}^{n} T_{aj}S_{ia}c_{ia}, i, j = 1, \ldots, n$. Now, the equation of motion in generalized coordinates can be rewritten as,

$$[L'] - [C][T] \times [m]([C''][T])^T[1_n] - ([C][T]) \times ({r_0}''[m][1_n] - [F]) = [M] + [S][Y] \tag{2.18}$$

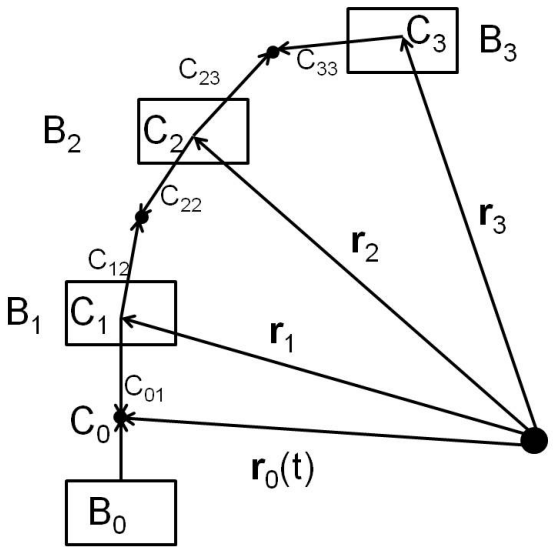

Figure 2.2.: Radius vectors of bodies.

As to current tree structure of rubber bushing, $[C]$, $[T]$, $[S]$,$[m]$ and $[{r''}_0]$ are known, the equation can be properly simplified with d_{ij}. From the definition, the d_{ij} of bodies in rubber bushing are shown in Figure 2.3. The path vector d_{ij} can be

obtained from the radius vectors using $r_i = r_0 - \sum_{j=1}^{n} d_{ij}$, which are represented in the following,

$$r_1 = r_0 - d_{11} = r_0 - c_{01} = r_0 \tag{2.19}$$

$$r_2 = r_0 - d_{12} - d_{22} = r_0 - (c_{01} + c_{11}) - c_{12} \tag{2.20}$$

$$r_3 = r_0 - d_{13} - d_{23} - d_{33} = r_0 - (c_{01} + c_{11}) - (c_{12} + c_{22}) - c_{33} \tag{2.21}$$

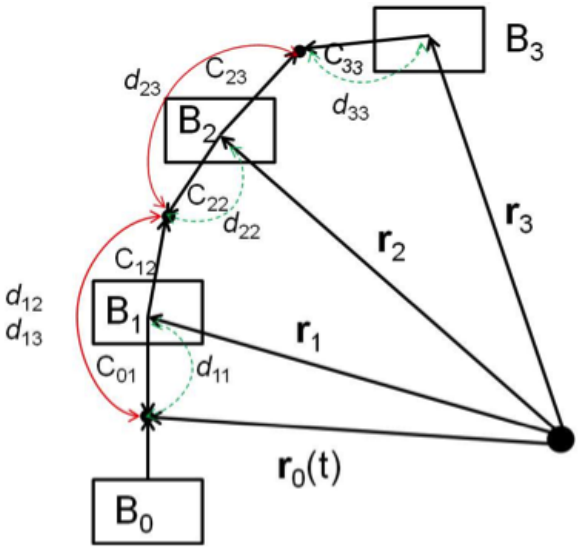

Figure 2.3.: Path vector d_{ij} arc.

Finally, the velocity of radius vector can be obtained by doing derivation of $r_i = r_0 - \sum_{j=1}^{n} d_{ij}$ and get the velocity in generalized coordinates,

$$\dot{r_i} = \dot{r_0} = \sum_{j=1}^{n} \omega_j \times d_{ij} \tag{2.22}$$

2.2.2 Model and Tree Structure of Rubber Bushing

Cylindrical rubber bushing is composed of three parts, internal steel sleeve, rubber core and outer steel sleeve. The external excitation from the suspension system of the vehicle is applied on the steel sleeves. Rubber bushing in current research is modeled as three bodies to facilitate kinetic and dynamic analysis. The steel sleeves and rubber components are combined by vulcanization bonding, which is relative thinner. The inner force between rigid bodies is represented using the spring-dashpot as in the multi-body analysis. Figure 2.4 is the sketch of the multi-body rubber bushing model.

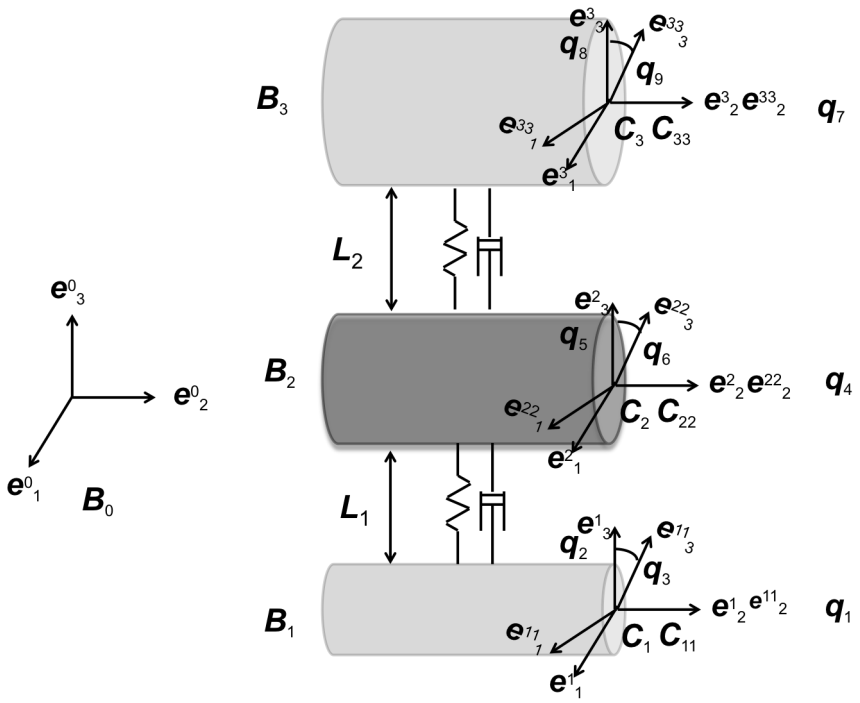

Figure 2.4.: Sketch of multi-body rubber bushing model.

This system includes four bodies, B_0 is a moving carrier body in the inertial space and the moving base e^0 is represented to prescribe its time-dependent movement. B_1 is the inner steel sleeve, B_2 is rubber core and B_3 is outer steel sleeve, which are interconnected with each other using springs and dashpots. B_1 is connected with B_0 by joint H_1, which is also written as H_{01} and H_{11} separately for

the joints ending with B_0 or B_1. The generalized coordinates of B_1 is defined as $q = [x_1, z_1, \phi_1]^T$ considering the three DOF. The mass center of B_1 is the origin of coordinates for base e^1 and e^{11}, which are fixed on the body. From Figure 2.4, it is found that base ${e^1}_2$ is parallel to the base ${e^0}_2$, which indicates that the direction cosine matrix $A_{0(1)}$ is identity matrix. Again, the base ${e^1}_2$ is always parallel with ${e^{11}}_2$, which represents another identity matrix $A_{0(11)}$. Similarly, the base e^2 and e^{22} are located at the mass center of body B_2. The corresponding joint attached with B_1 is H_{12} and the one attached with B_2 is H_{22}. There are three DOF for B_2, which is given in the generalized coordinates $q = [x_2, z_2, \phi_2]^T$ to describe its translation. The vector ${e^{11}}_2$ and ${e^2}_2$ are always parallel, as a result, the direction cosine matrix $A^{11(2)}$ is identity matrix. Similarly, the base ${e^{22}}_2$ is always parallel with ${e^2}_2$, which gives another identity matrix $A^{2(22)}$. Again, the mass center of B_3 is the location for the base e^3 and e^{33}. The three DOF of B_3 defines the generalized coordinates as $q = [x_3, z_3, \phi_3]^T$. The joint between B_2 and B_3 have H_{32} and H_{33}. It is easy to found that the vector base ${e^{22}}_2$ is parallel to ${e^3}_2$ and ${e^3}_2$ is again parallel to ${e^{33}}_2$. That shows two identity matrices $A^{22(3)}$ and $A^{3(33)}$. In sum, the rubber bushing system can be treated as a 9 DOF of tress structure coupling with a carrier body, which gives the dependent generalized coordinates as,

$$q = [x_1, z_1, \phi_1, x_2, z_2, \phi_2, x_3, z_3, \phi_3]^T \tag{2.23}$$

The generalized velocity and acceleration can be obtained from derivative of Equation 2.23,

$$V = [\delta x_1, \delta z_1, \delta\phi_1, \delta x_2, \delta z_2, \delta\phi_2, \delta x_3, \delta z_3, \delta\phi_3]^T \tag{2.24}$$

$$a = [\delta\delta x_1, \delta\delta z_1, \delta\delta\phi_1, \delta\delta x_2, \delta\delta z_2, \delta\delta\phi_2, \delta\delta x_3, \delta\delta z_3, \delta\delta\phi_3]^T \tag{2.25}$$

For convenience, define $cos(q_i)$ as C_i and $sin(q_i)$ as S_i, then the direction cosine matrix between bodies B_0 and B_1 can be expressed as,

$$A^{01} = A^{01}A^{1(11)} = \begin{bmatrix} C_3 & 0 & -S_3 \\ 0 & 1 & 0 \\ S_3 & 0 & C_3 \end{bmatrix} \tag{2.26}$$

It is easy to found that the transpose of direction cosine matrix is equal to its inverse, which gives $(A^{0(1)})^T = (A^{0(1)})^{-1}$. Similarly, the direction cosine matrix between bodies B_0 and B_2 can be derived from,

$$A^{02} = A^{01}A^{1(11)}A^{11(2)}A^{2(22)} = \begin{bmatrix} C_3C_6 - S_3S_6 & 0 & -C_3S_6 - C_6S_3 \\ 0 & 1 & 0 \\ S_3C_6 + C_3S_6 & 0 & -S_3S_6 + C_3C_6 \end{bmatrix} \tag{2.27}$$

The direction cosine matrix between bodies B_0 and B_3 can be obtained by multiply the A^{02} with the direction cosine matrix between bodies B_2 and B_3,

$$A^{03} = A^{01}A^{1(11)}A^{11(2)}A^{2(22)}A^{22(3)}A^{3(33)} =$$

$$\begin{bmatrix} C_3C_6C_9 - S_3S_6S_9 - C_3S_6S_9 - S_3C_6S_9 & 0 & -C_3C_6S_9 + S_3S_6S_9 - C_3S_6C_6 - C_6S_3C_6 \\ 0 & 1 & 0 \\ S_3C_6C_9 + C_3S_6C_9 - S_3S_6S_9 + C_3C_6S_9 & 0 & -S_3C_6S_9 - C_3S_6S_9 - S_3S_6C_9 + C_3C_6C_9 \end{bmatrix} \tag{2.28}$$

The tree structure of the rubber bushing model for dynamic analysis is described here with the vertices and arc, which represent the bodies and joints (Figure 2.5). The bodies $B_i(i = 0, 1, \ldots, n)$ are represented as $S_i(i = 0, 1, \ldots, n)$ in the tree structure. The connections or joints are symbolized as $u_a(a = 1, \ldots, n)$.

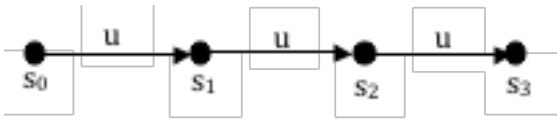

Figure 2.5.: Tree structure of the rubber bushing.

Figure 2.5 displays that each arc u_a begins with a vertex $i^+(a)$ and terminates with a vertex $i^-(a)$. Including the carrier body, there are four vertexes and three arc in current tree, that structure gives a connection relationship of arc u_a between vertex $i^+(a)$ and $i^-(a)$ as shown in Table 2.1.

Table 2.1: Connection arc of u_a

a	1	2	3	4
$i^-(a)$	0	1	2	3
$i^+(a)$	1	2	3	4

Similar to the discussion about single rigid body, an incidence matrix S_{ia} is listed here to describe the relationship between arc and joints in the tree structure of rubber bushing, which gives the incident matrix as,

$$S_0 = \begin{bmatrix} 1 & 0 & 0 & 0 \end{bmatrix} \tag{2.29}$$

$$S = \begin{bmatrix} -1 & 1 & 0 & 0 \\ 0 & -1 & 1 & 0 \\ 0 & 0 & -1 & 1 \\ 0 & 0 & 0 & -1 \end{bmatrix} \tag{2.30}$$

Where the row i in the incident matrix stands for the number of vertex and the column a stands for the number of arc. Since vertex is numbered from 0, it is better to separate the incident matrix into the row matrix S_0 and $(m \times m)$ matrix S. Another introduced matrix is path matrix T, which is defined to describe the path from the carrier body to other bodies in the tree structure. In order to reach vertex I, if arc a is on the way and pointing to vertex i, set $T_{ai} = -1$; if arc a is on the way but pointing to vertex 0, then set $T_{ai} = -1$; if none of two cases is satisfied, set

$T_{ai} = 0$. With this definition, the path matrix T of rubber bushing can be displayed as,

$$T = \begin{bmatrix} -1 & -1 & -1 & -1 \\ 0 & -1 & -1 & -1 \\ 0 & 0 & -1 & -1 \\ 0 & 0 & 0 & -1 \end{bmatrix} \tag{2.31}$$

Since the matrix S and T are applicable to the same tree structure, and both are unique to describe the relationship between vertices and arc, there must be a relationship to connect the two matrices. Actually, the incident matrix and path matrix can transfer to each other with,

$$T^T {S_0}^T = -1_n \quad \text{and} \quad TS = ST = E_n \tag{2.32}$$

With those characteristics about the tree structure of the rubber bushing, the kinematic and dynamic analysis of the directed tree structure is able to process. In current tree structure, spherical joints and plane movement are coexisting to control the movement of three-body.

2.2.3 Kinematic Equation of Model

To obtain the velocity in term radius in the general coordinates, vector ω_j should be derived. To solve this problem, the movement of rubber bushing in the inertia space is investigated. Two bodies shown in Figure 2.6 are good example to describe the relative movements between bodies. From previous discussion, it is easy to connect the two bodies of independent base. The connection can be described as $e^{(1)} = A^{01}e^0$, $e^{(2)} = A^{02}e^0$ and $e^{(3)} = A^{03}e^0$ using the direction cosine matrix. The relative orientations of vector bases have already presented in the tree structure modeling with $A^{01} = A^{02}G_2$ and $A^{02} = A^{03}G_3$, where G_2, and G_3 are orthogonality matrixes. The bases are also connected with $e^0 = e^1G_1$ and $e^1 = A^{01}e^0$, then $(e^1)^{-1}(A^{01})^{-1}e^1 = G_1$ or $(e^0)^{-1}(A^{01})^{-1}e^0 = G_1$. For bodies in Figure 2.6, the relative

location and orientation can be determined with G_2, c_{12} and c_{22}, which are expressed in generalized coordination, $c_{22} = c_{22}(q_4, q_5, q_6)$ and $G_2 = G_2(q_4, q_5, q_6)$.

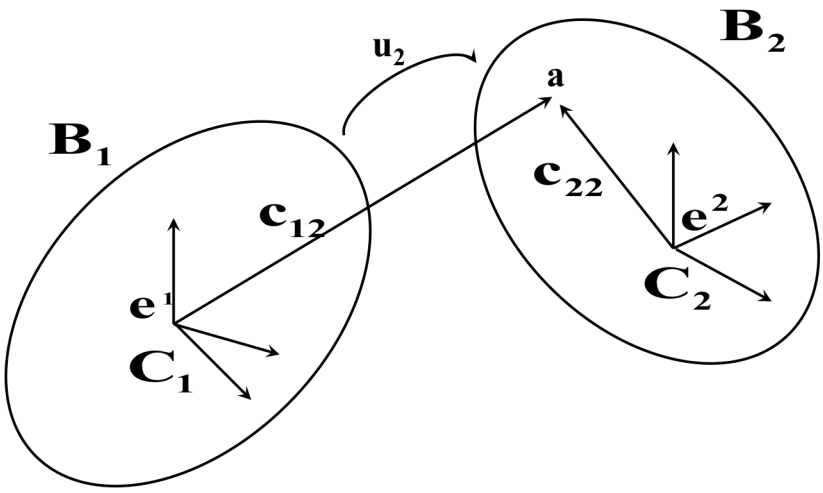

Figure 2.6.: Relative movement of rigid bodies in the inertia space.

Now, the relative angular velocity of B_2 to B_1 can be presented with the generalized coordination,

$$\Omega_a = \sum_{l=1}^{n_a} P_{al} \dot{q_{al}}, (a = 1, \ldots, n) \tag{2.33}$$

Where p_{al} is the unit vector of the joint rotation and it is not easy to read from the tree structure, thus, the Ω_{al} is commonly calculated from the direction matrix. Here G_2 is known, the Ω_2 is given as,

$$\begin{bmatrix} 0 & -\Omega_{23} & \Omega_{22} \\ \Omega_{23} & 0 & -\Omega_{21} \\ -\Omega_{22} & \Omega_{21} & 0 \end{bmatrix} = -\dot{G_2} {G_2}^T \tag{2.34}$$

As pro-mentioned, the total DOF of the tree is $q = [x_1, z_1, \phi_1, x_2, z_2, \phi_2, x_3, z_3, \phi_3]^T$ to include six translation movements and three rotations. Because the translation

movement does introduce joint rotation component, the rotation matrix element relative to translation movement is 0. That gives the rotation matrix p^T as,

$$p^T = \begin{bmatrix} 0 & 0 & p_{11} & 0 & 0 & 0 & 0 & 0 & 0 \\ 0 & 0 & 0 & 0 & 0 & p_{22} & 0 & 0 & 0 \\ 0 & 0 & 0 & 0 & 0 & 0 & 0 & 0 & p_{33} \end{bmatrix} \tag{2.35}$$

Where the Ω_a, q and p^T are set in the generalized coordinates. Define na as the DOF of every joint and the relative acceleration of $B_{i-(a)}$ to $B_{i+(a)}$ can be formulated as,

$$\dot{\Omega} = \sum_{l=1}^{na} p_{al}\ddot{q_{al}} + \omega_a = \sum_{l=1}^{na} p_{al}\ddot{q_{al}} + \sum_{l=1}^{na}\sum_{l=1}^{na} \frac{\partial p_{al}}{\partial q_{al}} \dot{q_{al}}\dot{q_{ar}} = P^T\ddot{q} + \omega(a = 1, .., n) \tag{2.36}$$

Now, with the obtained relative acceleration of $B_{i-(a)}$ to $B_{i+(a)}$, introducing the path matrix, the absolute angular velocity of B_i to B_0 can be derived. First, look at the relative angular velocity rewritten in the path matrix,

$$\omega = -T\Omega + \omega_0 1_n = -(pT)^T\dot{q} + \omega_0 1_n \tag{2.37}$$

Do derivative of Equation (2.37) and substitute ${\omega_a}^* = \omega_{i-(a)} \times \Omega_a$ to obtain the absolute angular acceleration of bodies as,

$$\dot{\omega} = -(pT)^T\ddot{q} - T^T(\omega + \omega^*) + \dot{\omega_0} 1_n \tag{2.38}$$

Now, still use the Figure 2.6 as example to investigate the relative velocity and acceleration of joint pointing to the bodies. Do derivative of c_{22} in the base $e^{(1)}$,

$$\dot{c_{12}} = \sum_{l=1}^{3} \frac{\partial c_{12}}{\partial q_{2l}} \dot{q_{2l}} \quad \text{and} \quad \dot{c_{22}} = \sum_{l=1}^{3} \frac{\partial c_{22}}{\partial q_{2l}} \dot{q_{2l}} \tag{2.39}$$

And do derivation again to obtain the relative acceleration of joint 2 to the bodies 1 and 2,

$$\ddot{c_{12}} = \sum_{l=1}^{3} \frac{\partial c_{12}}{\partial q_{2l}} \ddot{q_{2l}} + \sum_{l=1}^{3}\sum_{r=1}^{3} \frac{\partial^2 c_{12}}{\partial q_{2l}\partial q_{2r}} \dot{q_{2l}}\dot{q_{2r}} \tag{2.40}$$

$$\ddot{c_{22}} = \sum_{l=1}^{3} \frac{\partial c_{22}}{\partial q_{2l}} \ddot{q_{2l}} + \sum_{l=1}^{3}\sum_{r=1}^{3} \frac{\partial^2 c_{22}}{\partial q_{2l}\partial q_{2r}} \dot{q_{2l}}\dot{q_{2r}} \tag{2.41}$$

With the introduce of path matrix, the absolute location vector is rewritten as,

$$r_i = \sum_{a=1}^{n} T_{ai}(c_{i+(a)} - c_{i-(a)}) + r_0 (i = 1, 2, \ldots, n) \tag{2.42}$$

Do derivative of Equation 2.42 and the absolute velocity of the mass center is given as,

$$\dot{r_i} = \sum_{a=1}^{n} T_{ai}(\dot{c_{i+(a)}} - \dot{c_{i-(a)}}) + \dot{r_0} (i = 1, 2, \ldots, n) \tag{2.43}$$

$$\dot{c_{ia}} = \begin{cases} \dot{c_{ia}} + \omega_i \times c_{ia} = \sum_{l=1}^{n} k_{al} \dot{q_{al}} - c_{ia} \times \omega_i \quad (i = i^{+}_{(a)}) \\ \omega_i \times c_{ia} = -c_{ia} \times \omega_i \quad (i = i^{-}_{(a)}) \end{cases}$$

Where $C = S_{ia} c_{ia}$, $k_{al} = \frac{\partial C_{i+(a)a}}{\partial q_{al}}$ is only applicable to the translation movement. For the tree structure of rubber bushing, k_T is given as,

$$k^T = \begin{bmatrix} k_{11} & k_{11} & 0 & 0 & 0 & 0 & 0 & 0 & 0 \\ 0 & 0 & 0 & k_{21} & k_{22} & 0 & 0 & 0 & 0 \\ 0 & 0 & 0 & 0 & 0 & 0 & k_{31} & k_{32} & 0 \end{bmatrix} \tag{2.44}$$

After the introduce of path matrix, incident matrix, the absolute angular velocity and absolute angular acceleration of the mass center of B_i can easily be obtained from derivative of radius r_i once and twice,

$$\dot{r} = (pT \times CT - kT)^T \dot{q} + (CT)^T \times \omega_0 1_n + \dot{r_0} 1_n + \omega_0 \times c_{01} 1_n \tag{2.45}$$

$$\ddot{r_i} = -\sum_{a=1}^{n} T_{ai}(\ddot{c_{i+(a)}} - \ddot{c_{i-(a)}}) + \ddot{r_0} \tag{2.46}$$

Where $\ddot{r_0} = \ddot{r} + \dot{\omega_0} \times c_{01} + \omega_0 \times (\omega_0 \times c_{01}) + 2\omega_0 \times \dot{c_{01}}$. The acceleration of $c_{i\pm(a)a}$ can be represented using the path matrix and incident matrix, then the absolute angular velocity can be rewritten as,

$$\dot{r} = (pT \times CT - kT)^T \ddot{q} + (CT)^T \times v - T^T(g + h) + \ddot{r_0} 1_n \tag{2.47}$$

$$h_a = \sum_{l=1}^{na} \sum_{r=1}^{na} \frac{\partial^2 c_{i+(a)a}}{\partial q_{al} \partial q_{ar}} \dot{q_{al}} \dot{q_{ar}} + 2\omega_{i+(a)} \times \dot{c_{i+(a)a}} \tag{2.48}$$

$$g_a = \omega_{i+(a)} \times (\omega_{i+(a)} \times c_{i+(a)a}) - \omega_{i-(a)} \times (\omega_{i-(a)} \times c_{i-(a)a})(a = 1, 2, 3) \tag{2.49}$$

This is the kinetic equation of tree structure rubber bushing, which includes the description about angular velocity, variation of radius vector and angular acceleration in the generalized coordinates.

2.2.4 Dynamic Equation of Model

Similarly, the derivation of dynamic equation of rubber bushing still begins with the example of two bodies as shown in Figure 2.7. ρ_{12} and ρ_{22} are vectors on the two bodies. To any point on the bodies, the radius vector can be written as,

$$r = r_p + \rho; \quad \ddot{r} = \ddot{r_p} + \ddot{\rho}; \quad \delta r = \delta r_p + \delta\rho = \delta r_p + \delta\pi \times \rho \tag{2.50}$$

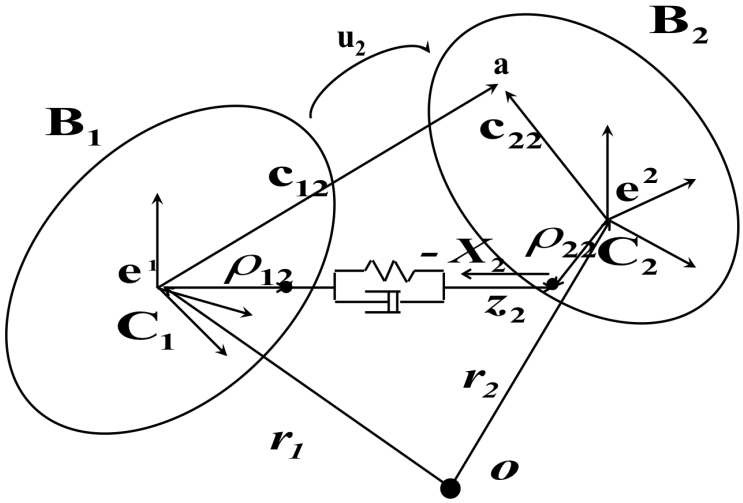

Figure 2.7.: Translation movement elements between B_2 and B_1.

Apply the virtual work principle to the Equation 2.50 and get,

$$\sum_{i=1}^{n} [\delta r_i (F_i - m_i \ddot{r}_i) + \delta\pi_i (L_i - J_i\dot{\omega}_i - \omega_i \times J_i\omega_i)] + \delta W = 0 \tag{2.51}$$

Where m_i and J_i is the mass of B_i and inertial tensor to mass center, F_i and L_i are force and torque applied on the mass center of B_i. The previous kinematic equation has already solved all the variants in that equation except for the virtual work W done by the spring and dashpot. As to the rubber bushing system, the virtual work of spring and dashpot in the generalized coordination is given as,

$$\delta W = \delta q^T Q \tag{2.52}$$

Where $Q = [Q_{11}, Q_{12}, Q_{13}, Q_{21}, Q_{22}, Q_{23}, Q_{31}, Q_{32}, Q_{33}]^T$ in current 9 DOF tree structure. There are two translation movements and one rotation movement for every rigid body. Starting from the translation movement, the expression of the relative distance of the two vectors should be written as,

$$z_2 = (r_2 + \rho_2) - (r_1 + \rho_1) \tag{2.53}$$

Derivative the relative distance to get the relative velocity of the two bodies, $\dot{z_2} = (\dot{r_2} + \omega \times \rho_2) - (\dot{r_1} + \omega_1 \times \rho_1)$. With the introduction of the incidence matrix, the relative velocity between bodies can be represented as,

$$\dot{z_a} = -\sum_{i=1}^{n}(S_(ia)\dot{r_i} + \omega_i \times S_{ia}\rho_{ia}) \quad \text{or} \quad \dot{z} = -(S^T\dot{r} - (S\rho)^T \times \omega) \quad (a = 1, 2, 3) \tag{2.54}$$

To continue the application of virtual work principle, variation of relative distance is analyzed and given as $\delta z = (S^T\alpha - P^T \times \beta)\delta q$, where $P_{ia} = S_{ia}\rho_{ia}$. Define the internal force applied on B_i as $+X_i$ and the force applied on B_2 as $-X_2$, then, the flat power elements have the virtual work as,

$$\delta W_1 = \sum_{a=1}^{n} \delta z_a X_a = -\delta z^T X = \delta q^T(\alpha^T S + \beta^T \times P)X \tag{2.55}$$

Where $\beta = -(pT)^T$ and $\alpha = (pT \times CT - kT)^T$. Now, the virtual work of translation movement are obtained.

To further the current calculation, the definition of augmented body is introduced. Define the vector from the mass center of the augmented body to the augmented bodies as B_i. The mass center of the sleeves and rubber are at the center

of cylindrical and $r = 0$ for all bodies. Thus, the mass center of the augmented bodies B_1, B_2 and B_3 also locate at the center of cylindrical, which means the mass center of the original body and the augmented body are overlapped. The augment body vectors of body B_1 is $b_{11} = 0$; $b_{10} = c_{11}$ and $b_{12} = b_{13} = c_{12}$. As to rigid body B_2, the mass center of B_1 and B_0 is the cylindrical center. Again, the mass center of augment body is $r = 0$, then, $b_{22} = 0$; $b_{20} = b_{21} = c_{12}$ and $b_{23} = c_{23}$. Similarly, for rigid body B_3, the augmented center is the center of cylindrical. Then, $b_{33} = 0$, $b_{30} = b_{31} = b_{32} = c_{33}$ and the inertia tensor of the three rigid body is given as,

$$J_1 = \frac{1}{2}m_1({r_1}^2 + {r_0}^2); \quad J_2 = \frac{1}{2}m_2({r_2}^2 + {r_1}^2); \quad J_3 = \frac{1}{2}m_3({r_2}^2 + {r_3}^2) \tag{2.56}$$

The excitation of the rubber bushing is caused by the external load from the stabilizing bar, which is taken as B_0 in this analysis. The active force and active torque applied on the rigid bodies are set as zero matrix. The inner metal sleeve is vulcanization bonding with the rubber bushing, and then the outer metal sleeve is compressed to assemble the bonded two layers. As to the vulcanization bonding B_1 and B_2, the force is relative smaller than the compressed assembly layers B_2 and B_3. For the inner force at the joint, the force applied on the B_1 is $-X_2$ and B_2 is $+X_2$. The force applied on the B_2 is $-X_3$ and on the B_3 is $+X_3$. Define the inner force at the joint 1 as zero. About the rotation torque applied on the system, since there isn$'$t any rotation torque, it is easy to define rotation torque as
$Y = [Y_1 \quad Y_2 \quad Y_3]^T = [0\ 0\ 0]^T$ for the three joints.

The next step deals with the application of virtual work on the rotation elements. As to the angular velocity given as $\Omega = P^T q$, the variation is $\delta\chi = P^T \delta q$. Then, that definition provides the expression of virtual work, $\delta W_{11} = -\delta q^T PY$, where $Y = [Y_1, Y_2, Y_3]^T$ is the moment of the internal force. Similarly, define the internal moment applied on B_1 as $+Y_2$ and the internal moment applied on B_2 as $-Y_2$, then, the total virtual work given by the combination of translation and rotation movement elements is,

$$\delta W = \delta W_1 + \delta W_{11} = \delta q^T[(\alpha^T S + \beta^T \times P)X - pY] \tag{2.57}$$

From the previous work, the kinematic equation of the rubber bushing tree structure is given as,

$$\delta r = \alpha \delta q; \quad \ddot{r} = \alpha \ddot{q} + u; \quad \delta \pi = \beta \delta q \quad and \quad \dot{\omega} = \beta \ddot{q} + v \tag{2.58}$$

Where $\alpha = (pT \times CT - kT)^T$, $\beta = -(pT)^T$ and $u = (CT)^T \times v - T^T(g + h) + \ddot{r_{01}} l_n$, Substitute the Equation 2.58 into the total virtual work principle to get,

$$\delta q^T(-A\ddot{q} + B) = 0 \tag{2.59}$$

Where $A = \alpha^T m \alpha + \beta^T J \beta$ and $B = \alpha^T(F - mu) + \beta^T(L - Jv - V) + Q$. Since the variation is independent, thus, the basic dynamic equation of current system is,

$$A\ddot{q} = B \tag{2.60}$$

Now, substitute $\alpha = (pT \times CT - KT)^T$, $u = (CT)^T \times v - T^T(g + h) + \ddot{r_{01}} l_n$ and $\beta = -(pT)^T$ into expression A to get,

$$\begin{aligned} A = {} & (pT \times CT)m(pT \times CT)^T + (pT)J(pT)^T - [pT \times G(TmT^T)k^T] \\ & - [pT \times G(TmT^T)k^T]^T + k(TmT^T)k^T \end{aligned} \tag{2.61}$$

Substitute the first item in Equation 2.61 into the virtual principle $\delta q^T(-A\ddot{q} + B) = 0$ and simplify A to get,

$$\begin{aligned} A = {} & (pT)K(pT)^T - [pT \times G(TmT^T)k^T] \\ & - [pT \times G(TmT^T)k^T]^T + k(TmT^T)k^T \end{aligned} \tag{2.62}$$

Similarly, substitute α, u and β into B to get,

$$\begin{aligned} B = {} & (pT \times CT - kT)\{F - m[(CT)^T \times v - T^T(g + h) + r_{01}1_n]\} \\ & - [pT \times (L - Jv - V) + Q \end{aligned} \tag{2.63}$$

B can be simplified further with the following two equations,

$$-(pT) \times (CT)m(CT)^T v + (pT)Jv = (pT)kv \tag{2.64}$$

$$(pT) \times (CT)m(CT)^T g + (pT)V = (pT)G \tag{2.65}$$

Finally, the expression of B can be represented as,

$$\begin{aligned} B = (pT)[Kv + G - L + (CT) \times (F + mT^T h - m\ddot{r_{01}}1_n)] \\ - (kT)[F + m[T^T(g + h) - m(CT)^T \times v - m\ddot{r_{01}}1_n]] + Q \end{aligned} \tag{2.66}$$

Now, the dynamic equation of rubber bushing tree structure in the generalized coordination is derived.

2.3 Modal Analysis of Rubber Bushing

Using the symbolical graph and tree structure, the kinetic and dynamic analysis of rubber bushing are finished. As discussed before, the rubber bushing is decomposed into three bodies, which are joined by spring and damper considering the large deformation and viscoelastic of rubber core. The following work continues to estimate the parameters of spring and dashpot through the hammer impact modal testing method. The first step is to detect the proper arrangement of multi-body pieces to represent the rubber core. The second step will optimize the parameters for each rigid body, spring and dashpots according to the measured frequency response function (FRF). Using the experimentally estimated stiffness and damping coefficient, the dynamic response of rubber bushing can be predicted utilizing the dynamic equation of multi-body. Furthermore, with the measured FRF, the working ranges of the rubber bushing can be identified to explore the structure stability.

2.3.1 Experiment Approach and Results

The sketch of the rubber bushing used in this research is given in Figure 2.8.For some of the model simulated using finite element method, certain simplification is applied in preprocessing, such as neglecting slight detail of sophisticated parts or using approximated material model. Especially, for the parts made of viscoelastic material, the current widely used material model is empirical and experimental. Therefore, it is highly recommended to verify or compensate the

FEA model with the conclusion derived from the experiment measurement and analysis. In view of the frequency-dependent modulus of viscoelastic material, the modal analysis is critical to identify the modal shape and corresponding energy dissipation. Hammer impact modal testing is a typical approach to process the structure dynamic problems (Halvorsen & Brown, 1977). One of the most applied and easiest testing measurements is the impulse technique by giving a known impulse force to collect the response of the tested structure.

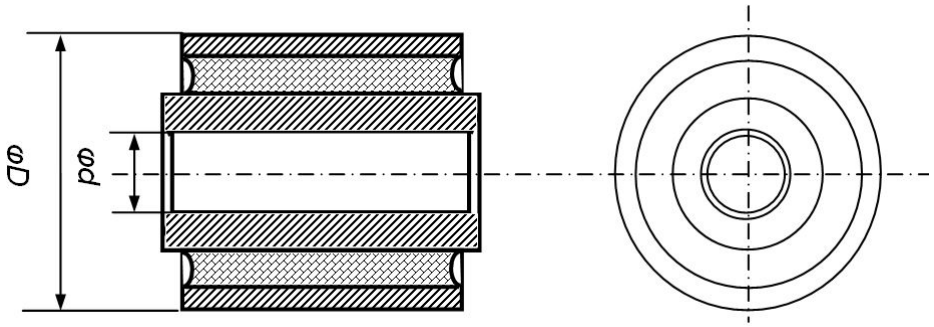

Figure 2.8.: Sketch of rubber bushing used for modal testing.

To guarantee the reliable date to acquire the appropriate FRF in fitting the rubber bushing, correct mechanical support is of great concern. The support applied in this test is clamped to simulate the rubber bushing as cantilever beam. Piezoelectric transducers is set for impulse and acceleration monitor. The purpose of current experimental modal analysis is trying to identify a theoretical model to represent the approximate dynamic behavior of the tested structure. Dual channel analysis is chosen in processing signal, which is shown in following flow chart Figure 2.9.

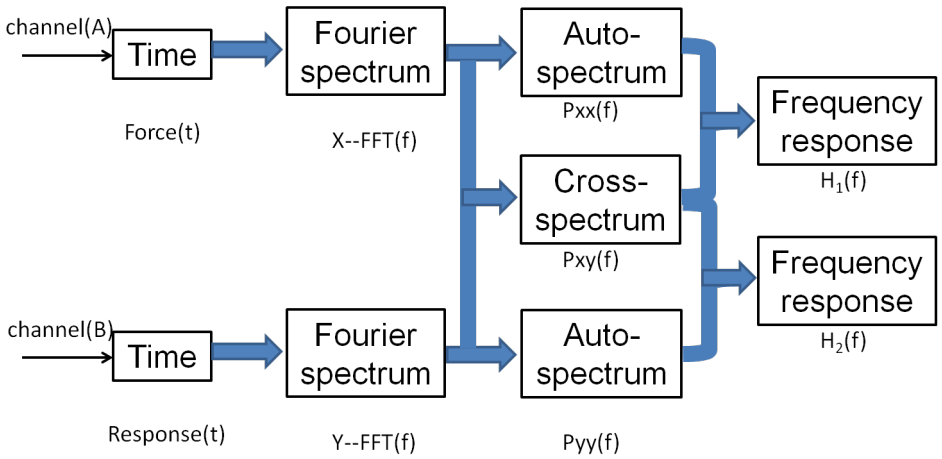

Figure 2.9.: Flowchart of frequency response function analyzer.

The power spectral density (PSD) of auto-spectrum and cross-spectrum (CPSD) are calculated with Fourier transferred instantaneous spectrum using,

$$Pxx(f) = E[fft(x) \bullet fft^*(x)] = E[|x|^2(f)] \tag{2.67}$$

$$Pyy(f) = E[fft(y) \bullet fft^*(y)] = E[|y|^2(f)] \tag{2.68}$$

$$Pxy(f) = E[fft^*(x) \bullet fft(x)] = E[|x(f)||y(f)|.e^{i(\phi_y(f)-\phi_x(f)}] \tag{2.69}$$

Where the E is the expected value and ϕ is the phase of the signal. Since the auto PSD is a function of amplitude of signal, the phase of the cross spectrum is also that of the total system. The application of cross spectrum is to reduce the interference of noise while the phase angle induced by the noise spectrum are summed up and averaged into zero.

The experiment sample and equipment are displayed in Figure 2.10. A softer impact hammer is chosen in this test considering the lower frequency of loading spectrum in the field test. The hammer is applied in axial and radius with similar amplitude to avoid the interference coming from the amplitude effect. The accelerometers are glued on the rubber busing to detect the dynamic response, which is used to estimate the FRF of the structure.

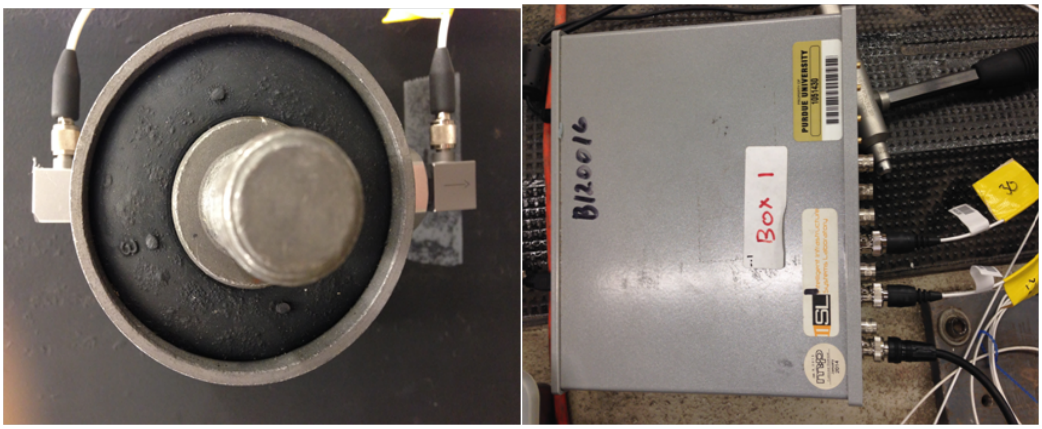

Figure 2.10.: (a) The accelerometer attached on the rubber bushing; (b) hammer and dynamic signal analyzer.

The experimental platform is depicted in Figure 2.11, the inner steel sleeve is tightly secured to a thick steel column. The steel column is fixed on the ground.

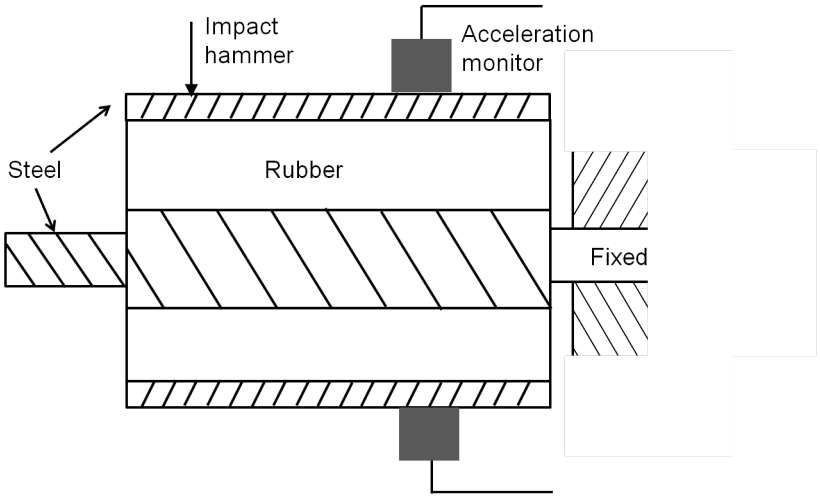

Figure 2.11.: Illustration of experiment platform setup.

Roving hammer impact test (20 averages) is employed in this study to minimize the error caused by the background noise. The impact force and output response collected with the acceleration monitor are shown in Figure 2.12. The general attenuate model of the radial and axial signal can be expressed in

exponential $Xe^{-\xi\omega t}$. X is the initial amplitude of the signal and ξ is the damping ratio. The two unknown parameters are estimated with the fitting tool in MATLAB, which show the overall ξ=0.08 in radial direction.

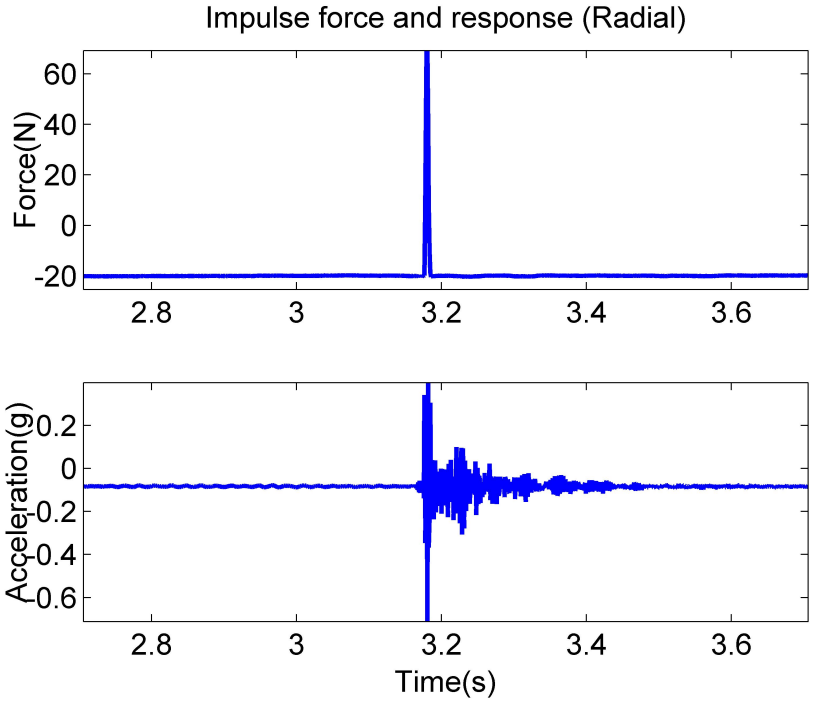

Figure 2.12.: Illustration of the impulse force and output (a) The impulse force given by each hammer impact; (b) the response caused by each hammer impact.

2.3.2 Parameter Identification of Transfer Function

Figure 2.13 are the results of single sided amplitude spectrum of acceleration. With this, the damped natural frequency of rubber bushing can be identified. The FFT result of radial response indicates that the important frequency are 51Hz, 132Hz, 310Hz, 337Hz, 355Hz, 397Hz, 413Hz, and 460Hz. The coherence indicates the reliability of radial signal in the frequency range 100∼300 is acceptable.

With the previous multi-body and modal analysis results, it is applicable to split the rubber core into multiple layers as sketched in the Figure 2.14.

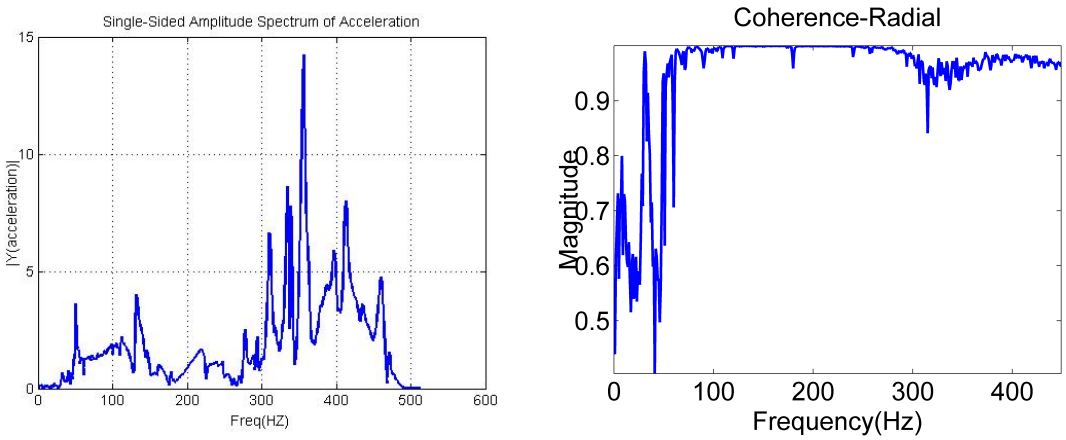

Figure 2.13.: (a) FFT of acceleration response in radial impact; (b) coherence estimate via Welch in radial direction.

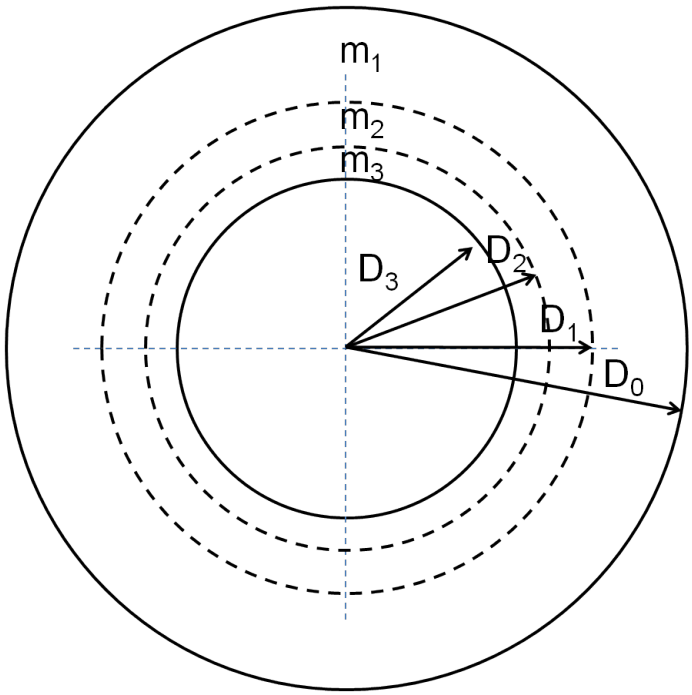

Figure 2.14.: Partition the rubber core.

To clarify the details of partition, the following procedures are calculated to characterize the transfer function of rubber bushing including the inner and outer sleeves. The mass of inner sleeves is taken as infinite as the inner surface of sleeves

is clamped with the land to analogize the cantilever beam. The DOF of rubber bushing is shown in Figure 2.15.

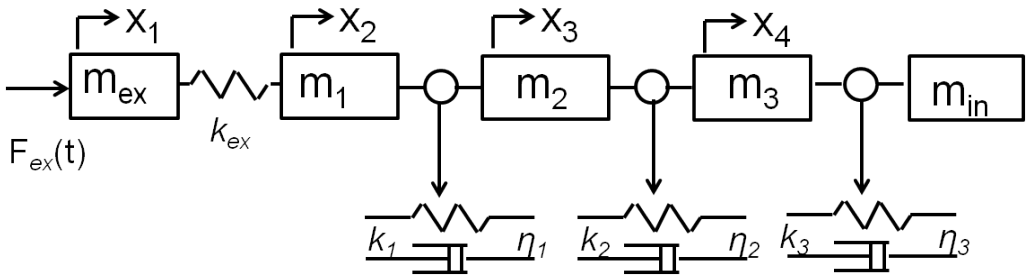

Figure 2.15.: DOF of rubber bushing.

The DOF and equilibrium of this system are represented in state space model as $X = (x_1\ v_1\ x_2\ v_2\ x_3\ v_3\ x_4\ v_4)^T_{1\times 8}$, where the $x_i(i = 1,\ 2,\ 3,\ 4)$ and $v_i(i = 1,\ 2,\ 3,\ 4)$ are displacement and velocity of each lumped mass. The force equilibrium of each mass can be presented as,

$$\begin{aligned}
\dot{x_1} = v_1;\ m_{ex}\dot{v_1} = F_{ex}(t) = k_{ex}(x_1 - x_2);\\
\dot{x_2} = v_2;\ m_1\dot{v_2} = k_{ex}(x_1 - x_2) - k_1(x_2 - x_3) - \eta_1(v_2 - v_3);\\
\dot{x_3} = v_3;\ m_2\dot{v_3} = k_1(x_2 - x_3) + \eta_1(v_2 - v_3) - k_2(x_3 - x_4) - \eta_2(v_3 - v_4);\\
\dot{x_4} = v_4;\ m_3\dot{v_4} = k_2(x_3 - x_4) + \eta_2(v_3 - v_4) - k_3x_4 - \eta_3v_4;
\end{aligned} \tag{2.70}$$

Now, assemble the force equilibrium of the system into matrix A,

$$A_{8\times 8} = \begin{bmatrix}
0 & 1 & 0 & 0 & 0 & 0 & 0 & 0\\
-\frac{k_{ex}}{m_{ex}} & 0 & \frac{k_{ex}}{m_{ex}} & 0 & 0 & 0 & 0 & 0\\
0 & 0 & 0 & 1 & 0 & 0 & 0 & 0\\
\frac{k_{ex}}{m_1} & 0 & -\frac{k_{ex}+k_1}{m_1} & -\frac{-\eta_1}{m_1} & \frac{k_1}{m_1} & \frac{\eta_1}{m_1} & 0 & 0\\
0 & 0 & 0 & 0 & 0 & 1 & 0 & 0\\
0 & 0 & \frac{k_1}{m_2} & \frac{\eta_1}{m_2} & -\frac{k_1+k_2}{m_2} & -\frac{\eta_1+\eta_2}{m_2} & \frac{k_2}{m_2} & \frac{\eta_2}{m_2}\\
0 & 0 & 0 & 0 & 0 & 0 & 0 & 1\\
0 & 0 & 0 & 0 & \frac{k_2}{m_3} & \frac{\eta_2}{m_3} & -\frac{k_2+k_3}{m_3} & -\frac{\eta_2+\eta_3}{m_3}
\end{bmatrix} \tag{2.71}$$

The B, C, D matrix are given seperately as,

$$B = [0 \ \frac{1}{m_{ex}} \ 0 \ 0 \ 0 \ 0 \ 0]^T_{1\times 8} \tag{2.72}$$

$$C = [-\frac{k_{ex}}{m_{ex}} \ 0 \ \frac{k_{ex}}{m_{ex}} \ 0 \ 0 \ 0 \ 0 \ 0]_{1\times 8} \tag{2.73}$$

$$D = [\frac{1}{m_{ex}}] \tag{2.74}$$

The response of rubber bushing subjected to the hammer impact can be represented using the four matrixes with the relationship, $\dot{X} = AX + Bu$ and $y = CX + Du$, where y is the measured acceleration obtained at the outer surface of the steel sleeves. The hammer impact can be described using impulse function $u = F_{ex}(t) = F_{ex}\delta(t)$, which is,

$$\delta(t) = \begin{cases} \inf & \text{if } t = 0 \\ 0 & \text{if } t \neq 0 \end{cases} \tag{2.75}$$

After Fourier transformation, the above two equations turn into,

$$\begin{aligned} SX(S) &= AX(S) + Bu(S) \\ y(S) &= cX(S) + Du(S) \end{aligned} \tag{2.76}$$

And then, the transfer function is formulated as,

$$G(S) = \frac{y(S)}{u(S)} = C(SI - A)^{-1}B \tag{2.77}$$

In order to estimate the mass, stiffness and damping coefficient in the proposed transfer function of rubber bushing, fit the transfer function with the experimental Bode plot, which is shown in Figure 2.16. Fitting 1 is a simple fitting with three curves, which indicates three modal are appropriate to present the Bode plot of rubber bushing. It is necessary to point out that acceleration Bode plot is drew here because the accelerometer is much more precise than the displacement measurement for such micro vibration test. Fitting 2 is sketched on the basis of transfer function expressed in Equation (2.77). The fitting is suitable for amplitude but not that satisfactory for the phase degree as the disturbance of noise.

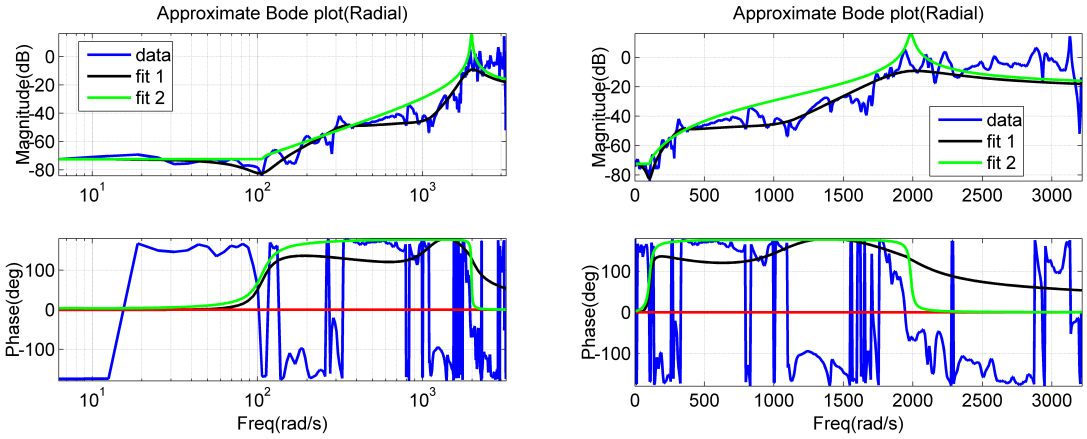

Figure 2.16.: Fitting of Bode plot against the experimental Bode plot (a) log scale; (b) linear scale.

For given parameters of stiffness, mass and damping coefficient k_{ex}, k_1, k_2, k_3, m_{ex}, m_1, m_2, m_3, b_1, b_2 and b_3, the transfer function in polynomial can be written as,

$$TF = \frac{p_8S^8 + p_7S^7 + p_6S^6 + p_5S^5 + p_4S^4 + p_3S^3 + p_2S^2 + p_1S^1 + p_0}{q_8S^8 + q_7S^7 + q_6S^6 + q_5S^5 + q_4S^4 + q_3S^3 + q_2S^2 + q_1S^1 + q_0} \tag{2.78}$$

where, the coefficients in the transfer function are,

$$q_0 = m_{ex}^2 * (k_1k_2k_3k_{ex})$$

$$q_1 = m_{ex}^2 * (b_1k_2k_3k_{ex} + k_1b_2k_3k_{ex} + k_1k_2b_3k_{ex})$$

$$q_2 =$$

$$m_{ex}^2 * (b_1b_2k_3k_{ex} + b_1k_2b_3k_{ex} + k_1b_2b_3k_{ex} + k_1k_2m_1k_{ex} + k_1k_2m_2k_{ex} + k_1m_1k_3k_{ex} + k_1k_2k_3m_{ex} + k_1k_2m_3k_{ex} + k_1m_2k_3k_{ex} + m_1k_2k_3k_{ex} + k_1k_2m_{ex}k_{ex} + k_1m_{ex}k_3k_{ex} + k_2m_{ex}k_3k_{ex}$$

$$q_3 = m_{ex}^2 * (b_1b_2b_3k_{ex} + b_1k_2m_1k_{ex} + k_1b_2m_1k_{ex} + b_1k_2m_2k_{ex} + b_1k_3m_1k_{ex} + k_1m_2b_2k_{ex} + k_1m_1b_3m_{ex} + b_1k_2k_3m_{ex} + b_1m_3k_2k_{ex} + m_2b_1k_3k_{ex} + k_1k_3m_{ex}b_2 + k_1m_3b_2k_{ex} + b_2m_1k_3k_{ex} + b_3k_1k_2m_{ex} + b_3k_1m_2k_{ex} + b_3m_1k_2k_{ex} + b_1m_{ex}k_2k_ex + b_2k_1m_{ex}k_{ex} + b_1m_{ex}k_3k_{ex} + b_3m_{ex}k_1k_{ex} + b_2m_{ex}k_3k_{ex} + b_3m_{ex}k_{ex}k_2)$$

$$q_4 = m_{ex}^2 * (b_1b_2m_1k_{ex} + b_1b_2m_2k_{ex} + b_1b_3m_1k_{ex} + b_1b_2k_3m_ex + b_1b_2m_3k_{ex} + b_1k_2b_3m_{ex} + b_1m_2b_3k_{ex} + k_1b_2b_3m_{ex} + m_1b_3b_2k_{ex} + b_2b_1m_{ex}k_{ex} + b_1b_3m_{ex}k_{ex} + b_3m_{ex}b_2k_{ex} + k_2m_1k_1m_{ex} + m_2k_1k_2m_{ex} + k_3k_1m_1k_{ex} + m_3m_1k_1k_{ex} + m_1k_2m_2k_{ex} +$$

$k_2k_1m_3m_{ex} + m_2m_{ex}k_3k_1 + m_2m_3k_1k_{ex} + k_2m_{ex}k_3m_1 + m_1m_3k_{ex}k_2 + m_1m_2k_{ex}k_3 + m_{ex}m_3k_{ex}k_1 + m_2m_{ex}k_{ex}k_2 + m_{ex}m_3k_{ex}k_2 + m_2m_{ex}k_{ex}k_3)$

$q_5 = m_{ex}^2 * (b_1b_2b_3m_{ex} + b_1k_2m_1m_{ex} + b_1b_2m_1m_{ex} + b_1k_2m_2m_{ex} + b_1k_3m_1m_{ex} + b_1k_{ex}m_3m_1 + k_1b_2m_2m_{ex} + m_1b_2m_2m_{ex} + m_1b_2k_1m_{ex} + k_2b_1m_3k_{ex} + b_1k_3m_{ex}m_2 + b_1m_3m_2k_{ex} + b_2m_3k_1m_{ex} + b_2m_1k_3m_{ex} + b_2m_3m_1k_{ex} + b_3m_2k_1k_{ex} + m_1k_2b_3k_{ex} + m_2m_1b_3k_{ex} + m_{ex}k_{ex}m_3b_1 + m_2b_2m_{ex}k_{ex} + b_2m_{ex}m_3k_{ex} + m_{ex}b_3k_{ex}m_2)$

$q_6 = m_{ex}^2 * (b_1b_2m_1m_{ex} + b_1b_2m_2m_{ex} + b_1b_3m_1m_{ex} + b_1b_2m_3m_{ex} + b_1b_3m_2m_{ex} + b_2m_{ex}b_3m_1 + k_1m_3m_1m_{ex} + m_1k_2m_2m_{ex} + m_2m_3k_1m_{ex} + k_2m_1m_3m_{ex} + m_1k_3m_{ex}m_2 + m_1m_3m_2k_{ex} + b_2m_3k_{ex}m_{ex})$

$q_7 = m_{ex}^2 * (b_1m_3m_1m_{ex} + m_1b_2m_2m_{ex} + b_1m_3m_2m_{ex} + m_1b_2m_3m_{ex} + m_1b_3m_2m_{ex})$

$q_8 = m_{ex}^2 * (m_1m_2m_3m_{ex})$

$p_0 = 2m_{ex} * (k_1k_2k_3k_{ex} + k_1k_2k_{ex}k_{ex} + k_1k_{ex}k_3k_{ex} + k_{ex}k_2k_3k_{ex})$

$p_1 = 2m_{ex} * (b_1k_2k_3k_{ex} + k_1b_2k_3k_{ex} + k_1k_2b_3k_{ex} + {k_{ex}}^2k_2b_1 + 2{k_{ex}}^2b_2k_1 + {k_{ex}}^2b_1k_3 + {k_{ex}}^2k_1b_3 + {k_{ex}}^2b_2k_3 + {k_{ex}}^2k_2b_3)$

$p_2 = m_{ex} * (2b_1b_2k_3k_{ex} + 2b_1k_2b_3k_{ex} + 2k_1b_2b_3k_{ex} + 2k_1k_2m_1k_{ex} + 2k_1k_2k_{ex} + 2k_1m_1k_3k_{ex} + k_1k_2k_3m_{ex} + 2k_1k_2m_3k_{ex} + 2k_1m_2k_3k_{ex} + 2m_1k_2k_3k_{ex} + k_1k_2m_{ex}k_{ex} + k_1m_{ex}k_3k_{ex} + k_2m_{ex}k_3k_{ex} + 2{k_{ex}}^2b_2b_1 + 2{k_{ex}}^2b_3b_1 + 2{k_{ex}}^2b_2b_3 + 2k_1m_3{k_{ex}}^2 + 2m_2k_2{k_{ex}}^2 + 2m_3k_2{k_{ex}}^2 + 2m_2k_3{k_{ex}}^2)$

$p_3 = m_{ex} * (2b_1b_2b_3k_{ex} + 2b_1k_2m_1k_{ex} + 2k_1b_1m_1k_{ex} + 2b_1k_2m_2k_{ex} + 2b_1k_3m_1k_{ex} + 2k_1m_2b_2k_{ex} + 2k_1m_1b_3m_{ex} + b_1k_2k_3m_{ex} + 2b_1m_3k_2k_{ex} + 2m_2b_1k_3k_{ex} + k_1k_3m_{ex}b_2 + 2k_1m_3b_2k_{ex} + 2b_2m_1k_3k_{ex} + b_3k_1k_2m_{ex} + 2b_3k_1m_2k_ex + 2b_3m_1k_2k_{ex} + b_1m_{ex}k_2k_{ex} + b_2k_1m_{ex}k_{ex} + b_1m_{ex}k_3k_{ex} + b_3m_{ex}k_1k_{ex} + b_2m_{ex}k_3k_{ex} + b_3m_{ex}k_{ex}k_2 + 2m_3b_1{k_{ex}}^2 + 2m_2b_2{k_{ex}}^2 + 2m_3b_2{k_{ex}}^2 + 2m_2b_3{k_{ex}}^2)$

$p_4 = m_{ex} * (2b_1b_2m_1k_{ex} + 2b_1b_2m_2k_{ex} + 2b_1b_3m_1k_{ex} + b_1b_2k_3m_{ex} + 2b_1b_2m_3k_{ex} + b_1k_2b_3m_{ex} + 2b_1m_2b_3k_{ex} + k_1b_2b_3m_{ex} + 2m_1b_3b_2k_{ex} + b_2b_1m_{ex}k_{ex} + b_1b_3m_{ex}k_{ex} + b_3m_{ex}b_2k_{ex} + k_2m_1k_1m_{ex} + m_2k_1k_2m_{ex} + k_3k_1m_1k_{ex} + 2m_3m_1k_1k_{ex} + m_1k_2m_2k_{ex} + k_2k_1m_3m_{ex} + m_2m_{ex}k_3k_1 + m_2m_3k_1k_{ex} + k_2m_{ex}k_3m_1 + m_1m_3k_{ex}k_2 + m_1m_2k_{ex}k_3 + m_{ex}m_3k_{ex}k_1 + m_2m_{ex}k_{ex}k_2 + m_{ex}m_3k_{ex}k_2 + m_2m_{ex}k_{ex}k_3 + k_{ex}k_1m_1m_2 + k_{ex}m_2k_1m_3 + k_{ex}k_2m_1m_3 + k_{ex}k_2m_1m_3 + k_{ex}m_1m_2k_3 + 2k_{ex}m_3m_2k_{ex})$

$p_5 = m_{ex} * (b_1 b_2 b_3 m_{ex} + b_1 k_2 m_1 m_{ex} + b_1 b_2 m_1 m_{ex} + b_1 k_2 m_{2,ex} + b_1 k_3 m_1 m_{ex} + 2b_1 k_{ex} m_3 m_1 + k_1 b_2 m_2 m_{ex} + 2m_1 b_2 m_2 m_{ex} + m_1 b_3 k_1 m_{ex} + k_2 b_1 m_3 k_{ex} + b_1 k_3 m_{ex} m_2 + 2b_1 m_3 m_2 k_{ex} + b_2 m_3 k_1 m_{ex} + b_2 m_1 k_3 m_{ex} + 2b_2 m_3 m_1 k_{ex} + b_3 m_2 k_1 k_{ex} + m_1 k_2 b_3 k_{ex} + 2m_2 m_1 b_3 k_{ex} + m_{ex} k_{ex} m_3 b_1 + m_2 b_2 m_{ex} k_{ex} + b_2 m_{ex} m_3 k_{ex} + m_{ex} b_3 k_{ex} m_2)$

$p_6 = m_{ex} * (b_1 b_2 m_1 m_{ex} + b_1 b_2 m_2 m_{ex} + b_1 b_3 m_1 m_{ex} + b_1 b_2 m_3 m_{ex} + b_1 b_3 m_2 m_{ex} + b_2 m_{ex} b_3 m_1 + k_1 m_3 m_1 m_{ex} + m_1 k_2 m_2 m_{ex} + m_2 m_3 k_1 m_{ex} + k_2 m_1 m_3 m_{ex} + m_1 k_3 m_{ex} m_2 + 2m_1 m_3 m_2 k_{ex} + b_2 m_3 k_{ex} m_{ex})$

$p_7 = {m_{ex}}^2 * (b_1 m_3 m_1 + m_1 b_2 m_2 + b_1 m_3 m_2 + m_1 b_2 m_3 + m_1 b_3 m_2)$

$p_8 = {m_{ex}}^2 * (m_1 m_2 m_3 m_{ex})$

In order to have the optimized transfer function, those parameters are identified from the curve fitting optimization, which give $k_1 = 1.797910^6$, $k_2 = 9.01810^6$, $k_3 = 1.68867510^7$, $m_1 = 0.0699kg$, $m_2 = 0.0293kg$, $m_3 = 0.0485kg$, $m_{ex} = 0.2556$, $b_1 = 136.7233$, $b_2 = 264.1990$, $b_3 = 175.1113$, and $k_{ex} = 1.2510^7$.

Figure 2.17 shows the root locus and Nyquist diagram of the estimated transfer function based on acceleration Bode plot. At low frequency, the zeros and poles are near each other and then form open loop dipole. The effect of the zeros and poles pairs on the stability of the system is trivial as cancellation occurs. The more zeros in the transfer function, the root locus will shift to left even more, which can greatly benefit the stability of the system. Furthermore, since the zeros are located at imaginary axis, the influence becomes more important. And in this case, the zeros are more close to the imaginary axis than the poles. The dipole near the original or coordinates can enhance the static stability of the system.

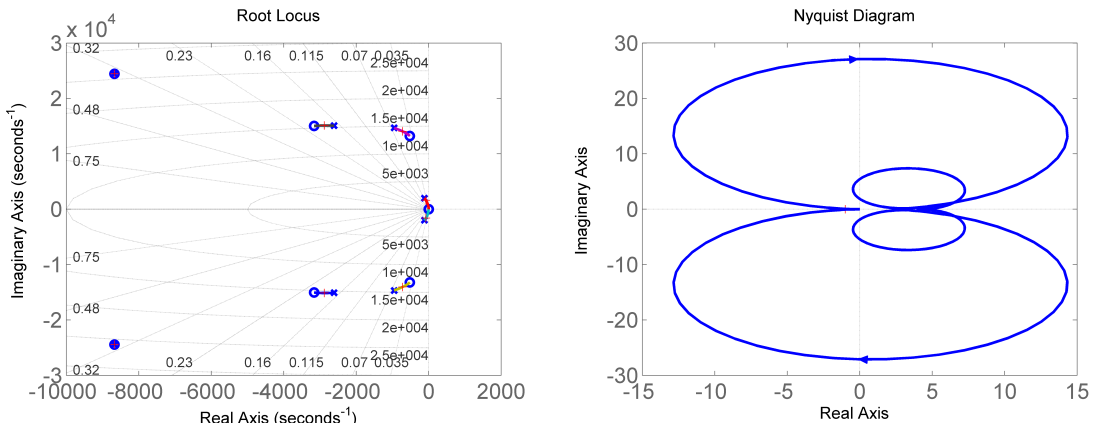

Figure 2.17.: Acceleration based transfer function of the clamped rubber bushing (a) Root Locus; (b) Nyquist diagram.

The zero/pole/gain of the acceleration response based transfer function with the identified parameters are given as,

$$\frac{3.91s^2(s^2+1038s+1.77e^8)(s^2+6320s+2.36e^8)(s^2+1.73e^4+6.73^8)}{(s^2+232.4s+3.95e^6)(s^2+1901s+2.17e^8)(s^2+5220s+2.34^8)(s^2+1.73e^4+6.73e^8)} \tag{2.79}$$

To have stability analysis, the root locus of the system on the basis of displacement

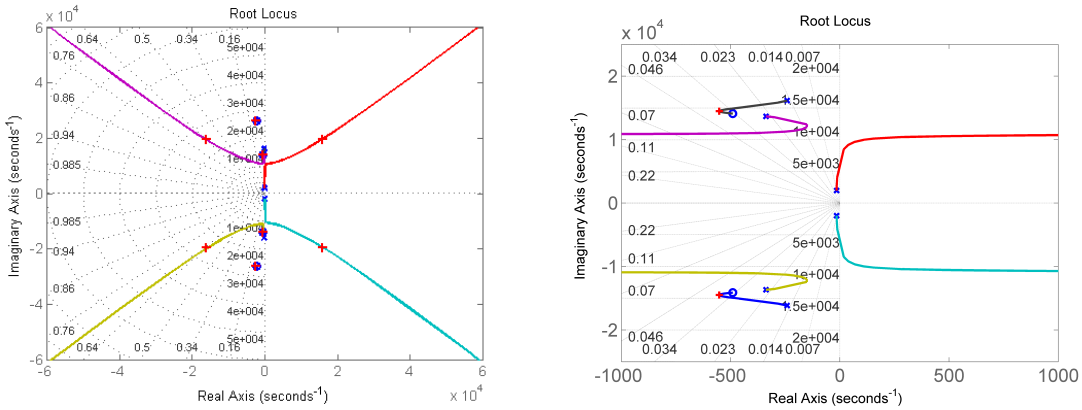

Figure 2.18.: Displacement based transfer function of the clamped rubber bushing (a) Original; (b) enlarged.

is plotted in Figure 2.18. That plot shows the critical frequency of structure stability

at 937.4Hz or 5890rad/s. In general, the working environment of vehicles is around 10Hz, which is much lower than the critical frequency. Thus, the possible failure mechanism of the rubber bushing can be viewed in the aspect of thermal damage.

2.3.3 Energy Dissipation Mechanism and Stability Evaluation

Under the harmonical external excitation, the energy dissipation of the rubber bushing system in a cycle period T can be calculated using,

$$\int_0^T m\ddot{x}(t)\dot{x}(t)dt + \int_0^T c\dot{x}(t)\dot{x}(t)dt + \int_0^T kx(t)\dot{x}(t)dt = \int_0^T F_0 cos(\omega t)\dot{x}(t)dt \tag{2.80}$$

Where, $F_0 cos(\omega t)$ is the sinusoidal force representing the real working environment of the rubber bushing. The three terms at the left side of the equation are kinetic energy, dissipation energy or damping and strain energy of the system. Kinetic and strain energy are conservative energy and the accumulated energy in one cycle are zeros. Thus, the work done by the external force will be equal to the dissipation energy inside of the rubber bushing.

Figure 2.19 plots the dissipation energy generated in the three parts of the rubber bushing at excitation frequency 100Hz. As to the three parts, the stiffness of part1 is lower than that of part 2 and part 3. As a result, the displacement is larger than that of the other two. The work($N.m$) done by the force is calculated using Newton integration method, and the calculated loop area is higher in part 1.

The structure made with higher modulus material will have the resonance at higher frequency than that made from lower modulus material. Thus, with the inner and outer steel sleeves, the first mode of the clamped rubber bushing will happen at higher frequency, which is much higher than the actual loading frequency of moving vehicle. The natural frequency of the clamped structure can be taken as 310Hz or 2000rad/s according to the Bode plot of rubber bushing. In the real driving situation and in the following discussion, the external excitation frequency is pretty low, and the dissipation energy loop formed by force/displacement or the

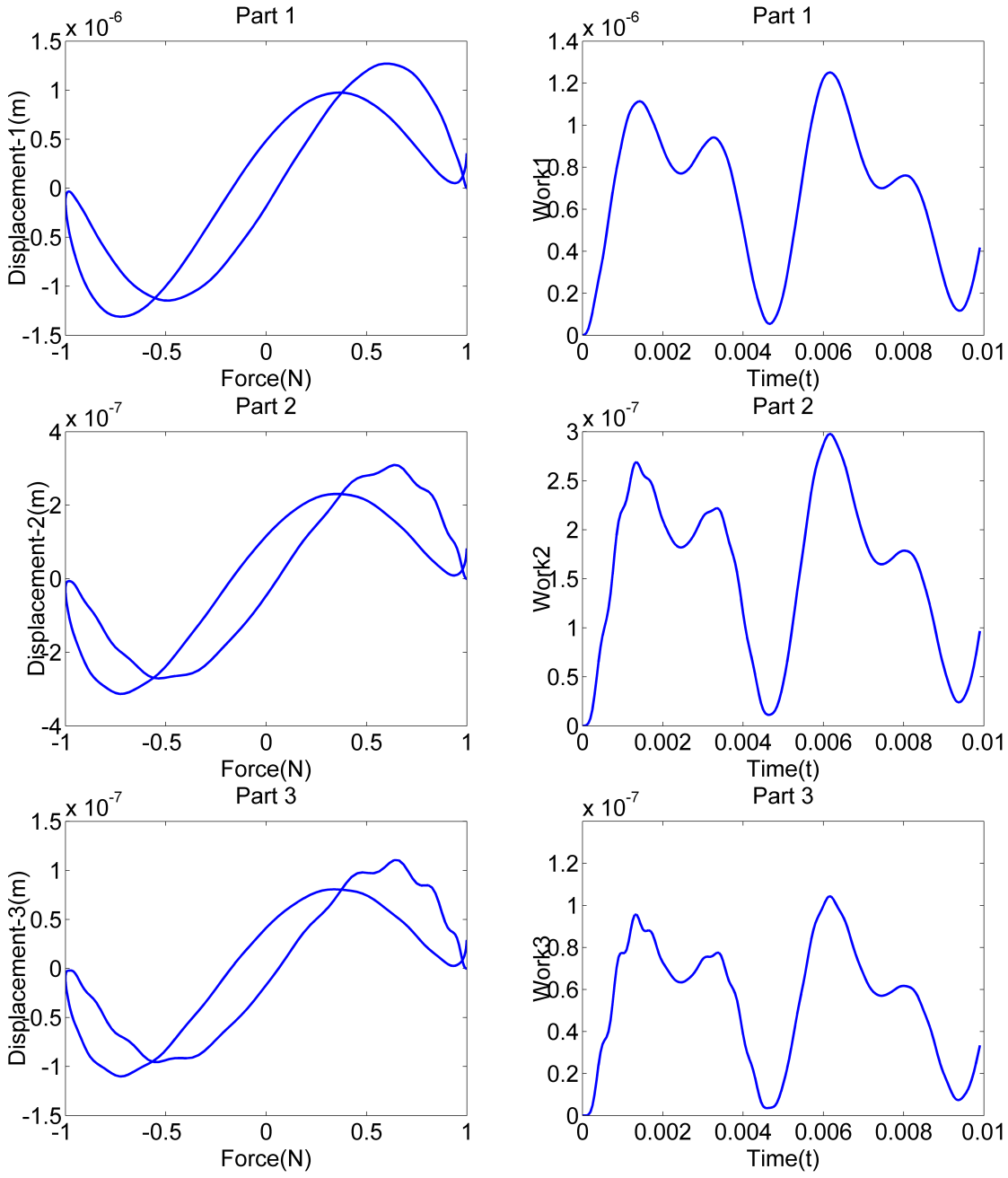

Figure 2.19.: Force against displacement of three parts of the rubber core and the accumulated work at 100Hz excitation.

loop formed by stress/strain is also pretty small. Before reach to the natural frequency, the more close of the excitation frequency to the natural frequency, the

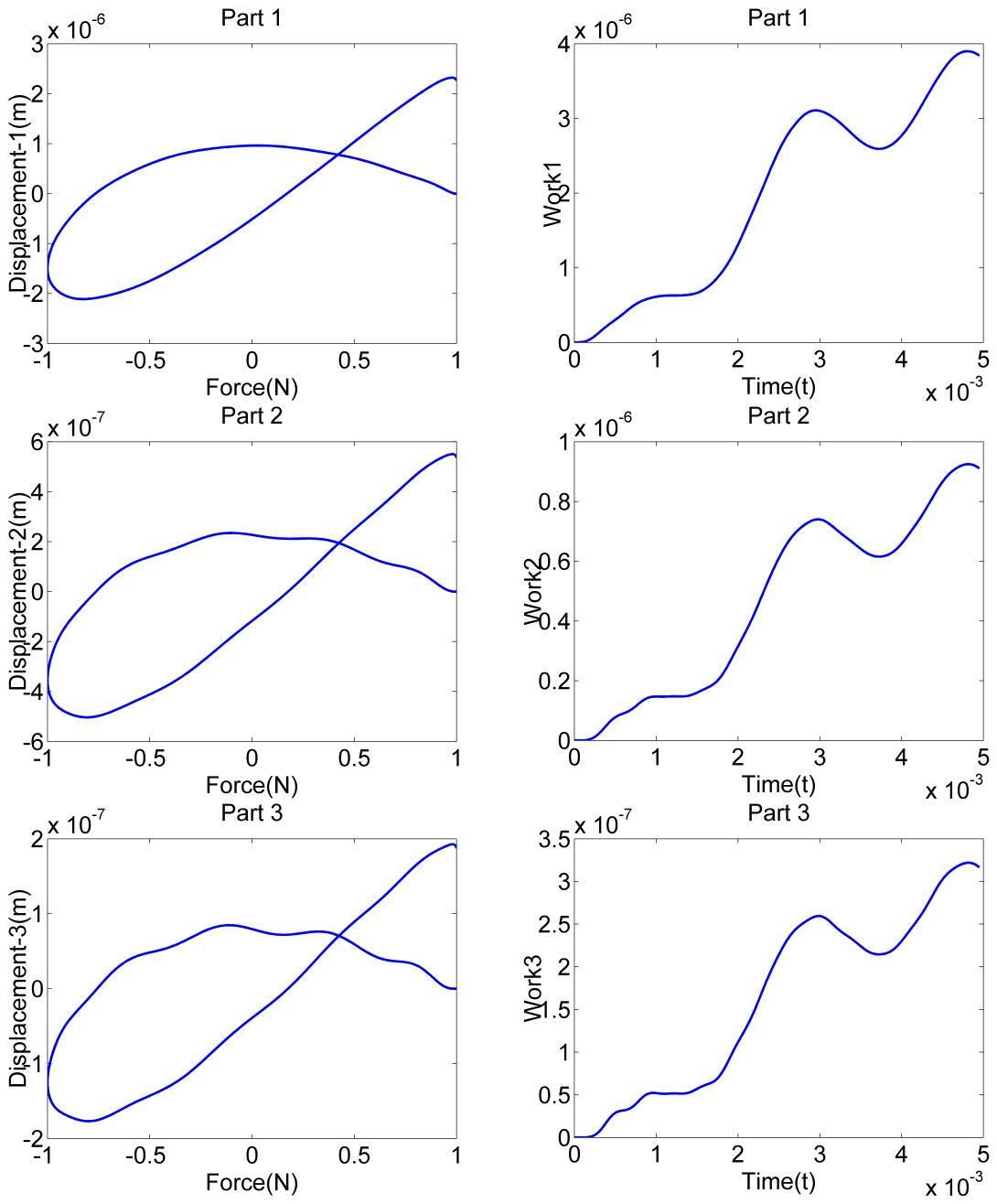

Figure 2.20.: Force against displacement of three parts of the rubber core and the accumulated work at 200Hz excitation.

larger the enclosed area of the loop. Again, the enclosed area is just the energy dissipation per cycle, at high frequency, more cycles′ dissipation energy are

accumulated in unit time, which accounts for the accumulated energy at high frequency. When the excitation frequency is pretty high, which may approximate to the second or third natural frequency, even though the displacement is smaller at that time, but the cycles in unit time is also pretty higher. As to the complicated modal shape at higher order modal, strain energy needed to launch that deformation is also pretty large. All in all, the two factors contribute the dramatically accumulation of the dissipation energy at higher frequency, which turns to the heat source inside the rubber components. Besides of the extremely high frequency loading leading to the structure instability, the failure mechanism of the rubber bushing can be attributed to the thermal aging at higher temperature.

As comparison, the dissipation energy of the three parts of the rubber core accumulated at the excitation frequency 200Hz are given in Figure 2.20. At frequency 100Hz or 200Hz, the stiffness of the structure is almost independent of the excitation frequency. The higher generation rate of dissipation energy at 200Hz is expected from the higher displacements at that frequency. Since the 200Hz is more close to the first natural frequency of the clamped rubber bushing, the resonance effect can properly explain the higher displacements and corresponding higher dissipation energy.

Using the multi-body analysis, the energy dissipation of each part of the rubber core is estimated. With the preset loading amplitude and frequency, the displacement of each piece can be calculated using the transfer function. Since stiffness of each part is higher than the whole piece of rubber core, the corresponding displacement of each part is lower than the whole piece. The dissipation energy of each piece of the rubber core is calculated individually with the loop formed by force and displacement of each lumped mass. That approach is similar to the principle used in the FEA while the later usually estimates dissipation energy with loop area form by stress and strain. Especially, in order to predict the temperature distribution of the rubber bushing, the rubber core has better to split into as many

pieces as possible. Each piece is a unique element with lumped mass and distinct dissipation energy calculated from the displacement of each node in each element.

In sum, the FEA approach and multi-dynamic analysis are interlinked in estimating the dissipation density of rubber core from the displacement of each individual element. In the multi-body analysis, each element is determined by the modal testing of the structure, while the element number in FEA is determined through the convergence curve of the mesh. The summing up displacement of the three pieces equals to the total displacement of the rubber core. Corresponding, the cumulative displacement of each element in the FEA turns to the overall displacement of the rubber core. Either in the multi-body analysis or in the FEA, it is the addition of the stiffness reciprocal of each piece or element to represent the stiffness of the rubber component. Thus, the individual stiffness of each piece or element is much higher and the corresponding displacement is much lower compared with the whole structure. The advantage of the multi-body approach is its feasibility and accuracy as long as limited assumptions. It is pretty useful for the multi-body analysis of suspension system or whole vehicle, which requires proper stiffness and damping coefficient to simulate the dynamic response of suspension system. However, modal shapes depend on structure and boundary condition, the current transfer function is not applicable to predict the rubber bushing dynamic response at tensile testing. Furthermore, the heat generation of the three pieces clamped rubber core is not uniform, thus, it is not comprehensive to represent the distribution of dissipation energy density merely using the three lumped heat source. To have more proper heat source, a more detailed distribution on the basis of many elements is more credible. Therefore, in the following work, the temperature distribution of rubber core using the distributed heat source from each element is explored.

2.4 Conclusion

In this work, the multi-body dynamic principle and it application on rubber bushing to predict the dynamic behaviors are discussed. The multi-body approach is commonly used in the suspension system or the whole vehicle simulation to estimate the response of vehicle upon various loading on the road. In current analysis, the symbolical graph initiated by Wittenburg is employed to format the kinetic and dynamic equation of rubber bushing. The method proves to be pretty concise and representative to illustrate the translation movement and rotation movement of each piece of the multi-body system. The dynamic equation is evaluated by introducing the driver from the suspension system and then predicting the response of the outer steel sleeves of the rubber bushing. This approach to calculate the dynamic transmission properties of suspension system is widely applied in automobile industry. While to continue the dynamic analysis of rubber bushing to simulate suspension system, the proper parameters identifications for mass of each body, spring and dashpot coefficients representing the connection force are carried out.

To get the spring stiffness and damping coefficient of the rubber core to facilitate the multi-body analysis, modal hammer testing is carried out. With the FFT of the acceleration response of rubber bushing upon the hammer impact, three pieces of lumped mass to represent rubber core is proposed. The parameter of mass, spring and dashpot are identified with the curve fitting optimization method on the basis of Bode plot. The structure instability of rubber bushing is predicted using Bode plot of displacement transfer function with the zero initial value assumption. Since the general driving frequency of vehicle is much lower than the critical frequency leading to the structure instability, the dominate failure mechanism can be attributed to the thermal aging of rubber core. Furthermore, the dissipation energy accumulated in each part of the body is estimated, which shows energy dissipation over each loading cycle at different frequency. The lumped dissipation energy density gives the motivation to explore the more detailed energy dissipation density and temperature distribution of rubber bushing over time.

CHAPTER 3. SPECTRAL ANALYSIS AND PARAMETER IDENTIFICATION OF CONSTITUTIVE MODEL

3.1 Constitutive Model and Spectral Analysis

There are many analogous models suggested to model rubber components′ mechanical properties using lumped or discrete elements in order to meet the reproduction accuracy (Stein, Zhang, & König, 1992), and (Stein, Zhang, & Huang, 1993). Berg′s three branches model encompassed the elasticity, viscosity and friction effect in rubber with fillers, which model provided a proper model to characterize the amplitude dependent hysteresis damping under quasi-static loading conditions. In Berg′s model (Figure 1.5), discrete elements with specific characteristics forming three branches to present the overall model structure of rubber components are applied in this dissertation. The total applied uniaxial load is shared by the three branches and each branch has the same individual strain. A short description of different elements in this rubber model is characterized in following.

Branch 1 is a spring element with modulus E_2 to represent the overall elastic behavior of rubber, branch 2 are connected spring element E_1 and dashpot element C_1, and the branch 3 is the friction element F_f to characterize the static friction between carbon black and molecular chain. The second and third branch can describe the amplitude and frequency-dependence of rubber separately. This construction gives a nonlinear reproduction of the parameter-dependence of hysteresis damping and viscoelastic damping in a large range of frequency and amplitude.

3.1.1 Static Friction (Hysteresis Damping)

In Berg′s model, the turning point of the hysteresis loop formed by the displacement and force are identified to develop mathematic relationship and characterize the dissipation (Berg, 1997). Because of the hysteresis harshness, the stiffness of the rubber displays obvious increase after the higher turning point. One disadvantage of the mathematic approach in approximate the stiffness dependence is the lack of universality. Especially, this approach couldnt cover the random excitation and didnt give a comprehensive estimation of stiffness for each stage of the deformation.

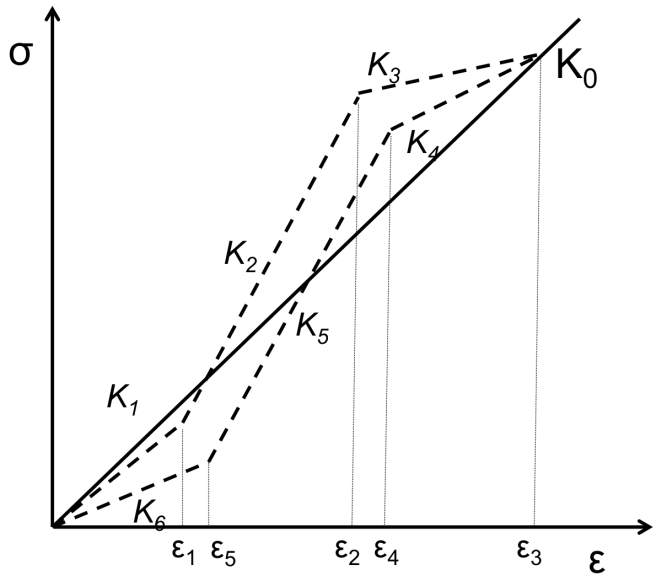

Figure 3.1.: Typical hysteresis curve of rubber under quasi-static harmonic excitation.

In Berg′s model, to describe frequency-independent hysteresis stiffness, maximum force and turning displacement point is needed to develop half of the maximum force. Similarly, the modified model about friction element also requires the measurement of the position of turning points, which split the loading and unloading curves into three pieces. The auxiliary stiffness of hysteresis damping coming from static friction effect is represented with spring K_2 and K_5, which are

located between turning points and much more hardened than the remaining springs. Due to the different stiffness at each stage in the hysteresis loop, a tri-linear model with multiple springs K_i is suggested, where $i = 1, 2, 3, 4, 5, and\ 6$. Stresses of different piece of the hysteresis loop therefore should be written as: stage 1 for strain ranging from 0 to ε_1; stage 2 for strain ranging from ε_1 to ε_2 and stage 3 for strain ranging from ε_2 to ε_3. In order to balance the model complexity and computation efficiency, the six springs′ stiffness can be simplified by setting $K_2 = K_5$, $K_1 = K_4$ and $K_3 = K_6$ according to the acknowledged profile of hysteresis curve. The total energy lost (E_f) per cycle caused by hysteretic damping can be produced from loop area calculation,

$$\begin{aligned} E_f =& \frac{K_1{\varepsilon_1}^2}{2} + \frac{K_2({\varepsilon_2}^2 - {\varepsilon_1}^2)}{2} + \frac{K_3({\varepsilon_3}^2 - {\varepsilon_2}^2)}{2} \\ & - \frac{K_4({\varepsilon_3}^2 - {\varepsilon_4}^2)}{2} - \frac{K_5({\varepsilon_4}^2 - {\varepsilon_5}^2)}{2} - \frac{K_6{\varepsilon_5}^2}{2} \\ & + b_2(\varepsilon_2 - \varepsilon_1) + + b_3(\varepsilon_3 - \varepsilon_2) - b_4(\varepsilon_3 - \varepsilon_4) - b_5(\varepsilon_4 - \varepsilon_5) \end{aligned} \tag{3.1}$$

The micro-level damage insider the rubber caused the stiffness decrease at larger strain, which is characterized as Mullins effect (Mullins, 1969). The rate-independent response hysteresis damping is related with the internal friction force under static excitation. In the subject of static or quasi-static conditions, time-independent and amplitude-dependent hysteresis loops are reported in plenty of literatures, even a change of magnitude of deformation rate couldn′t lead to significantly variation of the hysteresis loops. This conclusion indicates that the widely applied model about viscoelastic model is insufficient to character the quasi-static force-deflection response of rubber bushing. The tri-linear model of springs represents the response of rubber component due to the fact that the stiffness relaxation, hardening and relaxation occur with the ramping of strain.

The interaction between molecular chain in polymer and fillers is a primary cause of stiffness hardening and softening of rubber. Besides of the stiffness, the commonly added carbon black fillers also enhance the damping and abrasion resistance of polymer. Agglomerates of carbon black particles are linked together by

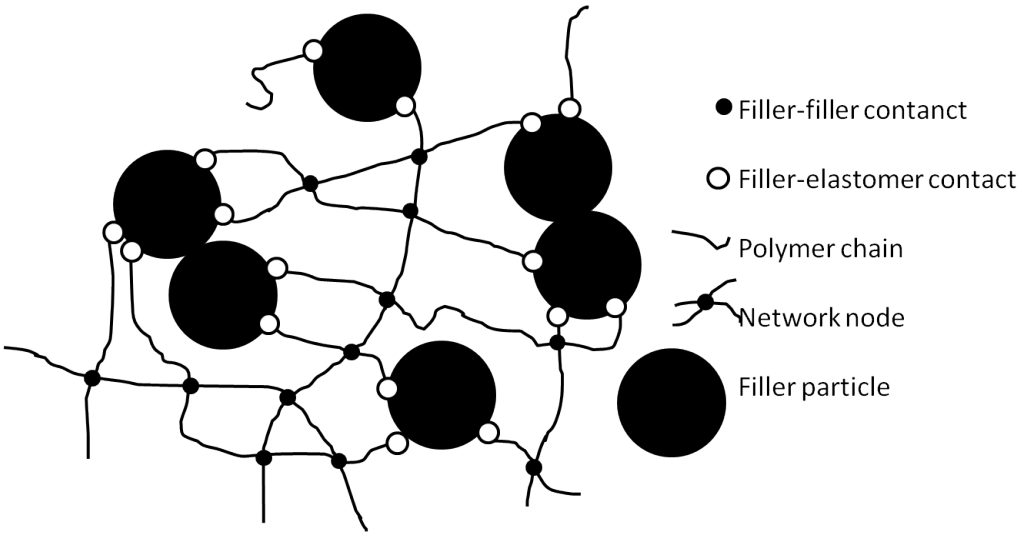

Figure 3.2.: Microstructure of a carbon black filled polymer network.

those molecular chains of polymer, which are of different lengths. Irreversible slipping process between polymer molecule chains and fillers can happen when the critical deformation of chain is reached. From the force-deflection test, the reduction of stiffness happens in a large range of strain, which is dependent on characters of different chain lengths. For molecular chain of different length, slipping process starts at different critical stretch force. With the increase of strain, the elastic limits of fillers were surpassed and that stimulated the relative slipping among agglomerates of fillers(Kaliske & Rothert, 1998), and (Dannenberg, 1975). The hardening and softening under cycle loading is also attributed to the recoverable stretched and rupture of molecule chains. Those molecule chains are of different length and elastic limits, thus, part of the molecule chains can be in relaxation and part of them are stretched tightly.

Figure 3.2 displays the microstructure of carbon black filled rubber and the connection between fillers and polymer chains. However, those connection can be broken if higher external excitation is applied. It is acceptable that the carbon black fillers can change its position relative to molecular chains cluster as a response upon increasing load. The stiffness of rubber at small strain is lower as the most of

molecular chains cluster are in relaxation. When carbon black particles shift from a position to another to coordinate the deformation, the stiffness of rubber increases obviously since more and more molecular chains clusters are stretched and starts to undertake load. Further increase of loading or lager strain pushes the carbon black particle shift to further position, as a response, molecular chains cluster will start to break once the elastic limit is reached. The turning points of hardening and softening are imprecise as the hardening and softening appears in a strain range because of the different strain limits of molecules chains. The straightening and breakage of molecular chains are partially reversible during unloading. As a result, the reversible deformation of molecule chains and the friction cause noticeable static hysteresis damping.

3.1.2 Viscous Damping and Frequency Domain Behaviors

Amplitude and phase behavior are used to characterize the dynamic systems and the complex notation is introduced to deal with the phase behavior. The damping of system in the time domain is displayed using the phase behavior of input and output variables. In terms of viscoelastic material, the constitutive model is time differential equation, which shows phase behavior in plots of stress against strain or force against displacement. There are multiple approaches to integrate the differential equation, while the primary approach of dealing with this type of differential equation is to introduce complex quantities. As a consequence, input loading history and output response history become function of $e^{i\omega t}$ and the corresponding transfer functions are complex quantities. Apply $\sigma = \sigma_0 e^{i(\omega t+\delta)}$ and $\varepsilon = \varepsilon_0 e^{i\omega t}$ in time differential equation of standard linear model and then cancel $e^{i\omega t}$ to get the simplified dynamic modulus of viscoelastic material(Meyers & Chawla, 1991). Since all oscillating quantities in the standard linear model are defined as

complex quantities, the derived complex modulus E^* is composed of the storage modulus and loss modulus,

$$E^* = E' + iE'' = k_2 + k_1\frac{\omega^2\tau^2}{1+\omega^2\tau^2} + ik_1\frac{\omega\tau}{1+\omega^2\tau^2} \tag{3.2}$$

Where, $E^* = \left(\frac{\sigma_0}{\varepsilon}\right)e^{i\delta}$ and $tan\delta = \frac{E''}{E'}$. The real part is the storage modulus E' and the imaginary part is the loss modulus E'' . With this linear representation of modulus, the dynamic stiffness and damping coefficients are given as,

$$E_{dyn} = |E^*| = \sqrt{E'^2 + E''^2}; \qquad C(\omega) = \frac{E''}{\sqrt{E'^2 + E''^2}} \tag{3.3}$$

The relaxation modulus is significant index to evaluate the reliability of the constitutive model and that modulus is directly related with the storage modulus and loss modulus. Considering the Heaviside function to simulate the strain,

$$\varepsilon(t) = \varepsilon_0 H(t); \qquad H(n) = \begin{cases} 1 & \text{t}\geq 0 \\ 0 & \text{t}<0 \end{cases} \tag{3.4}$$

Substitute the Heaviside function into constitutive equation and have, $\varepsilon\bar{(t)} = \varepsilon_0/S$ and $\varepsilon\dot{\bar{(t)}} = \varepsilon$. Define $\sigma(\infty) = \varepsilon_0 E(\infty)$ at the equilibrium and $\sigma_0 = \varepsilon_0(k_1 + k_2)$ at the beginning. The relaxation modulus can be obtained after reverse Laplace transfrom,

$$\sigma = k_2\varepsilon_0\left(1 - exp(-\frac{t}{\tau})\right) + \sigma_0 exp\left(-\frac{t}{\tau}\right) \tag{3.5}$$

With the relaxation modulus $Y(t) = \sigma(t)/\varepsilon_0$ derived from above equation, the creep compliance can be obtained from the relationship $Y\bar{(t)}J\bar{(t)} = S^{-2}$. That gives the creep compliance as,

$$\varepsilon = \frac{\sigma_0}{k_2}\left[1 - (1 - \frac{k_2}{k_1+k_2})exp(1 - \frac{k_2 t}{(k_1+k_2)\tau})\right] \tag{3.6}$$

According to the Boltzmann superposition principle, the viscoelastic integral relaxation constitutive can be written as,

$$\sigma(t) = Y_0\varepsilon(t) + \int_{0+}^{t}\varepsilon(\xi)\frac{\mathrm{d}Y(t-\xi)}{\mathrm{d}t-\xi)}\mathrm{d}\xi \tag{3.7}$$

The next step is to derive the modulus in frequency domain to characterize the influence of frequency. In the following discussion, two approaches are discussed to illustrate the steps to develop the modulus. In the first method, with the known integral relaxation constitutive model and Laplace transform, the relationship $\bar{\sigma(t)} = S\varepsilon(s)\bar{Y(s)}$ can be applied. After the Laplace transform, define $S = \alpha + i\omega$ and set $\alpha = 0$. Since the dynamic relaxation modulus is given as $\sigma(t) = \varepsilon(t)Y^*(i\omega)$, it is easy to get the connection between relaxation modulus and complex modulus, $Y^*(i\omega) = i\omega\bar{Y(i\omega)}$. In sum, do the Laplace transforms on the relaxation modulus and then replace S with $i\omega$ to get $\bar{Y(i\omega)} = k_2/(i\omega) + k_1\tau/(\tau i\omega + 1)$. Multiply this with $i\omega$, finally, the complex modulus from the relaxation modulus can be represented, which tally with the complex modulus derived in Equation 3.2.

The second approach to get the complex modulus is to set $\sigma(t) = \sigma_0 e^{i\omega t}$ and $\varepsilon(t) = \varepsilon^* e^{i\omega t}$. Substitute the two equations into standard constitutive equations, then, the complex relaxation modulus can be obtained from the relationship $Y(i\omega) = \sigma_0/\varepsilon^*$. With the modulus and strain in frequency domain, the stress and strain relationship can be characterized as,

$$\sigma(t) = E(i\omega)\varepsilon_0 e^{i\omega t} = E(i\omega)\varepsilon(t) \tag{3.8}$$

In the previous discussion, the advantage of standard linear model is generally motioned. To have comprehensive understanding about the construction principle of those constitutive models and give strong evidence to support the selection of proper material models for future analysis, the frequency domain and time domain testing are carried out on those models to have a thorough comparison. In the following discussion, the Maxwell model is termed as fluid model and the Voigt model is termed as solid model.

Apply $\sigma = \sigma_0 e^{i(\omega t+\delta)}$ and $\varepsilon = \varepsilon_0 e^{i\omega t}$ in time differential equation of fluid model, the loss modulus, storage modulus and dynamic modulus are,

$$E'' = \frac{\omega\eta k^2}{k^2 + \omega^2\eta^2}; \quad E' = \frac{\omega^2\eta^2 k}{k^2 + \omega^2\eta^2}; \quad E^* = E' + iE'' \tag{3.9}$$

Similarly, the loss modulus, storage modulus and dynamic modulus of solid model are,

$$E'' = \omega\eta; \quad E' = k; \quad E^* = E' + iE'' \tag{3.10}$$

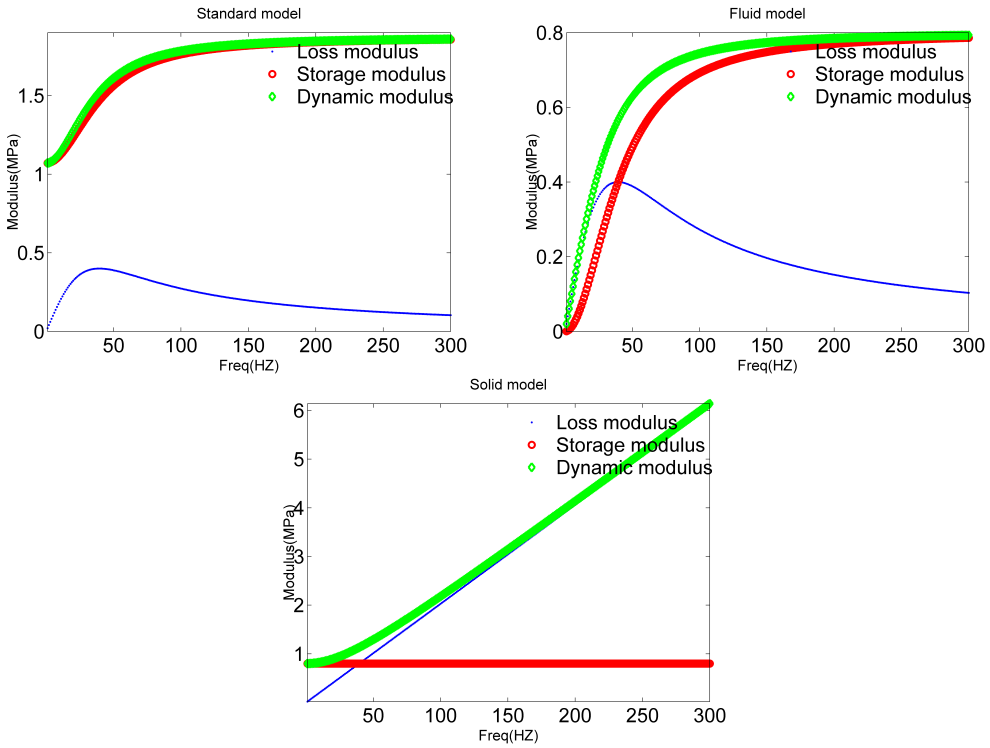

Figure 3.3.: Frequency dependent modulus of (a) Standard model; (b) fluid model; (c) solid model.

Setting the k_1 as 0.8×10^6MPa, k_2 as 1.07×10^6MPa, and η as 0.00323×10^6MPa.s, the modulus of the three models are plotted in Figure 3.3. With the comparison in Figure 3.3, the standard solid model is more appropriate to represent the modulus of viscoelastic material than the solid model and fluid model. In the solid model, the dynamic modulus and storage modulus start from zero in the frequency range, which indicates the static modulus as zero at 0Hz excitation and conflicts with the real property of rubber. While in the solid model, the dynamic modulus and storage modulus show linear increase with the excitation frequency but without maximum limitation. That behavior also disagrees with the

real situation in the rubber, which is independent with the frequency after the maximum modulus is reached. In sum, the standard solid model is the simplest proper model to represent the variation of modulus in frequency domain.

Actually, the current standard linear model (Figure 3.4(a)) is based on the fluid model, and there is analogous model shown in Figure 3.4(b). For clarification, in the following discussion, the previous discussed standard linear model is termed as model 1 and the later is termed as model 2.

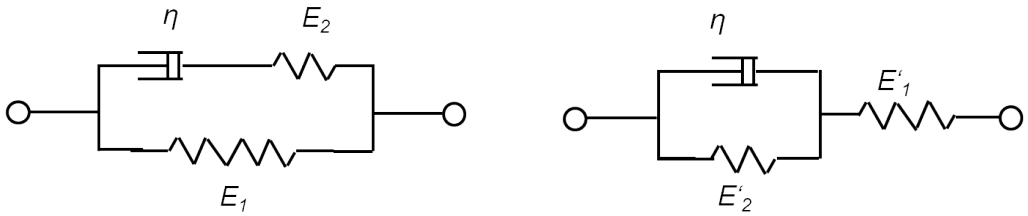

Figure 3.4.: Two standard linear models (a) Model 1; (b) model 2.

As to the model 1, the modulus at lower frequency and higher frequency are $\hat{E(0)} = E_1$ and $\hat{E(\infty)} = E_1 + E_2$ respectively. The corresponding constitutive relationship of the first model is,

$$\frac{\eta d\sigma}{E_2 dt} + \sigma = \frac{E_1 + E_2}{E_2}\eta\frac{d\epsilon}{dt} + E_1\epsilon \tag{3.11}$$

As to the model 2, the modulus at lower and higher frequency are $\hat{E'(0)} = \frac{E'_1 E'_2}{E'_1 + E'_2}$ and $\hat{E'(\infty)} = E'_1$ respectively. The corresponding constitutive relationship of the second model is,

$$\frac{\eta d\sigma}{(E'_1 + E'_2)dt} + \sigma = \frac{E'_1\eta d\epsilon}{(E'_1 + E'_2)dt} + \frac{E'_1 E'_2\epsilon}{E'_1 + E'_2} \tag{3.12}$$

Even though the two time differential equations are of different coefficients, with proper assignments of parameters for spring and dashpot elements, the two constitutive equations can represent the same material. Comparing the coefficients for each variable, three necessary conditions should be satisfied,

$$\frac{\eta}{E_2} = \frac{\eta'}{E'_1 + E'_2}; \quad \frac{E_1 + E_2}{E_2}\eta = \frac{E'_1\eta'}{E'_1 + E'_2}; \quad \frac{E_1 + E_2}{E_2} = \frac{E'_1}{E'_1 + E'_2} \tag{3.13}$$

Similarly, to represent the same material, the constitutive relationships in the frequency domain should overlap with each other. To satisfy the requirements in time domain and frequency domain, the following equations are posted,

$$E_1 = \frac{E_1' E_2'}{E_1' + E_2']}; \quad E_1 + E_2 = E_1'; \quad \eta' = \eta \frac{E_1' + E_2'}{E_2} \tag{3.14}$$

In the previous discussion, the parameters of the first model are set as E_1=1.07MPa and E_2=0.8MPa. To represent the same material with the second model, then, the corresponding parameters should be E_1'=1.87MPa, E_2'=2.50MPa and η'=5.46η on the basis of the Equation (3.14).

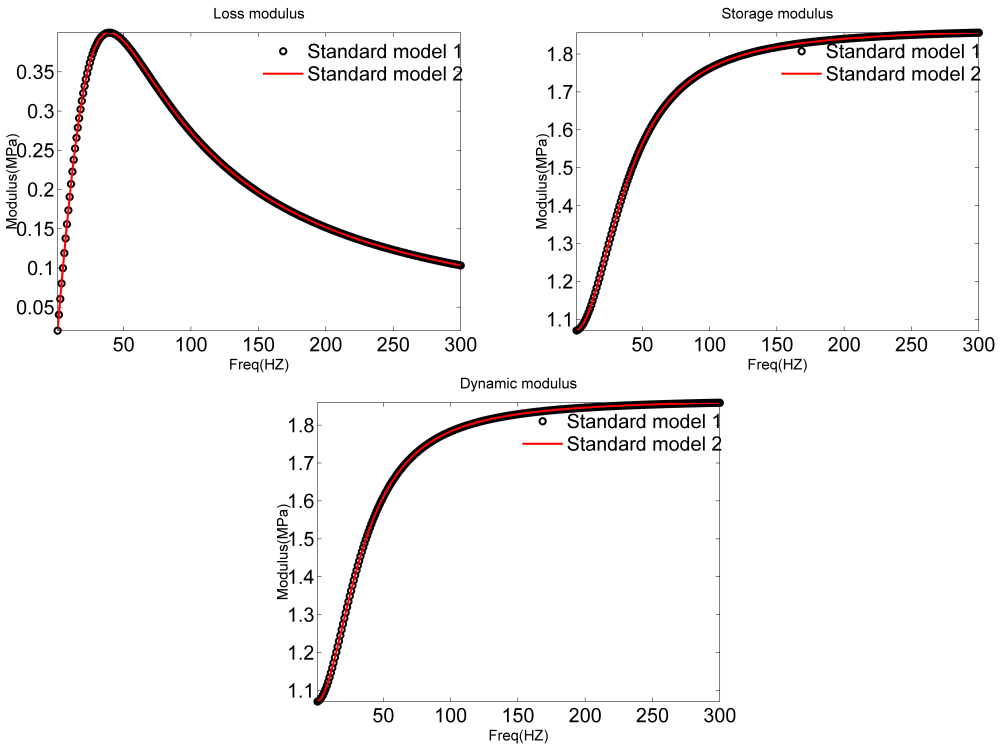

Figure 3.5.: Comparison of two standard models (a) Loss modulus; (b) storage modulus; (c) dynamic modulus.

With the proper selection of parameters for the two standard models, the frequency dependent modulus are compared in Figure 3.5. Even though the expressions of the constitutive equations are different and the coefficients of spring

and dashpot elements are different too, the loss modulus, storage modulus and dynamic modulus of the first standard model overlap with those in the second standard model. Those results indicate that both of the two standard models are appropriate to represent the mechanical behaviors of viscoelastic materials and are equivalent in describing the same material. However, the first standard model is used more frequent than the second one since it is easier to rearrange the first standard model to get the generalized Maxwell model.

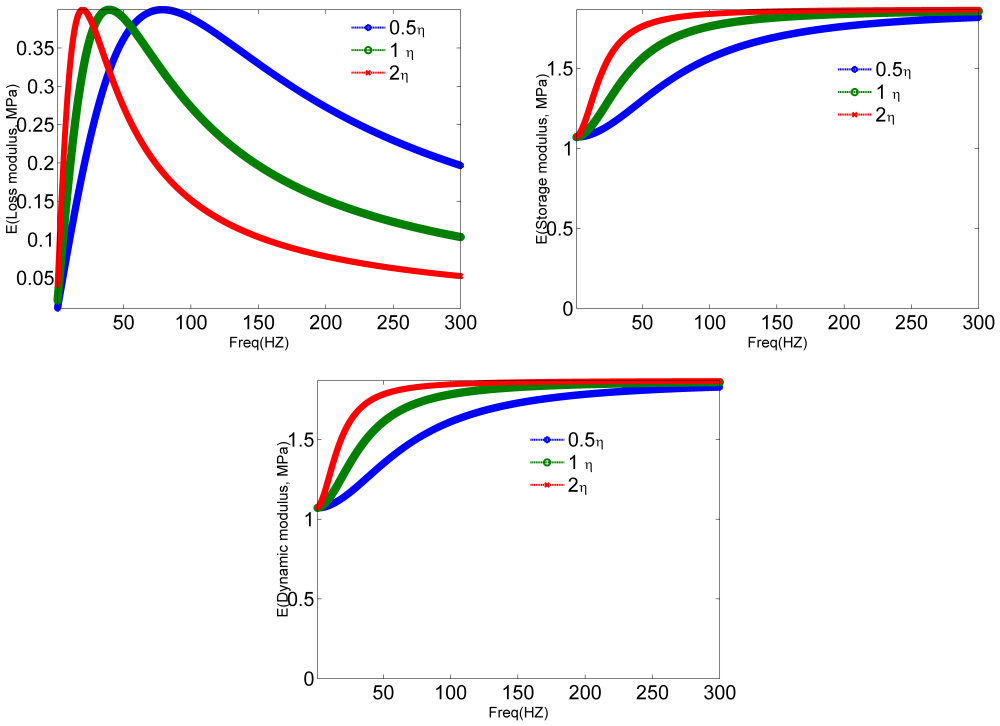

Figure 3.6.: Influence of damping coefficient on the modulus: (a) Loss modulus (b) storage modulus (c) dynamic modulus.

The damping ability of the rubber is critical in determining the performance of rubber component as it greatly affects the modulus at lower frequency range. To elaborate the effect of damping on the modulus, Figure 3.6 plots the frequency dependence of loss modulus, storage modulus and dynamic modulus.

With the introduction of complex quantities, each variable has real and imaginary parts and is function of $e^{i\omega t}$. The complex stress and strain expressions under single frequency excitation in the time domain are given in the following,

$$\epsilon = [\epsilon_R + i\epsilon_I]e^{i\omega t} = [\epsilon_R \cos(\omega t) - \epsilon_I \sin(\omega t)] + i[\epsilon_R \sin(\omega t) + \epsilon_I \cos(\omega t)] \tag{3.15}$$

$$\sigma = [\sigma_R + i\sigma_I]e^{i\omega t} = [\sigma_R \cos(\omega t) - \sigma_I \sin(\omega t)] + i[\sigma_R \sin(\omega t) + \sigma_I \cos(\omega t)] \tag{3.16}$$

Where the subscript I means real part of the variable and subscript R means imaginary part of the variable. To reconstruct the response of single frequency excitation in time domain, the real parts of the stress and strain are extracted. The real part is characterized on the basis of two time functions, one is sinusoidal function and another one is cosine function. Because of the existence of two time functions, the elapse of strain over stress is presented after the reconstruction of single frequency excitation in time domain. Whereas the single frequency excitation is the extreme case and the general loading history can be treated as superposition of multiple frequency excitations. To deal with the more complicated loading history, the spectral analysis can be introduced later to elaborate its application in the time domain analysis.

3.1.3 Application of Spectral Analysis and Reconstruction

In the time domain, the constitutive relationships of the three classical models representing viscoelastic materials are differential equations, which post a lot of challenges to integrate them in order to get the response in the time domain. From the definition of transfer function and the hereditary of viscoelastic material, the displacement history of the structure with viscoelastic material is represented as,

$$U(t) = \int_0^t G(t - t^*)P(t^*)dt^* \tag{3.17}$$

Where t^* is the elapsed time, $P(t^*)$ is the loading at time t^* and $G(t - t^*)$ is the transfer function, which is time dependent. In order to have the response at time t,

it is necessary to do the integral over all elapsed time. Similarly, the response at $t + dt$ needs to sum up the product of $G(t - t^*)P(t^*)$ from the beginning at time zero to the current time. That means the response at any time needs to calculate the integral over all past time. That integral is redundant and time consuming.

Viscoelasticity has the same meaning with hereditary in current case as the integral is required to calculate the current response. The kernel of the integral is the time dependent transfer function G. If discrete the Equation 3.17 in time domain and do the summation in a window with a thousand points, a thousand times integral should be completed in order to get the whole response in the time domain. That approach is very complicated and inefficient since it introduces a lot of calculation. Alternately, there are actually many more powerful skills to solve the integral, one of the most efficient approach is the spectral analysis using the FFT algorithm.

The fundamental method to solve the convolution is to do the Laplace transform, which transforms the integral into frequency domain and then do the product. The transformation from time domain to frequency domain implements the FFT and $IFFT$ algorithm, which is very efficient. This approach saves a lot of steps since no summation is needed expect for the product in frequency domain. The response of each point in the time domain can be obtained after the inverse FFT.

It is easier to work in the frequency domain when the structure is made of viscoelastic materials. There are some problems which begin in frequency domain and end in the frequency domain, such as sinusoidal vibration. It is convenient to understand the frequency response in single or frequency scan. While some of the problems begin in the time domain and end in the time domain, such as the creep behavior of different viscoelastic material models. As to the problem in time domain, the periodic and single frequency excitation is extreme loading case, whereas spectral analysis is applied to deal with the vibration problem under general loading types. With the Fourier analysis, any signal in time domain can represent as multiple harmonic signals at different frequency. Then, the loading and

displacement in the governing equation can be connected using the transfer function at each frequency components,

$$P(t) = \sum_n \hat{P}_n e^{i\omega_n t}, \quad u(t) = \sum_n \hat{u_n} e^{i\omega_n t} \tag{3.18}$$

The general flowchart in Figure 3.7 shows the process to tackle the vibration problem in time domain.

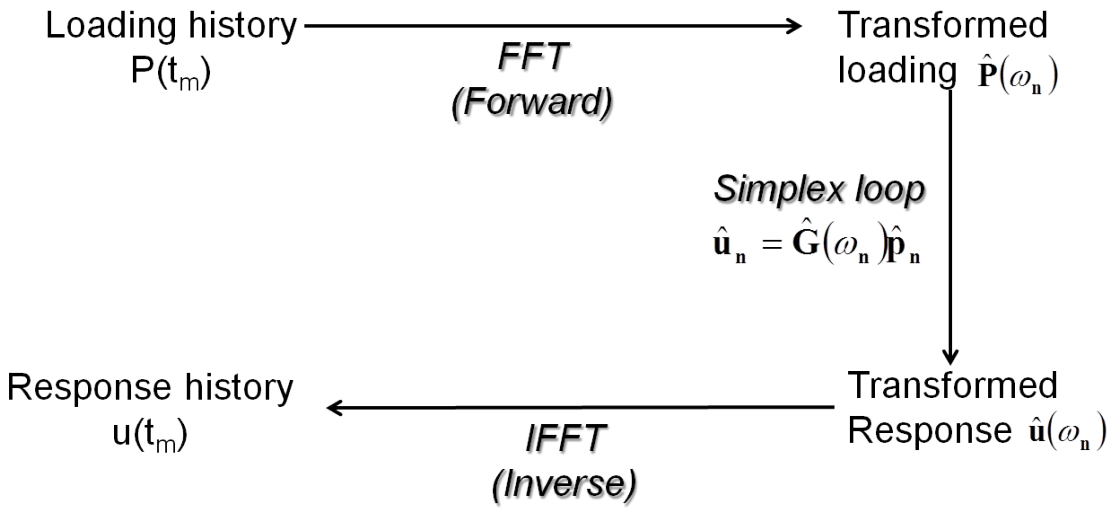

Figure 3.7.: Flowchart of using spectral analysis in general time domain problem.

The work in the flowchart includes three steps. The first step is to transform the loading history of the structure from time domain into frequency domain using the FFT algorithm. Then, the second is to include the constitutive relationship of the material model. All viscoelastic material models are frequency dependent, even though the constitutive relationships of those models are expressed as differential equation in time domain. Actually, frequency dependent modulus contributes to understand the material properties of the rubber and facilities the dynamic analysis in the frequency domain, especially the linear dynamic analysis. In the step two, a frequency loop is developed to calculate the response of the structure at each frequency (Doyle, 1989),

$$\hat{u}_n = \hat{G}(\omega_n)\hat{P}_n \tag{3.19}$$

$G(\hat{\omega}_n)$ is the transfer function of the system in frequency domain. The third step is to get the response in time domain after reconstruction using $IFFT$ algorithm.

3.1.4 Time Domain Behaviors of Constitutive Models

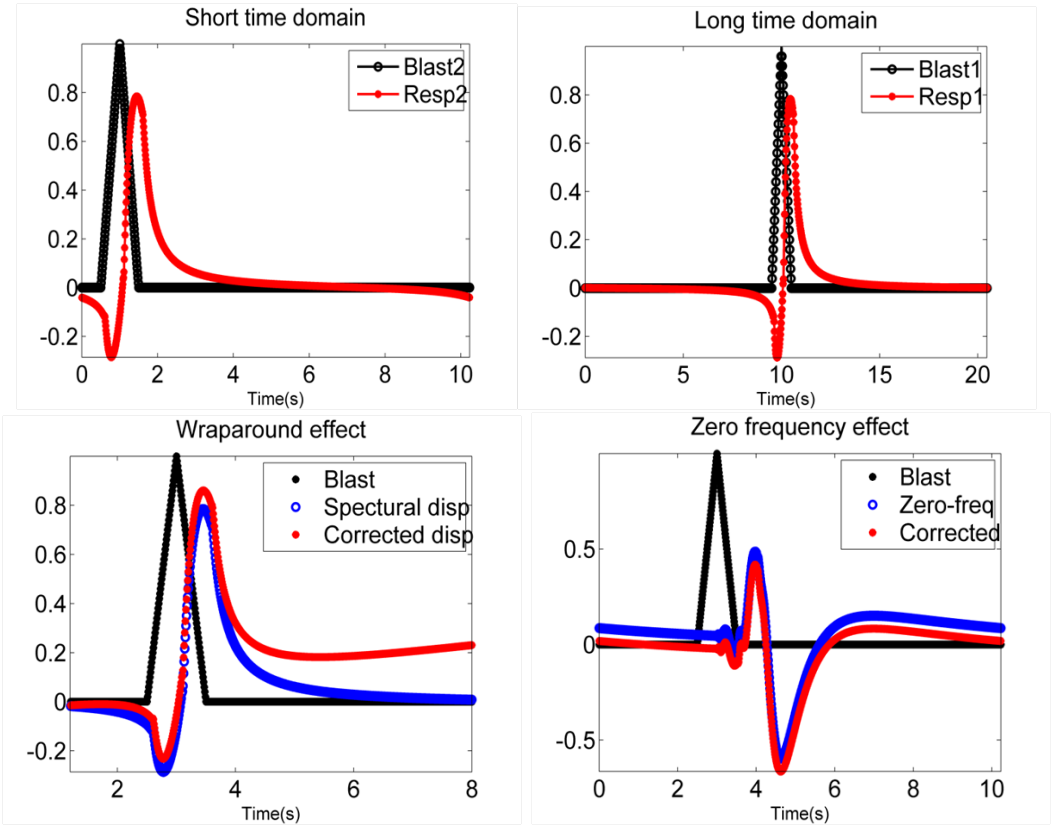

Figure 3.8.: (a) Short time domain; (b) long time domain; (c) wrap around effect; (d) zero frequency effect.

One of the standard problems in time domain is creep behavior of viscoelastic materials and the following discussion illustrates the capability of spectral analysis to predict the behavior. First of all, a loading history of stress should be specified as the input loading applied on the model. The loading history in time domain is discrete in frequency domain but an infinite content in the frequency domain is impossible. In order to avoid the jump up in the time domain

in case the infinite in frequency content, proper specifications about rising time and drop time are needed. A larger drop time or larger time domain is desired to avoid the periodicity of response since longer time window is preferred. That extra long time window is necessary to draw the loading in time domain but the long tail of loading information does not used for the reconstruction analysis.

Because of the periodicity, the beginning and ending value in the time domain are same to keep the continuity. While when the time window is short, the response of the loading is still nonzero at the end of window, as a result, the beginning value of the response in the time window is nonzero(Figure 3.8(a)). That is not acceptable since the response before the loading should be zero. One of the effective approaches to make sure the zero beginning value of the response is to have a longer time window as shown in Figure 3.8(b). Another problem encountered after reconstruction is the nonzero response before the start of the loading, which is termed as wrap around effect. When the input and output signal are of different differential level, the phenomenon becomes more obvious. Enlarged the time window size is helpful but not enough to remove the effect. The constant used in the integral over time domain is the primary reason for the initial nonzero signal of response. Fit the nonzero signal with a straight line and then subtract it from the reconstructed signal can minimize the wrap around effect. Figure 3.8(c) shows the comparison of original response obtained from spectral analysis and the corrected response after subtracting a fitted straight line. Another important drawback of the reconstruction attributes to the zero frequency components, which is uncertain and shows arbitrariness. The original reconstructed signal in Figure 3.8(d) is nonzero almost in the entire window. However, the signal can be corrected with the proper specification of zero frequency component as $\hat{u_0} = -\sum_{1}^{N-1} \hat{u_n}$.

Generally speaking, in order to avoid the warp around effect and zero frequency effect, a larger FFT number N and small time step dt are preferred. The practice of parameters in Figure 3.9 indicts that higher N and lager dt are effective and preferred to reconstruct the correct response signal.

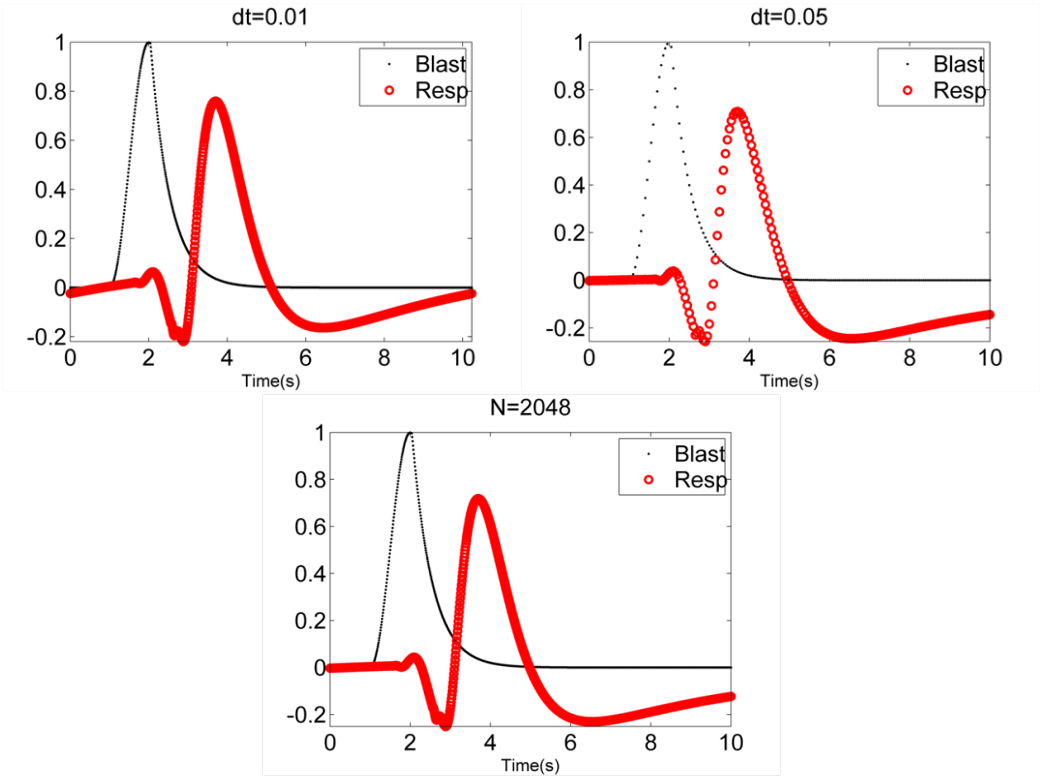

Figure 3.9.: (a)wrap around effect when dt=0.01; (b) Increase dt to get rid of wrap around; (c)increase the N to 2048.

In the current test, N is set as 8192 and time step dt is set as 0.1 to balance the accuracy and burden of computation. Here, the stress and strain relationship is applied to test the creep behavior, that governing equation can be represented as $\hat{\sigma} = \hat{H}\hat{\epsilon}$, where $\hat{H}$ is the frequency response function in those viscoelastic material model. While in the Simplex program, $\hat{H}$ is the finite cube under deformation. It is necessary to keep the frequency content nonzero in the interested frequency range. In order to test the factors affecting the creep behavior, different loading histories are tested. The first group assumes the same rising time and drop time of the loading stress, but the duration of stress are set as 2s, 20s and 200s. To have better testing results, some parameters are defined, which is different from the date obtained from experimental testing. Those parameters are E_2=6MPa, E_1=4MPa and η=32.3MPa.s.

As to the solid model, the stress and strain relationship and the corresponding frequency response function in complex are given as,

$$\hat{\sigma} = \hat{E}\hat{\epsilon} + i\omega\eta\epsilon; \quad \hat{H}_1 = \frac{1}{\hat{E} + i\omega\eta} \tag{3.20}$$

The governing equation of the fluid model and the frequency response function between the stress and strain rate in complex are given as,

$$\frac{\hat{\sigma}}{\hat{E}} + \frac{\sigma}{i\omega\eta} = \hat{\epsilon}; \quad \hat{H}_2 = \frac{i\omega}{\hat{E}} + \frac{1}{\eta} \tag{3.21}$$

For the standard model 1 and 2, the transfer function are,

$$\hat{H}_3 = \frac{E_1 + i\omega\eta}{E_1E_2 + E_1E_2i\omega\eta}; \quad \hat{H}_4 = \frac{i\omega\eta + E_1E_2}{i\omega E_1\eta + E_1E_2} \tag{3.22}$$

From the discussion in last section, with proper chosen parameters, the modulus behavior of the standard model 1 and model 2 are identical in the frequency domain, thus, in the following discussion, merely the creep behavior of standard model 1 will be discussed.

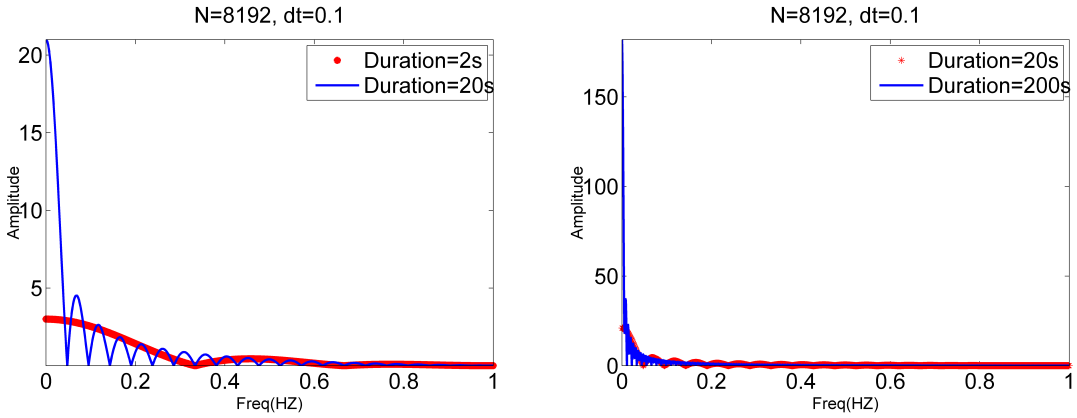

Figure 3.10.: Amplitude of frequency content at different duration(a) 2s and 20s;(b) 20s and 200s.

To have clear elaboration about the influence of stress duration on the creep, the FFT spectrum of the three loading histories are shown in Figure 3.10 on the basis of standard linear model. FFT results indicate the frequency amplitude is

nonzero in the low frequency range and the long stress duration produces high amplitude at the zero frequency component. The longer the stress duration, the higher is the amplitude of the lower frequency zone. In this test, the creep behavior is connected with the content of lower frequency components. In this group of comparison, the amplitude of zero frequency component are 4, 22, and 180, which are proportional to the stress duration.

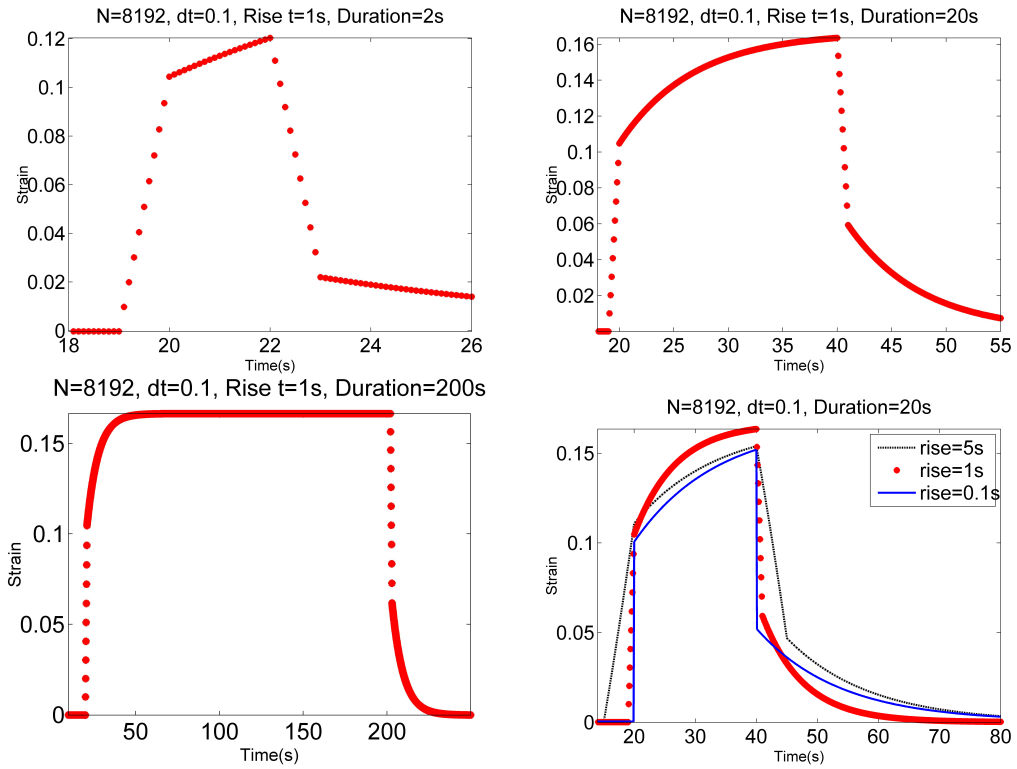

Figure 3.11.: Creep at different loading period(a)2s; (b)20s; (c)200s and Creep at different rising time.

Figure 3.11 shows the strain histories of the three cases of loading. The common phenomena in the three strain histories are the straight lines at the initial rising and drop stage, which present the immediate response of the material to the external stress. The initial part is purely elastic behavior, while the strain slowly increases nonlinearly for a certain period after this stage. With the assumed material parameters used in this test, the ongoing increasing strain or the creep

period happens in the initial 20s, after that stage, the strain keeps constant until the unloading. The further elongation of the stress duration couldn't bring higher strain over time.

The next group of test is to investigate the influence of rising time on the creep behavior. The different rising time 0.1s, 1s and 5s are chosen but stress duration 20s is kept for the three cases of loading. The rising time affects the amplitude of the high frequency components. The influence of rising time on the creep is plotted in Figure 3.11(d). When the rising time is pretty long, the strain increases gradually with the stress. As to loading history with short rising time, the initial strain can follow the stress immediately, which attributes to the elastic spring element in the standard linear model. This result indicates that the rising time affects the magnitude of high frequency components, which are instant elastic behavior area. However, the stress duration length is more critical to determine the final strain of the structure than the length of rising or fall time.

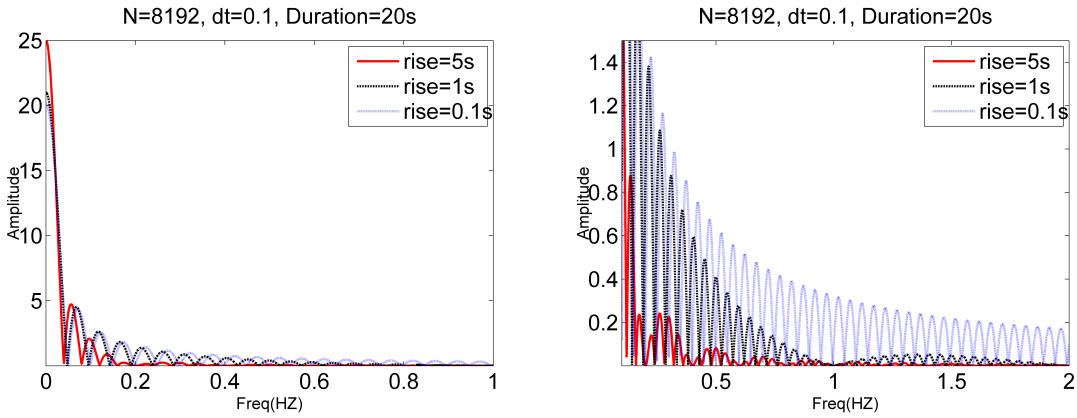

Figure 3.12.: FFT spectrum of the three loading with different rising time, 0.1s, 1s and 5s (a) Normal; (b) enlarged.

The FFT in Figure 3.12 shows the amplitude of the high frequency content for the 0.1s rising time is much higher than that of the two other cases. Generally speaking, the shorter the rising time, the amplitude of high frequency components is higher.

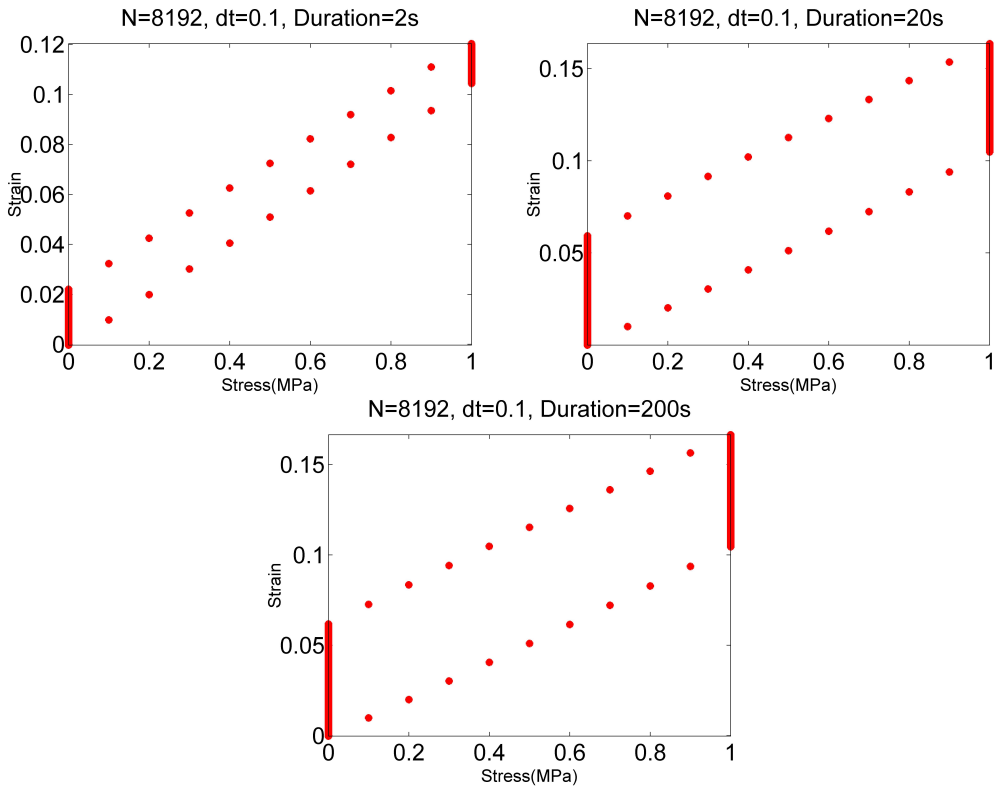

Figure 3.13.: Dissipation energy at different loading history (a) 2s; (b) 20s; (c)200s.

Figure 3.13 plots the strain against stress to present the energy dissipation during the loading history. From the previous analysis, the stress duration 20s is enough to present the creep behavior, as there is no obvious increase of strain after 20s. Thus, when the stress duration is set as 200s, the dissipation loop formed from the stress and strain history is similar to the loop formed from stress duration 20s. With current specified parameters, the energy dissipation of this model happens in 20s as no further strain accumulates in the remaining loading period. While loading history with the stress duration 2s has merely demonstrated the creep behavior and the dissipation energy is much lower than that in the other two loading cases.

The plot indicates that initial strains of the three cases of loading history are similar. The dissipation energy is determined by the time scale of creep behavior. As to the solid model, the dashpot has the properties, $\dot{\epsilon} \propto \sigma$ and $\epsilon = \int \dot{\epsilon} dt$. At the

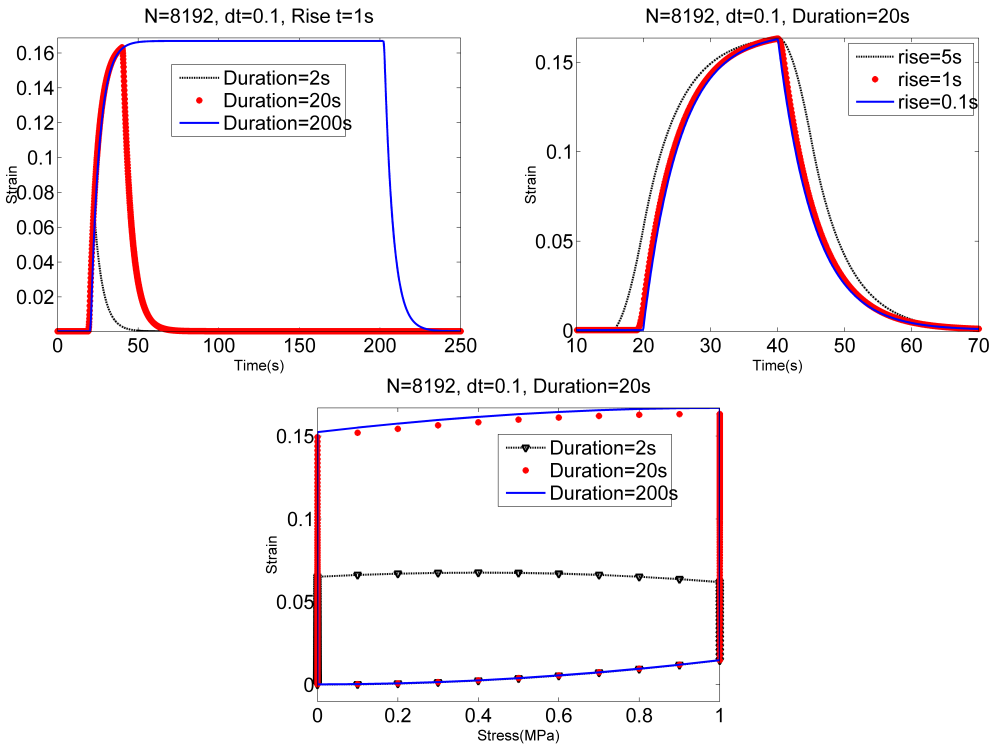

Figure 3.14.: Factors affect creep behavior of solid model (a) Stress duration; (b) rising time and (c) the dissipation.

very beginning stage of loading, the strain rate is nonzero but the strain is zero. The zero strain also confines the deformation in the spring element, thus, the strain of whole system is zero. During the constant stress period, the strain rate keeps constant. Since strain is obtained from the integral of strain rate over time, the strain constantly increases with time and reach a maximum value. Because the two branches of the solid model keep the same strain all the time, the deformation in the spring element also increases gradually. Since the external stress keep constant, the strain should have a maximum value. Initially, the dashpot and spring undertake the strain together, but later the spring bears the stress individually, as a result, the stress in the dashpot turns to zero and no further strain increase over time. From time 20s to 200s, nothing new happens. After unloading, the external stress turns to zero, the spring starts to recovery, however, the strain in the dashpot

resists the deformation. The free body analysis indicates the spring is in tension and the dashpot is in compression. This force applied on the dashpot is opposite to previous direction, so as the sign of the strain rate, then, the piston will push the dashpot to reduce the deformation. Now, the strain in the spring becomes smaller and smaller, so as the stress. Thus, the strain rate gradually close to zero and the deformation in the spring and dashpot turns to zero at same time.

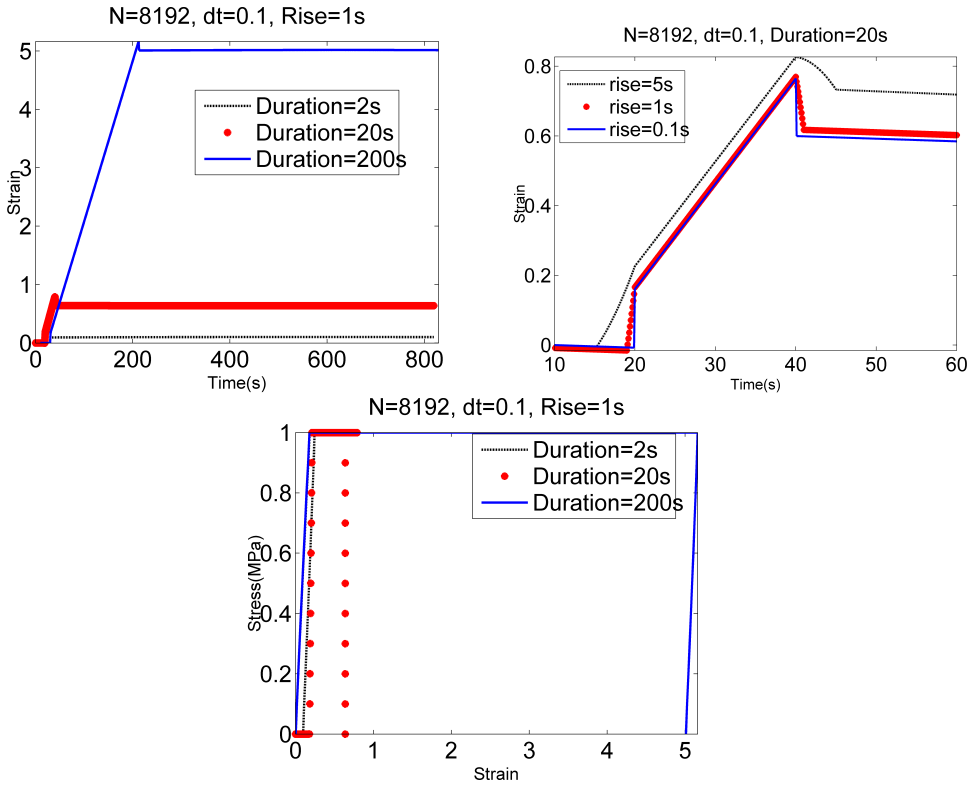

Figure 3.15.: Factors affect creep behavior of fluid model (a) Stress duration; (b) rising time and (c) the dissipation.

Figure 3.15 shows the creep behavior of fluid model and the factors affecting the performance. Similarly, the dashpot still embodies the relationship $\dot{\epsilon} \propto \sigma$ and $\epsilon = \int \dot{\epsilon} dt$. In this system, the spring and dashpot undertake the same external stress all the time. The deformation of the spring happens immediately with the external force, thus, the initially linear increase of the displacement is attributed to the

spring element. The dashpot is also under the same external force, that means the strain rate is kept as constant all the time. As the strain is the integral of strain rate over time, the initial strain is zero and later, the strain increases linearly with time. Because in this model, the deformation of spring and dashpot are independently, it is a linear increase. Now, the deformation of dashpot is independent on the spring, as a result, the deformation in the strain can continue to increase with time until the unloading. After unloading, the deformation caused by the spring turns to zero immediately. Since there is no external force and strain rate of dashpot turns to zero too. No further strain happens on dashpot anymore but the already happened strain is kept.

In the previous analysis about wrap around effect, the beginning value and ending value are zero because of the enforced periodicity. When apply IFFT to reconstruct the response in time domain, the last point in the time window is forced to zero. While in the fluid model, the final strain is kept as a nonzero constant, which is contrary to the requirement in reconstruction. Furthermore, for current case, no matter how large of the window size, the reconstructed strain using IFFT is not zero and the IFFT approach is not feasible. However, the strain rate of fluid model displays the beginning and ending value as zero, which is proper for the IFFT reconstruction. In that case, Fourier transform should apply on the strain rate rather than strain to get the reconstruction of strain rate. With the obtained strain rate, strain can be calculated from the integral over time using trapezoidal rule, which multiples each value of strain rate by dt and add it to the previous one.

As to the solid model, even the initial part of the deformation is not purely elastic. The three loading cases with different stress durations present three different behaviors. The longer stress duration shows creep behavior but the short stress duration doesnt display creep behavior. In the testing, the maximum value of stress is set as 1MPa, and the maximum strain is about 0.16. Figure 3.14(a) presents exponential increase and drop of strain after reconstruction with IFFT. During the fast application of the stress, there is no elastic behavior, which is not

true in reality. The rising time has very little influence on the shape of strain in the solid model. The Figure 3.14(c) plots the strain against stress of different loading history. Similarly, there is no linear increase and linear fall of strain in this plot. Those figures indicate that the solid model is a bad model to simulate the mechanical properties of rubber.

With the analysis, it can tell that the simplest model is the standard solid model since it can show the elastic deformation even from the 2s stress duration and also has limitation about the final strain. The plot of stress against strain gives even more direct information about the elastic deformation at the beginning of loading. From the turning point location of strain, the response can be divided into three time scales. In this standard linear model, the stress is set as 1MPa, E_1 is set as 4MPa and E_2 is set as 6MPa. In the loading case 2s, the strain is about 0.11, which gives the plot of elastic part as 9MPa. Consider the combination of two spring elements, if they are in series connection, the equivalent modulus of the system is $\frac{E_1 E_2}{E_1+E_2}$. As to the current in parallel series, the equivalent modulus is $E_1 + E_2$. Because in the very beginning, the dashpot undertakes very limited stress, there are almost two springs in parallel series and giving a modulus close to 10MPa. Next, look at the strain when the stress duration is 20s. At this case, the strain is about 0.16, and the modulus of the system about 6.25MPa. That number is equivalent to the modulus of the two springs in series connection. It is important to point out that that rising and fall part of the strain are identical as the rising and fall time in the stress history are identical.

Figure 3.16 shows the corresponding response of the viscoelastic materials charactering in three different models. In the Figure 3.16(a), the abrupt step stress leads to the direct strain of the spring immediately and the gradually increase of strain later. In the Figure 3.16(b), the abrupt applied loading couldn′t lead to immediately elongation of spring since the dashpot is in parallel with the spring and prevents the spring to extend immediately. The strain of the Voigt model happens gradually while the spring starts to afford more and more loading. In the

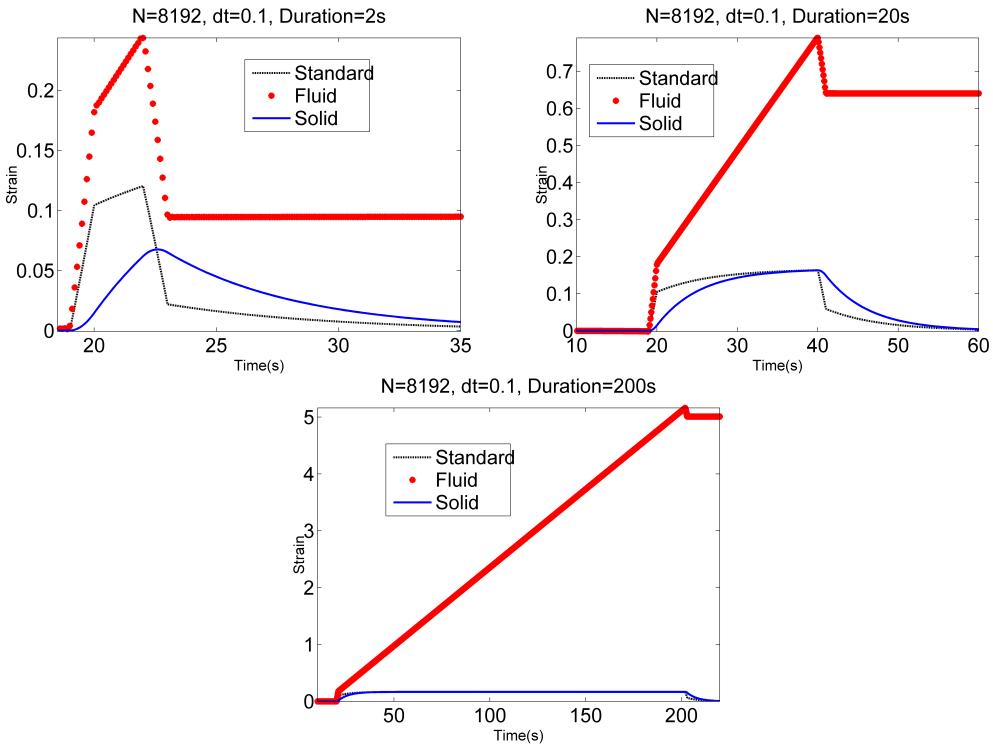

Figure 3.16.: Comparison of three models at different stress duration (a) 2s; (b) 20s; (c) 200s

Figure 3.16(c), it displays an immediately elongation at the initial time since there is a spring element existing in one branch, later, the spring in the branch including the in series connected spring and dashpot starts to elongated. Unload the unit step force at $t = t_1$, the strain response of every model can be treated as the reversal procedure of loading. Generally speaking, the elastic deformation will disappear immediately while there is some remaining deformation existed in the material and the remaining strain will decrease exponentially.

The standard linear model and fluid model present the linear elastic behavior at the beginning of stress rising and fall. The ultimate strain in the standard linear model and solid model will reach a steady state, which is dependent on the coefficient of the spring only branch in those models. As to the generally mechanical behaviors of rubber material, the initial elastic period appears before the creep and

there is a limitation over the final strain. As a result, the standard linear model is recommended as the simplest model to represent the viscoelastic of rubber materials.

In sum, the Maxwell model can display relaxation better but not good at creep modeling, on the contrary, Kelvin-Voigt model can display the creep better but not good at relaxation representation. Furthermore, the relaxation and creep are function of time, which illustrate pretty obvious time dependent behavior, while the real viscoelastic materials present pretty slow rheological behavior. Thus, more elements composed model to approximate the viscoelastic materials is proposed in recent decades. But in reality, the accuracy should balance with the redundant computation and experimental tests when more elements are introduced in one model.

3.2 Experiment Research for Material Characterization

Three unknown parameters has to be identified with the typical rubber coupons prepared from the vehicle bushing′s rubber core. A series experiment test procedures are laid out to obtain more and comprehensive physical, thermal and mechanical properties of the researched rubber material. As to linear viscous elastic materials, there are three approaches to characterize its mechanical properties. The most direct representation is based on the creep and relaxation behaviors, which can be obtained using the creep or relaxation experiment under quasi-static conditions. The corresponding results are represented with constitutive equation in integral formals. The second method studies the strain rate-dependent of the viscoelasticity and then represents the constitutive equation in differential formats. The third one measures the periodic dynamic response using the dynamic mechanics analysis equipments and that result will be represented in complex. The third one is the most popular one and mostly applied in the viscoelastic materials research because it is more convenient to explore to nonlinear viscoelastic properties from the current linear characterization. During the rolling of drive, the vehicle, especially the tire

will experience sustainable periodic dynamic loading, as a response, the rubber bushing in current case also under the same external excitation. It is important to clarify the difference of non linear mechanical properties of rubber and linear complex representation. Actually, the dynamic mechanic testing at small train still produces almost sinusoidal signal rather than the expected harmonic. The obvious harmonic phenomenon appears at higher amplitudes, then, the linear storage and loss modulus would be inappropriate to describe material behaviors, this feature is terms as harmonic paradox (Heinrich & Klüppel, 2002).

3.2.1 Testing Conditions and Experiment Results of MTS

Figure 3.17 shows the instrument of MTS tensile machine and rubber sample, which is prepared according to the ASTM standard test methods for rubber property-compression set (D 395). The test is performed to find the Mooney-Rivlin constants for dynamic rolling simulation. The Mooney-Rivlin material model is used to describe the super elastic properties of rubber. Compression test is designed to test the elasticity of materials, especially the ability to retain elastic properties under the larger compression or deformation. In this test, the force and applied deformation rate is set up to get the corresponding displacement. Tests are carried at room temperature to detect the static mechanical properties of rubber. The test specimen is a cylindrical disk, which is cut from the bulk rubber bushing specimen. The dimensions of the specimens are 6.0±0.2mm in thickness and 13.0±0.2mm in diameter.

To have the elastic stiffness variation with the strain and deformation rate, large batch of tests have been done to get the comprehensive conclusion. All of the samples are tested in three groups, the first group test has same deformation rate 0.01mm/s, but ramping the total strain from 5% to 40%, specifically, 5%, 10%, 15%, 20%, 25%, 30%, 35%, and 40%. The second group of samples experience the total strain 20% but the deformation rate ranges from 0.01mm/s to 0.8mm/s, specifically,

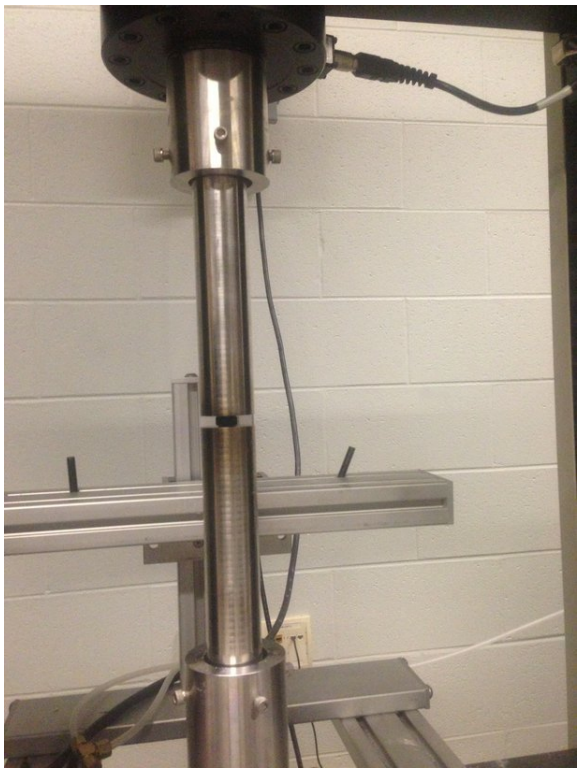

Figure 3.17.: MTS and rubber coupon used for the compression test.

0.01mm/s, 0.02mm/s, 0.04mm/s, 0.06mm/s, 0.08mm/s, 0.1mm/s, 0.2mm/s, 0.4mm/s, and 0.8mm/s. The third groups of samples varies in velocity, which changes from 0.01 to 0.8mm/s as the second group, but the strain of this group is set at 50%.

The compression test results of rubber sample are plotted in the Figure 3.18. The compression strain and stress curves display non-linear relationship. The influence of total strain percentage isn′t that significant in determining the shape of curves, but it can be deduced that the slopes of those curves increase over all.

Figure 3.18(a) shows the behaviors of group 2 specimens, which is fixed at strain rate 20%. As a comparison, Figure 3.18(b) gives the behaviors of specimens when the strain rate is 50%. At relative low strain, the strain and stress curves are almost proportional straight line. Even though the rate =0.8mm/s is 80 times higher than the rate=0.01mm/s, the shape of the two curves shows slight difference.

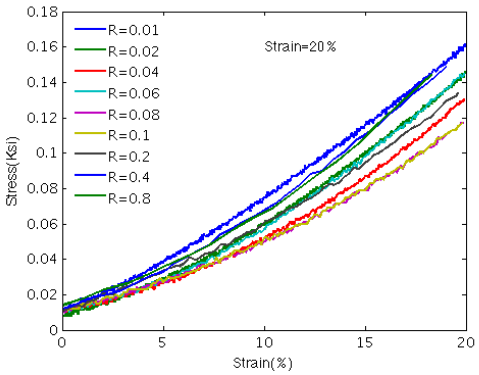

(a) Fixed strain at 20%

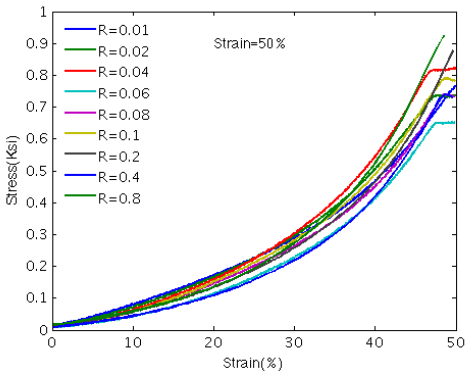

(b) Fixed strain at 50%

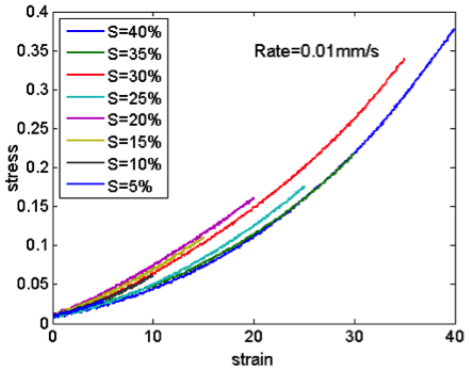

(c) rate=0.01mm/s

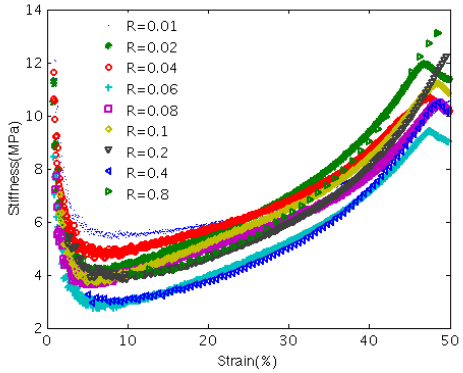

(d) Stiffness at fixed strain 50%

Figure 3.18.: Effect of the total strain and deformation.

That means the elastic stiffness is not totally deformation rate-independent, even though the effect is not that significant.

It is interesting to found in Figure 3.18(a) and Figure 3.18(b) that the highest two deformation rates and lowest two deformation rates have their stress and strain curves at higher position than the remaining curves. The tensile rate is fixed and the strain changes in Figure 3.18(c). It is easy to found the deformation rate and strain range will affect the stress-strain relationship. The stiffness of rubber sample increases gradually with strain when the strain rate is pretty low, thus it is reasonable to attribute this phenomenon as static friction effect. With the increase

of strain, more and more molecular chains clusters have been straighten, that leads to the increase of stiffness at higher strain. From this viewpoint, the positions should be higher when the total strain is set larger. While, the plastic deformation happens when the critical elastic or elastic-viscous point is reached, which is shown in Figure 3.18(d). The rubber starts to yield when the strain reaches to 50 %.

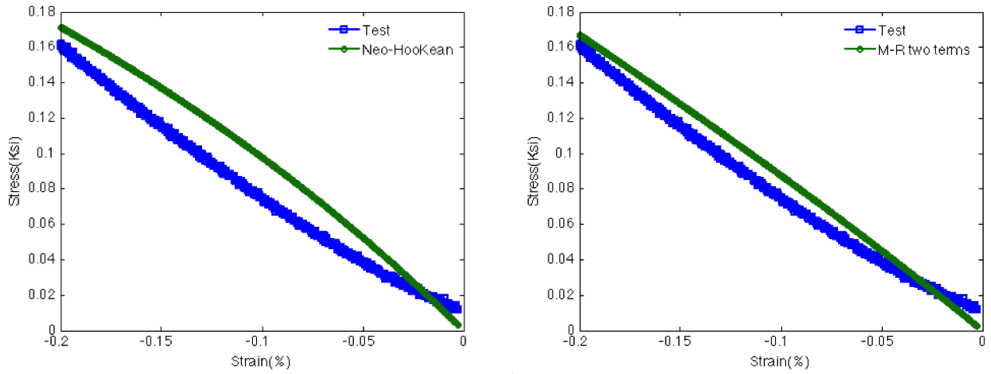

(a) Neo-Hookean model (b) Mooney-Rivlin model

Figure 3.19.: Fitting of super-elastic model.

Figure 3.19 shows the fitting results of super-elastic with two classical models. Both present good approximation to predict the static mechanical properties of rubber. However, in the following FEA analysis, viscoelastic model is taken to represent the frequency-dependent modulus, thus, super-elastic properties of rubber is out of the discussion.

3.2.2 Testing Conditions and Experiment Results of DMA

The dynamic mechanical analysis test is operated on the DMA of TA instructions Figure 3.20(Willett, 1973). This instrument is designed to measure the mechanical properties of polymers upon the temperature, frequency and amplitude, especially to properly describe the influence on the viscoelastic behaviors. The stress or strains signal are applied in sinusoidal, which are convenient to express the

complex modulus. Due the physical properties of viscoelastic materials, there is a phase delay occurring on the strain compared with stress.

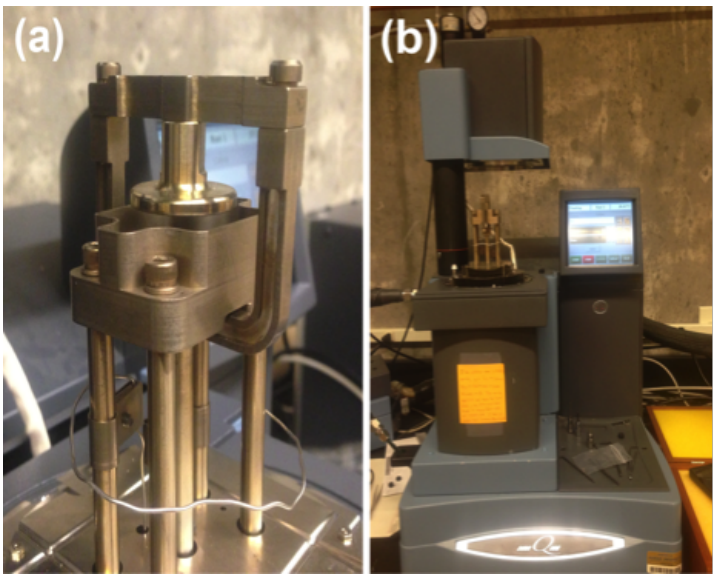

Figure 3.20.: DMA test instrument Q800 (a) Compression test clamp; (b) full view of the DMA.

Submersion compression clamp is chosen in current measurement, the sample size is 25mm in diameter and the thickness is up to 10mm following the TA instruments brochure about DMA. The sample in the submersible configuration can keep the environment at specified temperature if liquid is set and heated up. The sinusoidal stress is applied using an oscillating plate while another flat surface holding the sample is fixed. The selected output values from this DMA are temperature(°C), storage modulus (MPa), loss modulus (MPa), stiffness(N/m), damping(N/m), tan delta (δ), frequency(Hz), stress(MPa), strain(%), amplitude(μm), force(N) and displacement (μm).

The experimental results of rubber components subjected to static load and harmonic excitation are obtained to identify parameters of each element in the Berg′s rubber model. All of the data measurements are finished using equipment DMA, which records the influence of frequency, time and temperature on materials′

mechanical properties. Harmonic excitation operated using this instrument is supposed to run over a wide frequency range, from 0.001Hz to 200Hz. However, the tests at frequency lower than 0.01Hz and higher than 100Hz are failed to apply the load in this measurement because the limitation of the instrument.
Parameterization is complicated and time consuming, furthermore, based on the characterization of viscoelastic model, it is common to separate the test into two steps, quasi-static load and high frequency harmonic excitation.

3.2.2.1. Parameter Identification for Friction Damping

In the case of static load, loading at lower velocity and excitation frequency is appropriated approximation to simulate the quasi-static loading condition due to impractical static loading. The quasi-static frequency is collected in the range from 0.01Hz to 0.1Hz. The quite low frequency is required to make sure that the contribution of viscous damping is of negligible proportion. The stress is selected in the range of 0.001MPa to 0.05MPa for the amplitude-dependency research. The corresponding real-time reports about stiffness, damping, tan delta and amplitude is outputted automatically as long as the pre-set working condition is reached and cycle loading becomes stable. Figure 3.21 shows the variation of amplitude under quasi-static low frequency excitation.

Figure 3.21(a)is the Payne effect describing the amplitude-dependence of stiffness With the increase of loading amplitude, the stiffness of rubber decreases. This phenomenal is associated with the weak van der Waals bonds existing in the filler agglomerates (A. Payne & Whittaker, 1971). The break of physical bonds at higher amplitudes or high strain explains the reduction of stiffness in macro level. For the very small amplitude of stress, friction plays dominate role to increase stiffness. The rupture of molecular chains in micro level presents as the friction release. In order to describe the hysteresis loop formed at quasi-static and the amplitude dependence of stiffness, a tri-linear model is proposed. The coefficients of

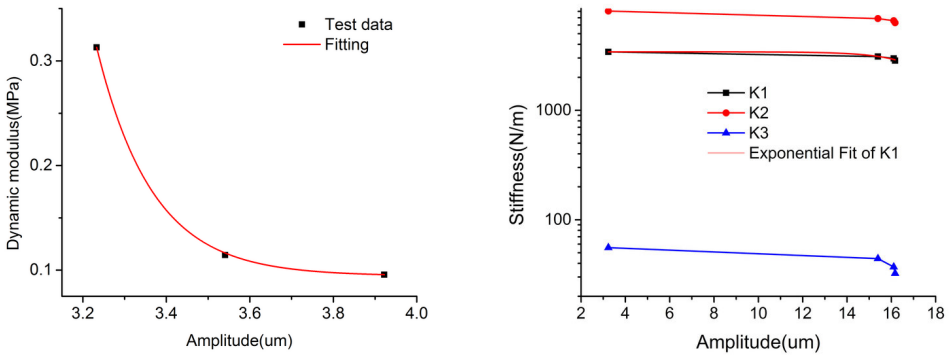

(a) Modulus variation (b) Spring fitting

Figure 3.21.: Amplitude-dependence of modulus under quasi-static excitation and its influence on stiffness fitting of K_1, K_2 and K_3.

those coefficients in the model are identified with multivariable constrained approach. The equation formulated for parameterising the hysteresis loop is based on the ratio of energy dissipation over total storage energy,

$$min \sum \left[\frac{|(\frac{S'}{S} - \tan\delta)|}{\tan\delta} \right] \tag{3.23}$$

Where S' is the area in side of hysteresis loop, and S is the storage energy during loading. $\tan\delta$ for each loading condition and the corresponding strain can be collected from the DMA report. The area S' and S can be estimated using the tri-linear model. There are three stiffness values in the hysteresis model need to be identified, which means at least two groups of data under the same or close excitation frequency required to implement the parameter identification. Stiffness before and after the hysteresis harness during quasi-static measurement are set as the initial value for K_1 and K_2. Note that K_1, K_2 and K_3 slightly decrease with increasing amplitude and K_3 is much lower than K_1, which also agrees well with the previous description about molecular chains. It is also reasonable to inference that the fracture of molecular chains causes even more reduction of stiffness than the chains′ relaxation. It is important to point out that the characterization of Payne

effect is confirmed in the small strain range, usually 0.001 to 0.15. Outside the range of strain, the storage or loss modulus will not change over strain amplitude (Heinrich & Klüppel, 2002).

3.2.2.2. Parameter Identification for Viscoelastic Damping

For the dynamic stiffness except the hysteresis damping, the model is a combination of advanced Maxwell system and spring element, which means three parameters k_1, k_2 and c_1 required to determine the frequency response of dynamic behaviors, see Equation 3.2. The rubber coupon prepared for the DMA measurement is about 5mm in thickness and 10mm in diameter. The testing range of stress is less than 0.1MPa to avoid the inaccuracy of data and the measured displacement is rather low. The loading frequency of vehicle is commonly at the frequency about 20Hz. Thus, low frequency force-deflection relations should be discussed here to seeking after stability and passenger comfort for vehicle system (Knothe & Grassie, 1993). In current research, the harmonica excitation is applied in the range from 1Hz to 100 Hz with step 10Hz to balance the representativeness of data and redundancy of calculation. The stress of each frequency is applied from 0.01MPa to 0.1MPa to investigate the amplitude-dependence of viscous damping. Beyond the testing range of frequency and stress, the data collected from the equipment is not reliable and inaccurate.

The overall variation of dynamic stiffness and damping over amplitude and frequency are plotted in Figure 3.22. With the increase of frequency and amplitude, the dynamic stiffness keeps decreasing. As a comparison, the damping presents a peak when the excitation frequency is about $f = 30$Hz no matter the variation of amplitude. Before more depth discussion, the storage modulus, stiffness and other relevant output are sketched to complement the previous results.

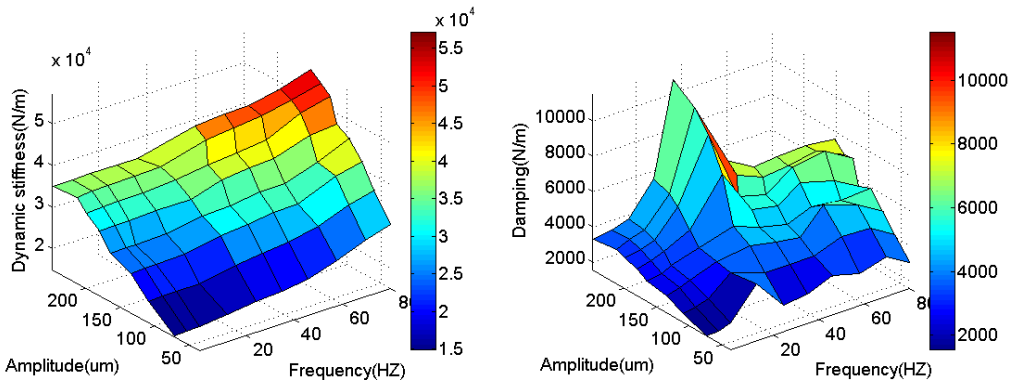

(a) Dynamic stiffness(N/m) (b) Tan delta

Figure 3.22.: Response of harmonic excitation versus amplitude and frequency.

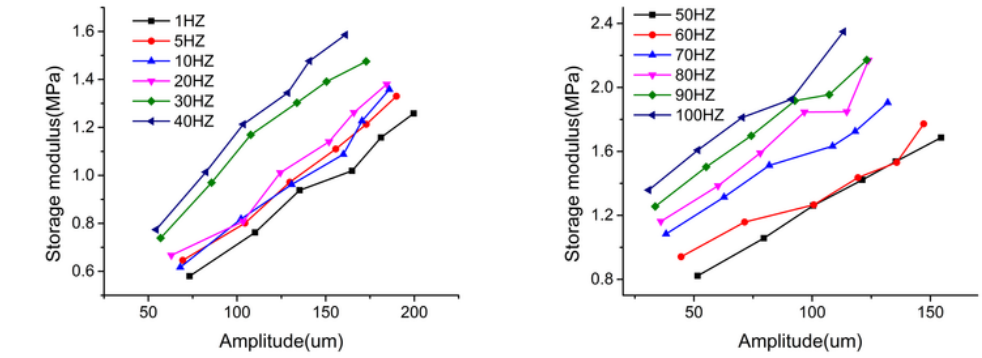

(a) Storage modulus(MPa) (b) Storage modulus(MPa)

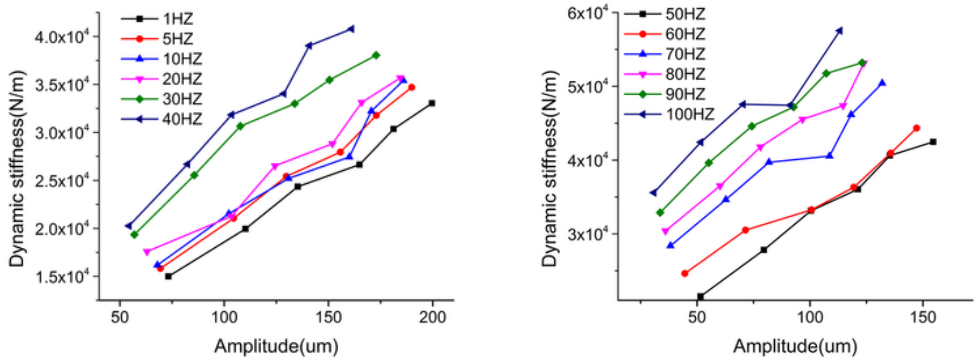

(c) Dynamic stiffness(N/m) (d) Dynamic stiffness(N/m)

Figure 3.23.: Illustration of variation upon frequency and amplitude.

Figure 3.23 shows that both the storage modulus and dynamic stiffness increase almost linearly with frequency and amplitude, which clearly illustrates the amplitude and frequency-dependence of dynamic behaviors. Storage modulus monotonously increases with the input stress and frequency.

Tan delta shown in Figure 3.21is not linearly increase with frequency or amplitude. Loss modulus, damping and tan delta display a peak value around frequency 30Hz, especially at higher strain amplitude (Figure 3.24(a)).The increase of strain is slight under the low frequency range and the increase of frequency also has little effect on the locations of those lines in Figure 3.23. Considering the slight variation of tan delta in the low frequency loading range, the variation of tan delta over the frequency is fitted with a straight horizontal line just as the treatment applied on the quasi-static harmonic excitation at 0.01Hz. The slop of the fitting curve of tan delta is 2.12×10^{-4} under quasi-static loading, which indicates the much lower amplitude dependent hysteresis damping compared with the storage energy. Before explore the viscoelastic damping, the dissipation attributed by the hysteresis has to excluded for further parameter identification in Equation 3.2.

As to damping, it increases with frequency gradually at the very beginning and abruptly reaches to maximum at frequency around $30Hz$. The damping declines to zero after the peak value with the increasing frequency and this character is more apparent at higher strain amplitude. Base on the mechanism, the performance of damping includes three steps. The rubber at low frequency behaviors close to elastic material with low damping as molecular chains of rubber can almost simultaneously follow excitation. Similarly, the small out of phase between input and output appears at very high excitation loading, such the $10Hz$ loading in current test. After this frequency, the rubber performs as glass, which is of low damping. Thus, the most complicated damping behaviors displays around $30Hz$ in Figure 3.24(c), which is a typical for excitation at medium range frequency. Under that loading, most of those molecular chains are failed to catch up with the macro deformation of rubber, which leads to large phase lag between force and deflection and higher damping.

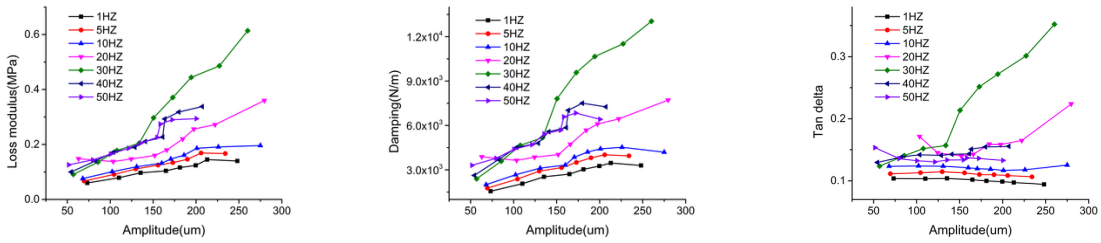

(a) loss-modulus (b) damping (c) tan-delta

Figure 3.24.: Variations on frequency and amplitude.

Three parameters k_1, k_2 and c_1 should be identified to model the frequency dependent of stiffness and damping of rubber. The parameter identification guarantees the optimization of stiffness and tan delta in the frequency range and the multivariable equation is given in Equation 3.24,

$$min \sum \left[\frac{|\sqrt{E'^2 + E''^2} - \frac{\sigma_0}{\epsilon_0}|}{\frac{\sigma_0}{\epsilon_0}} + \frac{|\frac{E''}{E'} - \tan\delta|}{\tan\delta} \right] \tag{3.24}$$

Dynamics stiffness is defined as $E_{dyn} = \sqrt{E'^2 + E''^2} = E'[1 + (\tan\delta)^2]^{1/2}$. Tan delta is less than 0.2 in almost all testing condition, therefore, E_{dyn} is approximated to E' with the error less than 2%. Furthermore, it could be shown from Equation 3.24 that E' is close to k_2 as long as the excitation frequency is pretty low, finally, dynamic stiffness E_{dyn} is selected as the initial value of k_2. Considering the friction effect of rubber upon the quasi-static deformation and its contribution to the hysteresis stiffness, the data used for the dynamic behavior′s parameter identification should reduce the quasi-static stiffness and tan delta. The influence of hysteresis stiffness reduction becomes non-significant if the amplitude of dynamic excitation is set as pretty large since the reduction from the rupture of physical bond between carbon black particles is only confined in a certain range of strain. The static stiffness variation upon amplitude is usually described in exponential form or hyperbola decreasing model. The static stiffness plus the auxiliary from friction is simply treated as constant under the excitation in the high range of

frequency. The initial value of k_1 usually starts from 0.7 E_{dyn} to accelerate the optimization calculation in current procedures. Damping coefficient is relative low and 1000 MPa.s should be a good initial point.

Figure 3.25 and Figure 3.26 show the comparison of experiment curve against predicted curve plotted with the parameters obtained from optimization. The stress of this group of data is ramping from 0.01MPa to 0.08MPa. It can be seen easily that dynamic stiffness increases with frequency and there is a damping peak with the increasing of frequency. As discussed from previous amplitude-stiffness analysis, the dynamic stiffness and damping are generally amplitude-dependence.

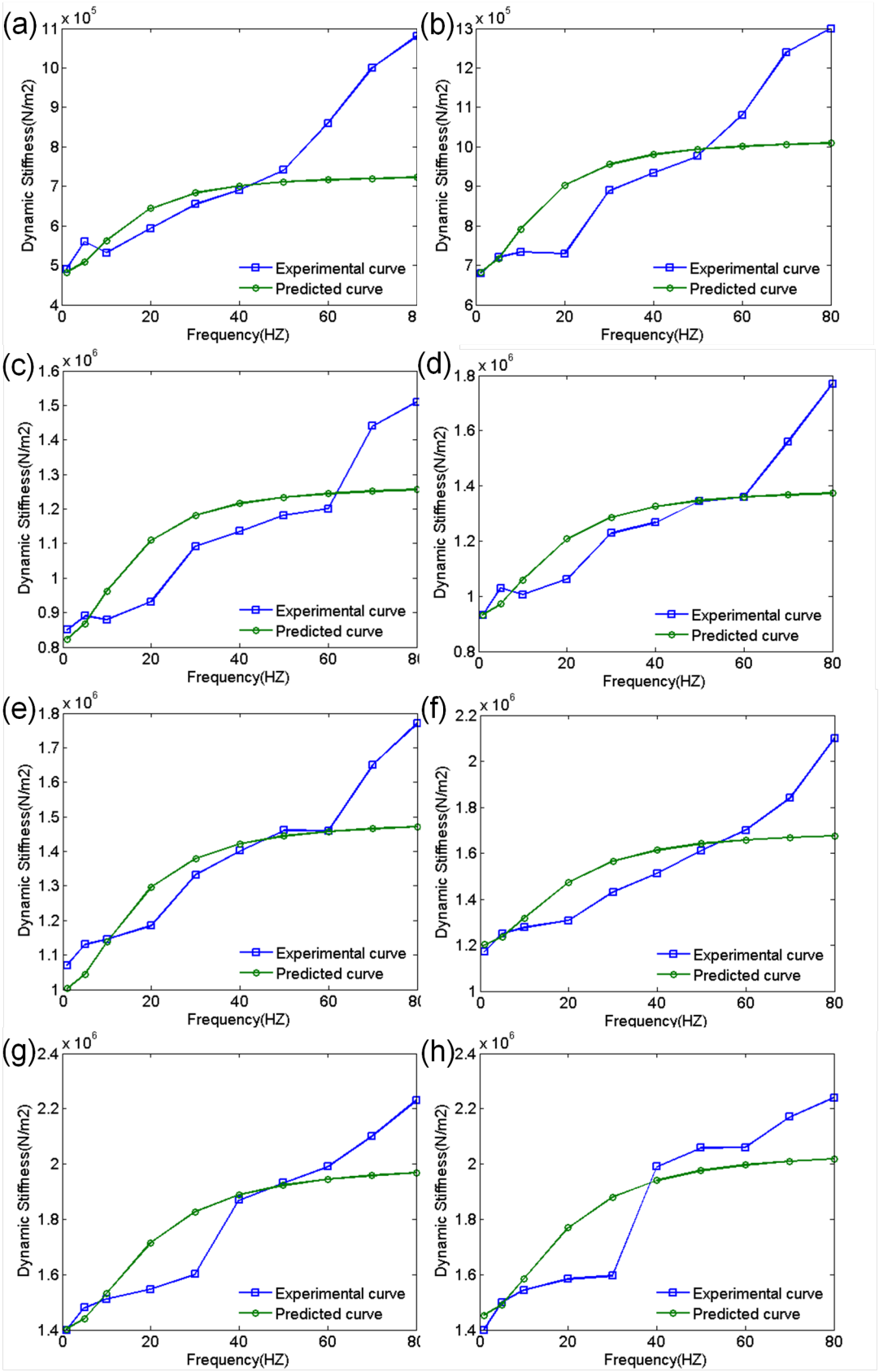

Figure 3.25.: Experiment measurements against predicted dynamic modulus at different stresses (a)=0.01 MPa; (b) =0.02 MPa; (c) =0.03 MPa; (d) =0.04 MPa; (e) =0.05 MPa; (f) =0.06 MPa; (g) =0.07 MPa; (h) =0.08 MPa.

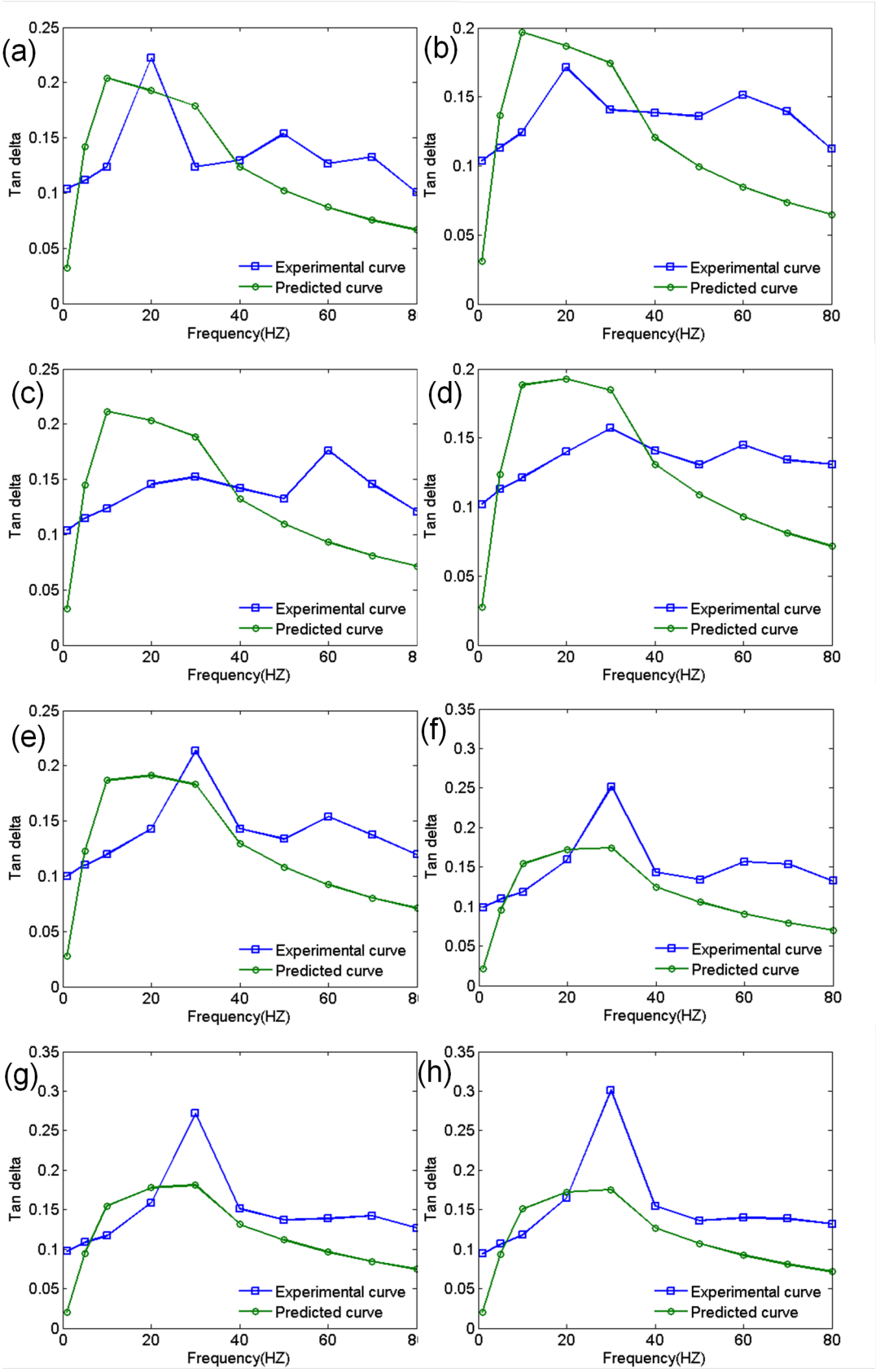

Figure 3.26.: Experiment measurements against predicted tan delta at different stresses (a) =0.01 MPa; (b) =0.02 MPa; (c) =0.03 MPa; (d) =0.04 MPa; (e) =0.05 MPa; (f) =0.06 MPa; (g) =0.07 MPa; (h) =0.08 MPa.

The error analysis is illustrated in Figure 3.27 and the results indicate that optimization with experimental data at lower stresses is poor compared with that from medium or higher stress excitation. This may attribute to the error of hysteresis stiffness estimated for quasi-static condition, which highly affects dynamic output at lower frequency excitation. As to the medium frequency excitation, dynamic stiffness and damping reach almost maximum value, then, relative error of dynamics stiffness is minimized due to the absolute increment of stiffness. Tan delta is barely affected by frequency or amplitude in quasi-static excitation, therefore, there is no obvious increment of relative error varying with dynamic excitation testing conditions. Higher stress and higher frequency excitation condition is kind of out of the service scope of DMA testing equipment, hence, the slightly narrowed error at highest stress 0.1MPa may partly due to the much less data collected for the optimization calculation.

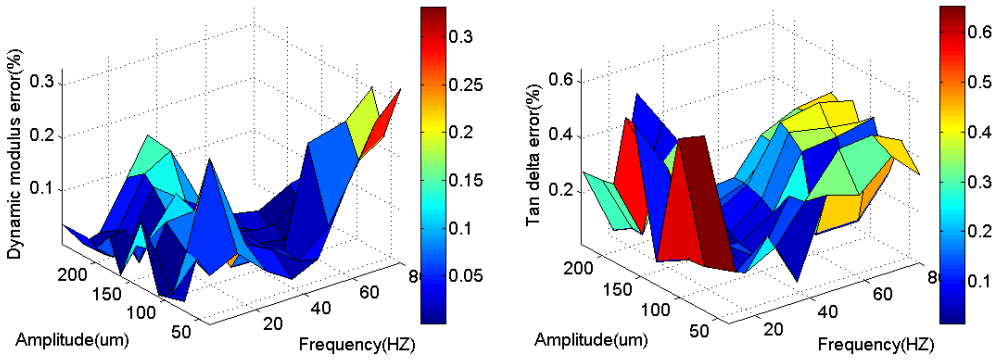

(a) Error of dynamic modulus

(b) Error of tan delta

Figure 3.27.: Erroneous analysis of dynamic modulus and Tan delta upon with the variation of amplitudes and frequencies.

The error analysis of amplitude and frequency dependency of stiffness and tan delta are plotted in on the Figure 3.27to choose the best stress range to identify the parameter for frequency dependent model. That figure indicates the medium amplitude loading gives the minimum error in fitting the viscoelastic model.

Similarly, if frequency range is needed to confirm to characterize the amplitude dependent model of rubber, the medium frequency is also a better selection as depicted in Figure 3.27. In view of the three dimensional error analyses at different amplitude and frequency, the excitation at 0.05MPa is employed to identify parameter for the standard linear model of viscoelastic model. The calculated stiffness of rubber coupon is pretty close the dynamic stiffness at 1Hz, that result endorses the initial value assumption for the optimization procedure. The error analysis presents higher error value in fitting tan delta compared with that in fitting dynamic stiffness. Actually, the phenomena was discussed in some publication, within which deviation existing in the loss modulus fitting is much higher than the storage modulus fitting (Ulmer, 1996). To minimized the error in tan delta fitting, a modification about loss modulus expression is given as,

$$\tan\delta = k_1\frac{\omega\tau}{1+\omega^2\tau^2}\Big/\left(k_2 + k_1\frac{\omega^2\tau^2}{1+\omega^2\tau^2}\right) + a\exp(-(\omega/10-3)^2/b) \tag{3.25}$$

where the parameter a and b are merely used to improve the precise of fitting and without practical meaning. The parameter identification results give k_1=0.8MPa, k_2= 1.009MPa and C=0.028MPa.s at stress 0.5MPa finally. In the modified model, two parameters without practical significance are introduced on the basis of fitting experience to minimize the fitting error in the loss modulus related terms. While, this correction merely pays attention to the variation of frequency, for more concise expression, the correction term considering the effect of temperature and static amplitude should be included.

3.3 Conclusion

This chapter presents a detailed review about the current researched models to characterize the rubber materials, which include the hyperelastic and viscoelastic models. The principles to build a hyperelastic model are classified into two theories, one is the strain energy density and the other one is the statistic mechanical method. While in current research, viscoelastic models are applied to further the exploration

about the hysteresis and viscous damping. Commonly used viscoelastic models are also elaborated and their merits and shortcomings are analyzed with the comparison of creep and relaxation function. Because the mechanical properties of rubber are time, frequency and temperature-dependent, the thermal properties of rubber and the structure-thermal coupling is illustrated in the following part of the dissertation.

This chapter includes two major contributions. The first part is the experiment measurement to collect data of dynamic behaviors needed to proceed the parameter identification. With the derived the kinetic equations of three parameters model, the optimized parameters are identified. This part presents the approach to have proper parameter identification to reproduce the rubber′s viscoelastic properties. More important, with the current model and parameters, the FEA simulation in next chapter becomes achievable.

CHAPTER 4. FINITE ELEMENT ANALYSIS WITH FORTRAN PROGRAM

The finite element analysis (FEA) includes three parts, preprocessing, numerical solution and post processing. To have completed FORTRAN program to compile the three processes for the non-linear FEA, it is far beyond the time and energy allowed for a PhD student. Prof Jame.S. Doyle developed coding development environment of FEA program for more than 20 years, which products implement the preprocessing and post processing(Doyle, 2009). The FEA coding environment is named as Simplex and includes static, dynamic, stability, nonlinear analysis modules and so on to specify different types of problems. On the basis of existing source code of Simplex, the subroutine force-frequency is developed to describe the frequency-dependence of viscoelastic material. QED is a user friendly interface incorporating the mesh generation and plot and simulation result views. In the following research, the developed force-frequency module is termed as Simplex in order to differentiate with the already completed modules in QED. The structural date file is generated using QED and Fast Fourier transform (FFT) algorithm is implied for the feasibility of frequency scan. Hex20 finite element and 27 point integration method are used in the preprocessing and post processing separately.

4.1 Preprocessing and Postprocessing of FEA

The development of force-frequency module is initialized from the governing equation of dynamic vibration. In the following section, the feasibility to create the nonlinear module for viscoelastic material on the basis of the principle of the elastic module is elaborated, and then, the characterization of Hex20 element is described.

4.1.1 Forming of the Governing Equation

In reality, damping or energy dissipation can be found in all system in motion. The governing equation of motion or the force equilibrium of a system is,

$$M\ddot{u} + C\dot{u} + Ku = P(t) \tag{4.1}$$

Where $M\ddot{u}$ is the inertia force, $C\dot{u}$ is the damping force, Ku is the elastic force and $P(t)$ is the applied loading force. From the field test simulating the external excitation applied on the rubber bushing installed on the exhaust piping system, the vibration in large time window can be approximated using single frequency excitation after the spectral analysis. In that extreme case, the particular loading can be characterized as sinusoidal or cosine function. Under harmonic excitation, the force equilibrium of the damped system can be written as,

$$[K]v + [C]\dot{v} + [M]\ddot{v} = P\cos(\omega t) \tag{4.2}$$

The complementary force equilibrium of the system is,

$$[K]w + [C]\dot{w} + [M]\ddot{w} = P\sin(\omega t) \tag{4.3}$$

All those variables in the two equations are real and the only difference is the loading phase. Combine the two linear systems with the definition of complex displacement, $u = v + iw$, then, the new created governing equation turns to,

$$[K]u + [C]\dot{u} + [M]\ddot{u} = Pe^{i\omega t} \tag{4.4}$$

The complex displacement can also be written as $u = \hat{u}e^{i\omega t}$. The system of the equation is taken as pseudo-static as the loading is periodical. In the damped system, it is tedious to solve the equation in the function of sinusoidal, cosine or exponential. Especially, for a system with time differential governing equation, the introduction of complex quantities can greatly simplify the solving process. After remove the exponential term at two sides, the equation turns to frequency dependent, which explains the variation of response at different excitation frequency,

$$|[K] + i\omega[C] - \omega^2[M]|\hat{u} = P \tag{4.5}$$

The left term in the bracket is the dynamic stiffness matrix $[\hat{K_D}]$. In the Simplex program, the structure damping of elastic material is generally characterized using the damping coefficient C. As to a system constructed using Rayleigh damping, the damping matrix is proportional to the structural stiffness and mass matrices,

$$[C] = \alpha[M] + \beta[K] \tag{4.6}$$

Where, the α and β are constants. And the corresponding dynamic stiffness is given as,

$$\hat{K}(\omega) = [K] - \omega^2[M] + i\omega(\alpha[M] + \beta[K]) \tag{4.7}$$

Nevertheless, as to the viscoelastic structure, the damping inherited in the material overwhelms the structure damping, and thus, the latter is negligible in the following programming. As to the homogenous material in one model, each element has the same material tag. The frequency dependent modulus of the viscoelastic structure can be simulated by multiplying $\phi(\omega)$ with the assembled dynamic stiffness matrix $[\hat{K_D}]$. With the identified parameters in the constitutive equation of standard linear model, the stiffness matrix can be represented as,

$$\hat{K}(\omega) = \frac{i\omega\eta(\frac{E_1}{E_2} + 1) + E_1}{E_1 + i\omega\eta}[K] = \phi(\omega)[K] \tag{4.8}$$

In the case of the complicated structure, for example, the sandwich cylindrical bushing composed of two materials, the boundary nodes belong to two materials and the K matrix is assembled based on the modulus of two materials, it is not recommended to time the unique $\phi(\omega)$ with the $[\hat{K_D}]$. In that case, the coefficient $\phi_1(\omega)$ and $\phi_2(\omega)$ should be multiplied separately with the two materials before the assembly.

In the force-frequency subroutine, all input and output variables are in frequency domain. The time domain loading history is implemented in the Simplex after FFT and the response at time domain can be reconstructed with IFFT from frequency domain. The Simplex FEA program deals with the displacement, strain, stress and energy dissipation in frequency domain for single frequency or frequency

scan. Corresponding, all outputs have imaginary part accompanying with real part as the modulus of the material is complex variable.

4.1.2 Hex 20 Element

In the Simplex program, the 3-D solid is recommended to model with Hex20 element, which has 20 nodes and 60 DOF for elasticity applications. The solid structure is formed with an assembly of discrete elements representing homogenous or non-homogeneous properties. The advantage of the finite element method is the ability to simulate the complicated structure without being simplified to classical simple model as the approaches used in analysis solution. That makes the FEA more powerful and applicable than the approximated mathematical analysis in the theoretical analysis. Especially, with the development of computer calculation capability, the DOF of the model is almost exponentially increased and that makes the solution even more concisely elaborated.

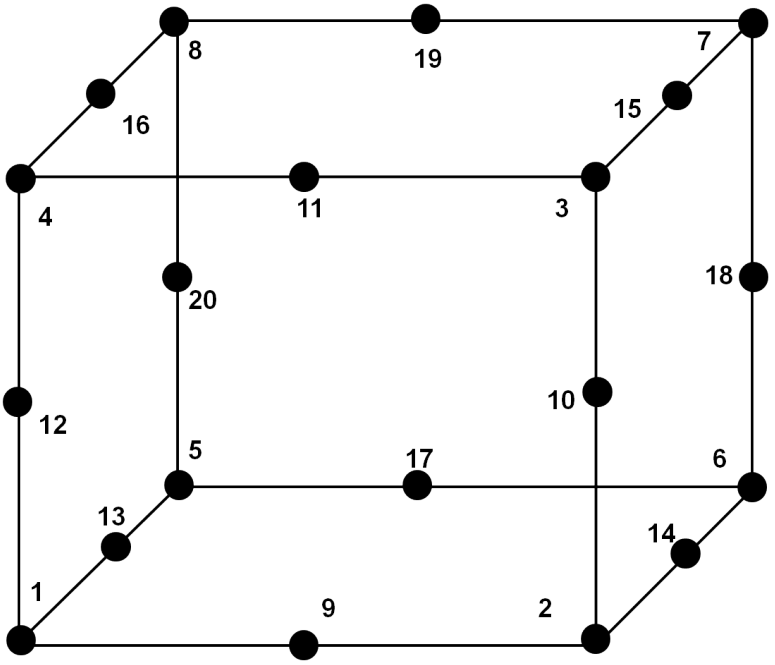

Figure 4.1.: Sketch of Hex20 element in isoperimetric coordinates.

Hex20 element is better than the tetrahedron element since the latter requires quite robust meshing routine. Furthermore, Hex20 has better performance in dealing with rubber or other incompressible material and plastic material compared with tetrahedral element. Figure 4.1 gives the sketch of Hex20 element in the isoperimetric coordinates after mapping from the physical coordinates. The three DOF of each node are listed in the following(Doyle, 2014),

$$x^0 = \sum_{i=1}^{20} h_i(s,r,t){x_i}^0; \qquad y^0 = \sum_{i=1}^{20} h_i(s,r,,t){y_i}^0; \qquad z^0 = \sum_{i=1}^{20} h_i(s,r,,t){z_i}^0 \tag{4.9}$$

Where the interpolation function $h(r,s,t)$ in the isoperimetric coordinates are,

$$\begin{aligned}
&i = 1-8: && h_i = \tfrac{1}{8}(1+r_i r)(1+s_i s)(1+t_i t)(r_i r + s_i s + t_i t - 2)\\
&i = 9,11,17,19: && h_i = \tfrac{1}{4}(1-r^2)(1+s_i s)(1+t_i t)\\
&i = 10,12,18,20: && h_i = \tfrac{1}{4}(1+r_i r)(1-s^2)(1+t_i t)\\
&i = 13,14,15,16: && h_i = \tfrac{1}{4}(1+r_i r)(1-s_i s)(1-t^2)
\end{aligned} \tag{4.10}$$

And the isoperimetric nodal coordinates of the Hex20 element are given in Table 4.1,

Table 4.1: Isoperimetric nodal coordinates r_i, s_i, t_i

i	1 2 3 4	5 6 7 8	9 10 11 12	13 14 15 16	17 18 19 20
r_1	-1+1+1-1	-1+1+1-1	0+1 0-1	-1+1+1-1	0 +1 0 -1
s_i	-1-1+1+1	-1-1+1+1	-1 0+1 0	-1-1+1+1	-1 0+1 0
t_i	-1-1-1-1	+1+1+1+1	-1-1-1-1	0 0 0 0	+1+1+1+1

The derivative of the isoperimetric coordinates is connected with the global coordinates through the inverse matrix of Jacobian operator, $\{\frac{\partial}{\partial x^o}\} = [J_e{}^-1]\{\frac{\partial}{\partial r}\}$. The matrix form of the $[J_e]$ for the Hex20 element is expressed as,

$$[J_e] = \begin{bmatrix} h_{1,r}, & h_{2,r}, & h_{3,r}, & h_{4,r}, & \ldots, & h_{20,r} \\ h_{1,s}, & h_{2,s}, & h_{3,s}, & h_{4,s}, & \ldots, & h_{20,s} \\ h_{1,t}, & h_{2,t}, & h_{3,t}, & h_{4,t}, & \ldots, & h_{20,t} \end{bmatrix} \begin{bmatrix} x^0{}_1 & y^0{}_1 & z^0{}_1 \\ x^0{}_1 & y^0{}_1 & z^0{}_1 \\ \vdots & \vdots & \vdots \\ x^0{}_{20} & y^0{}_{20} & z^0{}_{20} \end{bmatrix} \tag{4.11}$$

4.1.3 Stress and Strain with Gauss Integration Method

With the solution about displacements at each node, the stress and strain can be calculated using the quadratic hexahedral interpolations. Figure 4.2 gives the sketch of the 27 integration points used in the Simplex program.

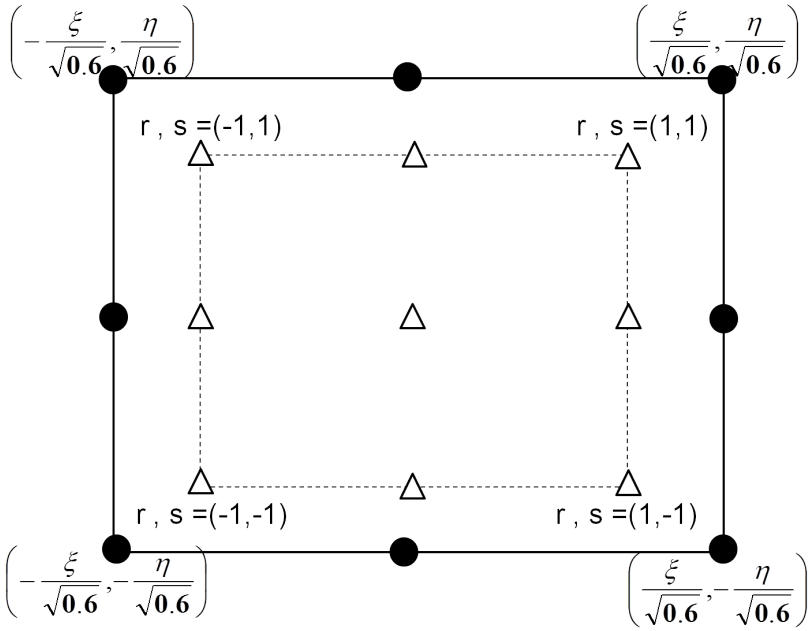

Figure 4.2.: Integration points inside the Hex20 element.

Gauss Lagrange quadrature is chosen to approximate the integrated stress and strain at each node. The sampling location of each integration points and

weights are $r_i = s_i = t_i = [-\sqrt{0.6}\ \ 0\ \sqrt{0.6}]$ and $W_i = [-5/9\ \ 8/9\ \ 5/9]$. In this approach, the best fitting straight line using least squared algorithm intersects the parabola at exactly the three points.

Define xyz as the corresponding original coordinates of the 20 nodes per element. uuc is a 60×1 array, which records the x, y, z displacement of nodes for each element, $uuc = [u_1,\ v_1,\ w_1,\ u_2\ v_2,\ \ldots,\ w_{20}]^T$, the stress at each integration point can be calculates using $\epsilon = [B_L]uuc$. Each term is presented as,

$$[B_L] = \begin{bmatrix} A_x & 0 & 0 \\ 0 & A_y & 0 \\ 0 & 0 & A_z \\ A_y & A_x & 0 \\ 0 & A_z & A_y \\ 0 & 0 & A_x \end{bmatrix}, \quad \begin{bmatrix} \cdot, x^0 \\ \cdot, y^0 \\ \cdot, z^0 \end{bmatrix} \equiv \begin{Bmatrix} A_x \\ A_y \\ A_z \end{Bmatrix}_{I=1,N} \quad , and \quad \epsilon = \begin{Bmatrix} \epsilon_{11} \\ \epsilon_{22} \\ \epsilon_{33} \\ \gamma_{23} \\ \gamma_{13} \\ \gamma_{12} \end{Bmatrix} \tag{4.12}$$

The stress is associated with strain through Hooke′s law $\sigma = [D][B_L]u$, where,

$$[D] = \frac{E}{(1+\nu)(1-2\nu)} \begin{Bmatrix} 1-\nu & \nu & \nu & 0 & 0 & 0 \\ \nu & 1-\nu & \nu & 0 & 0 & 0 \\ \nu & \nu & 1-\nu & 0 & 0 & 0 \\ 0 & 0 & 0 & (1-2\nu)/2 & 0 & 0 \\ 0 & 0 & 0 & 0 & (1-2\nu)/2 & 0 \\ 0 & 0 & 0 & 0 & 0 & (1-2\nu)/2 \end{Bmatrix} \tag{4.13}$$

Now, the strain and stress of the 27 integration points are obtained, with that, the post processing can be initialized to get the strain and stress at each node. Let the (r, s) be coordinates for the integration point, and then define $r = 1$ when $\xi = \sqrt{0.6}$ and $s = 1$ when $\eta = \sqrt{0.6}$. That gives $r = \xi/\sqrt{0.6}$, $s = \eta/\sqrt{0.6}$ and $t = \zeta/\sqrt{0.6}$. The strain and stress at each node can be extrapolated using the 27 interpolation points,

$$\epsilon_i = \sum_{p=1}^{27} N_p(r,s,t)\epsilon_p \quad and \quad \sigma_i = \sum_{p=1}^{27} N_p(r,s,t)\sigma_p \tag{4.14}$$

With current program, the stress and stress of the 20 nodes can be calculated for each element. However, if a node is shared by two or more elements, then, the stress and strain at this node have multiply values. To solve this problem, nodal strain and stress are smoothed after this process to get unique value.

4.2 Application of FEA on Elastic Structure with Damping

Figure 4.3 shows the mesh of a beam clamped at two ends and the marked nodes ranging from left to right are nodes 36, 37, 38, 39, 40, 41 and 42. The elastic material is set as steel and the damping matrix of the structure is proportional to the stiffness and mass matrix. Frequency scan is carried out to identify the natural frequency of the structure. The harmonic loading is applied on the central line of the upper surface of the beam and the displacements of those marked nodes are collected.

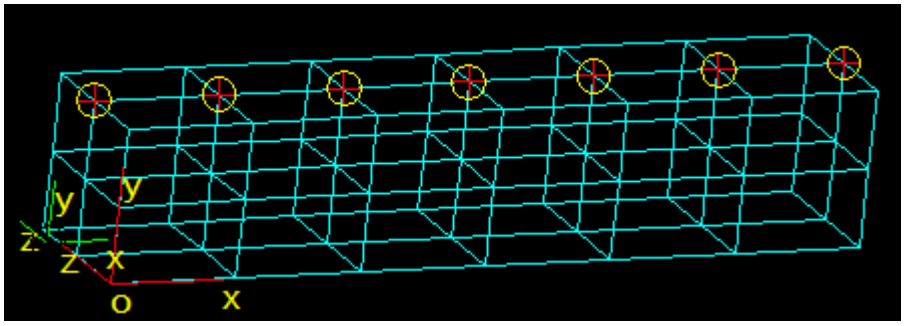

Figure 4.3.: Mesh of elastic beam with damping.

Vertical displacements of nodes at different excitation frequency are plotted in Figure 4.4. Because of the relative low damping in structure made of steel, the imaginary part of the displacement is much lower than the real part and the magnitude of the displacement is dominated by the real parts. The two plots

indicate the first natural frequency of the beam is 3182Hz and the second natural frequency is 11822Hz. The displacement in node 39 is higher than that at node 37, which is closer to the fixed boundary and movement constrained.

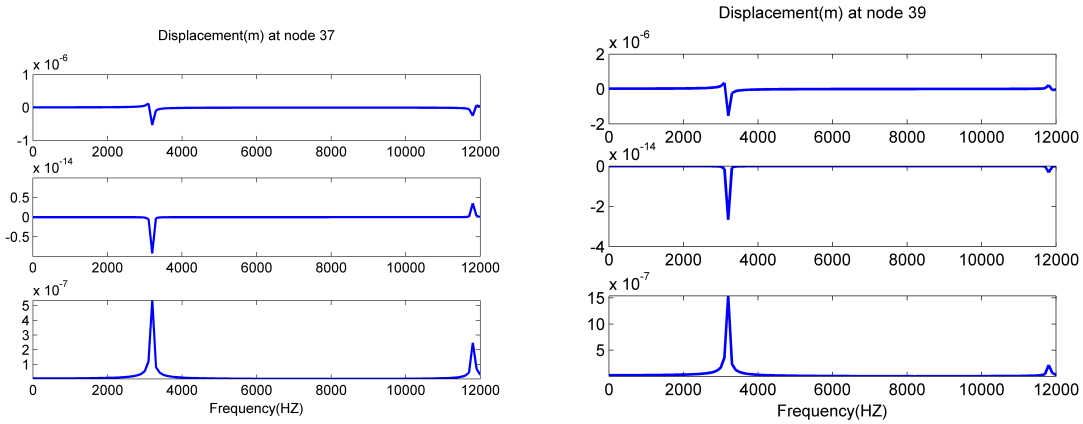

Figure 4.4.: Frequency scan in Y direction (a) Node 37; (b) node 39.

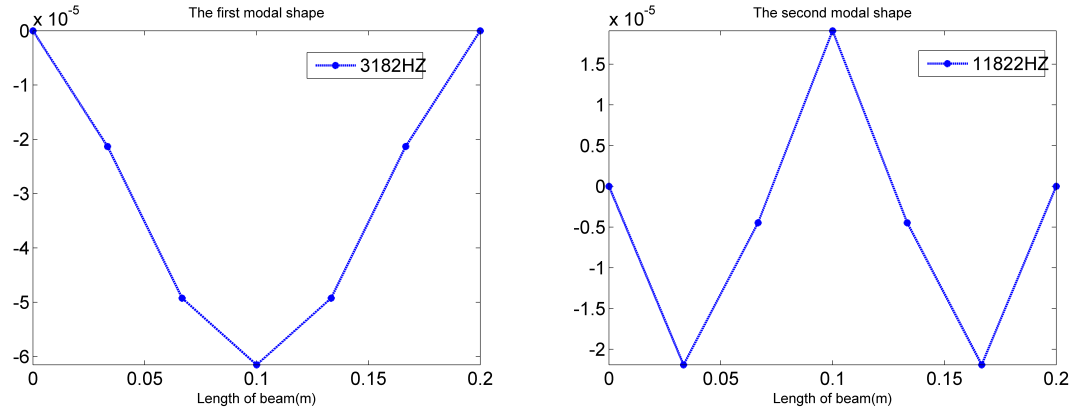

Figure 4.5.: The displacement in Y direction (a) The first modal shape; (b) the second modal shape.

Figure 4.5 presents the vertical displacement of the beam under the excitation of first two natural frequencies. The distribution of vertical displacement is symmetric over the central line of the beam. As to the first modal shape, the displacement is gradually decreasing from the central to the fixed ends of the beam.

While the second modal shape is more complicated, the node 37 has slightly higher displacement than node 39 because of the resonance.

To elaborate the application of FEA and spectral analysis on the structure analysis, the more complicated cylindrical structure made of two materials has been practiced. The inner shaft is made of higher modulus material-steel, which is bonded with the lower modulus material-rubber. In this test, the structure made of steel and rubber is defined as elastic structure with damping, which is characterized using Rayleigh damping. The outer steel sleeve confines the movement of the external surface of the rubber and imposes zero DOF on those nodes considering the extremely large modulus difference between steel and rubber. The mesh of the steel shaft and rubber is plotted in Figure 4.6, where the outer blue sketch is rubber and the inner yellow sketch is steel shaft. The vertical harmonic excitations at different frequencies are applied on the steel shaft to simulation the working environment on the suspension system of vehicles.

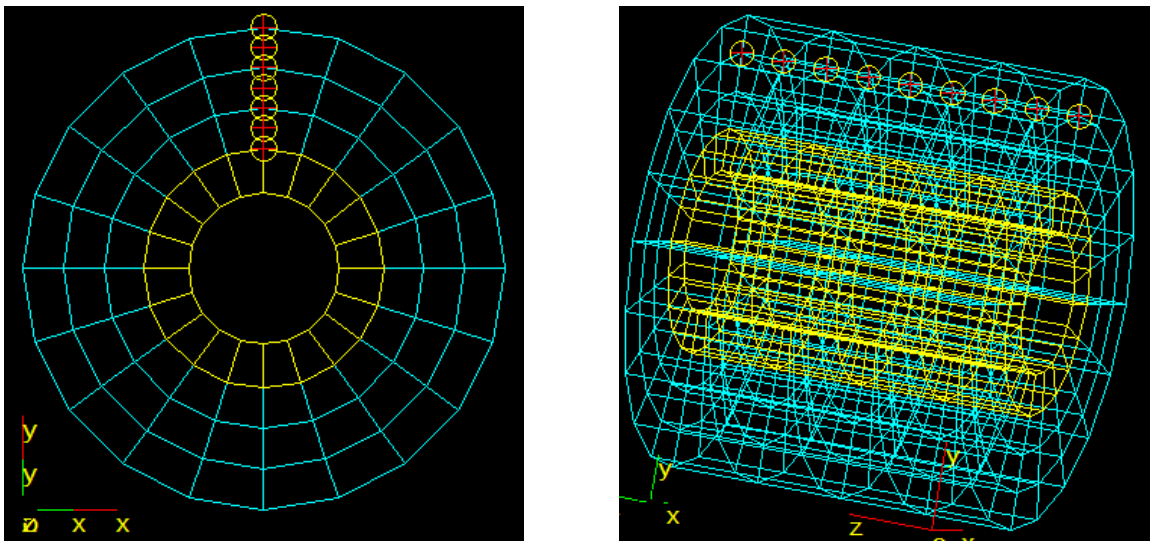

Figure 4.6.: Mesh of cylindrical structure (a) Radial distribution of nodes; (b) axial distribution of nodes.

The nodes in radial direction shown in Figure 4.6(a) are 21, 42, 77, 108, 124, 174, and 213 ranging from bottom to the top and their vertical displacements are

collected and compared. The nodes in axial direction shown in Figure 4.6(b) are 124, 262, 427, 562, 724,862, 1025, 1162, and 1327 from left to the right. Before the frequency scan, the Eigen value vibration analysis has been carried out to identify the modal shape and natural frequency of the structure using QED.

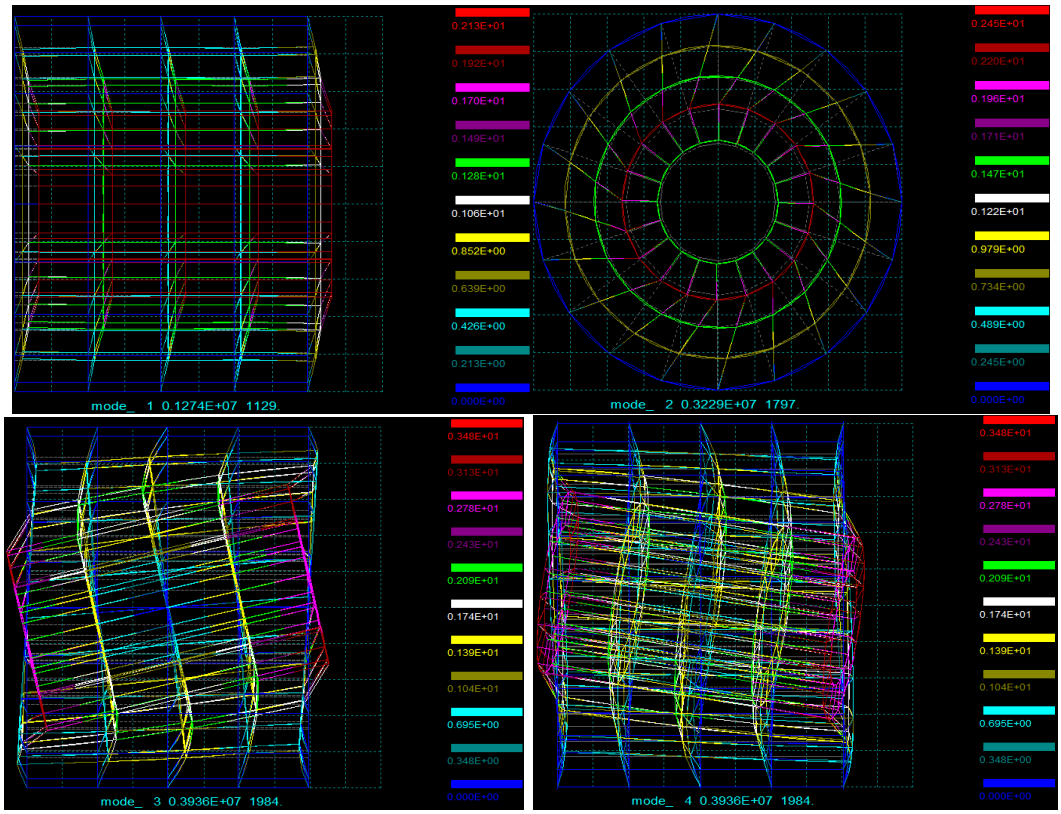

Figure 4.7.: (a) Modal shape 1; (b) Modal shape 2; (c) Modal shape 3; (d) Modal shape 4.

Figure 4.7 shows the initial four modal shapes of this cylindrical structure composed of two materials. The first modal shape shows the deformation in axial direction, the second modal shape shows the rotation, and the third and fourth modal shapes show the rocking. In the Simplex, the loading is applied on the steel shaft in the vertical direction and the expected modal shape displaying the vertical movement of the steel shaft. Since the stiffness in the radial direction is much

higher than that in the axial direction, the expected modal shape happens at higher natural frequency.

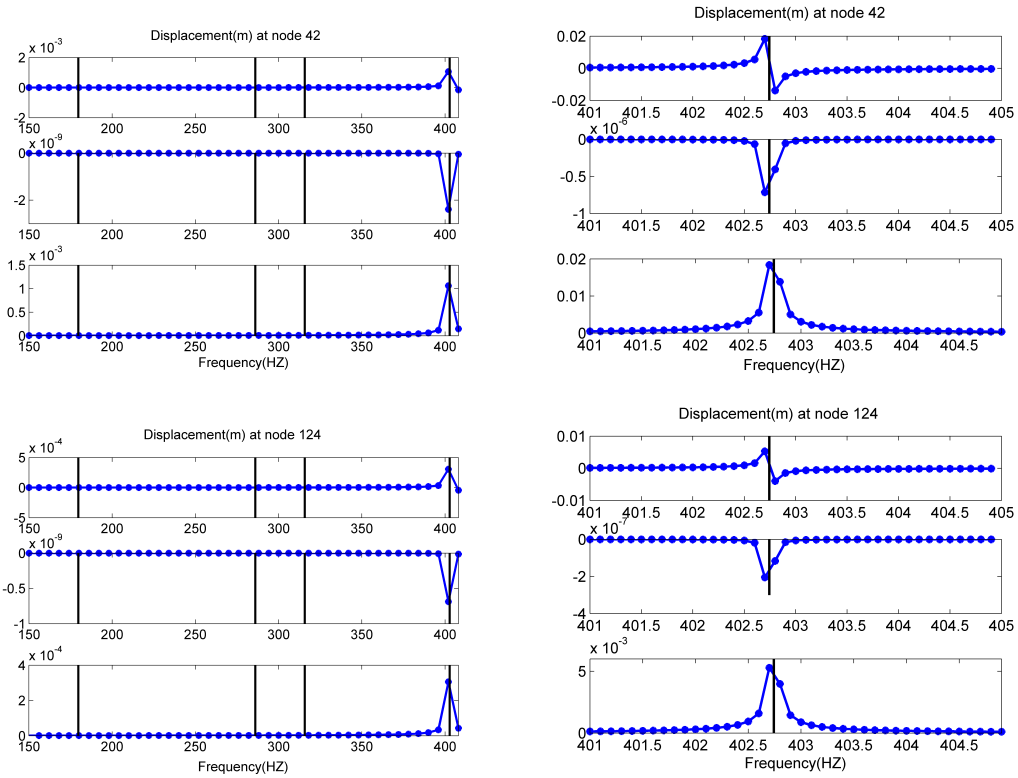

Figure 4.8.: Displacement of nodes under frequency scan (a) and (b) node 42; (c) and (d) node 124.

The frequency scan analysis is displayed in Figure 4.8. The frequency effect indicates that the resonance in the radial deformation happens around 402.7Hz. Because of the low damping defined in the elastic structure, the real part of the displacement overwhelms the imaginary part of that and dominates the modal shape of the cylindrical structure. The black lines are the undamped natural frequencies calculated from the QED, the resonance of the first three black lines are not excited as only the vertical loading is applied in this frequency scan.
Figure 4.8(c) and (d) show the damped natural frequency is slightly higher than the

undamped natural frequency. The displacement at node 42 is larger than that at node 124 since node 124 is closer to the fixed external surface of rubber.

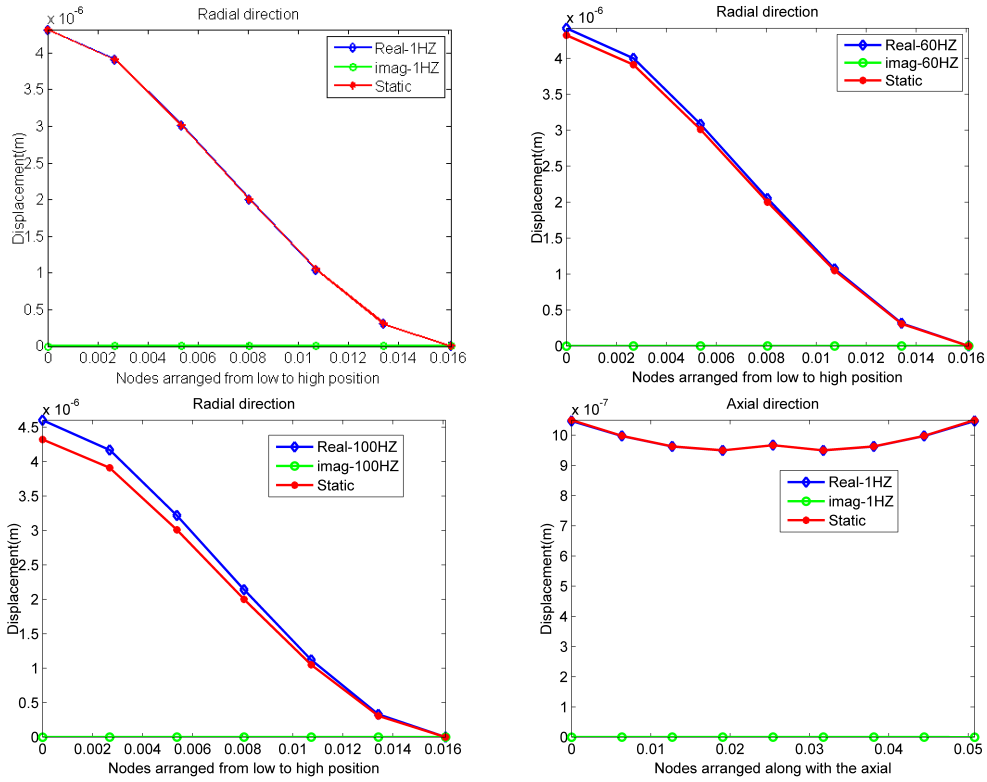

Figure 4.9.: Displacement distribution at Radial direction (a)1Hz; (b)60Hz; (c)100Hz; (d) axial direction.

To have more clear demonstration of the displacement in radial direction, Figure 4.9 plots the displacement of those nodes marked in Figure 4.6. The vertical displacements of those nodes show nearly proportional decreasing when the nodes are away from the steel shaft. With the increase of excitation frequency, the displacements of nodes in radial direction increase slowly. However, since the modal shape in radial direction happens at natural frequency 402.7Hz, the frequency effect is not so significant to vertical displacement in the frequency range 0Hz to 100Hz. Axial distribution of the displacement under the first natural frequency is plotted in Figure 4.9(d), which is collected from the nodes marked in Figure 4.6(b). The

displacements at the two ends increase dramatically because of the free boundary condition applied on the two sides.

The circumference distribution of displacement under the first natural frequency is also collected to have the comprehensive understanding of the deformation of rubber core. Because of symmetry of the structure, only half of the nodes in circumference are analyzed. The nodes marked in Figure 4.10(a) are 121,122,124,126,145,146,143,147,149,152 and 153 ranging from left to right and their displacement is plotted in Figure 4.10(b). Nodes locate at horizontal line and vertical lines have the maximum displacements compared with other nodes at other positions.

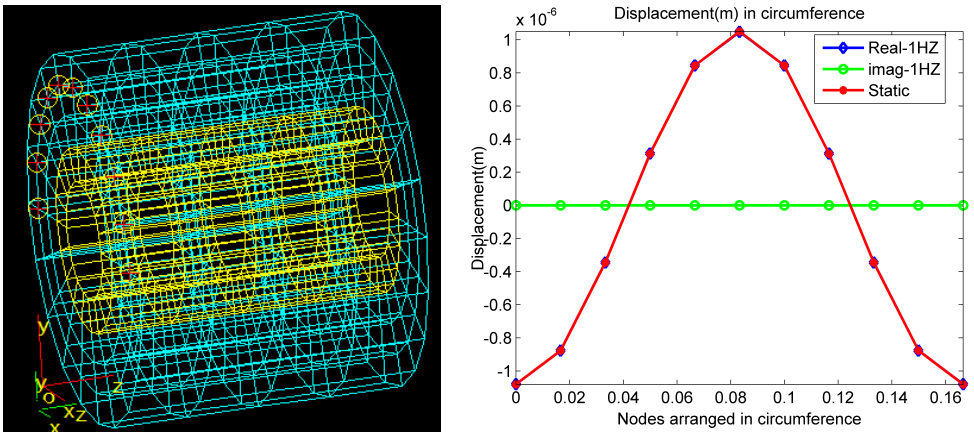

Figure 4.10.: Displacement at first natural frequency (a) Nodes collected in circumference; (b) the circumference distribution.

The stress distribution in radial, axial and circumference directions are also plotted against the static stress distribution calculated from QED in Figure 4.11. As to the radial and axial direction, the stresses of loading direction are attractive while the shear stress in circumference direction is more significant. The elastic structure implemented in the QED is of no damping and the structure in Simplex is elastic with damping, thus, the Simplex generates complex stress and a scale is multiplied to match the QED results. Figure 4.11(a) and (b) compares the stress σ_{yy}

distribution at 1Hz and 100Hz. The overlap of real part stress and static calculation indicates the reliability of Simplex in dealing with complex variables. Figure 4.11(c) and (d) compares the stress σ_{yy} distribution in axial direction at frequency 1Hz and 100Hz. While as to the circumference direction, the shear stress σ_{xy} shown in Figure 4.11(e) and (f) is attractive and compared. The three groups of comparison indicate that with the increase of external excitation frequency, the magnitude of the stress increases slightly as the frequency effect on the displacement.

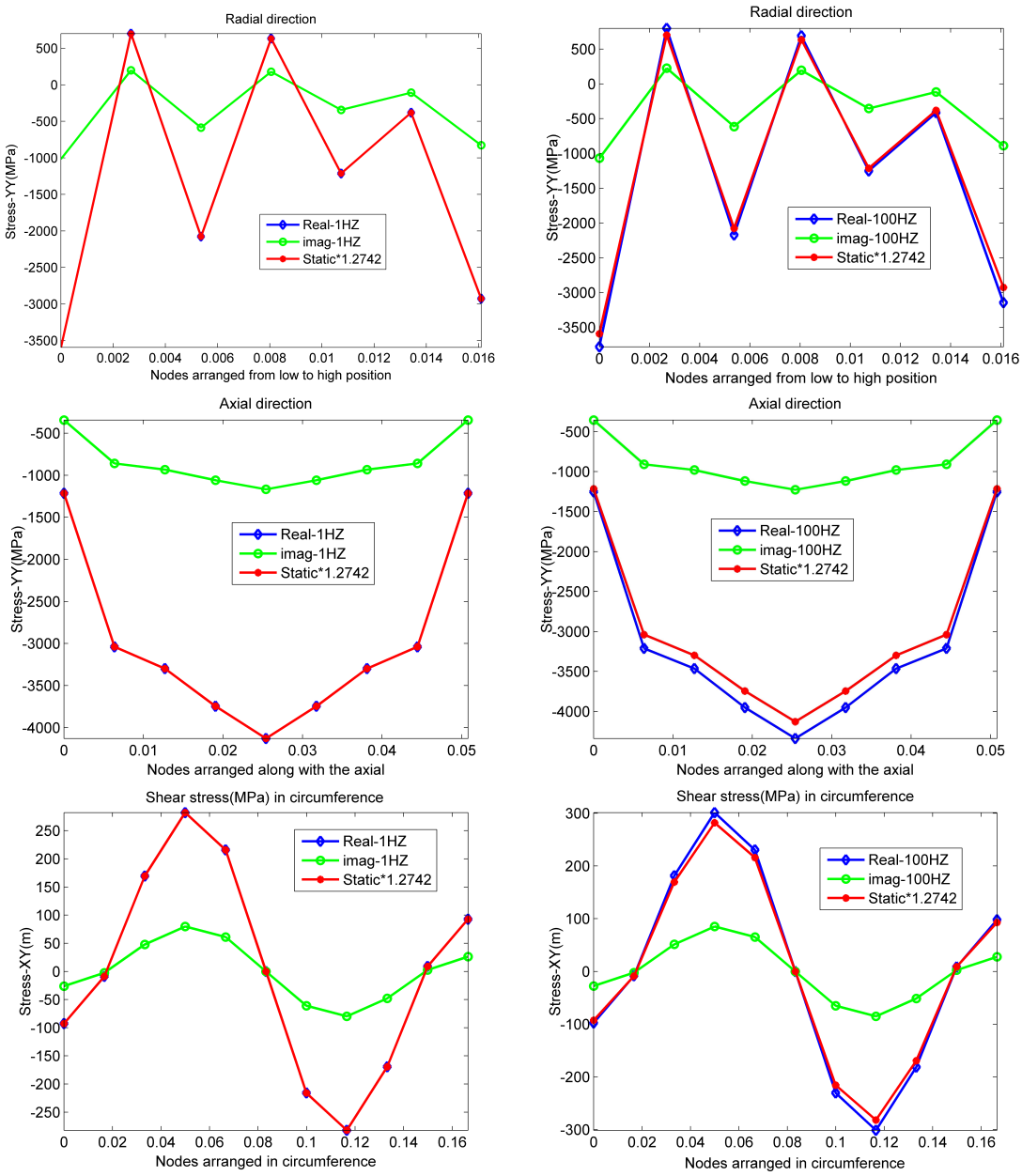

Figure 4.11.: Stress distribution (a) and (b) Radial; (c) and (d) axial; (e) and (f) circumference.

4.3 Spectral Analysis and Dissipation Energy

4.3.1 Approach to Estimate the Modal Shape and Dissipation Energy

To elaborate the model shape and dissipation energy developed in FEA, a rod segment with two elements is shown in Figure 4.12.

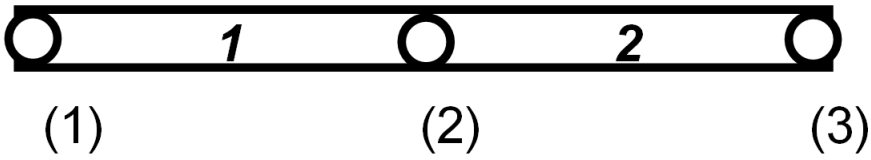

Figure 4.12.: Rod segment.

The displacements of the three nodes are u_1, u_2 and u_3, where u_2 and u_3 are unknown. Assuming the rod as homogenous material with constant cross area and same element length, the mass matrix of the structure after assembling the two elements of the rob segment is,

$$[M] = \frac{\rho AL}{12}\begin{bmatrix} 2 & 1 & 0 \\ 1 & 4 & 1 \\ 0 & 1 & 2 \end{bmatrix} \tag{4.15}$$

With the introduction of the frequency dependent modulus, the stiffness matrix of the system becomes,

$$[K] = \frac{i\omega\eta(\frac{E_1}{E_2}+1)+E_1}{E_1+i\omega\eta}\frac{E_2 A}{L}\begin{bmatrix} 1 & -1 & 0 \\ -1 & 2 & -1 \\ 0 & -1 & 1 \end{bmatrix} - \omega^2\frac{\rho AL}{12}\begin{bmatrix} 2 & 1 & 0 \\ 1 & 4 & 1 \\ 0 & 1 & 2 \end{bmatrix} \tag{4.16}$$

Essential boundary condition of this system is u_1=0 and the natural boundary condition is f_2=0, and $f_3 = 1e^{i\omega t}$, where f_2 and f_3 are the loadings applied on node

2 and node 3. With those boundary conditions, the solution of the unknown displacements and counter force are,

$$\begin{bmatrix} \hat{u_2} \\ \hat{u_3} \end{bmatrix} = \left(\phi(\omega) \frac{E_2 A}{L} \begin{bmatrix} 2 & -1 \\ -1 & 1 \end{bmatrix} - \omega^2 \frac{\rho A L}{12} \begin{bmatrix} 4 & 1 \\ 1 & 1 \end{bmatrix} \right)^{-1} \begin{bmatrix} 0 \\ 1e^{i\omega t} \end{bmatrix} \tag{4.17}$$

$$\hat{f}_1 = -\phi(\omega) \frac{E_2 A}{L} \hat{u_2} + \omega^2 \frac{\rho A L}{12} \hat{u_2} \tag{4.18}$$

That solution indicates the displacements of nodes are frequency dependent. Figure 4.13 plots the displacement against frequency at node 2 and node 3. With the identified parameter from DMA test, the resonance of the rod can happen at 60Hz and 216 Hz.

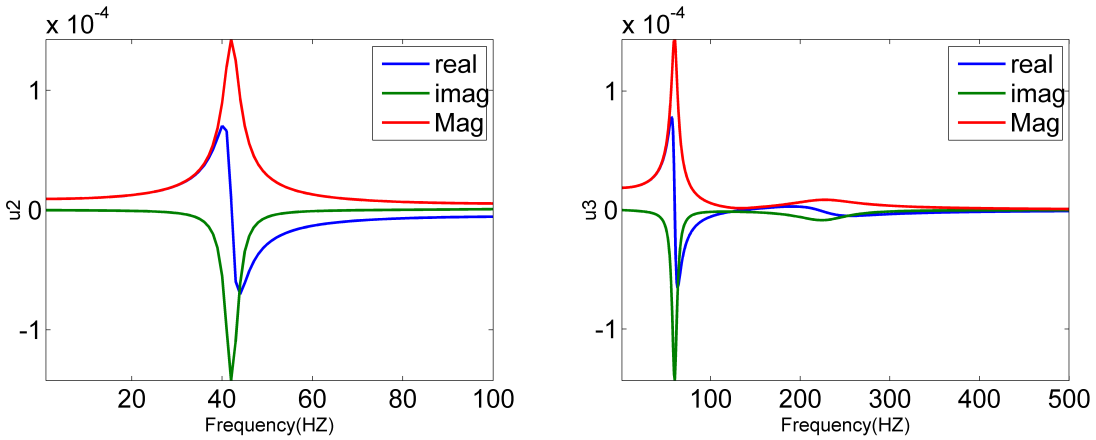

Figure 4.13.: Excitation frequency-dependent displacement (a) Node 2; (b) node 3.

The amplitude is pretty high at resonance since spring and mass elements of the system store the vibration energy (kinetic energy). The number of natural frequency is the same as the total DOF, for a rod segment with only two DOF, there are only two resonance frequencies.

In the structure made of elastic material, the strain energy is related to the displacement square or strain square. For the simple spring and mass system, the strain energy can be easily estimated through $1/2Ku^2$. Nevertheless, in a structure

with viscoelastic material, square of the displacement doesn′t mean the magnitude of the response because the displacement is complex. Thus, the true response of the structure depends on the real part of the governing equation. In this testing, displacement of node 2 at harmonic excitation is applied as example to explore the response in time domain. The complex displacement of node 2 in the rod segment is reconstructed as,

$$u_2 = [u_{R2} + iu_{I2}]e^{i\omega t} = [u_{R2}\cos(\omega t) - u_{I2}\sin(\omega t)] + i[u_{R2}\sin(\omega t) + u_{I2}\cos(\omega t)] \quad (4.19)$$

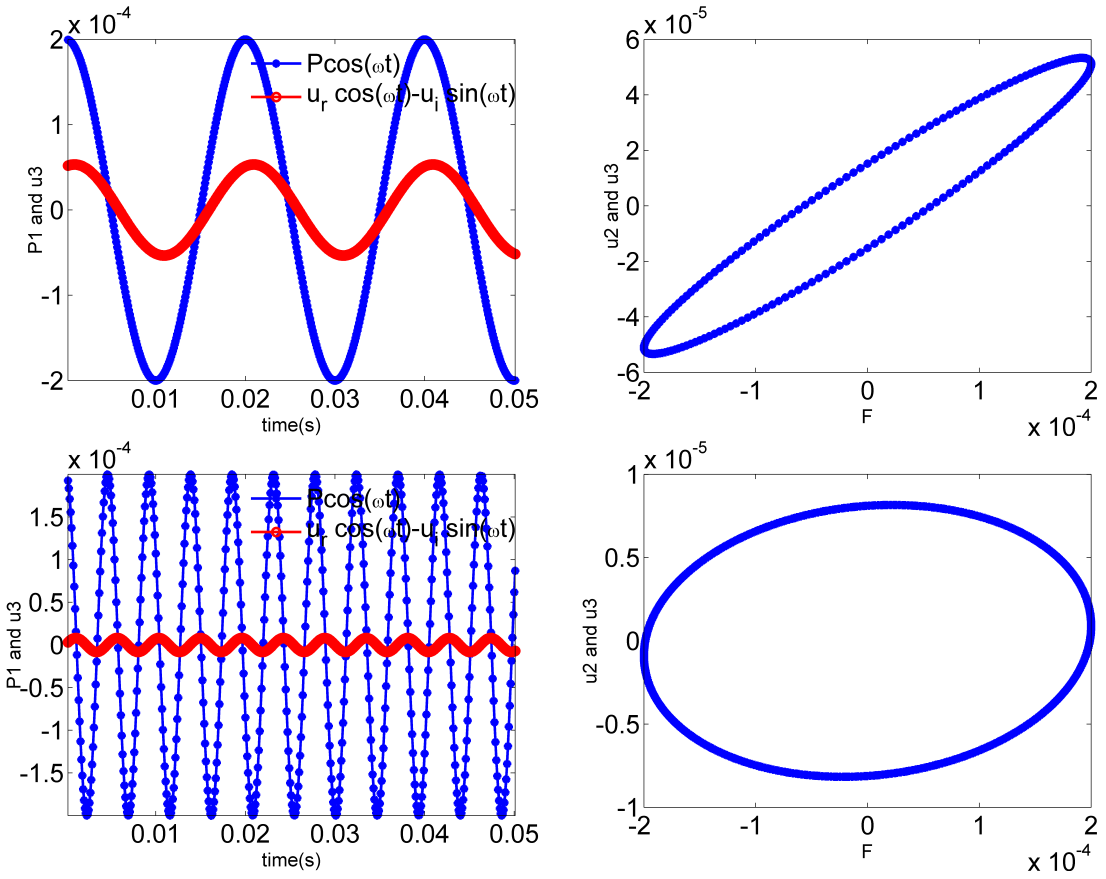

Figure 4.14.: (a) and (b) Phase shift and dissipation at 50Hz; (c) and (d) phase shift and dissipation at 216Hz.

Figure 4.14(a) and (c) show the phase lag between output and input in the time domain at the excitation frequency 50Hz and 216Hz. Because the magnitude

of loading is higher than that of response, a scale 0.001 is multiplied with loading to facilitate the comparison. Figure 4.14(b) and (d) plot the force against displacement in one cycle to present the energy dissipation of the node. For the rod segment with two elements, the total dissipation energy of the system is the sum of dissipation at node 2 and node 3.

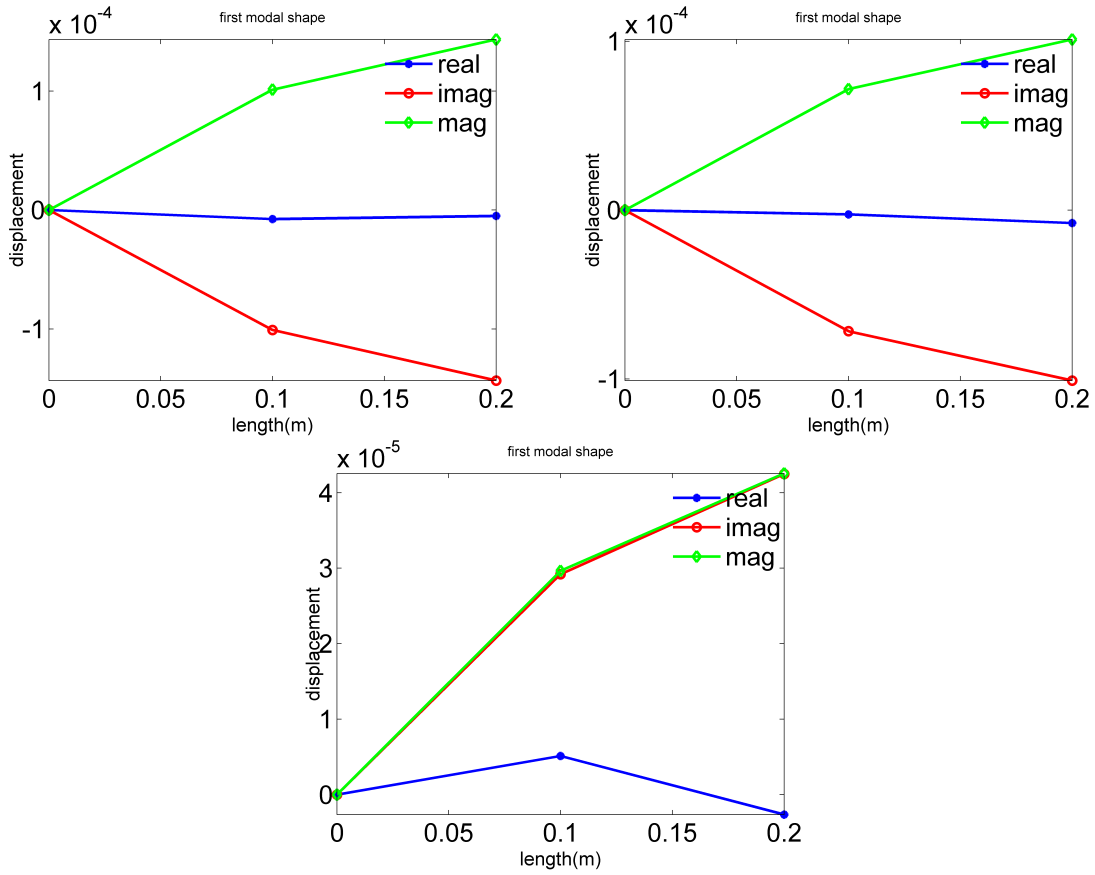

Figure 4.15.: The first modal shape at loading types(a)The first ; (b) the second; (c) the third.

With the calculated displacement, the modal shapes of the structure are plotted. To have comprehensive understanding of the influence of loading type on the modal shape, three type of loading are tested in the following. Node one is fixed and the loading applies on node two f_2 and three f_3. The first loading model is $[f_2, f_3] = [0, 1]$, the second loading type is $[f_2, f_3] = [1, 0]$ and the third loading

model is $[f_2, f_3] = [1, -1]$. The first modal shapes of the three loading cases are given in Figure 4.15.

With the solution about displacement at each node, the following post processing of FEA discusses the interpolation function to get stress and strain. For the two element rod segment, the strain and tress of each element e in this rod segment can be obtained using the linear interpolation,

$$\hat{\epsilon}^e = \frac{1}{L}[-1\ 1] \begin{bmatrix} \hat{u}_1^e \\ \hat{u}_2^e \end{bmatrix}; \quad \hat{\sigma}^e = \hat{E}\hat{\epsilon}^e \tag{4.20}$$

Assume the applied force is $P\cos(\omega t)$, and the real part of displacement at node 2 can be rewritten as $A\cos(\omega t + \phi)$. Figure 4.14 plots the displacement against the force and forms loop representing the dissipation energy in one period. While the summation of the dissipation energy calculated from the displacement and force can merely display the total dissipation energy of the whole structure. In order to get the dissipation energy distribution density over the whole structure, it is necessary to calculate that in each element.

The complex stress and strain expression of the structure with damping have been derived in the spectral analysis. In the post-processing, plotting the strain against stress forms the energy dissipation at each interpolation point. The stress and strain at each interpolation point is given as,

$$\epsilon(t) = [\hat{\epsilon}_R \cos(\omega t) - \hat{\epsilon}_I \sin(\omega t)], \quad \sigma(t) = [\hat{\sigma}_R \cos(\omega t) - \hat{\sigma}_I \sin(\omega t)] \tag{4.21}$$

Similarly, the strain $\epsilon(t)$ against stress $\sigma(t)$ shows the existence of phase delay. The loop area of each integration point can be calculated from,

$$Diss = \int_{t=0}^{t=1/2\pi f} \sigma(t) d\epsilon(t) \tag{4.22}$$

While for the whole structure, the energy equilibrium of the structure is given as,

$$W - U - \tau = D \tag{4.23}$$

Where W is the work done by the external force, U is the strain energy stored in the system, τ is the kinetic energy stored in the system and D is the dissipation energy obtained from sum of all elements. To have the energy conservation, the work done by the external work is totally transferred to the dissipation energy caused by the out of phase between strain and stress. In each cycle, the kinetic energy and strain energy are conservative and do not lead to energy accumulation or dissipation. In the Simplex program, in order to estimate the external work, firstly, record the loading of each node as F_i, and then record the complex displacement at each node as u_i. The summation of loop area calculated from each pair of the load and displacement is the external work. For the rod segment, the total strain energy is calculated after summing up strain energy from each node,

$$U = \frac{1}{2}ku^2 = \frac{EA}{2L}\begin{bmatrix} u_1 \\ u_1 \end{bmatrix}^T \begin{bmatrix} 1 & -1 \\ -1 & 1 \end{bmatrix} \begin{bmatrix} u_1 \\ u_2 \end{bmatrix} = \frac{1}{2}E\epsilon^2 dv \tag{4.24}$$

The first step is to calculate the real part of the displacement of each node and its strain. The second step is to calculate the complex stress by multiplying the strain with the complex modulus and then get the real part of the stress. The third step is to calculate the loop area from the strain and stress of the each node. The summation over nodes gives the total strain energy of the system. The approach to get the kinetic energy elaborated using the rod segment is,

$$\tau = \frac{1}{2}Mv^2 = \frac{\rho AL}{12}\begin{bmatrix} v_1 \\ v_2 \end{bmatrix}^T \begin{bmatrix} 2 & 1 \\ 1 & 2 \end{bmatrix} \begin{bmatrix} v_1 \\ v_2 \end{bmatrix} \tag{4.25}$$

The first step is to get the lumped mass of each node. The second step is to use the square of the real part of the velocity to multiply half of the mass. The third step is to have the summation over node to get the kinetic energy of the total system. The real part velocity of each node is given as,

$$v = -\omega u_R \sin(\omega t) - u_I \omega \cos(\omega t) \tag{4.26}$$

The $P(t)$ at each node is known and the $u(t)$ is solved, then, the increment of displacement at each time step can get from $du(t) = u(t) - u(t-1)$. The work done

by the external force at each node can calculated from the integral over $p(t)du(t)$ in the time domain. After one cycle, the accumulation of strain energy and kinetic energy is zero, thus, the work done by the external force turns to the dissipation energy.

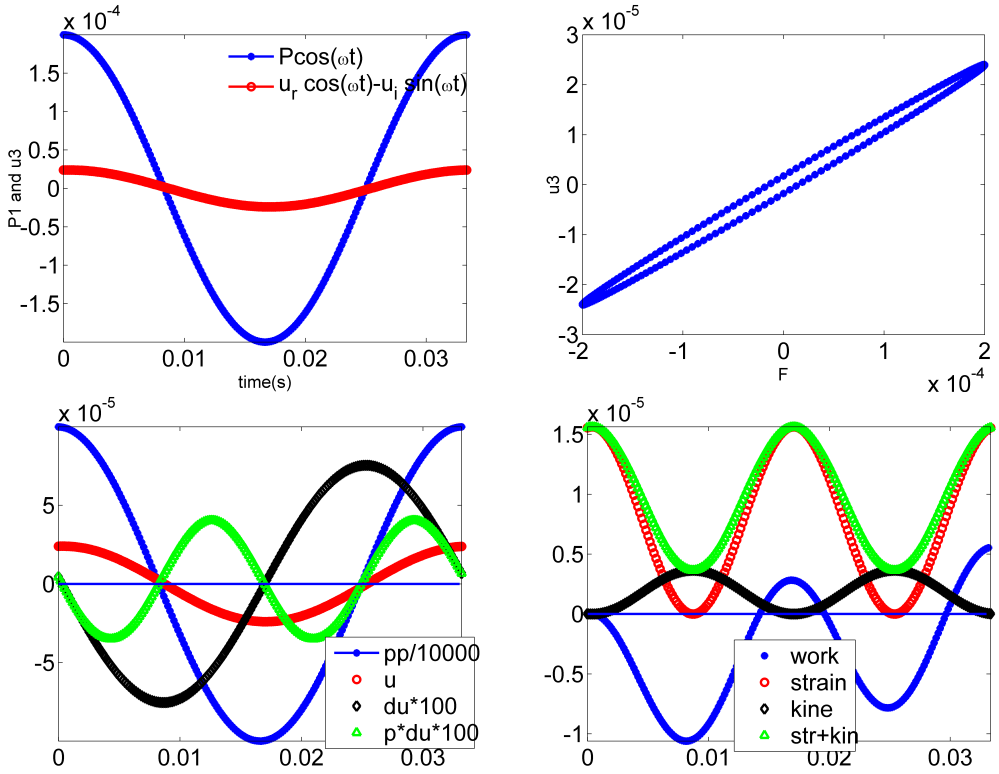

Figure 4.16.: Energy in time domain (a) Phase shift; (b) dissipation; (c)external work and (d) strain and kinetic energy.

Figure 4.16 plots the variation of external work and energy in on cycle when the first load model is applied at excitation frequency 30Hz. In the Figure 4.16(c), pp is loading, u is displacement, du is displacement increment and $p * du$ is the work done at each time step. In order to compare the four variables in one figure, different scales are applied for each variable. The four curves in this Figure 4.16(d) show the accumulation of work, strain energy, kinetic energy of node 3. After one cycle, the strain energy and kinetic energy turns back to the original value while the

summation of work shows a positive value. In view of the conversation of energy, the work done by the external force turns to dissipation energy. This plot shows the perfect explanation of energy dissipation in structure with damping.

Before apply the Simplex program to the complicated cylindrical rubber bushing, a clamped beam is developed in this chapter to test the reliability of the FORTRAN program. In view the research topic about FEA dealing with viscoelastic materials in literatures, the modal and natural frequency are calculated and compared. Furthermore, for more widely application, the response of the viscoelastic beam to the blast load is estimated. As long as those tests give effective simulation, the more complicated rubber bushing can be modeled for further analysis. It is worth noting that the dynamic response and dissipation energy estimation are just a portion of the Simplex program, the successful modeling of the program makes it possible to deal with even more complicated problem, such as wave propagation in large and complicated structure.

Figure 4.17 shows the comparison between Simplex calculated modulus with the theoretical calculation. The overlap of those curves indicates that the modulus expression used in the simplex is correct and can be used for further application. In the comparison of natural frequency, the modulus is set as 1.87 in Simplex and QED. The first two natural frequencies in the direction Y are 42.6 and 141.9Hz. When the damping coefficient of the material model used in the Simplex is set as zero, the displacement under the frequency scan show the resonance happening at the same frequency, which verifies the calculation in the Simplex.

4.3.2 Dissipation Energy Distribution in Viscoelastic Beam

The coefficient in this example is merely 0.1η to have more obvious modal shape in case the response is over damped. In theoretic, Poisson ratios(υ) 0.5 or 0.495 should be assigned to this nearly incompressible material, however, 0.5 or close to 0.5 causes trouble in the data processing of the binary encoding. To avoid

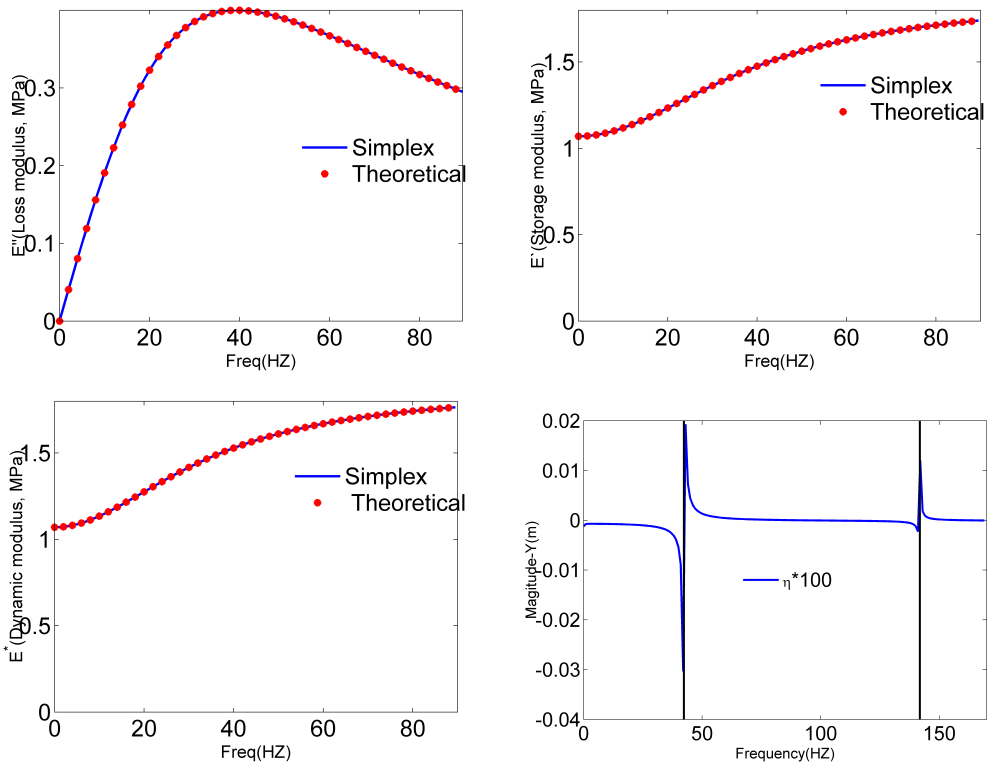

Figure 4.17.: Verification of modulus (a) Loss modulus; (b) storage modulus; (c) dynamic modulus and (d) natural frequency.

the problem, Poisson ratio (υ) is set as 0.475 in the Simplex. According to the definition of Poisson ratio (υ), and the properties of uniaxial strain, the strain and stress in X and Y directions follow the relationship, $\upsilon = -\frac{\epsilon_y}{\epsilon_x} = 0.475$. The load is applied at the central of the clamped beam as shown in Figure 4.18 for excitation frequency at 1Hz and first natural frequency 29.4Hz.The geometry of the beam is set as 0.2m, 0.04m and 0.04m for length, width and height. The beam meshing includes 24 elements with six in length, two in width and two in height.

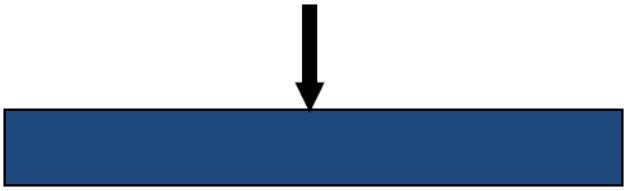

Figure 4.18.: Sketch of excitation at 1Hz and 29.5Hz.

Figure 4.22 shows real and imaginary part of the strain at 1Hz to verify the uniaxial strain properties of the program. The X-axis gives the total length of the beam in the example. The strain curve in X direction multiplying the Poisson ration matches well with the strain curve in the Y direction. The frequency dependent modulus of rubber indicates that the structure is nearly elastic when the external excitation is applied at extremely low frequency. Thus, the imaginary of the displacement, strain and stress are lower than the real part of that in three order of the magnitude.

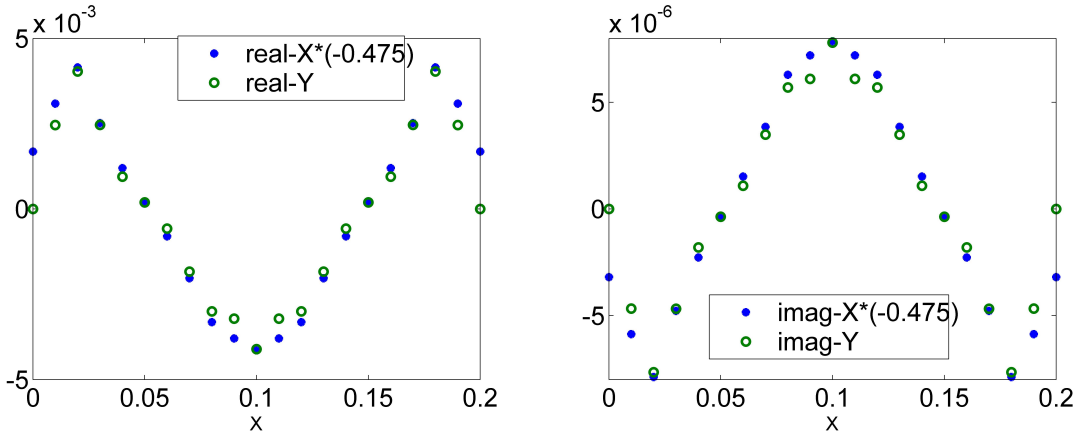

Figure 4.19.: Verification of uniaxial strain (a) Real part; (b) imaginary part.

At lower frequency, the real part of the displacement plays the dominate role while the imaginary part is nearly negligible. Since the influence of imaginary part of the modulus is pretty insignificant, it is reasonable to take it as static deformation. The displacement calculated from Simplex nearly tallies with the QED

at 1Hz excitation. The maximum strain appears at the central part of the clamped beam and the strain is symmetrical over the central part. Figure 4.20 confirms the accuracy of the Simplex program through the comparison of the static strain from QED with the quasi-static strain at 1Hz from Simplex.

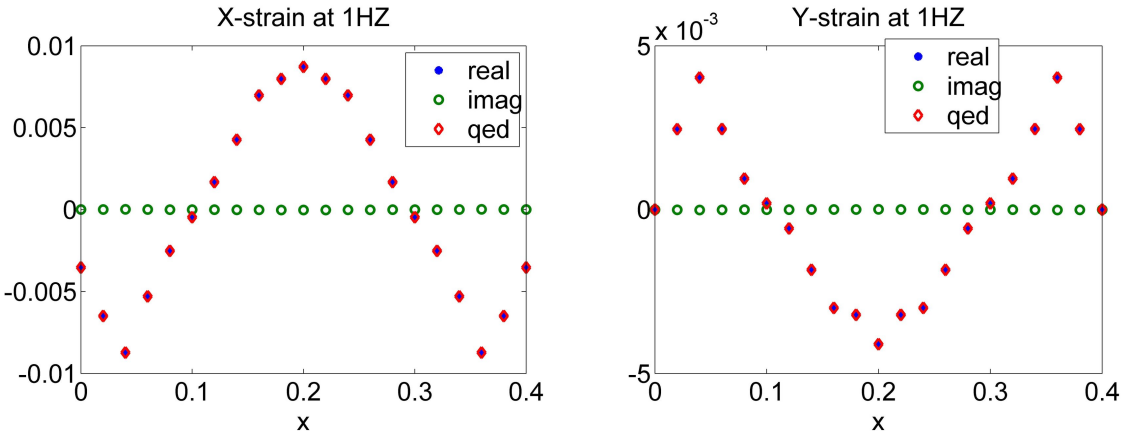

Figure 4.20.: Comparison of strain from QED with that from Simplex at 1Hz (a)X-direction; (b) Y-direction.

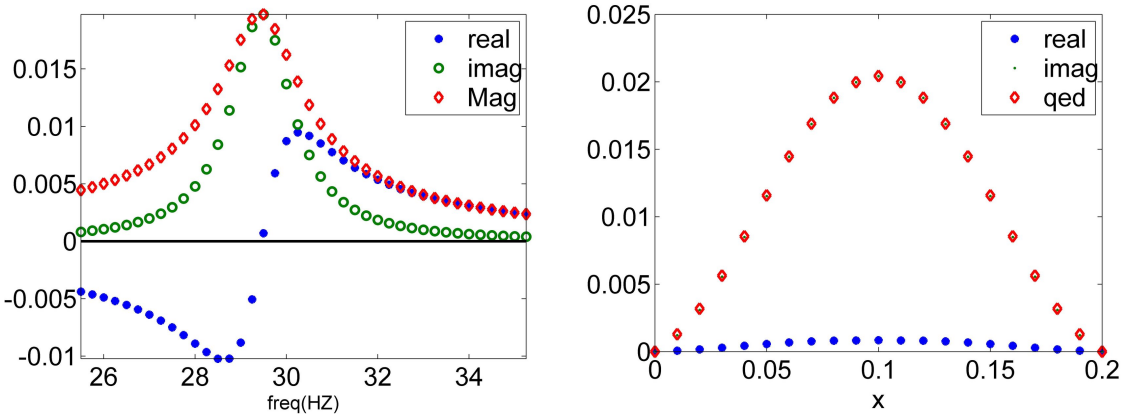

Figure 4.21.: Eigen frequency analysis (a) The first natural frequency; (b) the first modal shape.

From the response of the beam under frequency scan, it is convenient to get the damped natural frequency. Figure 4.21(a) shows the first natural frequency as

29.5Hz and the modulus at this frequency is 1.08MPa. Figure 4.21(b) shows the first modal shape, which also indicates that the imaginary part of the displacement overwhelms the real part of the displacement. Since the QED gives the static deformation while the Simplex presents the resonance deformation, a scale is applied to plot the comparison. Nevertheless, the perfect match of the Simplex model shape with that from the QED verifies the effectiveness of the Simplex in dealing with the viscoelastic structure.

The modulus is affected by the excitation frequency, as a result, the displacement of the clamped beam is affected by the frequency. The two black lines

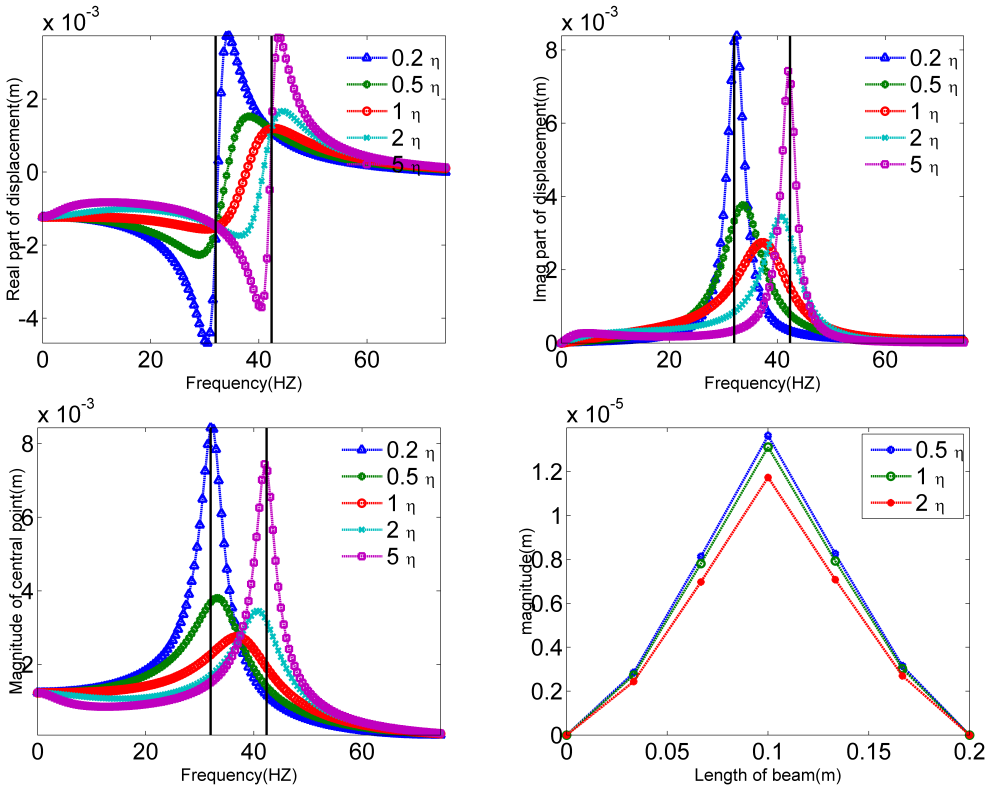

Figure 4.22.: Influence of damping coeffience on displacement at the central part of the beam (a) Real; (b) imag; (c) magnitude and (d)displacement of whole beam

are the first natural frequency of the purely elastic structure calculated from QED. When the modulus in the QED is set as $E = E_2$ =1.07MPa, the first natural

frequency is 32.02Hz. When the modulus in the QED is set as $E = E_1 + E_2$ =1.87MPa, the first natural frequency is 42.4Hz. Figure 4.22 indicates that higher η increases the dynamic modulus and shifts the location of the peak to right. No matter the real part or imaginary part, at the beginning, the magnitude decreases with the increasing η. But later, the increasing of η leads to higher displacement. In the frequency range 30-40Hz, the imaginary displacement dominates the magnitude, thus, the displacement plotted from the magnitude is similar to the displacement calculated from the imaginary part.

From the initial simulation, the second modal shape is anti-symmetrical over the central part of the clamped beam. Since the more complicated the modal shape, the lower the amplitude considering the strain energy needed in the structure. Thus, in order to exaggerate the second modal shape over the first modal shape, an anti-symmetrical load is applied at about one fourth and third fourth position of the beam in opposite direction. The sketch of the anti-symmetrical load is given in Figure 4.23.

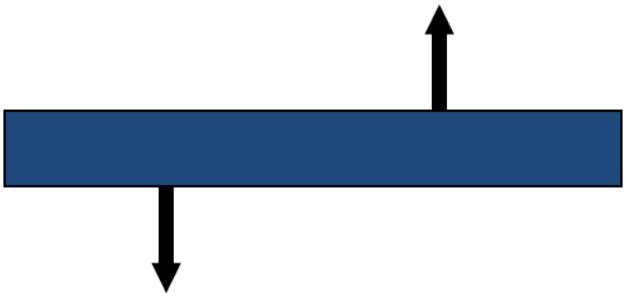

Figure 4.23.: Sketch of excitation at 66Hz.

Figure 4.24(b) shows the displacement of the node in the frequency range 60-90Hz, which locates the second damped natural frequency of the viscoelastic beam. Near the frequency 66Hz, the real part of the displacement is negligible and the imaginary part of the displacement reaches maximum in this range. That indicates the second damped natural frequency is 66Hz and corresponding modulus of rubber at this frequency is 1.10MPa. Figure 4.24(b) is the sketch of the second

modal shape of the beam, which matches well with the static deformation obtained from QED. Similarly, the imaginary part of the displacement dominates the modal shape over the real part.

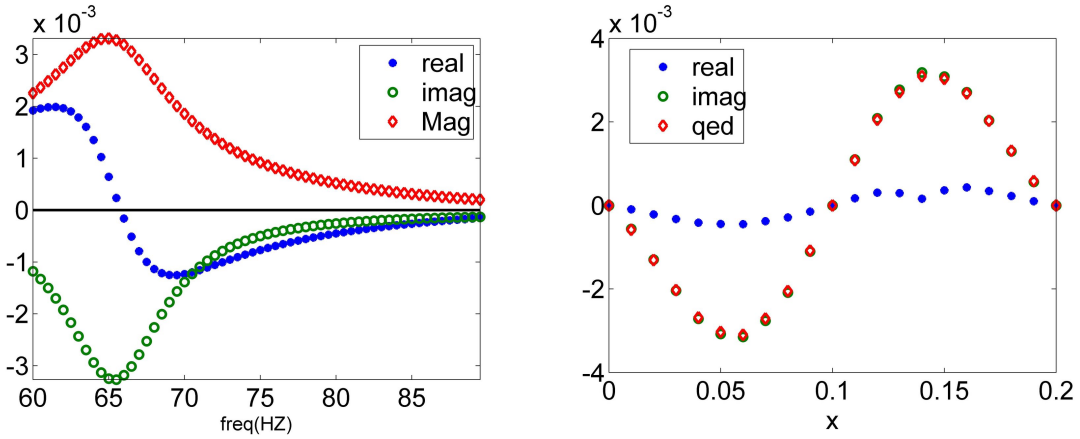

Figure 4.24.: Eigen frequency analysis (a) The second natural frequency; (b) the second modal shape.

The third damped natural frequency is detected in the frequency range 100-125Hz. Figure 4.26(a) shows that the resonance happens at 108Hz and the modulus at that frequency is 1.14MPa. The third modal shape in the transverse direction is symmetrical over the central part of the clamped beam again. Similarly, in order to emphasis the third modal shape, the load shown in Figure 4.25 is applied in Simplex and QED. Figure 4.26(b) indicates that the static response from the QED tallies with the modal shape given by the imaginary part of the displacement.

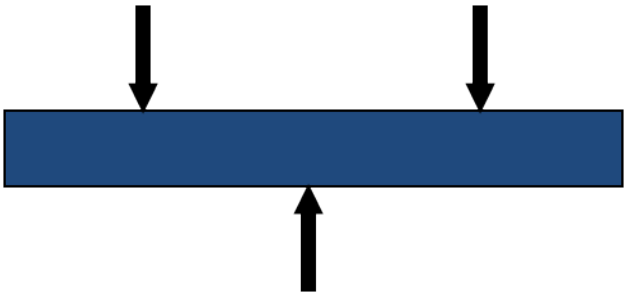

Figure 4.25.: Sketch of excitation at 108Hz.

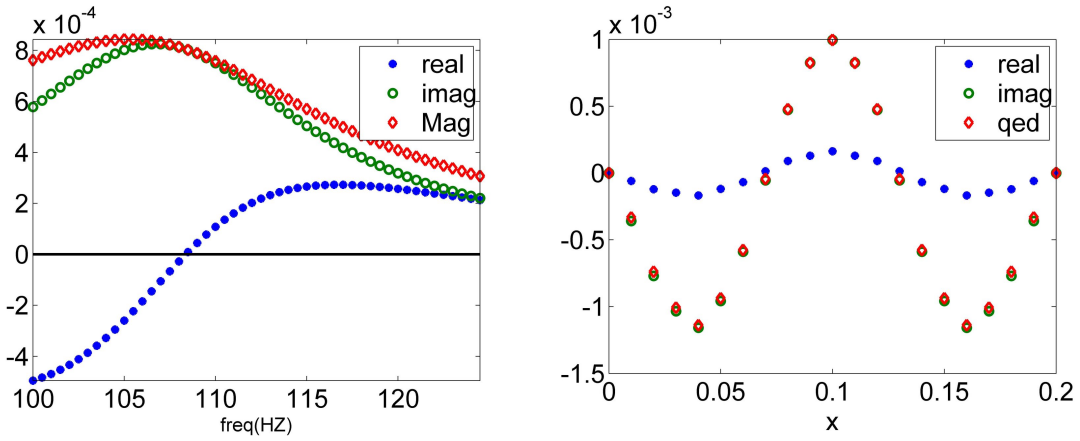

Figure 4.26.: Eigen frequency analysis (a) The third natural frequency; (b) the third modal shape.

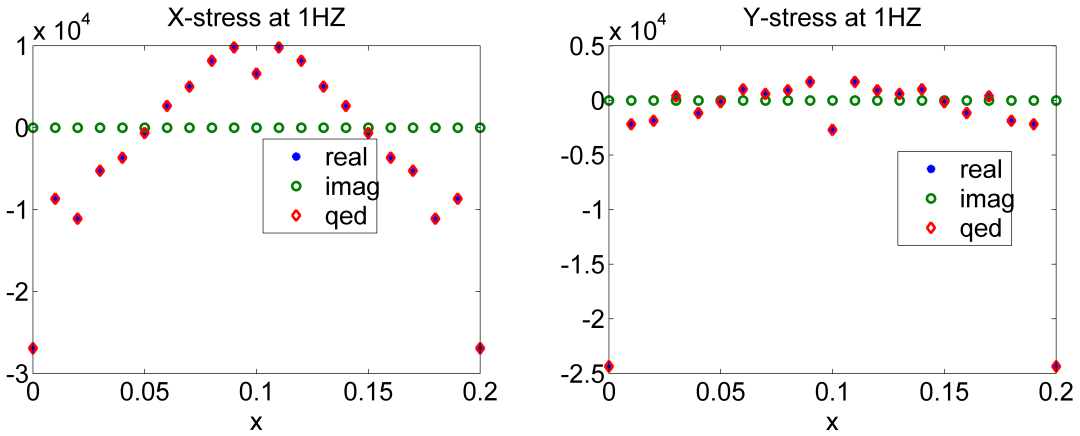

Figure 4.27.: Stress distribution at X and Y direction at frequency 1Hz.

In the previous discussion, the uniaxial strain properties at quasi-static 1Hz have been verified. In this section, the stress at quasi-static is compared with QED to encourage the following work. The same clamped beam is used in this part as demonstration and the load is applied at top surface of the central part. The comparison between quasi-static 1Hz Simplex response and the static QED results is plotted in Figure 4.27. The stress of the real part is much larger than the imaginary part since the imaginary modulus is three orders lower than the real modulus in

that excitation frequency. About the stress in the transverse direction, it is lower than the axial stress because the beam is not constrained in the Y direction.

The last section states the dissipation energy of viscoelastic material is attributed to the out of phase between force and displacement. The multi body analysis has shown the effect of frequency on the energy dissipation rate. Similarly, excitation at 1Hz, 45Hz and 90Hz are compared in the Simplex to explore the frequency effect on dissipation energy.

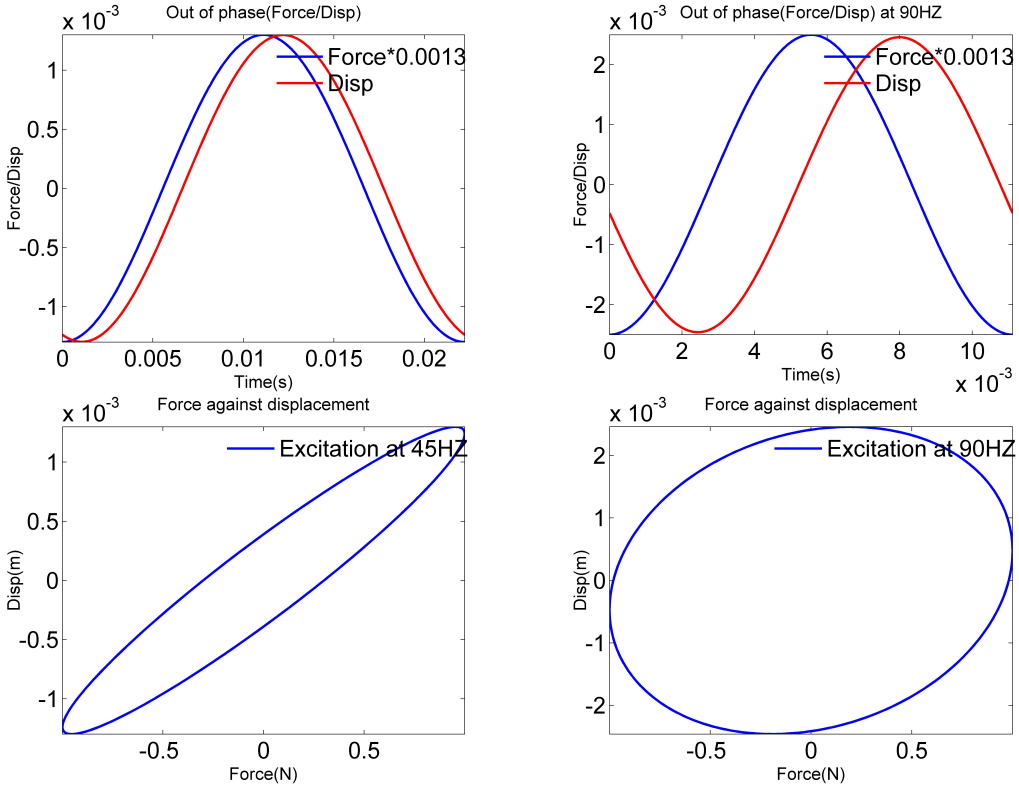

Figure 4.28.: Frequency effect on dissipation energy(a) Out of phase at 45Hz; (b) out of phase at 90Hz; (c) dissipation loop at 45Hz; (d) dissipation loop at 90Hz.

Figure 4.28(a) and (b) show the out of phase between force and displacement at 45Hz and 90Hz, which indicates the phase of displacement lagging behind more at 90Hz than that at 45Hz. To have more vivid observation about the frequency effect, the dissipation loop formed by plotting force against displacement at 45Hz

and 90Hz are compared in Figure 4.28(c) and (d). The higher dissipation energy can be deduced from three aspects. Firstly, in this model, unit load is applied on the nodes of the top line, while the displacement at 90Hz has larger displacement than the displacement at 45Hz. Secondly, the ellipse loop formed at 90Hz is much closer to a full circle than that formed at 45Hz. The simple mathematic equation calculating the area of ellipse can prove the larger enclosed area at 90Hz. Thirdly, the higher the excitation frequency, the accumulation rate of the dissipation will be higher. In sum, the 90Hz excitation generates more dissipation energy than that at the 45Hz in unit time.

In order to verify the programming of the Simplex in energy dissipation estimation, the energy equilibrium of the entire system is calculated in the time domain. Set Poisson ration ν as 0.475 and damping η as 0.000323MPa.s. The element number of the viscoelastic beam is 40 and the damped natural frequency of the current model is 33.5Hz. The strain and stress of the 27 integration points in each element can be obtained from the displacement of the 20 nodes in each element. For each element, the total energy dissipation is generated with the summation of the 27 integration points. The general expression of the strain energy in each element is given as,

$$U = \frac{1}{2}\int_{V^0} u^T [B_L]^T [D][B_L] u dV^0 \tag{4.27}$$

While it is not convenient to calculate the dV_0 since the mesh is not uniform for some complicated structure, thus, the isoparametric volume is recommended to replace dV_0 as $dV_0 = |J_e| drdsdt = |J_e| dV_c$, where the J is the Jacobian matrix. Therefore, the strain energy of the element turns to,

$$U = \frac{1}{2} u^T \int_{V_0} [B_L]^T [D][B_L][J_e] dV_c u \tag{4.28}$$

As to the Hex20 element, the complex strain ϵ of the 27 interpolation points are derived using $u * B_L$ and the complex stress σ of the 27 interpolation points are derived using $u * B_L * D$. Extract the real parts of the complex strain and stress at

each interpolation point and plot the real strain against real stress to form the dissipation energy. Integrate the product of stress and strain in time domain to calculate the loop area and then sum up over the 27 interpolation points, which gives the dissipation energy of a Hex20 element.

The next step is the calculation of potential energy in each element, which is given as,

$$U = \frac{1}{2} u^T [K] u \tag{4.29}$$

The stiffness matrix $[K]$ of each element can be written as,

$$[K] = \int_V [B_L]^T [D][B_L] |J_e| dV_c \tag{4.30}$$

To calculate the potential energy using the Simplex, the real part of the displacement of each node in the Hex20 element is extracted. The time dependent strain of the 27 interpolation points are obtained by multiplying with matrix BL. Then, the time dependent stress of the 27 interpolation points are obtained by multiplying strain with matrix D. It is important to point out that the displacement, strain and stress in this step are real components since only the real part of the displacement is extracted at the very beginning of the calculation. Then, sum up the products of stress and strain at the 27 interpolation points to have the total potential energy in each element.

The mass matrix of Hex 20 element is needed to calculate the kinetic energy, which is formed as,

$$m_{IJ} = \int_{V_c} \rho h_I(r,s,t) h_J(r,s,t) |J_e| dV_c \tag{4.31}$$

With the Simplex program, the external work done on the clamped beam, potential energy, kinetic energy and dissipation energy (strain energy) at different excitation frequency are calculated to verify the application of FEA in viscoelastic structure. Figure 4.29(a) shows the accumulated work, the dissipation energy, potential energy and kinetic energy in one cycle at 1Hz. As the pretty low frequency, the structure experiences deformation slowly under the quasi-static excitation. First of all, the

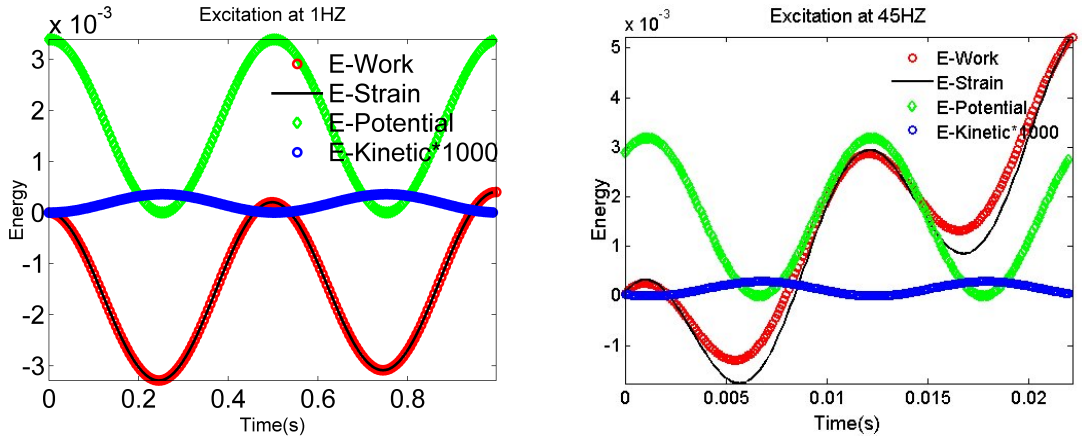

Figure 4.29.: Compare the energy at 1Hz and 45Hz.

kinetic energy is quite small compared with others since the velocity of the deformation is fairly slow. Thus, a scale 1000 is applied to enlarge the variation of kinetic in the plot. The potential and kinetic energy are energy storage components, which display the variation of energy but finally return to initial value after one cycle. It is well known the static excitation does not cause the energy accumulation in the viscoelastic material. In current simulation, the accumulated work done by the external work presents the similar tendency but the summation of energy slightly increases at the end of one cycle. To verify the accuracy in the prediction of the energy accumulation, the energy dissipation calculated from the product of strain and stress in each integration point of the system is plotted in solid line. The energy accumulations calculated through the two approaches are coincident with each other and the totally accumulated dissipation energy is very slight at 1Hz. Figure 4.29(b) shows the dissipation energy at 45Hz increases pretty obviously in one cycle, even though the period is only 1/45s. Just as expected, the accumulated external work matches well with dissipation energy calculated using the strain energy.

Figure 4.29 elaborates the dissipation energy accumulation in cycle. The plots shows in Figure 4.30 indicates those energy accumulation are periodic. The

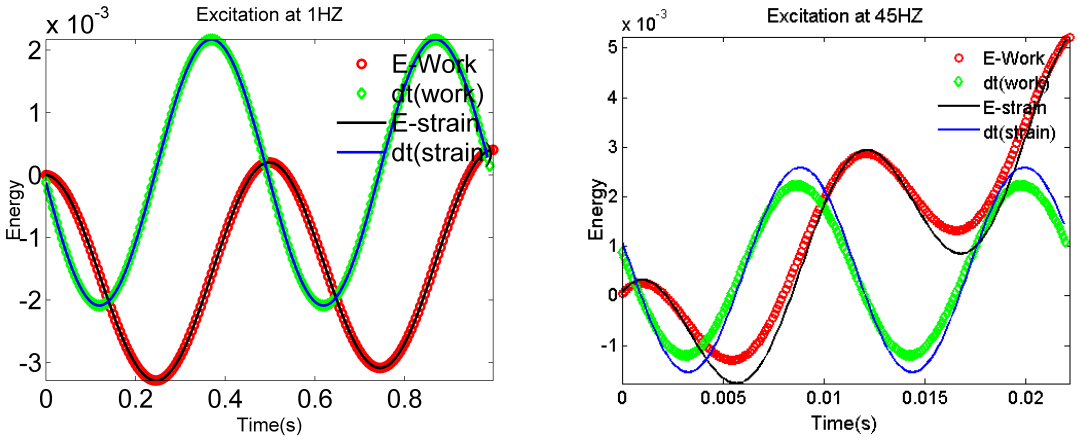

Figure 4.30.: Periodicity of the work and strain energy.

$dt(work)$ and $dt(strain)$ in the Figure 4.30 are obtained through differential over the external work and strain energy in time domain. Since the $dt(work)$ and $dt(strain)$ are sinusoidal wave, the accumulated work and strain energy obtained from the integration of the sinusoidal wave are definitely periodic in time domain. Thus, it is applicable to assume the constant heat generation rate as long as the harmonic force field is applied.

4.4 Response of Viscoelastic Beam to the Blast Load

The response of rubber bushing to the hammer impact has been discussed in Chapter two. The modal analysis from the acceleration of displacement can be used to derive the transfer function of the rubber bushing. With the identified coefficients of transfer function, the energy dissipation of the rubber bushing at different excitation frequency can be predicted and the stability of the structure can be analyzed. However, for a large scale structure, the response measured at different position is different under the same impact, which means the transfer function is also dependent on the measured location. Generally speaking, multiple accelerometers can be set up to record the response at different location. However, using the modal testing approach to evaluate multiple similar products is kind of

time consuming and redundancy. The Simplex program developed in frequency domain enables the user to evaluate the similar products much easier and faster.

The force-frequency Simplex program is actually a transfer function $G(\hat{\omega}_n)$ in frequency domain. If the unit amplitude harmonic excitation is applied on the structure, the output of any node on the structure stands for a unique transfer function. To elaborate Simplex program in presenting the transfer function, a beam in Figure 4.22 is applied in the following discussion. Since $G(\hat{\omega}_n)$ is presented in frequency domain, the blast load should be transformed into frequency domain with FFT. FFT is used rather than the Laplace transform due to the special requirement in coding. The calculated displacement is still in frequency domain, inverse fast transformation (IFFT) is necessary to reconstruct the time history of the response.

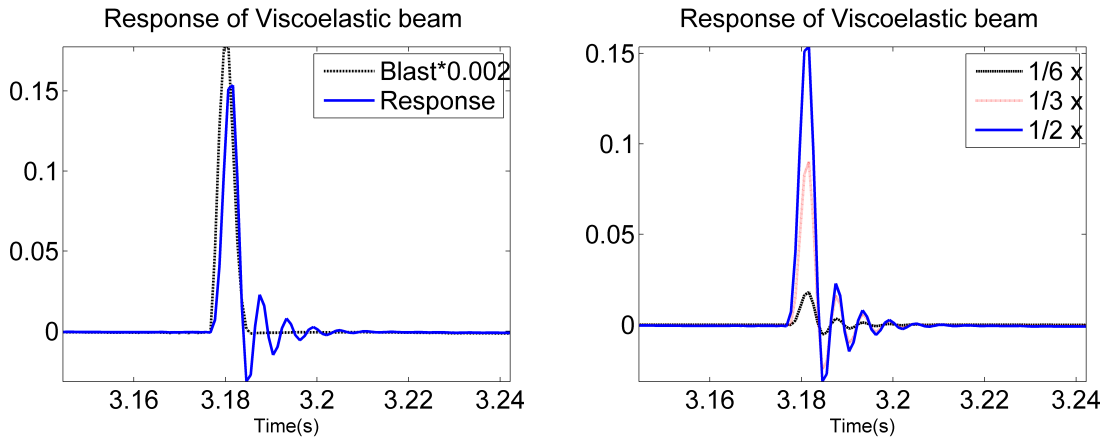

Figure 4.31.: Response of viscoelastic beam to the blast load (a) Compare with the blast; (b) effect of the measured location.

Figure 4.31(a) shows the blast load and the displacement at the central part of the clamped beam. The blast is multiplied with a scale 0.002 to have same magnitude as response in the plot. Because of the damping of rubber, the response of displacement is weakened in exponential quickly. Figure 4.31(b) compares the displacement at different locations of the clamped beam. $1/2\ x$ is the central of beam, which displays maximum displacement. $1/6\ x$ and $1/3\ x$ are the distances

from the fixed end of the beam to the measured point. Just as expected, the closer of the measured position to the fixed end, the lower is the peak value of the response.

As to elastic material, the response is similar to the loading history in time domain if the transfer function of the structure is non-dissipative. However, as to the viscoelastic material, the transfer function is definitely dissipative. Then, the response is different from the loading history. The Figure 4.31 gives a proper demonstration of the dissipative wave propagation.

4.5 Dissipation Energy Distribution in Rubber Bushing

In the previous testing of Simplex, a frequency function multiplying with the dynamic stiffness of the elastic structure turns the stiffness into complex variable and frequency dependent in order to represent the stiffness of viscoelastic structure. Whereas the precondition is the uniform material properties in all elements, which is inconsistent with the current rubber bushing composed of rubber and steel. To solve this problem, an approach is implemented to minimize the influence considering the modulus difference between rubber and steel. A group of comparison is listed in the Figure 4.32 assuming the second material′s modulus as frequency dependent. In this comparison, the damping coefficient is set as constant and spring coefficients are varied to simulate the stiffer second material. Figure 4.32(b) indicates that with the increase of the two spring coefficients, the increase of storage modulus and loss modulus becomes slower. Especially, when the second material′s spring coefficient is 1000 times of the rubber′s, the frequency effect on modulus is almost negligible. Since the modulus of steel is ten thousands time higher than that of rubber and the testing frequency is in the range of 0Hz to 100Hz, that means the modulus of steel is still constant in the testing range even though it is expressed in frequency function in Simplex. However, Figure 4.32(c) shows that the second material′s loss modulus increases linearly with the testing frequency. The further increase of spring coefficients has little change on the loss modulus behavior as the three straight lines

overlap with each other. To guarantee the applicability of the program in structure composed of two materials, another pre-condition is the negligible dissipation energy in the steel compared with that in the rubber.

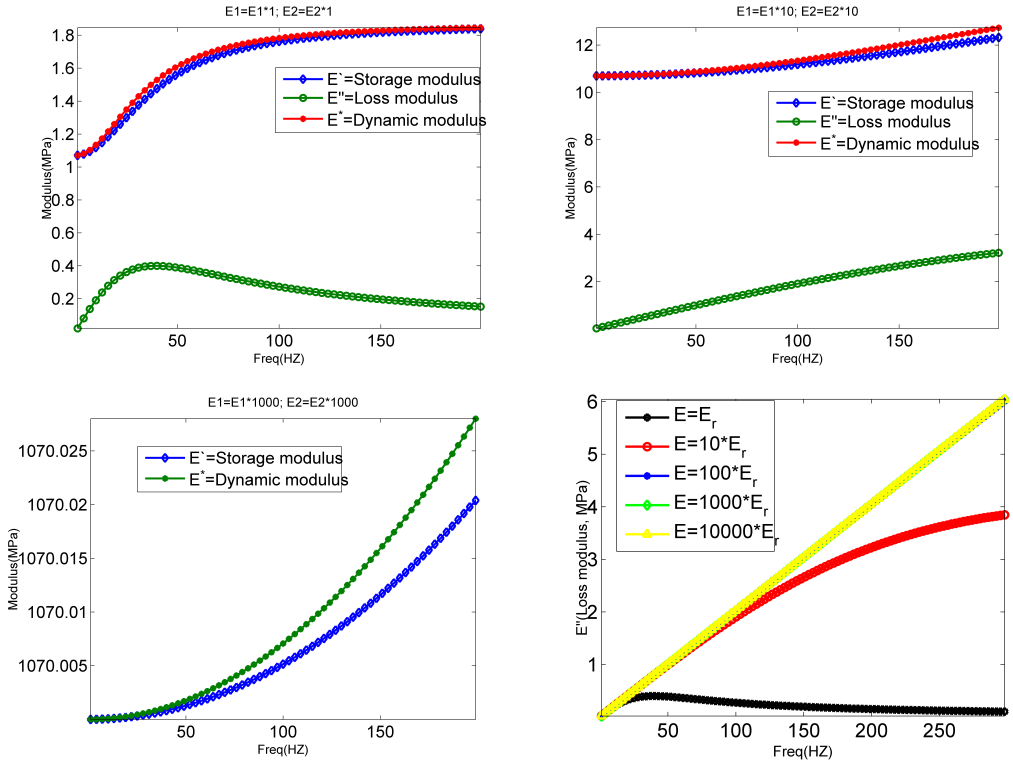

Figure 4.32.: Frequency response of material with different spring coefficients.

Figure 4.33 compares the dissipation energy distribution in the beam when the second material′s spring coefficients are 10, 100, 1000, 10000 and 100000 times of the rubber′s. For more straightforward demonstration, the ratio of dissipation energy in the two materials is compared, where E_1 is the rubber and E_2 is the stiffer material. In this testing, the external excitation frequency is 30Hz and applied on the central surface of the beam. Because the loss modulus of the second material increases with the frequency in the testing frequency range when the modulus difference between the two materials is not too large, the dissipation energy in the two materials are pretty close. However, once the two spring coefficients of the second material is extremely larger than that of rubber, for example, the steel in the

Figure 4.33(b), the ratio of dissipation energy between steel and rubber is as high as 14000 times. Thus, the dissipation energy in the steel is negligible compared with rubber and the Simplex program is applicable to structure composed with two materials as long as the second material′s modulus is much higher than rubber.

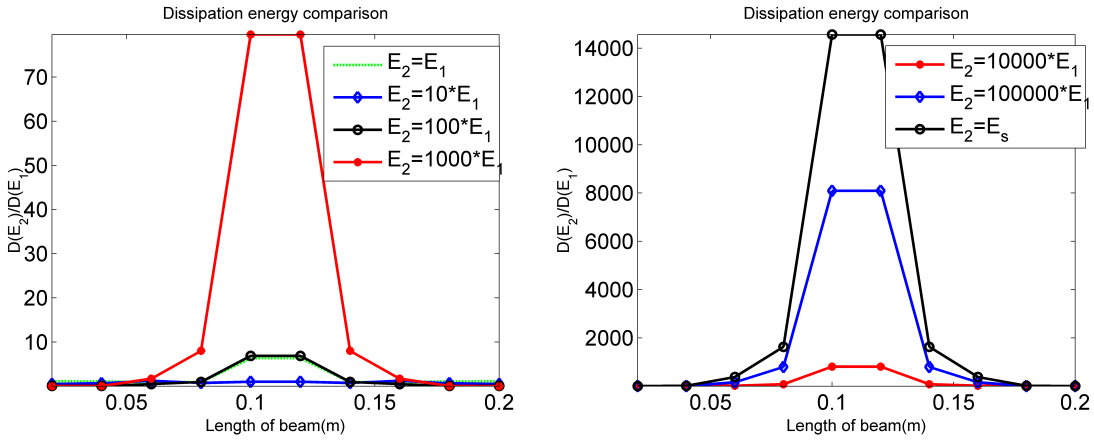

Figure 4.33.: Comparison of dissipation energy distribution at 30Hz in two materials.

Figure 4.34 displays the frequency scan of the beam composed of two materials. For the convenience of natural frequency identification in the viscoelastic structure, the Eigen values of the corresponding elastic structure are calculated using the low and high modulus separately, which are plotted as black vertical lines. With the increase of the second material′s low and high modulus, the first resonance frequency turns to higher. In the Figure 4.34(a), both of the two layers materials are rubber and the first natural frequency is 14.2Hz and the frequency plays dominate role to determine the displacement of the beam in the testing range 0Hz to 30Hz. Even though when the second material′s modulus is 100 times higher than the rubber′s, the frequency effect is still obvious in the testing range less than 100Hz. Figure 4.34(c) gives the frequency scan result of beam composed of rubber and steel. Because of the higher modulus of steel, the damped natural frequency appears at 850Hz, as shown in Figure 4.34(d). However, besides of the frequency

effect presented in the resonance, the frequency dependence of rubber materials displays in the testing range 0Hz to 100Hz. Because of the rising dynamic modulus of rubber, the imaginary displacement reaches to maximum value before 100Hz and dominates the deformation of the beam.

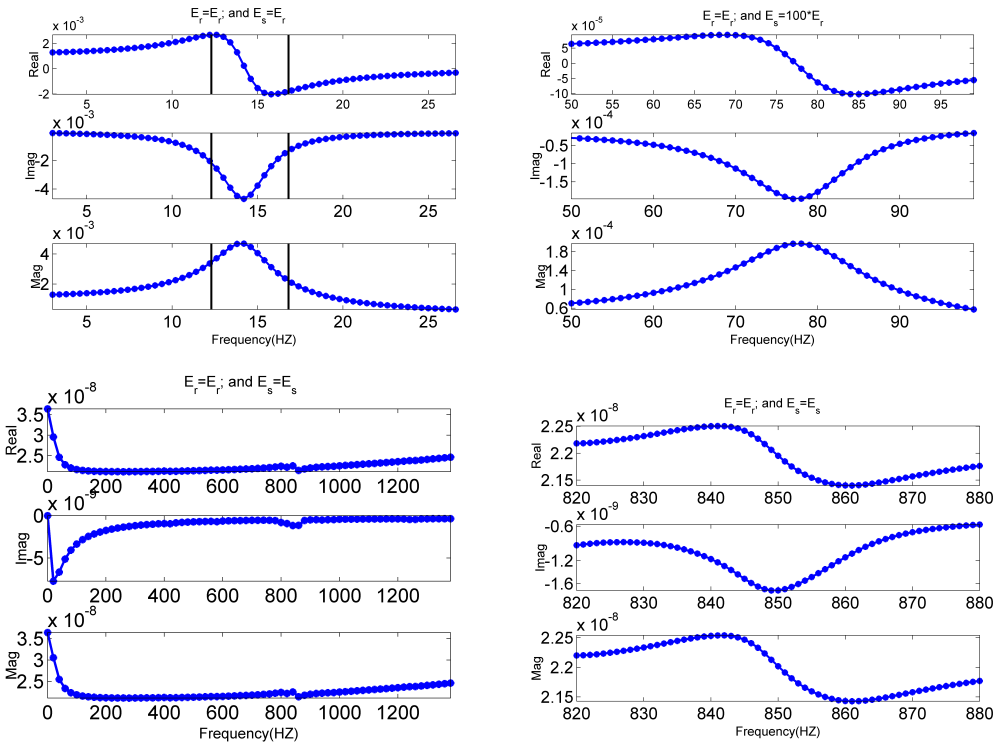

Figure 4.34.: Frequency scan of the beam composed of two materials.

Similar, the frequency scan is applied on the cylindrical structure composed of two materials. Figure 4.35 compares the damped natural frequency with the natural frequency (black line) of the corresponding elastic structure, and the natural frequency is always higher than the damped natural frequency. With the modulus increase of the second material, the first vertical resonance frequency turns higher. Especially, when the second material is steel, in the high frequency range, the resonance affects the behavior of the structure, but in the low frequency range, the viscoelastic of rubber affects the behavior of the structure. This characteristic is

unique in structure composed with viscoelastic material since the frequency effect at low frequency is negligible in elastics structure.

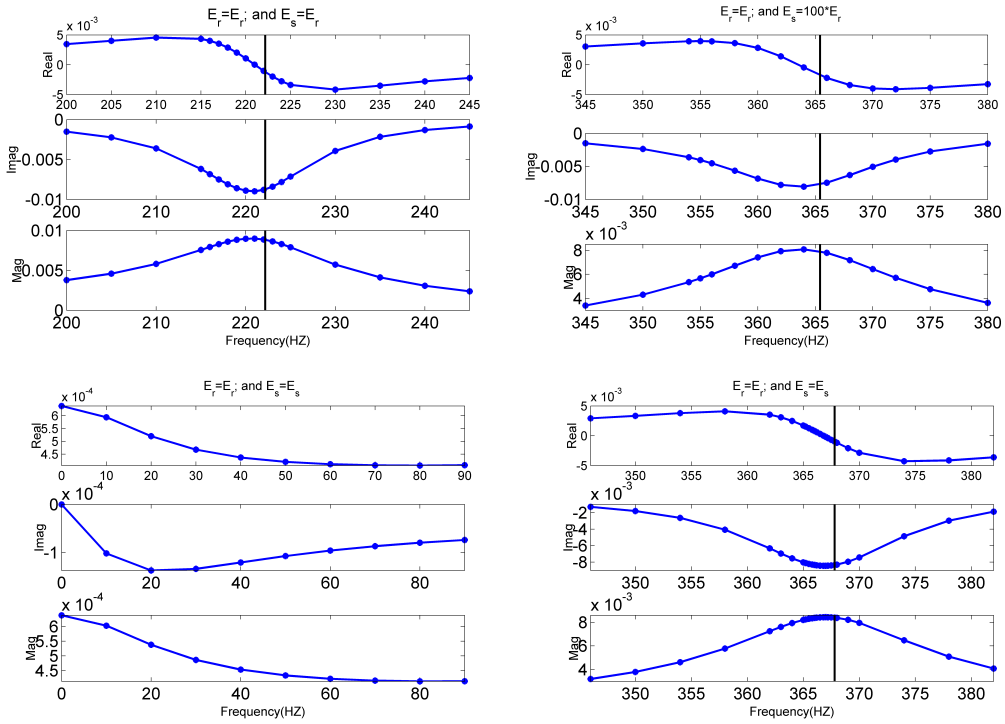

Figure 4.35.: Frequency scan of viscoelastic cylindrical structure.

The dissipation energy of the viscoelastic structure composed of two materials is shown in Figure 4.36. Because of symmetry of the dissipation energy distribution, only half of the elements are considered. In this testing, the vertical loading is applied on the steel and the outer surface of the rubber is fixed. The rubber mesh in radial includes three layers of elements, including inner layer, middle layer and outer layer. The orientation of elements indicates the coordinate of elements in circumference. Overall, the inner layer of elements shows higher dissipation energy density, however, the minimum dissipation energy density displays in the middle layer of rubber core. The frequency effect on viscoelastic material at lower frequency is demonstrated again in the Figure 4.36(b). Because of

the higher modulus of rubber at 60Hz than 30Hz, the displacement at 30Hz is lower and the dissipation energy is also lower than that at 60Hz.

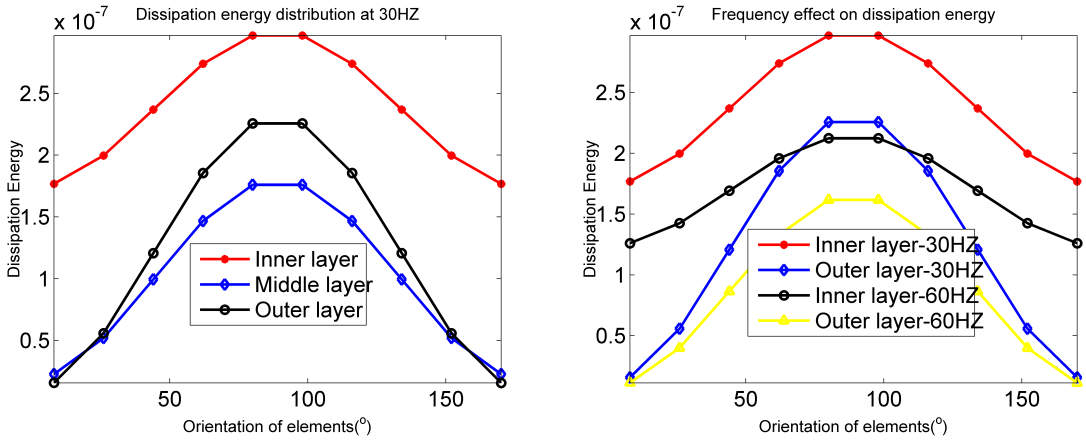

Figure 4.36.: Dissipation energy distribution (a) in the three layers; (b) at frequency 30Hz and 60Hz.

Figure 4.37(a) shows the nonuniform displacement of rubber core during the tensile test. The unit load is applied at the outer surface of the rubber core to simulate the tensile test. The inner surface of the rubber is attached with the steel shaft and assumed as fixed in the model. The real part and magnitude of displacements decrease from the outer surface to the inner surface of rubber core. Figure 4.37(b) shows the frequency dependence of the displacement on top node. Because of the high natural frequency of the viscoelastic cylindrical rubber bushing, the frequency effect at lower frequency is dominated by the properties of viscoelastic material rather than the resonance phenomena. The real part and magnitude of the displacement decrease with the increase of frequency, which is attributed by the increase of dynamic modulus.

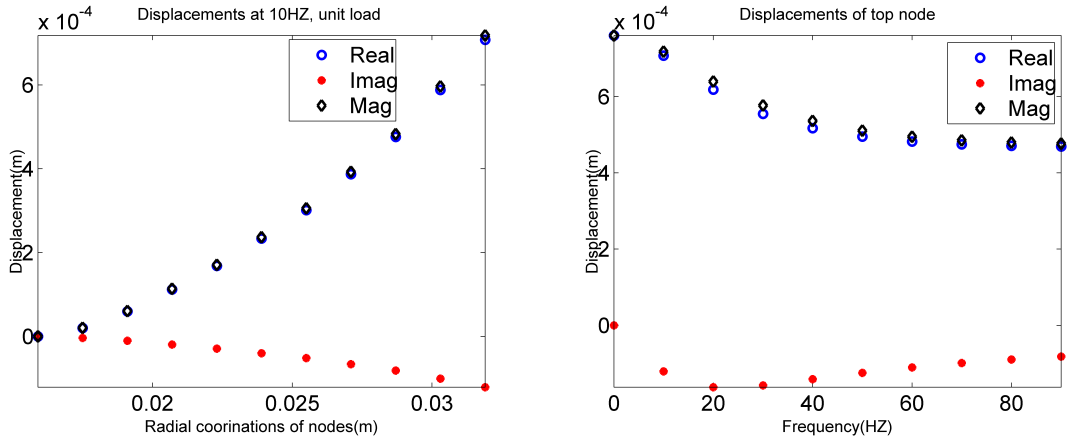

Figure 4.37.: Displacements of the rubber core (a) Nodes in radial rection; (b) top node at different frequency.

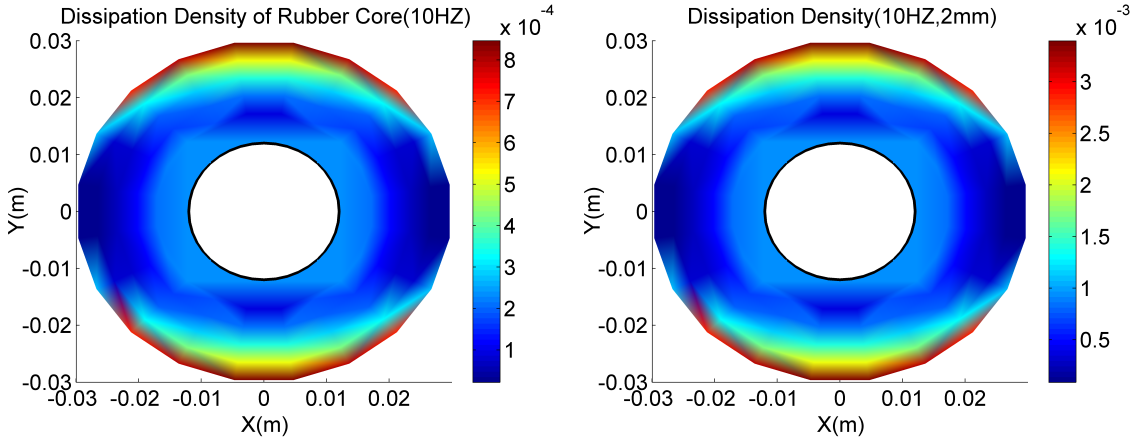

Figure 4.38.: Density of dissipation ererngy in rubber core(a) Amplitude=1mm; (b) amplitude=2mm.

The dissipation energy distribution of rubber core at excitation frequency 10Hz is displayed in Figure 4.38. The amplitude of the excitation is indicated using the amplitude of the top node, which has the maximum displacement. The loading area of the rubber bushing presents the highest dissipation density and that distribution isn′t changed after double the amplitude. This dissipation energy distribution tallies well with the displacements of nodes in radial direction. The

higher displacements of nodes cause more energy dissipated and accumulated. The central area of the rubber core is of low displacement and the corresponding dissipation energy density is pretty low.

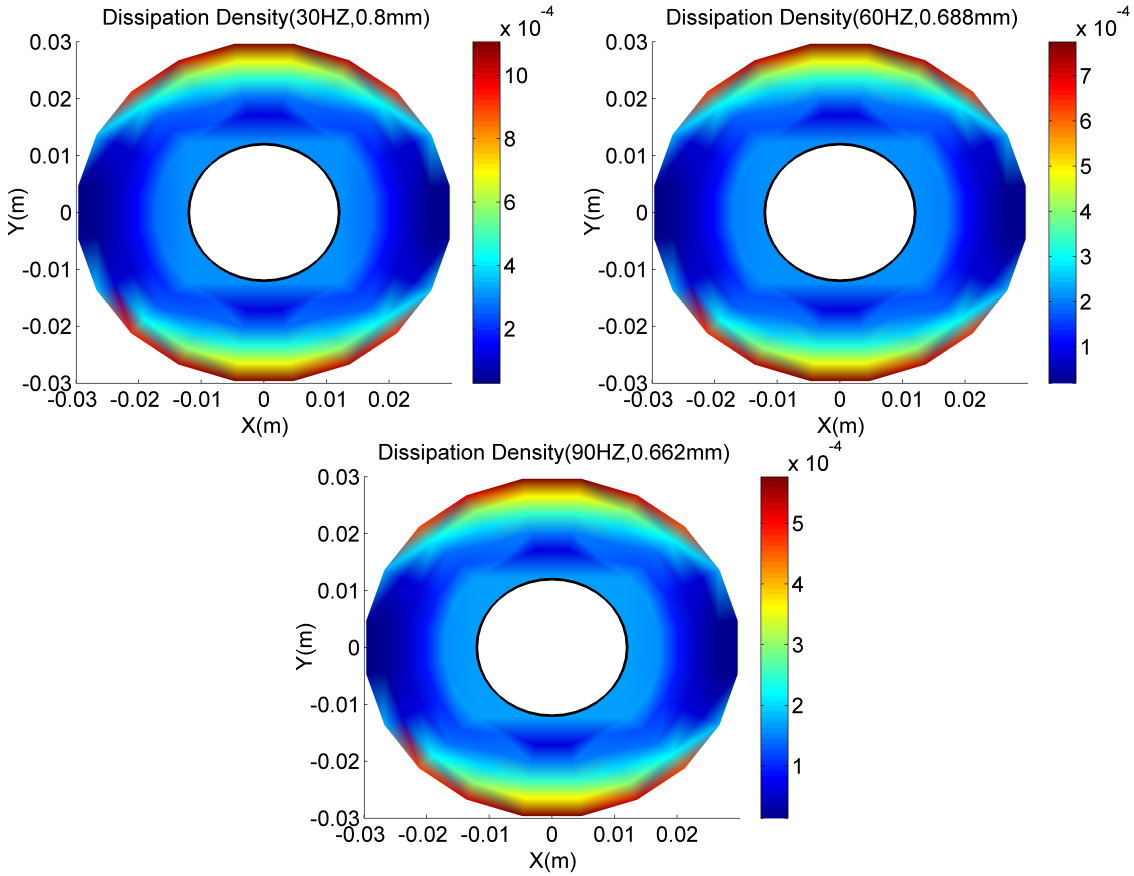

Figure 4.39.: Density of dissipation ererngy in rubber core (a) 30Hz; (b) 60Hz; (c) 90Hz.

The frequency effect on the distribution of dissipation energy is presented in Figure 4.39. The simulation results indicate that the amplitude at higher frequency is lower due to the hardening of rubber core. The amplitudes at 10Hz, 30Hz, 60 Hz and 90Hz under the same excitation load are 1mm, 0.8mm, 0.688mm and 0.662mm. The quick increase of modulus happens in the range of 10Hz to 60Hz and the modulus approaches to constant when excitation frequency approximates to 100Hz. From 10Hz to 30Hz, or from 30Hz to 60Hz, the stiffness of the structure changes

significantly and leads to the almost 20% reduction of amplitude. Nevertheless, after 60Hz, the slowly increase of modulus just slightly affects the stiffness and has little effect on the excitation amplitude.

4.6 Conclusion

In consideration of the complicated characterization of the nonlinear mechanical properties of the viscoelastic material and barely satisfactory simulation in the commercial software, the finite element analysis is applied in this dissertation to explore the dynamic response of complicated structure composed with viscoelastic materials. Solid knowledge about the principle in FEA is elaborated at the very beginning in order to describe the preprocessing. The FORTRAN source code initially targeting at elastic structure is implemented to facilitate the development of current Simplex program. The clamped beam is practiced in the testing process to verify the reliability of the program through the comparison with the theoretical analysis or the quasi-static simulation. Each step of the Simplex program is scrupulously confirmed before moving to the next step. The principle and approach to calculate the dissipation energy in each element and over the entire system are elaborated. Similarly, simulation results of each step are attached to have a more direct and authentic demonstration of the FEA. Furthermore, the system transfer function developed in the frequency domain, and the response of structure subjected to the blast load become feasible with the convenient of FFT and IFFT algorithm. Even though research target of the dissertation is rubber bushing, the developed Simplex program can be applied to any structure, regardless how sophisticated and what type of loading is applied on the model. Nevertheless, the last but not the least part of the FEA in this chapter is the dissipation energy accumulation in each element, which provides the heat source for the following heat transfer analysis. Again, this Simplex program can be applied for dynamic analysis about many interesting components or structures.

CHAPTER 5. TEMPERATURE DISTRIBUTION OF RUBBER BUSHING USING FVM

5.1 Coupling of Structure and Thermal

It is well known that natural rubber materials lose its viscosity and turn to more rigid after serving for a certain time. The degeneration of properties is usually termed as aging. Actually, besides of aging, the rubber materials′ fatigue life is also being highly shortened after certain serving life. Hysteresis loss is the main reason to account for the aging process, which is monotonically increasing with the ambient temperature (Choi, Kang, Jeong, Lee, & Yoon, 2005). The increase of rubber′s temperature or environment temperature can lead to decrease of modulus at small strain, and decrease the effect of carbon black′s percentage on the magnitudes of modulus. The temperature, strain and carbon black concentration dependence on the modulus become much less sensitive at the larger strain range(A. R. Payne, 1962). To the manufactured rubber components, the ambient heat from the environment and internal heat caused by the dynamic behaviors are highly destructive to the rubber, which make heat as the primary role in weakening the properties of rubber (Gehman, 1967). Similarly, the aging and fatigue life of rubber components are extremely dependent on the heat generation and temperature rising rate (Mars & Fatemi, 2004), and (Beatty, 1964). At higher temperature, the thermal effect has more atmospheric oxygen, which leads to more stress relaxation or stress decay (Kalfayan, Silver, & Mazzeo, 1975). In sum, it is extremely crucial to explore the coupling relationship of thermal and structure and determine the better serving condition of rubber components to optimize the service life.

The rubber bushing installed on the suspension system is exposed in the ambient environment. The thermal accumulated in the rubber core of the bushing partially transfers to the lower temperature ambient air. The heat transfer coefficient of rubber is tremendously lower than that in steel sleeves. Thus, to predict the temperature distribution of rubber bushing during the dynamic loading, the heat transfer mechanism should be clarified besides of the heat generation mechanism. Furthermore, those spring and dashpot elements combinations are lumped heat source and couldn′t provide discrete dissipation density. Considering the special property of viscoelastic material model, the FEA estimated dissipation energy density is applied as heat source inside of the rubber core.

5.1.1 Physical and Thermal Properties of Rubber

From the previous multi-body dynamic analysis, the rubber components experience the translation movements and rotation movement. In either way of movements, the hysteresis damping and viscous damping should be included to predict a comprehensive temperature distribution of rubber bushing. To start the analysis of thermal field in MATLAB, the heat sources should be clarified and the corresponding parameters of heat transfer should be identified. The geometry of rubber bushing used for the heat transfer analysis is given in Table 5.1.

Table 5.1: Geometry of rubber bushing for test

Parts	outter sleeve	rubber core	inner sleeve
Diameter(inch)	2.755	2.515	1.25
Length(inch)	2.0	2.0	2.29

Composition of rubber used for the parameter identification is carried out using thermal gravimetric analysis (TGA). The principle of TGA is the weight loss

of rubber during the increase of temperature. The TGA is used here to determine the composition of rubber used for the following analysis. Being exposed in different gas environment, the different components of rubber react differently, which process can be monitored and give a quantified result of the compositions. Generally, the common gas systems include inert gas (high purity nitrogen commonly) and air. Initially, inert gas flow is on and then gas source is switched to air by hand or automated by setting the program. The gas switching systems are critical to quantify the components of rubber, which is composed of polymer and carbon black mainly.

The weight range of sample in the test is highly recommended as 10-15 milligrams. The tray is delicate and couldn′t afford a heavy sample. Furthermore, polymer combustion will release pungent gas, which requires a much better air circulation system of TGA. Since limited sample is tested every run, multiply measurements are necessary to acquire credible results. In current test, three duplicate tests are run and consistent results are obtained every time. The following are the detailed steps to have a rubber analyzed by TGA instrument. The TGA results are displayed in Figure 5.1.

To correctly operate the instrument and collect reliable data, the procedures and results analysis are elaborated in the following,

Step 1: Set the test program in the TGA software to have the temperature ramping from room temperature to 900 °C. Turns on the inert gas and then ramps the temperature at 10 °C per minute. The initial weight loss is due to the volatization of minor components before the temperature reaches to 300 °C. Those minor components include stabilizers, lubricants, plasticizers, and other small molecules. The TGA results display a total of 6.621% weight loss in this stage.

Step 2: Majority weight loss happens in this stage ranging from 200 °C to 600 °C and the loss is taken as polymer percentage. During this temperature range, backbone of polymer is cracked down into volatile fragments and the weight loss in this test is 63.92%.

Step3: Before switch the air system from inert gas to air after temperature reaching to 600 °C, nitrogen is hold for a few minutes at 600 °C in order to make sure all polymers has been cracked down. Later, keep the temperature at 600 °C for 15 minutes and switch on the air system. After exposed in the high temperature and air, carbon black will start to combust and the weight loss in this stage can be used to estimate the content of carbon black. The result in Figure 5.1 indicates the weight loss is about 20.05%.

Step 4: Ramps the temperature again at 10 °C per minute after it dwells at 600 °C for almost 20 minutes. In this period, only calcium oxide should be left after calcium carbonate presenting decarboxylates. Theoretically, calcium carbonate, the content of $CaCO_3$ can be obtained on the basis of weight loss in this stage. The remaining mass after the test is of ash, some mineral materials. While in our test, there is no obvious weight loss in this stage.

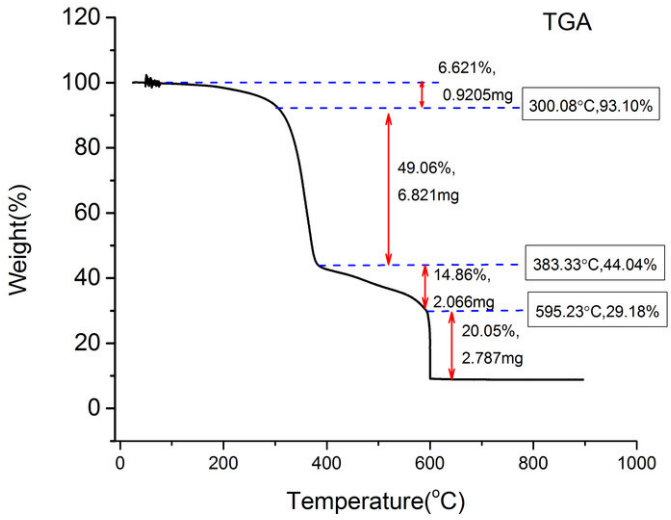

Figure 5.1.: TGA analysis of the rubber sample.

Transient plane source (TPS) method applied by the hot disk thermal analysis instrument is used to measure the heat conductivity and other thermal characterization of rubber (Figure 5.2).

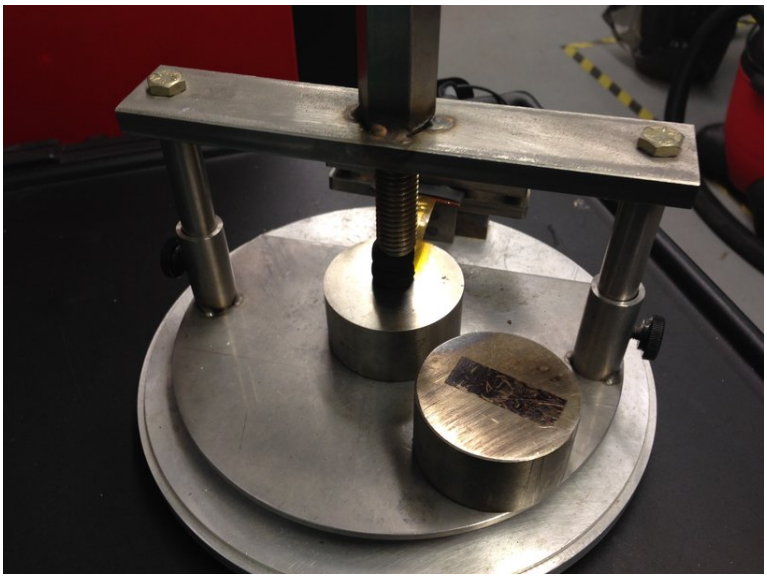

Figure 5.2.: TPS used to measure the thermal properties of rubber.

The specific heat and heat transfer coefficients can be estimated using the rule of mixture assuming the compositions of rubber are carbon black and polymer and neglecting the trivial components. The physical and thermal properties of rubber material properties used in the simulation are given in Table 5.2.

Table 5.2: Physical properties of rubber

Properties	Poisson's ratio	Heat transfer coeff	Static Mdulus
Value	0.495	$10(W/(m^2.K))$	0.01(GPa)
Heat Capacity	Thermal diffusivity	Density	Thermal conductivity
1611.44(J/Kg.K)	$0.202(mm^2/s)$	952.54 (Kg/m^3)	0.343(W/m.K)

There are some assumptions about the heat transformation in rubber bushing. Firstly, heat source of rubber bushing comes from hysteresis damping and viscous damping no matter the harmonic excitation or arbitrary loading is applied. Secondly, the outer surface of the steel sleeves and two ends of the rubber bushing

are exposed to ambient air at room temperature. The heat convection is the main approach to transfer the heat from rubber bushing to air. Thirdly, the inner steel sleeve is installed on the balancing bar of the suspension system, which has little space to be exposed in the ambient air. Thus, compared with the outer surface, the heat transfor of the inner surface is relative slow and less, thus, that part can be treated as insulated for analysis. Fourthly, the heat flows are of two directions, which are through inner steel sleeve and outer steel sleeve, considering the cylindrical geometry of the rubber bushing.

5.1.2 Boundary Conditions of Rubber Bushing

The following part will discuss the principle of heat transfer to build the heat convection model of rubber bushing in the air. The energy conservation law gives the heat transfer governing equation in rubber bushing as,

$$\frac{\partial T}{\partial t} = \frac{1}{\rho}(\lambda_x \frac{\partial^2 T}{\partial x^2} + \lambda_y \frac{\partial^2 T}{\partial y^2} + \lambda_z \frac{\partial^2 T}{\partial z^2}) + \frac{q}{c\rho} \tag{5.1}$$

λ_x, λ_y and λ_z are heat conduction coefficient in the direction x, y and z. q is heat generated in unit volume, ρ is the material density, α is the coefficient of heat transfer, c is the specific heat capacity and K is temperature unit Kelvin. From the previous analysis, the heat generation of rubber is set as plane problem after simplified the thermal equation of the rubber bushing system,

$$\frac{\partial T}{\partial t} = \frac{1}{\rho}(\lambda_x \frac{\partial^2 T}{\partial x^2} + \lambda_y \frac{\partial^2 T}{\partial y^2}) + \frac{q}{c\rho} \tag{5.2}$$

The above partial differential equation (PDE) of the heat conduction is dependent on the variables of time and position. To solve this equation, initial and boundary conditions applied to the domain or surface of the researched items are needed to be specified. Those specifications are generally classified into three scopes (Kreith & Black, 1980): environment temperature, surface temperature gradient condition and airflow condition. The specified temperature or the environment temperature is called as Dirichlet or essential boundary conditions. This type of boundary

condition is written as $T = T_{given} = T\ |_{\Gamma} = T(x, y, z, t)$, which specifies the temperature variation of certain boundary surface over time. The second specified condition on surface is the temperature gradient or termed as heat flux at surface,

$$k_n \frac{\partial T}{\partial n} \mid \Gamma = Q(x, y, z, t) \tag{5.3}$$

Where k_n is the normal thermal conductivity coefficient (W/mk). The third boundary condition describes the convection and radiation with air (Browne & Wickliffe, 1980),

$$Q = (h_c + h_r)(T_s - T_a) \tag{5.4}$$

The boundary conditions of rubber bushing are shown in Figure 5.3, which shows a rubber bushing exposed in the air. Rubber bushing is installed on the stabilizing

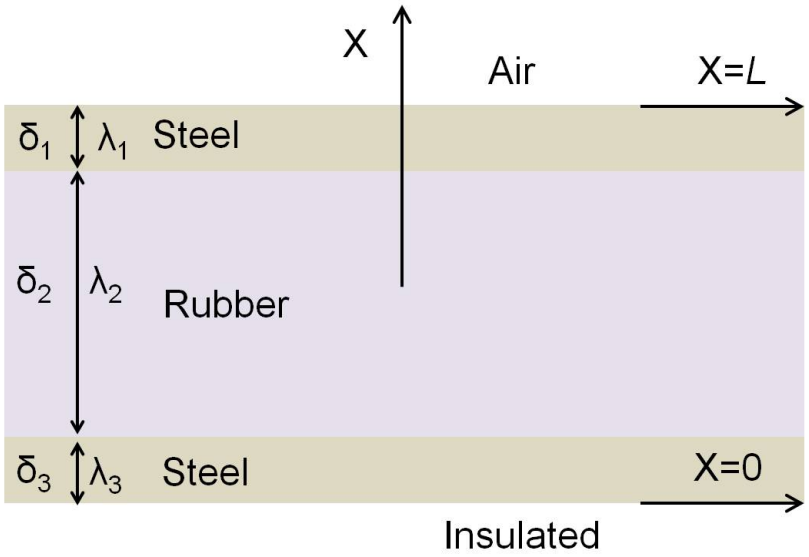

Figure 5.3.: Idealized cross section of rubber bushing.

bar and gap may exist between the two surfaces during the driving. But the air flow existing in the gap is poor to conduct the heat transfer, which leads to extra thermal resistance. The temperature jump will happen at the two materials because the thermal resistance. In current case, if the temperature of stabilizing bar is room

temperature, then, the surface of the inner surface maybe a little bit higher than room temperature. The heat flux rate can be given as,

$$q = \frac{T_1 - T_2}{R_c} = h_c(T_1 - T_2) \tag{5.5}$$

Because the rubber bushing is exposed in the air and that can slow down the temperature rising at the surface. The radial heat transfer dominates the temperature distribution inside the rubber core. The heat generated inside of rubber should transfer to the inner and outer steel sleeves, which may highly shape the temperature distribution of rubber core. Thus, besides of the heat generation mechanism of rubber under the external excitation force, the heat transfer between rubber and sleeves are also pretty critical to estimate the possible working performance of rubber bushings. Surface 1 and surface 2 are typical heat flux boundary between steel sleeves and rubber, that type of boundary drives lots of people to study the concise coefficients. The environment temperature of rubber bushing now can be determined assuming the constant air temperature T_0. At the beginning without heat source, the initial temperature of all the surfaces are given as,

$$T_{s1} = T_{s2} = T_{s3} = T(x, y, z, t) = T_0 \tag{5.6}$$

While at other time, the temperature distribution should be estimated using the second and third boundary conditions. As to the rubber bushing, the temperature increase can be simply attributed to the heat generation over a certain time period, $T = T_0 + \frac{QL}{\lambda St}$, T_0 is environment temperature, T is the rubber bushing temperature, Q is the accumulated heat per cycle, L is the thickness of rubber bushing, S is the heat flux surface area, λ is the heat conductivity and t is time in that equation. The temperature of rubber bushing increases with the generated heat under the external loading. Due to the highly complicated complex coupling of thermal and dynamic mechanics, one way coupling approach is performed by many researchers to provide the temperature distribution of moving rubber components, so as in current research.

From the definition of thermal emissivity, the energy is dissipated from the normal direction of the surface. While for the rubber bushing, especially the cylindrical rubber bushing, the convex rotating surface indicates that the received energy is actually lower than the generated energy. Correction is needed to take the influence of shape.

There is a convenient way to evaluate the convection heat transfer coefficient from the definition of the second boundary condition. With the known surface temperature and environment temperature, the heat transfer coefficient can be written as,

$$h = -\frac{k}{T_\Gamma - T_{\text{inf}}} \frac{\partial T}{\partial n} \mid \Gamma \tag{5.7}$$

Divide the heat transfer coefficient with the angular velocity, and then the ratio turns to velocity-dependent. With good estimation, ratio of different velocity overlaps with each other and tallies with the theoretical estimation.

Base on the conservation of energy, the generated heat in the rubber components needs to keep the thermal equilibrium on the system and account for the heat flux from rubber to the ambient air (Yavari, Tworzydlo, & Bass, 1993). As to those models to solve the thermal mechanical problems, the heat flux characterization has been discussed in many publications (J. Clark & Schuring, 1988). Browne constructed a platform to show the effect of sample size, surface conditions and environments on the coefficients of convection heat transfer and provide some significant data (Browne & Wickliffe, 1980). In that research, the flat plate exposed to the laminar stream are presented to discuss the effect of air speed, that theory obtained a strong connection between velocity of air speed and heat flux coefficients. Schuring (Schuring, 1980) claimed that the rubber tire stopped to absorb more heat energy once the heat equilibrium has been reached. That indicated all of the generated heat dissipated to the ambient air after a certain period. Similarly, when the rubber bushing internal thermal equilibrium has been estimated, the generated heat due to the dynamic damping diffused to the air through the surface of steel sleeves and two ends of the rubber bushing.

The process of programming about the heat transfer in the cross section of rubber bushing includes the following two parts. First step is the materials properties collection, which include density, heat conductivity coefficient, special heat, heat diffusion coefficient, heat generation rate. The second step is the time difference program using finite volume method and specifications of boundary conditions.

5.2 Temperature Distribution of Rubber Bushing

5.2.1 Analytical Solution with Constant Heat Source

Analytical solution about uniform heat generation rate has been tested before the application of heat source calculated from the Simplex program. About the boundary condition applied on the thermal analysis, the inner surface of the steel sleeve is taken as insulated since it is confined on the balance bar, that heat transfer is much slower than the air conduction at the outer surface of the steel sleeves. All the analytical solution and numerical solution are programmed using MATLAB to predict the temperature distribution on the cross section of the rubber bushing. Particular attention should be given to constitutive modeling, which includes several steps: solve the governing equation and found heat generation rate; get clear the principle and flow chart of programming, and calculate the temperature distribution. A main contribution of those steps is a consistent constitutive relation and analytical solution of temperature distribution in radial direction of rubber bushing.

Assumptions about the rubber bushing to model the heat transfer are listed in the following,

1): The heat generation rate S_0 is constant in rubber component.

2): The outer surface is exposed to ambient air of constant temperature and the heat convection rate is high in air.

3): The inner surface is in contact with the stabilizing bar and is insulated from environment.

4): For symmetry, only half of the cross section of rubber bushing is considered and no heat flow in the axial direction.

Those assumptions about boundary conditions to solve the governing equation are,

1): The initial temperature is T_0 at every location.

2): Convection of air at the outer surface $x = L$ is the major heat loss.

3): The inner surface x=0 is insulated and there is no heat loss.

The governing equations of the heat transfer in rubber bushing and its corresponding boundary conditions can be formulated as,

$$\begin{aligned} c\rho\frac{\partial T}{\partial t} &= K\frac{\partial T}{\partial x^2} + S_0 \\ T(x,0) &= T_0 \\ K\frac{\partial T(L,t)}{\partial x} &+ HT(L,t) = 0 \\ K\frac{\partial T(0,t)}{\partial x} &= 0 \end{aligned} \tag{5.8}$$

Considering the three layers structures of rubber bushing, the heat capacity is estimated using composite mix rate $\rho c = 1/\sum_{1}^{3}\frac{1}{c_i m_i}$, and the heat conductivity is given as $1/K = \sum_{1}^{3}\frac{\delta_i}{\lambda_i}$. The following work can be seperated into two steps, 1) calculate the stable temperature distribution, and 2) study the thermal behavior in a transient regime. First of all, the steady state solution for $K\frac{\partial T}{\partial x^2} + S_0 = 0$ with the given boundary conditions is,

$$T^* = -\frac{S_0 x^2}{2K} + \frac{S_0 L^2}{2K} + T_0 + \frac{S_0 L}{H} \tag{5.9}$$

Figure 5.4 draws the equilibrium temperature distribution of rubber bushing in radial direction. This is the temperature distribution of steady state or it is can

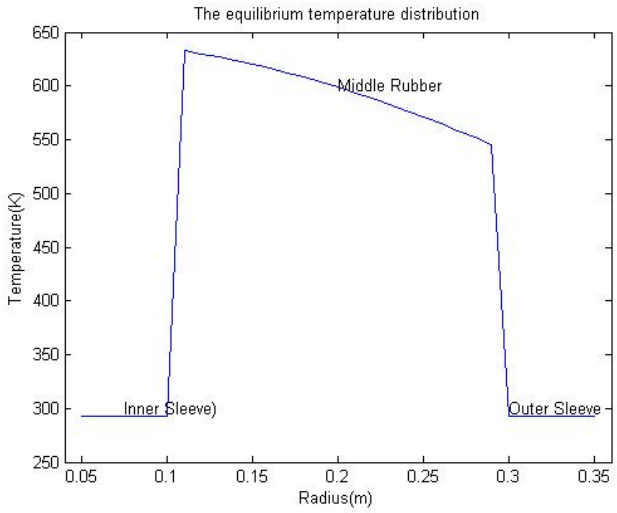

Figure 5.4.: Equilibrium temperature distribution.

be treated as equilibrium solution of Equation (5.8). The transient temperature distribution can be solved with the following boundary condition,

$$T = T^* + \omega(x,t) = -\frac{S_0 x^2}{2K} + \frac{S_0 L^2}{2K} + T_0 + \frac{S_0 L}{H} + \omega(x,t) \tag{5.10}$$

Substitute this into the initial Equation (5.8) and get,

$$\begin{aligned} &\omega(x,0) = \omega_0(x) = \frac{S_0 x^2}{2K} - \frac{S_0 L^2}{2K} - \frac{S_0 L}{H} \\ &k\frac{\partial^2 \omega}{\partial x^2} - \frac{\partial \omega}{\partial t} = 0 \\ &\frac{\partial \omega(L,t)}{\partial x} + \frac{H}{K}\omega(L,t) = 0 \\ &\frac{\partial \omega(0,t)}{\partial x} = 0 \end{aligned} \tag{5.11}$$

Where $k = K/\rho c = 2.7206 \times 10^{-5}$ is thermal diffusivity and $\omega_0(x)$ is the initial distribution of transient term at time $t = 0$. Separation of variables is applied to solve the partial differential equation, $\omega(x) = X(x)T(t)$, which leads to,

$$\frac{X''}{X} = \frac{T''}{kT} = \lambda = -\frac{\beta^2}{L^2} \tag{5.12}$$

That equation indicates that X and T are independent with each other. The prime indicates differentiation with respect to distance and time. With the boundary

conditions, set $X'(0) = 0$; $X_n = B_n cos(\beta_n x/L)$; $X'(1) + X(1)\frac{H}{K} = 0$ and then substitute X_n into Equation (5.12) to get $\beta_n tan\beta_n = \frac{HL}{K}$. From this solution, the root for β_n with the known H, L and K can be solved (Figure 5.5).

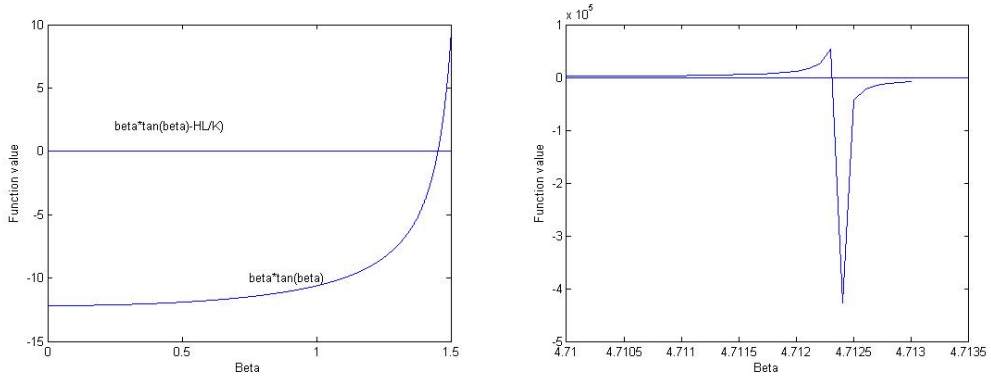

Figure 5.5.: (a) The first root of β=1.42; (b) the second root of β= 4.7099.

Next, get the solution for X, and solve the $T_n = A_n e^{-kt{\beta_n}^2/L^2}$. Now, get $\omega_n = X_n T_n = C_n cos(\beta_n x/L) e^{(-kt{\beta_n}^2/L^2)}$. Then,

$$\omega(x,t) = C_0 + \sum_{n=1}^{\inf} \omega_n = C_0 + \sum_{n=1}^{\inf} C_n cos(\beta_n x/L) e^{(-kt{\beta_n}^2/L^2)} \tag{5.13}$$

And then,

$$\omega(x,0) = C_0 + \sum_{n=1}^{\inf} C_n cos(\beta_n x/L) \tag{5.14}$$

$$C_n = \frac{2S_0L^2}{K\beta_n} sin\beta_n - \frac{2S_0L^2}{K{\beta_n}^3} sin\beta_n - \frac{2S_0L}{\beta_n H} sin\beta_n \tag{5.15}$$

After this, the solution of the transient temperature distribution of rubber bushing can be given as,

$$T = T^* + \omega(x,t) = -\frac{S_0x^2}{2K} + \frac{S_0L^2}{2K} + T_0 + \frac{S_0L}{H} + \sum_{n=1}^{\inf} C_n cos(\beta_n x/L) e^{(-kt{\beta_n}^2/L^2)} \tag{5.16}$$

With this equation, the time elapsed before the system reaching to thermal equilibrium can be estimated. It is accepted that the first item of the Fourier series dominates the temperature distribution (Trivisonno, 1972). Thus, the root of $n = 1$ is calculated here to plot the distribution of temperature in the rubber bushing.

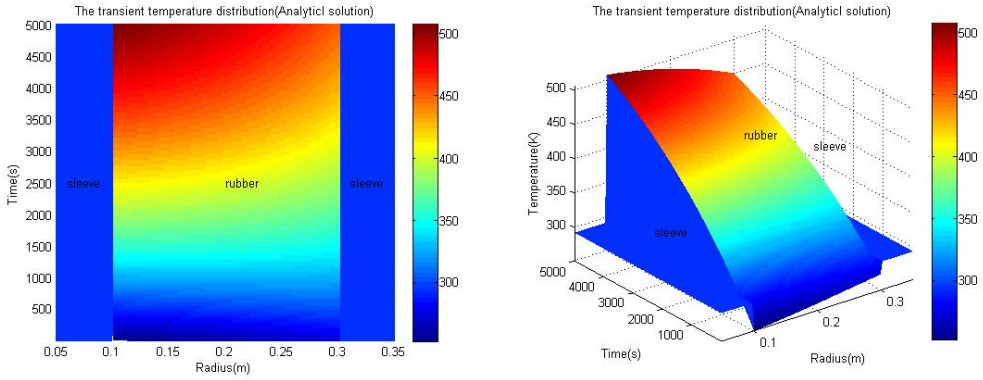

Figure 5.6.: Temperature distribution considering the first term in the Fourier series.

According to the conventional definition, when the exponential part is close to 1, the temperature in the studied case turns to stable, which is expressed as,

$$kt{\beta_1}^2/L^2 = 1 \tag{5.17}$$

The obtained $t = 4.5573 \times 10^3$ is the time needed to keep the thermal equilibrium inside the rubber bushing in current example.

Figure 5.7 gives the temperature distribution at equilibrium time considering one or two terms of the Fourier series. That result indicates the approximation with one Fourier term is enough to estimate the temperature distribution.

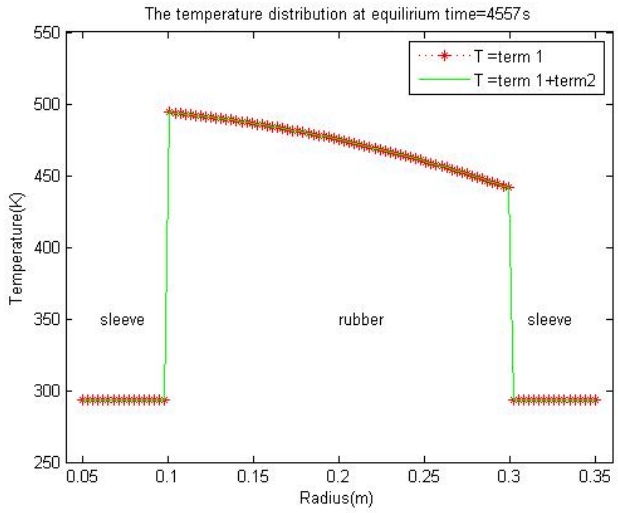

Figure 5.7.: Temperature distribution at equilibrium time.

5.2.2 Numerical Solution Based on the Dissipation Energy Distribution

Before the thermal-structure analysis, the rubber bushing model is built. Considering the geometry of the cylindrical rubber bushing and negligible heat transfer in axial direction, just the cross section of the rubber bushing is applied in current simulation. To keep the consistency, the mesh of the cross section should tally with the mesh in the FEA simulation since the density of the heat source is on the basis of each element. It is better to have fine mesh on rubber core and coarse mesh on steel sleeve. Whereas the thickness of the steel sleeves is pretty small, fine mesh is necessary to guarantee the convergence and reliable results.

Structure analysis is the first step to estimate the heat generation rate. The load is applied on the outer surface of steel sleeves to simulate the external harmonic loading on the rubber bushing. Heat generation comes from the hysteresis damping and viscous damping inside the rubber core and the thermal properties has been presented in the previous discussion.

With the heat generation derived from the structure analysis, the MATLAB thermal analysis can be lunched. It is important to notice that the heat generation is frequency and temperature-dependent. Nonetheless, in this research, only frequency and amplitude influence are considered because the limited experimental data collection to verify the MATLAB program.

The grid generation of rubber bushing for the heat transfer analysis is shown in Figure 5.8.

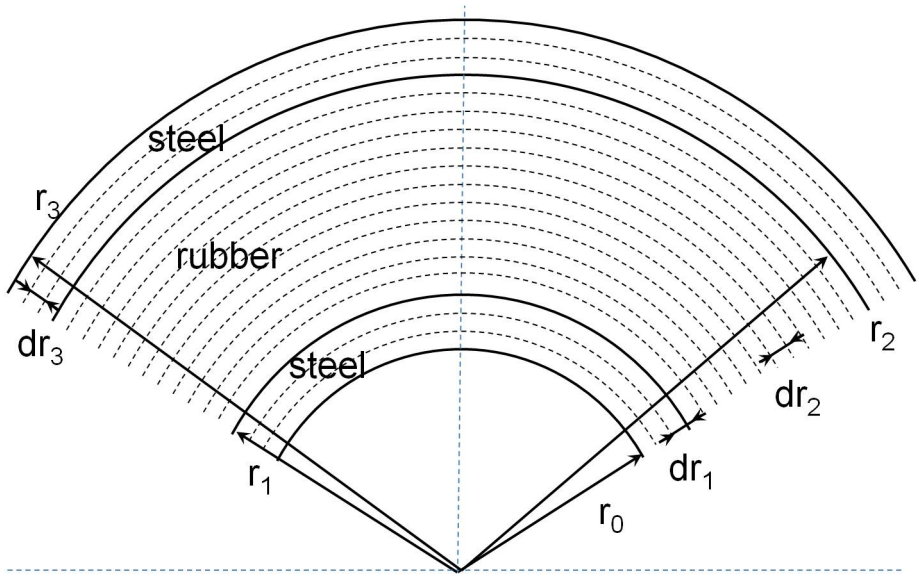

Figure 5.8.: Arrangement of control volumes in radial direction.

In the cylindrical coordination system, the governing equation of transient heat transfer problem is given as,

$$\rho c \frac{\partial T}{\partial t} = \frac{\partial}{dx}(\lambda \frac{\partial T}{\partial x}) + \frac{1}{r}\frac{\partial}{\partial r}(r\lambda \frac{\partial T}{\partial r}) + S \tag{5.18}$$

In the following discussion, the heat flux density is uniform in each control volume and the implicit scheme is employed. Integrate over the control volume in the Figure 5.9 and over the time from t to $t + \Delta t$. In order to finish the integration, the distribution of T with time can be represented using the current T and the old T, which are indicated as,

$$\int_t^{t+\Delta t} T dt = [fT^{t+\Delta t} + (1-f)T^t]\Delta t = [fT + (1-f)T^0]\Delta t \tag{5.19}$$

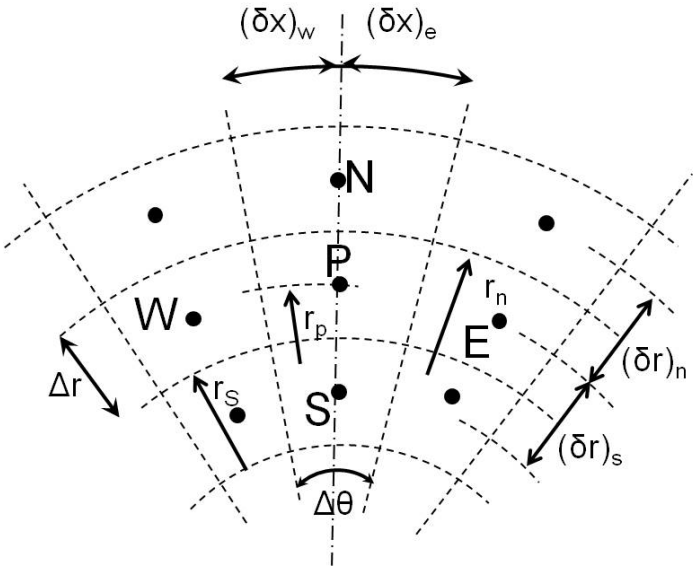

Figure 5.9.: Grid system of cylindrical axisymmetric coordinate.

For convenience, the super script $t + \Delta t$ is deleted and t replaced with 0. In the following discussion, f is the weight factor. f=0, 1, and $\frac{1}{2}$ represent the explicit, implicit and crank-Nicolson algorithm respectively. First, integrate the transient term,

$$\int_s^n \int_w^e \int_t^{t+\Delta t} \rho c \frac{\partial T}{\partial t} dr dx dt = (\rho c)_p \times (T_p - T^0{}_p)\Delta x \Delta r \tag{5.20}$$

Then, the diffusion term,

$$\begin{aligned} &\int_t^{t+\Delta t} \int_s^n \int_w^e \frac{\partial}{\partial x}(\lambda \frac{\partial T}{\partial x}) dr dx dt + \int_t^{t+\Delta t} \int_s^n \int_w^e \frac{1}{r}\frac{\partial}{\partial r}(r\lambda \frac{\partial T}{\partial r}) dr dx dt \\ &= \left[\lambda_e \frac{T_E - T_p}{(\delta x)_e} - \lambda_w \frac{T_p - T_w}{(\delta x)_w}\right] \Delta r \Delta t + \left[\lambda_n \frac{T_n - T_p}{(\delta r)_n} - \lambda_s \frac{T_p - T_s}{(\delta r)_s}\right] \Delta x \Delta t \end{aligned} \tag{5.21}$$

Later, the source term,

$$\int_s^n \int_w^e \int_t^{t+\Delta t} S dr dx dt = (S_c + S_p T_p)_p \Delta x \Delta r \Delta t \tag{5.22}$$

Reorganize the integration to get,

$$a_p T_p = a_E T_E + a_W T_W + a_N T_N + a_S T_S + b \tag{5.23}$$

Where $a_E = \frac{r_p \Delta_r}{(\delta x)_e / \lambda_e}$; $a_W = \frac{r_p \Delta_r}{(\delta x)_W / \lambda_W}$; $a_N = \frac{r_n \Delta_x}{(\delta x)_N / \lambda_N}$; and $a_S = \frac{r_s \Delta_x}{(\delta x)_S / \lambda_S}$. Solve this equation to get

$$a_p = a_E + a_W + a_N + a_S + a^0 p - S_p \Delta V \tag{5.24}$$

Where $a^0 p = \frac{(\rho c)_p \Delta V}{\Delta t}$, $b = S_c \Delta V + a_p^0 T_p^0$ and $\Delta V = 0.5(r_n + r_s)\Delta r \Delta x$.

The schematic diagram about the boundary between rubber bushing and air is displayed in Figure 5.10.

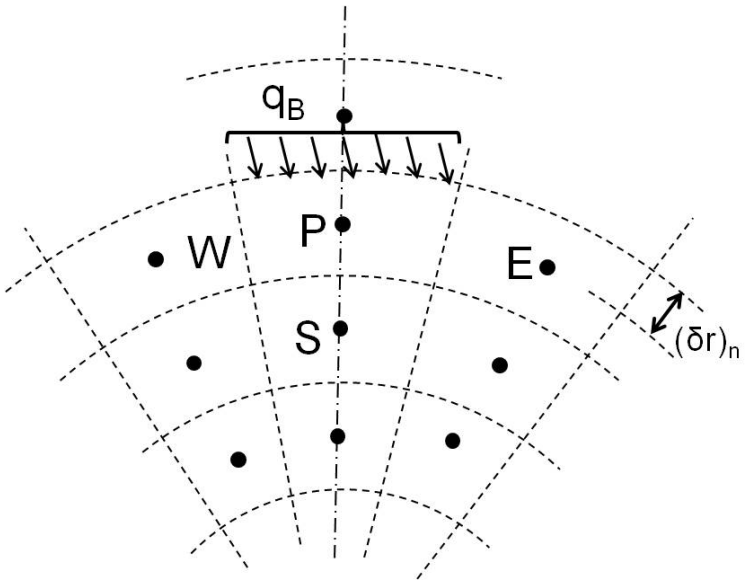

Figure 5.10.: Schematic diagram of boundary between rubber bushing and air.

This is the third type of boundary conditions. The temperature in the air is assumed as room temperature, which is defined as constant. Additional source term method is applied here to describe the boundary temperature.

$$(a_p - a_N) T_p = a_E T_E + a_W T_W + a_N (T_N - T_p) + a_S T_S + b \tag{5.25}$$

Where $a_N(T_N - T_p) = \frac{r_n \Delta_r (T_N - T_p)}{(\delta_r)_n / \lambda_n} = q_B \Delta_r$, then the governing equation turns to $a'_p T_p = a_E T_E + a_W T_W + q_B \Delta_r + a_s T_s + b$. In current case, assume the $q_B = h(T_f - T_N)$ and $q_B = \frac{r_n (T_N - T_p)}{(\delta r)_n / \lambda_n}$. From the Fourier law, we have $q_B = \frac{T_f - T_N}{1/h} = \frac{T_N - T_p}{(\delta r)_n / \lambda_n r_n} = \frac{T_f - T_p}{1/h + (\delta r)_n / \lambda_n r_n}$. Thus, as to this boundary, the iteration equation can be written down as,

$$\left(a'_p + \frac{\Delta_r}{1/h + (\delta r)_n / \lambda_n r_n} \right) T_p = a_E T_E + a_W T_W + \frac{T_p}{1/h + (\delta r)_n / \lambda_n r_n} \Delta_r + a_S T_s + b \tag{5.26}$$

This equation can be applied to the three materials for their inner surface nodes. Now, consider the second type of boundary condition. When the thermal properties of the two materials in the interface are different, there are two approaches to approximate the properties of thermal conduction. A more directed method is treating the step face as the interface of two control volume and later, using harmonic mean to estimate the thermal conductivity. Generally speaking, the second method will give more concise results. In this method, the step face is set as a node. By doing this, the temperature gradient at the two sides of the step face is different. First, analyze the step face between outer steel sleeves and rubber in Figure 5.11.

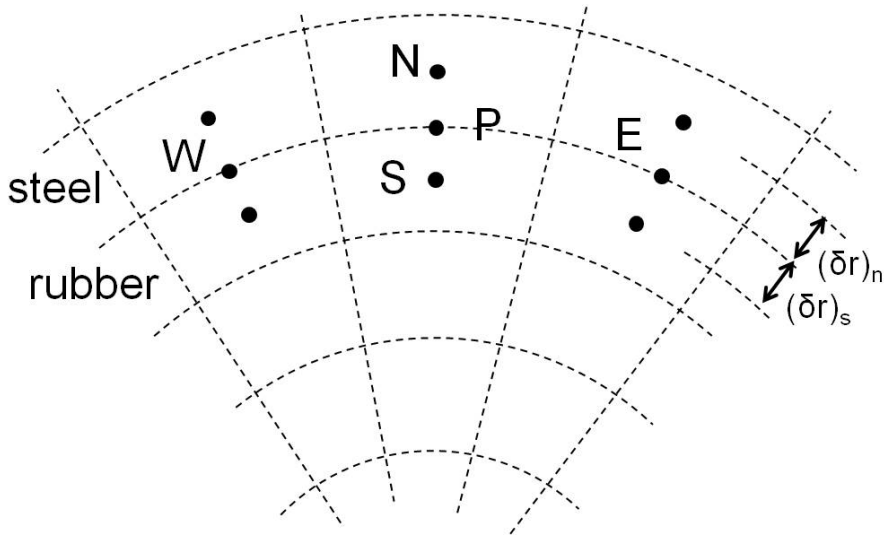

Figure 5.11.: The treatment of interface nodes of different materials properties.

That sketch shows the treatment of interface nodes when the materials properties is changed. For steel, without heat source, the thermal equilibrium is written as,

$$a_p = a_E + a_W + a_N + a_S + a^0 p - S_p 0.5(r_n + r + s)\Delta r_s \Delta x \tag{5.27}$$

$$b = S_c 0.5(r_n + r_s)\Delta r_s \Delta x + a^0 p T^0 p \tag{5.28}$$

Now, about the boundary between rubber bushing and air, the schematic diagram is displayed in Figure 5.10. Since it is hard to estimate the heat conduction coefficient at the interface for the heat conduction in radial direction, thus, the harmonic method is applied here. If just consider the node in steel, the $q_B = \frac{r_n(T_N - T_p)}{(\delta r)_n/\lambda_n}$ and again consider the node in rubber, the $q_B = \frac{r_s(T_p - T_s)}{(\delta r)_s/\lambda_s}$. According to the Fourier law, the heat flux at the interface can be written as $q_B = \frac{r_s(T_N - T_S)}{(\delta r)_n/\lambda_n r_n + (\delta r)_s/\lambda_s r_s}$.

With the density of dissipation energy generated from the Simplex program in Chapter four, the temperature distribution of the rubber bushing′ cross section is presented in Figure 5.12. From the previous discussion, the excitation frequency of driving vehicle is about 10Hz and the heat generate rate is periodical. The accumulated dissipation energy can cause the rising of temperature over time. The maximum temperature of rubber bushing changes from 315K, 330K, and 340K to 350K at loading time 600s, 1800s, 3600s and 7200s. At the beginning, the temperature rise quickly and concentrates around the tensile loading zone. Because of the low heat conductivity of rubber core, the temperature gradient inside the rubber core is much larger than that in the steel sleeves. If the rubber bushing′s heat conductivity is 10 times higher, the temperature distribution of rubber core should be much more uniform from the very beginning and the heat concentration effect could be minimized.

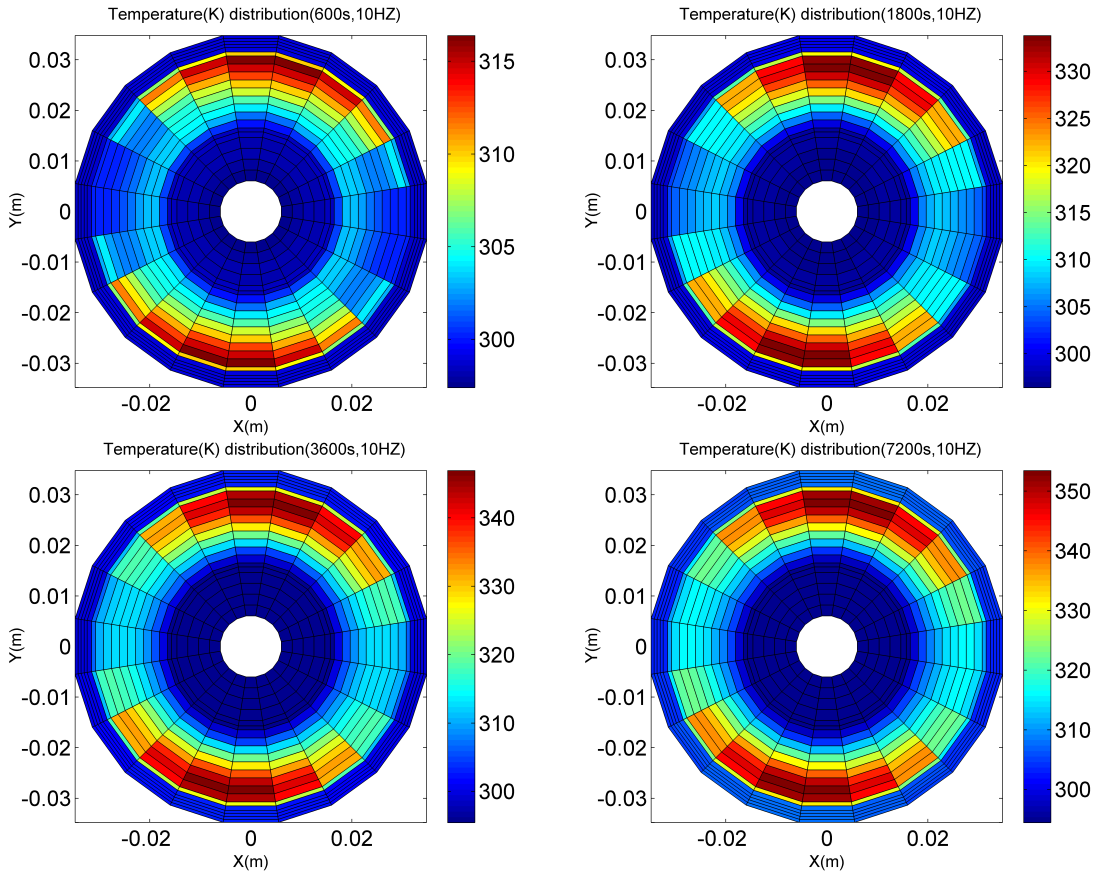

Figure 5.12.: Surface temperature distribution of the rubber bushing at 10Hz; (a)600s; (b)1800s; (c)3600s; (d) 7200s.

Figure 5.13 compares the amplitude effect on the temperature distribution of rubber bushing under harmonic loading at 10Hz and after 120s. The maximum temperature is about 303K when amplitude is set at 1mm. When the amplitude is set at 2mm, the maximum temperature near the loading zone is about 315K, which is similar to the temperature distribution at 10Hz, 1mm and after 600s. This comparison indicates that twice the amplitude can greatly shorten the time needed to reach the expected temperature.

Figure 5.14 compares the frequency effect on the temperature distribution of rubber bushing at the same loading and after 120s. With the increase of frequency, the amplitude of excitation decreases due to the frequency-dependent modulus of

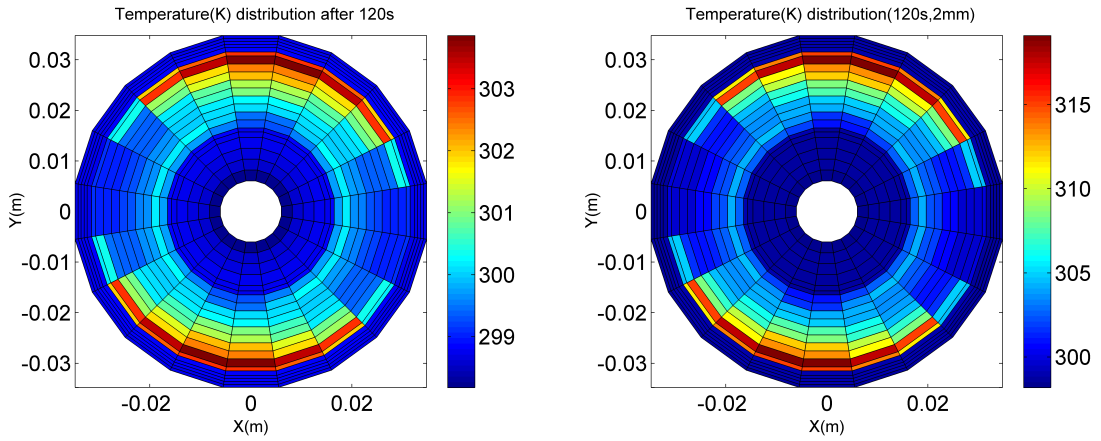

Figure 5.13.: Temperature distribution of rubber core at amplitude (a) 1mm; (b) 2mm.

rubber core. The amplitude deceases from 0.8mm, 0.688mm to 0.622mm as excitation frequency changes from 30Hz, 60Hz to 90Hz. Since the modulus increases quickly in the range $0 \sim 45Hz$, then grows slowly in the range of $45 \sim 90$Hz, and finally almost reaches to constant after 90Hz, the amplitude drops much more from 30Hz to 60Hz than that from 60Hz to 90Hz. From the previous analysis, the decrease of amplitude means the lower dissipation energy density in one cycle. However, the higher dissipation energy in unit time at higher frequency makes the accumulated heat source at higher frequency overwhelms that at the lower frequency. As a result, the temperature distribution is higher at 90Hz compared with that at 30Hz excitation. When the frequency is higher than 90Hz, the modulus is frequency-independent and the amplitude can keep constant over the frequency range. Then, the increase of frequency can generate more dissipation energy in unit time and cause higher temperature distribution.

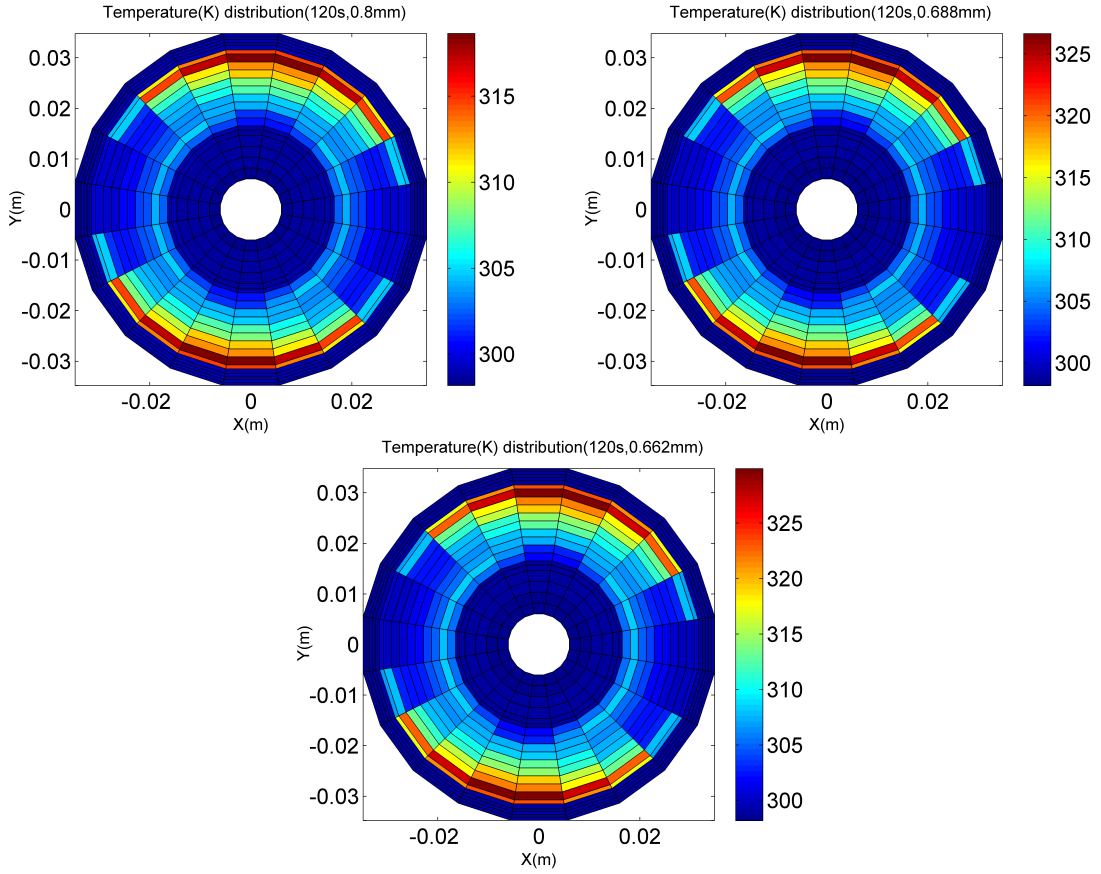

Figure 5.14.: Temperature distribution of rubber core (a) 30Hz; (b) 60Hz; (c) 90Hz.

5.3 Conclusion

The thermal properties of rubber are reviewed and the corresponding thermal properties are measured using TPS. On the basis of the dissipation energy density calculated from the Simplex program at various amplitude and frequency, the temperature distribution of the rubber bushing is estimated in this chapter. In the initial work, the analytical solution of the temperature distribution is discussed in the case of uniform heat source. Later, numerical solution is developed using finite volume method to predict the temperature distribution at different amplitude and frequency. The FVM allows different heat source at each volume, which method gives more authentic temperature distribution. Thus, the second approach is more

applicable in view of the nonuniform dissipation energy density of rubber core. The simulation results indicate the influence of amplitude overwhelms the effect of frequency at 10Hz. In the low frequency range, with the increase of frequency, the loading should be increased to keep the expected excitation amplitude. At high frequency, when the modulus is not frequency-dependent any more, the influence of frequency on the temperature distribution attributes to the increasing heat generation at per unit time.

CHAPTER 6. COMSOL SIMULATION AND EXPERIMENTAL DYNAMIC TESTINGS

6.1 FEA Simulation with COMSOL

Vehicle driving condition is used to refer the dynamic behaviors of rubber bushing installed on the suspension system. For a frequently retreated truck tire, the general service life is about 1 million Km, which means $300 \sim 500$ million cycles considering the larger diameter of tire (LaClair & Zarak, 2005). Rubber bushing follows the cycle rate of tire but bushings are rarely replaced compared with tire. Considering the behaviors, the serving life of rubber bushing is much higher and its durability is much more critically dependent on the design and material properties. Considering the complicated condition of tire rolling, the Fourier series presenting stress and strain are applicable, but the commonly employed linearized complex modulus still leads to certain error, as a result, the further FEA simulation may involve perturbations.

The dissipative properties of viscoelastic materials under harmonic excitation can be represented in three ways, power law, tabular input and Prony series expression with shear and bulk relaxation modules. In the current commonly used FEA commercial software, such as COMSOL and Abaqus FEA, the implemented viscoelastic models are mainly generalized Maxwell model, which is conveniently represented using the Prony series.

6.1.1 Prony Series Parameters and Thermal properties

In this research, the FEA simulation with COMSOL is carried out to elaborate the heat generation rate and temperature distribution of rubber bushing. The experimental identified parameters are taken to characterize the Prony series of the standard linear model. In this part, Berg′ model is employed to include the frequency dependent part viscous damping and the amplitude dependent hysteresis damping to calculate the energy accumulation. Prony series are used to present the shear stress relaxation modulus and bulk modulus. The general expression is,

$$G\left(t\right) = G\left(\infty\right) + \sum_{i=1}^{N} G_i exp^{(-\frac{t}{\tau_i})} \tag{6.1}$$

Where τ_i is the relaxation time for each exponential components, $G\left(\infty\right)$ is the modulus when t is approximated to infinite and $G(0)$ is the initial modulus at $t = 0^+$. The Prony series is also commonly represented with the normalized dimensionless relative modulus,

$$g_R(t) = \frac{G_R(t)}{G(0)} = \frac{G\left(\infty\right) + \sum_{i=1}^{N} G_i exp^{(-\frac{t}{\tau_i})}}{G\left(\infty\right) + \sum_{i=1}^{N} G_i} = 1 - \sum_{i=1}^{N} g_i[1 - exp^{(-\frac{t}{\tau_i})}] \tag{6.2}$$

Where $g_i(t) = \frac{G_i(t)}{G(0)}$ and $\sum_1^N g_i(t) = 1$. Here, the model used in current analysis is the standard linear model, which is the simplest generalized Maxwell model. The relaxation modulus derived in previous can be applied directly in COMSOL to characterize stress and strain relationship of viscoelastic material.

As to the viscoelastic material, Poisson′s ratio is time dependent, $\mu = \mu(t)$. Considering the very tiny variation of Poisson′s ratio with time and the economy of optimization, constant μ is also a reasonable selection. μ is defined as 0.475 for the following calculations as done in the Simplex program.

The outer sleeve is exposed to the air and the proper estimation of the convection coefficient for a high speed driving truck is also pretty troublesome. Browne carried out parametric study to probe the factors affecting the convective heat transfer coefficients (Browne & Wickliffe, 1980). That research indicated that air flow velocity, tire surface size and conditions, such as surface roughness, wetness

and cleanliness affects the effective convective heat transfer coefficients. Per influence was characterized qualitatively but no conclusive parameterized expression was built to facilitate the further prediction of heat transfer coefficients with known parameters of tire. For the limited experimental platform, the empirical value is chosen in COMSOL for the convection coefficient in the air.

The inner steel sleeve is installed on the stabilizing bar and its heat transfer is characterized as conductive. There are two approaches to describe the interface between inner sleeve and stabilizing bar. One simplified method defines the interface as adiabatic and the corresponding heat transfer coefficient is zero. This treatment approaches to the real situation in the case of tight connection between inner sleeve and stabilizing bar. While, in some rubber components, the gap between stabilizing bar and inner sleeve allows the air convection, which affects heat transfer. At to latter situation, the nonzero but much smaller heat transfer coefficient compared with the outer sleeve is adopted by many researchers. It is obviously to found that the inner sleeve coefficient is driving speed-dependent and a proportional coefficient can be chosen to describe the heat transfer coefficient. In all, precise heat transfer coefficient is extremely needed to correctly predict the temperature distribution of rubber bushing during service. But to have credible temperature distribution, the stress and strain of rubber bushing is prerequisites.

Because of the strain or amplitude dependence of the rubber components, characterization of rubber materials is critical in predicting the energy dissipation during the working conditions. The amplitude dependency of hysteresis damping upon the quasi-static excitation shows the decreasing modulus at high amplitude. Furthermore, the viscoelastic behaviors of rubber elements are temperature dependent, which implies the thermal-structure coupling analysis in the next FEA discussion. Frequency affects the storage and loss modulus, but has little effect on tan delta. Based on the linear complex modulus model, the strain under harmonic excitation can be calculated easily. Generally speaking, the out of phase stress and strain under harmonic excitation can be specified to facilitate the further analysis

(Mark, Erman, & Roland, 2013). Ebbott proposed the linearized viscoelasticity to describe the hysteresis loops and estimate the energy dissipation by taking the mid line as a straight line because the linear complex modulus of the viscoelastic materials was on the basis of small deformation and linear viscoelastic theory (Ebbott et al., 1999). The rheological generalized model, such as generalized Maxwell model or the developed models was investigated by many researchers. Lin proposed to build instantaneous stress response using the material time derivative of the Kirchhoff stress and logarithmic strain (R. Lin, 2001). In the following discussion, the thermal-structure FEA analysis is based on the standard linear model and the harmonic excitation assumption.

6.1.2 Stress and Thermal Results With COMSOL

Some assumptions and simplifications are made for the simulation.

1): Owing to the geometric symmetry, half of the rubber bushing is modeled.

2): The rubber bushing is composed of three layers, rubber, inner and outer steel sleeves. The two steel sleeves are of the same material properties and the outer steel sleeve is exposed in the air.

3): Rubber core is assumed to be isotropic, homogeneous, and incompressible and displays viscoelastic properties during the working temperature range.

4): The harmonic excitation is applied vertically on the external surface of the outer steel sleeve and the inner steel sleeve is fixed.

The linear viscoelastic properties are expressed in Prony series on the basis of the standard linear model. The Mooney-Rivlin constant is calculated using the Yeoh model to characterize the large strain or lager deformation which is non-monotone and nonlinear (Yeoh, 1993). With the data obtained from the MTS, the three coefficients C_{i0} are indentified for the Mooney-Rivlin model. The structure and thermal coupling analysis is separated in two steps. The first step is the dynamic structure analysis by applying external harmonic excitation on rubber

bushing. Due the damping effect, part of the input energy is saved as dissipation energy and accumulated in the rubber core. The second step is the time dependent thermal analysis by setting the generated dissipation energy as the heat source. The other end of the rubber bushing is fixed and thermal insulated, that means zero displacement and room temperature all the time. The simulation results are shown in Figure 6.1. After 20s, the two surfaces of rubber core present the maximum displacement and higher temperature.

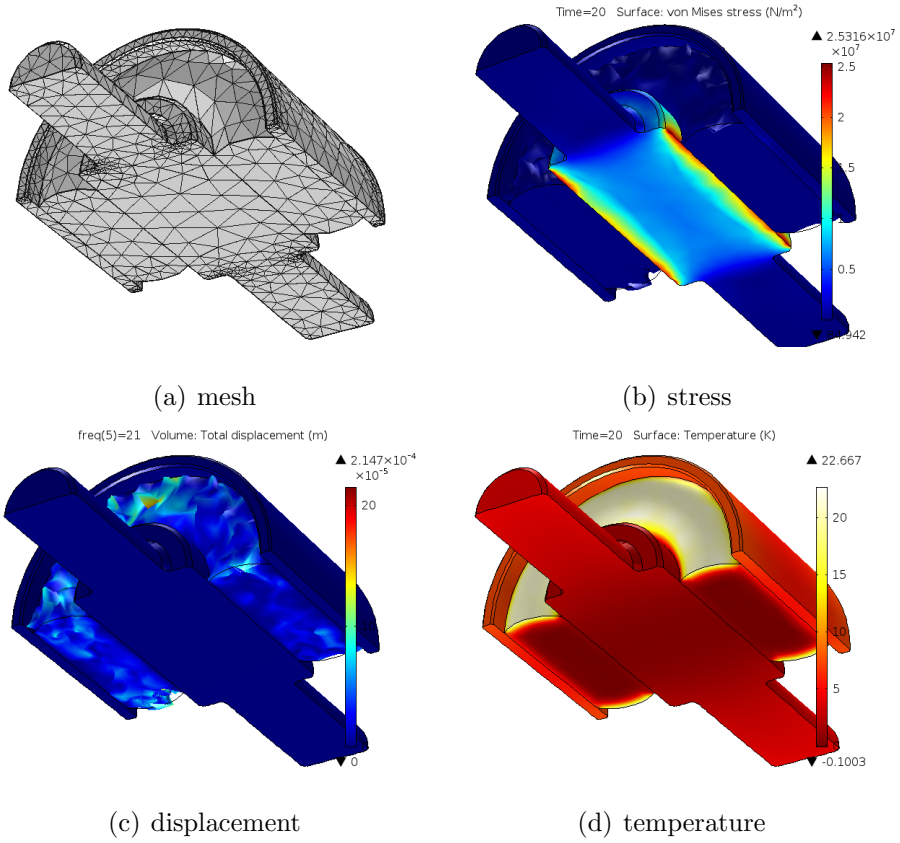

(a) mesh (b) stress

(c) displacement (d) temperature

Figure 6.1.: COMSOL simulation results.

6.2 Dynamic Radial Test and Temperature Distribution

The Mullins effect can be avoided after loading and unloading several times before running the specified testing. The stress softening in the first deformation at high strain disappears after the pre-loading. Sometimes, the static strain is applied before the dynamic loading, for example, the pre-deformation of rubber maybe 30%. Generally, the influence of frequency on modulus is pretty trivial at the static strain. Considering the pre-deformation of rubber bushing, if the dynamic behavior is affected by the static strain, then, the dynamic behaviors should be the reconsider.

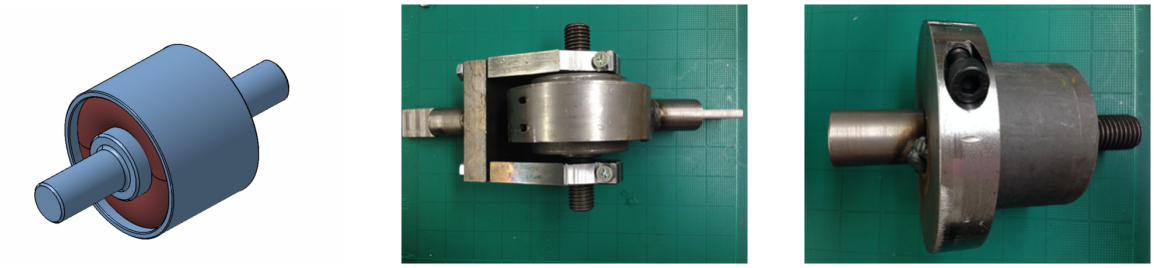

(a) Rubber bushing (b) Tension/compression (c) Torsion

Figure 6.2.: Fixture for MTS dynamic test.

The FEA simulation with Simplex program and COMSOL has shown the temperature rising over time under the dynamic loading. The temperature rising of the rubber core under the single frequency excitation attributes to the aging speed up or failure of rubber bushing. Dynamic radial testing and torsion testing have been carried out to verify the temperature distribution of rubber bushing. The dynamic test instruments have restricted requirements about the sample dimensions. The fixtures made for the radial and torsion dynamic testing are designed and machined in MDL lab to fit the clamps of MTS. Figure 6.2(a) shows the original geometry of the rubber bushing, and Figure 6.2(b) and (c) are samples with fixture for radial and torsion testing separately.

6.2.1 Dynamic Radial Testing Parameters and Results

The test components should be mechanically conditioned before starting the test program to eliminate the Mullin′s effect. One method to eliminate the effect is setting the maximum displacement or load and then applying 10 cycles on the previously unstrained rubber components. The servo-hydraulic test instrument with upper and lower rigid cross head for the dynamic radial testing is shown in Figure 6.3. The thermal imager is fixed on the platform with two magnetic indicator holders to record the temperature variation during the dynamic test. In order to guarantee the accuracy of the measured displacement, rubber cushion is installed between the instrument and the table to minimize the transmission of vibration from the test instrument to platform.

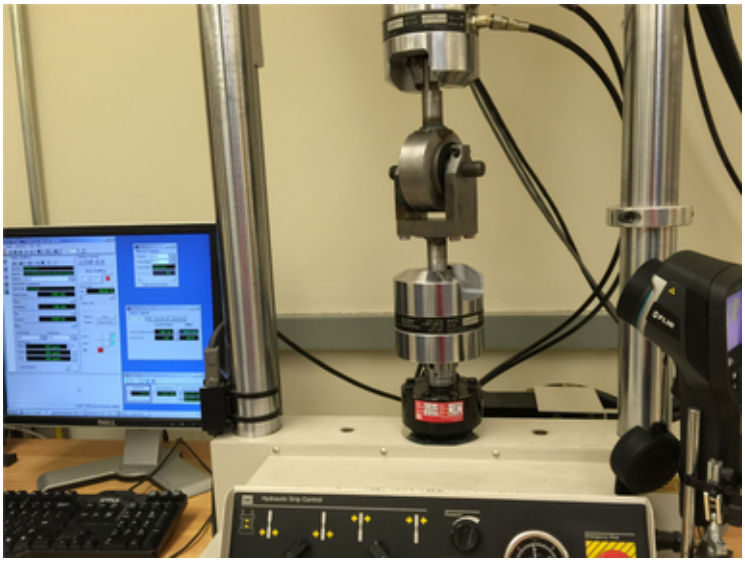

Figure 6.3.: Dynamic radial testing equipment.

6.2.1.1. Quasi-static Test

The quasi-static deformation usually performs at larger displacement and lower frequency, such as 1Hz and 1mm displacement. The rate of quasi-static test for current component should be less than 0.05mm/s. At least three cycles are recorded

to obtain reliable data. The recommended frequency and amplitude are represented in Table 6.1.

Table 6.1: Quasi-static radial test parameters

$TestNo.$	1	2	3	4	5	6
$Amplitude(mm)$	0.01	0.05	0.1	0.01	0.05	0.1
$Frequency(Hz)$	1	0.2	0.1	0.05	0.03	0.01

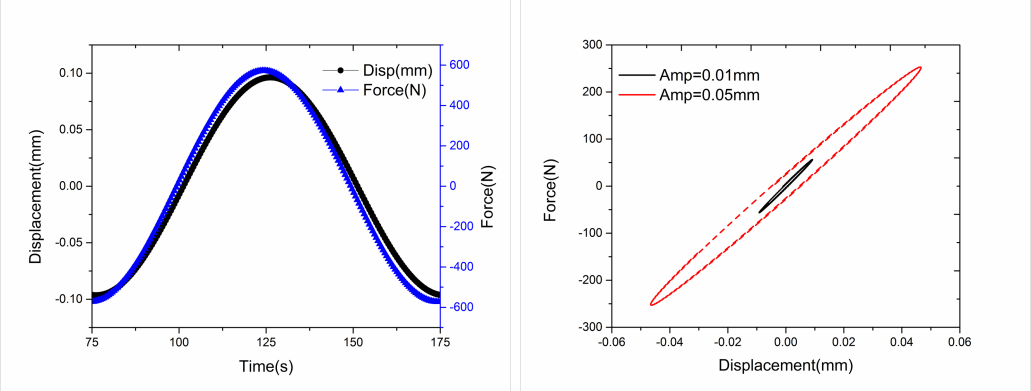

Figure 6.4.: Quasi-static test (a) Out of phase at 0.01Hz and amplitude 0.1mm; (b) the amplitude dependence of the stiffness at 0.03Hz.

Figure 6.4(a) shows the out of phase between force and displacement at excitation frequency 0.01Hz. Since the frequency is very low, the two curves are almost in sync except for slightly lagging behind after 100s. The stiffness of rubber bushing at different sinusoidal amplitude is compared in the Figure 6.4(b).The dynamic frequency is set as 0.03Hz to have the quasi-static deformation. Linear fitting generated stiffness of the curve at amplitude 0.01mm is 6149.48(N/mm) and the curve at amplitude 0.05mm is 5414.21(N/mm). With the increase of amplitude, the stiffness of the rubber bushing is decreasing during quasi-static testing.

6.2.1.2. Dynamic Radial Test

Stepped sine displacements is set up to excite the rubber bushing from initial frequency 1Hz and ramping to maximum 100Hz, with frequency step 10Hz and amplitude 0.1mm. The data collecting time for loading condition can be set as 10s.

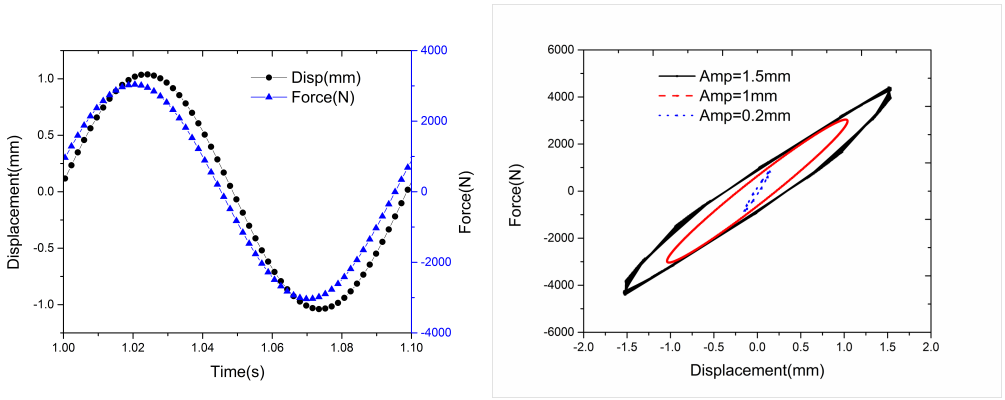

Figure 6.5.: Dynamic test (a) Out of phase at 10Hz and amplitude 1mm; (b) the amplitude dependence of the stiffness at 10Hz.

In order to record the temperature rising, the thermal imager is used during the dynamic test. The amplitude of the dynamic test should be at least 1mm with current test sample. However, the test range of the instrument on campus is failed when the amplitude is set as 2mm. Again, when the excitation frequency is set as 30 or 60Hz, the amplitude will drop to about 0.1mm automatically. Finally, only excitation at 10Hz and 1mm amplitude is successful to record the temperature rising of rubber bushing. The stiffness of amplitude-dependence of rubber bushing at 10Hz is plotted in Figure 6.5.

Compared with Figure 6.4, out-of-phase at 10Hz is more obvious than that at 0.01Hz. Figure 6.4(b) plots the dissipation loop at frequency 10Hz of different amplitude. Compared the loop area form by the excitation at amplitude 1.5mm, the loop area of the excitation at amplitude 0.2mm is negligible. Again, similar to amplitude dependence at quasi-static excitation, the stiffness softening of rubber bushing at dynamic excitation happens as the amplitude increases.

6.2.2 Temperature Distribution under Radial Testing

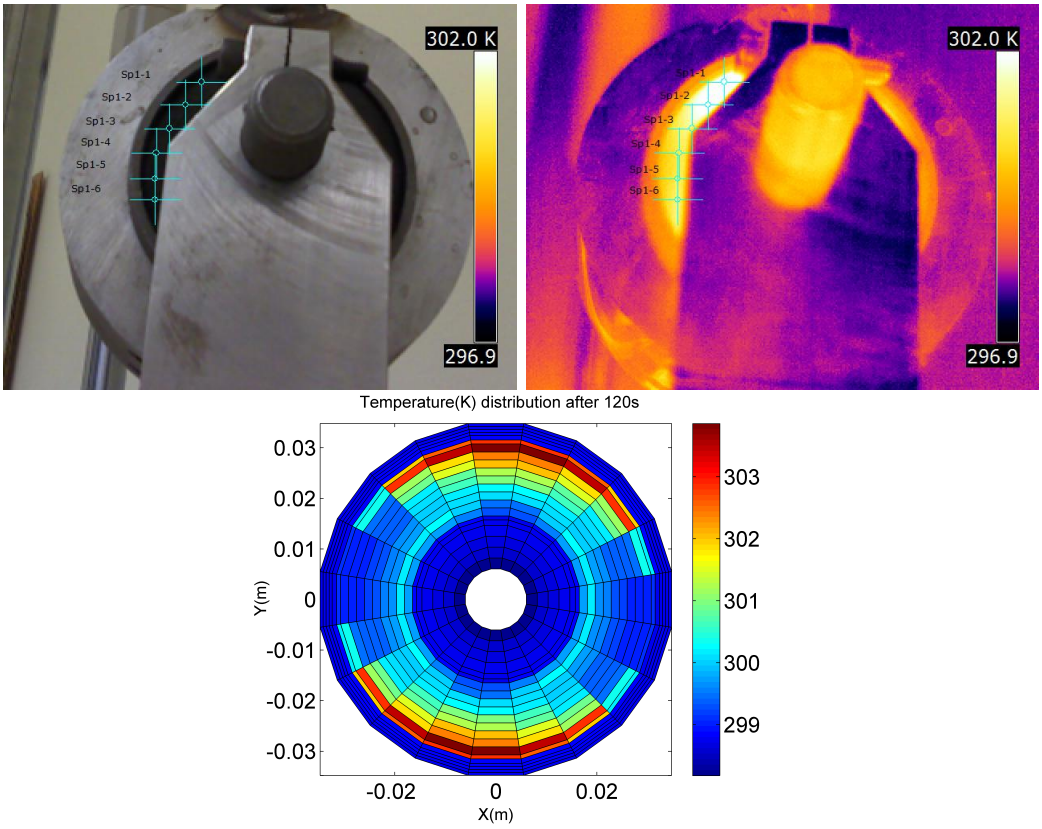

Figure 6.6.: Temperature distribution on the surface of rubber core (a) Digit camera; (b) thermal; (c) numerical simulation.

Figure 6.6 shows the temperature distribution on the surface of the rubber bushing. The room temperature is about $298K$. The thermal picture shows the rising temperature of rubber core under 10Hz excitation. Six points from the top of the rubber core to the bottom of the rubber core are collected and the temperatures are given in Table 6.2. The temperature decreases from the loading area to the central area of the rubber core and then increases gradually near the bottom loading area. Especially, the point 4 and 5 are of the same temperature because they are almost symmetrical over the central horizontal line. Due to the special design of the fixture to fit for the radial test, a majority part of the rubber core has been occluded. The bottom part temperature of the rubber bushing is not detectable,

however, the symmetrical temperature distribution is expected from the current measurement. To compare with the FEA and MATLAB simulation, the temperature distribution at 10Hz, 120s is shown here again. The heat concentration and temperature rising over the 120s obtained from radial testing matches well with the Simplex simulation. Those results confirm the reliability of Simplex to estimate the dissipation energy density and MATLAB to conduct the heat transfer.

Table 6.2: Temperature distribution on the surface of rubber bushing

Points No.	1	2	3	4	5	6
Temp(K)	303.0	302.5	300.8	300.7	300.7	300.9

The pattern of the eight photos in Figure 6.7 is organized from left to right and from top to bottom. For each photo, temperature at three points are collected and plotted in Figure 6.7. With the thermal imager, the temperature rising of the rubber bushing core in 120s has been recorded and shown in Figure 6.8. Point sp3 is near the loading area of the clamp, which has the maximum temperature rising in 120s. Point sp1 is near the central symmetric line and shows the minimum temperature rising in 120s. From previous discussion, it is clear that the temperature of rubber core decreases from the axial loading zone to the central part. The short time recording indicates the more and more larger temperature gradient inside of the rubber core. That loading zone accumulates dissipation energy faster and higher than its surrounding area. Nevertheless, the heat conductivity is relatively slow compared with the fast heat generation rate, thus, the failure of the rubber core may happen at the loading zone.

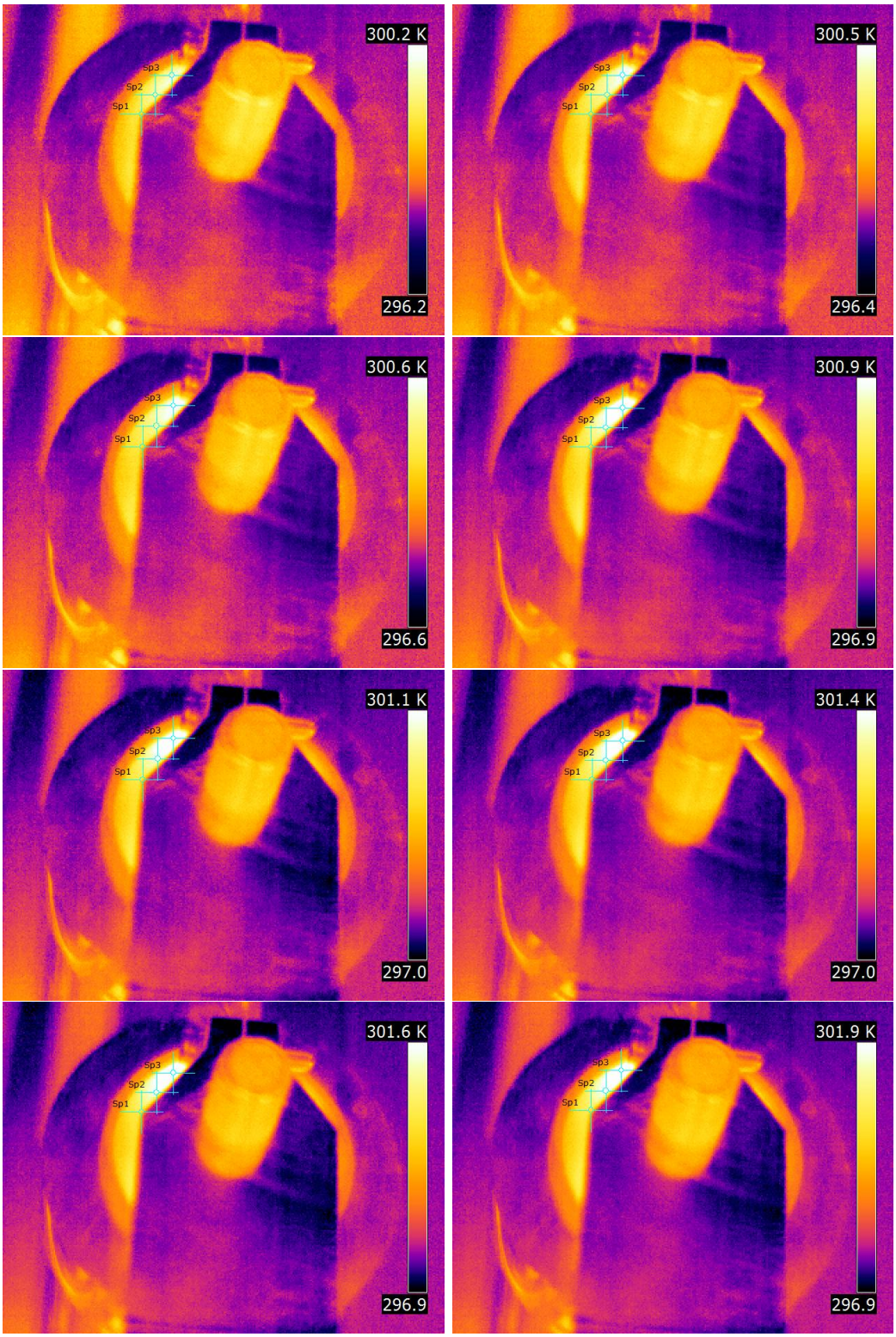

Figure 6.7.: Temperature distribution on the surface of rubber core(a) t=4s; (b) t=15s; (b) t=31s; (b) t=45s; (b) t=58s; (b) t=72s; (b) t=84s; (b) t=99s.

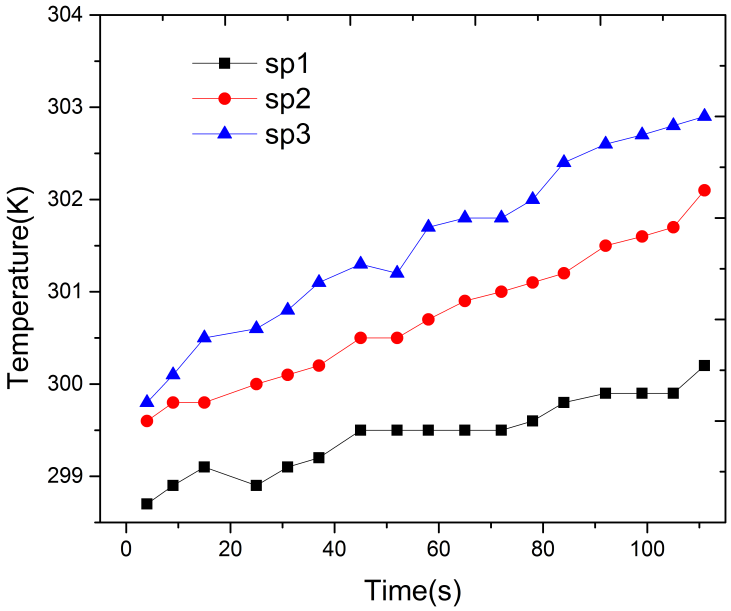

Figure 6.8.: Rubber bushing surface temperature rising over time.

6.3 Dynamic Torsion Testing and Temperature Distribution

Torsion testing is carried out with thermal imager recoding to have more comprehensive analysis about the temperature rising of rubber core under the dynamic harmonica excitation. The multi-axial loading of the rubber bushing implies the mechanic properties and temperature distribution of that state is very significant. Furthermore, compared with the servo-hydraulic radial instrument, the equipment (Figure 6.9) used for torsion test has wider testing range and provides more information for thermal mechanism exploration.

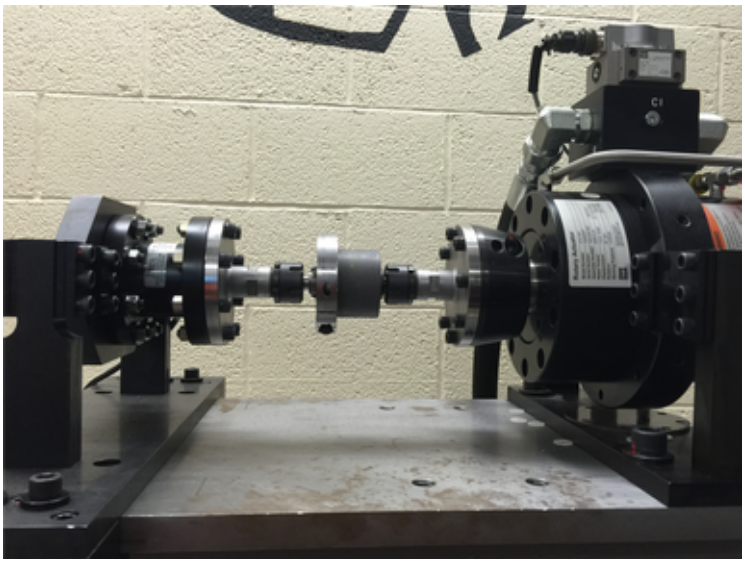

Figure 6.9.: Dynamic torsion testing equipment.

6.3.1 Dynamic Torsion Testing Parameters

To compensate the limited test range of radial testing, the torsion testing is planned in more groups. The detailed test group of different frequency and amplitude are laid out in Table 6.3 and Table 6.4.

Table 6.3: Parameters of quasi-static torsion testing

$Degree(o)$	5	5	5	5	5	5
$Frequency(Hz)$	1	0.2	0.1	0.05	0.03	0.01

Table 6.4: Parameters of dynamic torsion testing

$Degree(o)$	5	5	5	5	5	10	5	5
$Frequency(Hz)$	10	15	20	25	10	10	5	5

The dissipation energy accumulation caused by the out of phase between torque and displacement are shown in Figure 6.10. Figure 6.10(a) compares the torque and amplitude angle at 1Hz, which slightly lags behind of amplitude angle even though the excitation frequency is 1Hz. With the increase of frequency, the phase angle between torque and amplitude angle becomes more obvious.
Figure 6.10(b) and (c) show the dissipation energy loop by plotting the torque against amplitude angle. The frequency 0.01, 0.1 and 1Hz are pretty low and can be treated as quasi-static deformation and almost frequency independent, thus the stiffness of the rubber material decreases with the rising of amplitude. Furthermore, when the frequency changes from 0.01Hz to 0.1Hz, the variation of modulus is negligible. The amplitude angle determines the stiffness and dissipation density per cycle.

6.3.2 Temperature Distribution under Torsion Test

Table 6.5: Temperature distribution at torsional angle 5^o and 10Hz

Points No.	1	2	3	4	5	6	7
Temp(K)	303.2	304.8	306.4	309.1	311.4	309.0	307.5

The temperature gradient in radial is given in Table 6.5. In the radial testing, the heat source is concentrated around the loading zone where displays

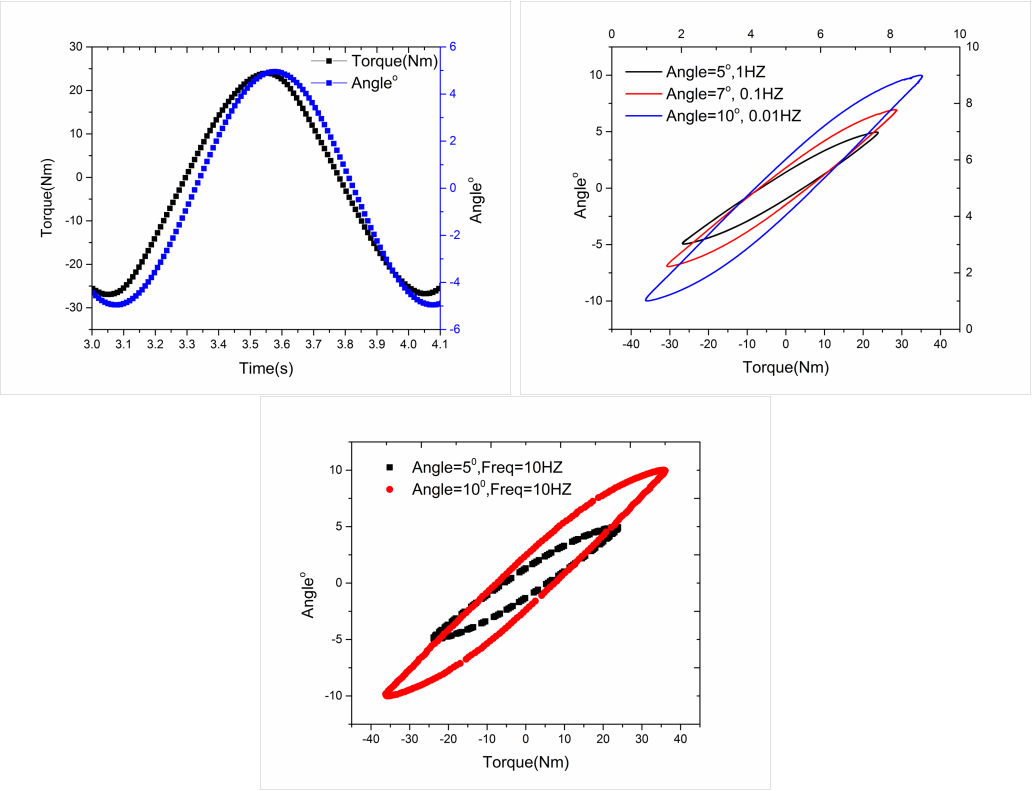

Figure 6.10.: (a)Out of phase ; (b)amplitude dependence at low frequency; (c)amplitude dependence at high frequency.

higher temperature than other area. While in the torsion test, the deformation of rubber core is uniform in circumference and nonuniform in the radial direction.

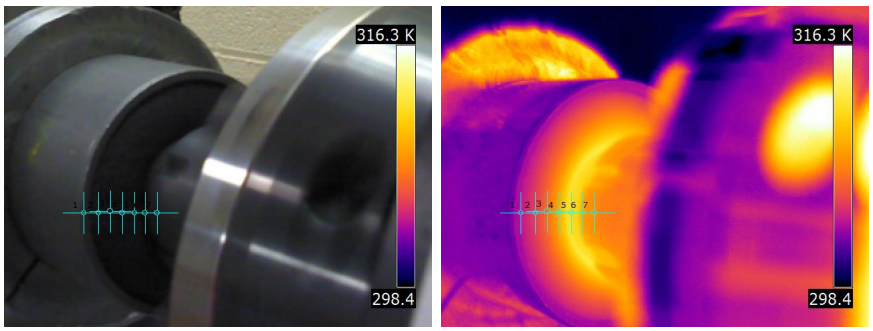

Figure 6.11.: Temperature distribution of rubber bushing at torsional amplitude 5^o and excitation frequency 10Hz (a) Digit camera; (b) thermal.

A group of points are selected in the radial direction (Figure 6.11) to show the variation of temperature. Because the inner surface and outer surface of the rubber core are attached on the steel sleeves and very limited deformation is allowed, the high deformation and higher temperature appear in the middle of the rubber core.

Figure 6.12 records the temperature of rubber bushing over time at amplitude angle 10^o and 10Hz torsional excitation. The maximum temperature shows in the central part of the rubber core, thus, the maximum temperature of the picture also indicates the maximum temperature of rubber bushing. The maximum temperature rises from 326.4 to 331.1K in 48 seconds. While the maximum temperature increases 3K in 120s at 1Hz, which indicates the amplitude angle 10^o is very critical.

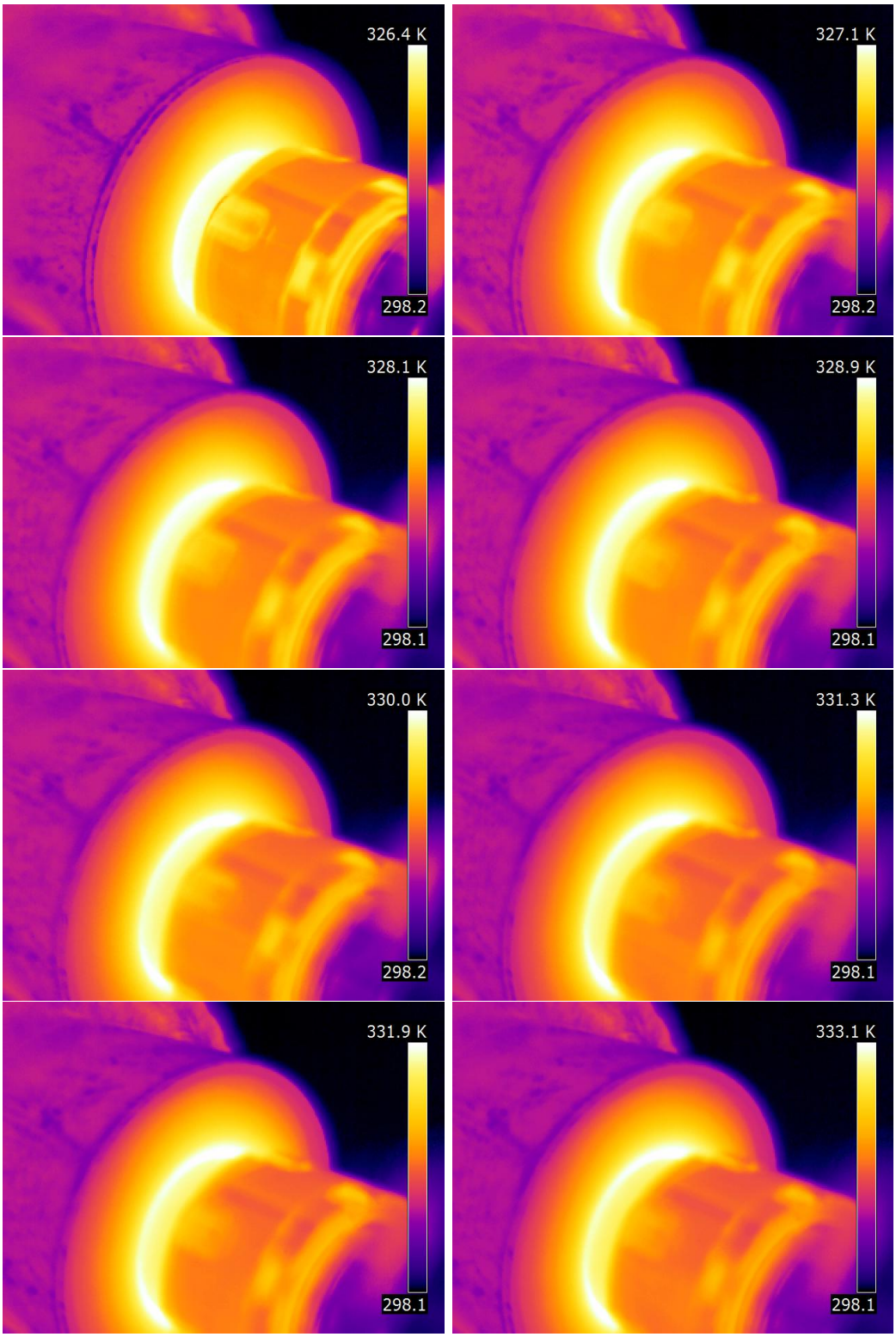

Figure 6.12.: Temperature distribution on the surface of rubber core(a) t=0s; (b) t=8s; (c) t=15s;(d) t=21s;(e) t=27s; (f) t=33s; (g) t=41s; and (h) t=48s.

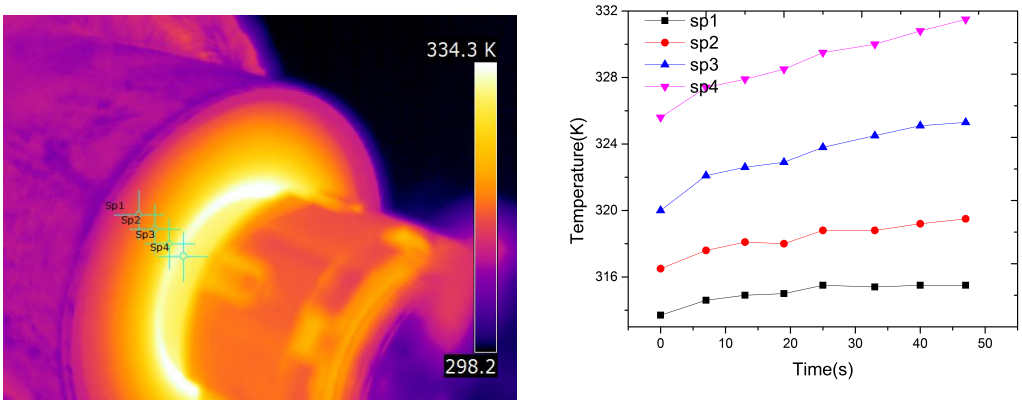

Figure 6.13.: Temperature distribution in the radial direction (a) Four points; (b) temperature rising.

The previous discussion shows different temperature at radial direction as the deformation is confined by the boundary condition of the rubber core. Figure 6.13 shows the temperature rising in the radial direction because of the different dissipation energy density and slow heat conductivity of rubber core. That result indicates that the high temperature zone also has higher temperature rising rate. Generally speaking, the area close to the inner steel sleeves displays heat concentration under the tension loading and becomes the most possible failure area.

Upon the radial testing, the temperature distribution is frequency and amplitude-dependent. Similarly, the torsional testing also shows the similar tendency. Figure 6.14(a) shows the higher temperature rising at amplitude 10^o when the frequency is set as 10Hz. That can be attributed to the higher dissipation energy density per cycle at higher amplitude. The higher frequency 25Hz shows more rising temperature than that at 10Hz when the amplitude angle is set as 5^o. That can be attributed to the higher dissipation energy density per unit time at higher frequency. Figure 6.14(b) shows the temperature rising at different frequency. When the amplitude angle is fixed at 5^o, the torque needed to excite the expected amplitude is different. As the modulus increases with frequency, the torque needed at higher excitation frequency is also higher.

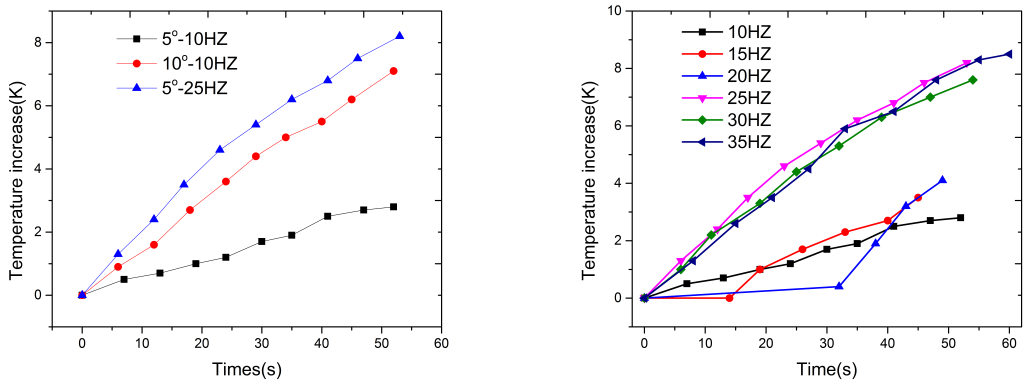

Figure 6.14.: Temperature distribution of rubber bushing (a) The dependence of amplitude degree; (b) the dependence of excitation frequency, amplitude degree 5^o.

During the torsional test, the temperature of rubber busing is affected by the attached driver, which causes the overall temperature rising of rubber bushing. At that time, the heat transfer from the rubber bushing to the surrounding air affects the heat transfer inside the rubber bushing. Thus, the temperature rising at 25Hz, 30Hz and 35Hz are close to each other.

6.4 Conclusion

In this chapter, the FEA using the commercial software is simulation to present the dissipation energy under the harmonic excitation. Prony series to express the mechanical properties of viscoelastic material in time domain is used in current multi-physics software COMSOL. While in order to guarantee the convergence in FEA, the time step is usually small, that means time consuming in order to have long hours temperature distribution. Thus, the self-developed Simplex program to estimate the energy dissipation in frequency domain is still preferred. To verify the accuracy and applicability of the Simplex program and following MATLAB coding, dynamic experimental testing is carried out. That result indicates that the simulated temperature matches well with the measured. In order

to get clearer about the dissipation energy density and temperature distribution, the torsional testing is carried out. The radial testing indicates that the higher temperature appears around the loading zone while the higher temperature at torsional testing happens at the central but close to the inner surface of the steel sleeves. Those results show that those loading areas are tended to be damaged and need special attention. The frequency and amplitude-dependence of the two tests show the combination of higher frequency and higher amplitude can cause higher temperature distribution. Thus, if the loading is specified, the excitation frequency should be limited not only to avoid the resonance but also to avoid the thermal failure of rubber components.

CHAPTER 7. CONCLUSION AND FUTURE WORK

In this dissertation, the rubber bushing used on the suspension system of the vehicle is researched to investigate its heat generation mechanism and temperature distribution during service. The results indicate the developed FORTRAN and MATLAB program can satisfactorily approximate the thermal field of the rubber bushing. There are several aspects of the innovations in the research.

First, it is the application of multi-body dynamics analysis to describe the possible kinetic and dynamic conditions of rubber bushing. There are large amount of publications about the dynamic conditions of full vehicle by investigating the rolling tire. Similarly, in view of the rolling tire behaviors, the response of suspension system and rubber bushing can be extrapolated using the multi-body dynamic method. Based on the multi-body analysis, the rubber core can be split into pieces jointed with springs and dashpots. To make clear how many rigid bodies are appropriate to represent the rubber core, modal hammer testing is carried out and the acceleration of the response is measured. The spring stiffness and damping coefficients are identified with the Bode plot of the clamped rubber bushing. By doing this, the transfer function of the rubber bushing can be derived to explore the stability of the structure at high frequency range and the energy dissipation mechanism.

The second contribution is the connection between multi-body dynamic and continuum mechanism in the analysis of rubber bushing. With the modal testing results, the rubber core can be treated as several pieces of bodies and the dissipation energy can be analyzed individually for each piece with its loading and displacement. Similarly, the continuum mechanics treats each element as individual part with unique strain and stress, with which the dissipation energy of each element can be estimated. As to the multi-body dynamic analysis for suspension

system or whole vehicle, the proper identification of the stiffness and damping coefficient of rubber bushing can simplify the overall simulation. As for the temperature distribution of rubber bushing, it is more appropriate to turn to FEA on the basis of continuum mechanics to have more pieces or elements to represent the dissipation energy density.

The third point is the development of Simplex program using FORTRAN on the basis of the source code. Frequency domain transfer function and FFT algorithm are implemented to develop the subroutine. In the current commercial software, the modulus is represented in Prony series, which is the time domain expression. With the FFT algorithm, the input of the loading can be easily analyzed in the frequency domain and then transferred back to the time domain. With this approach, the accumulated dissipation energy becomes more applicable to estimate. Except for the dissipation energy estimation, the developed Simplex is applicable at various tests, such as blast loading, creep and even in wave propagation for larger structures. Furthermore, even though the Simplex is developed to solve the rubber bushing of simple geometry, actually, this work can also be applied to deal with those very complicated structures.

The fourth is the prediction of temperature distribution of the rubber core, which is critical to explore the failure mechanism. With the known dissipation energy density, the rubber core can have the similar mesh and each element is given specialized heat source. The commonly used finite volume method in heat transfer analysis is implemented here to calculate the temperature distribution in time domain.

However, this is just initial work of rubber bushing thermal analysis, for more thorough and comprehensive research, more work needs to be done. First, the fatigue analysis is critical to predict the serving life of rubber, thus, proper fatigue test and creep tests are beneficial to analyze the fatigue properties. Secondly, the coupling of thermal-structure analysis can include the temperature effect, then, the current one way coupling can be transformed to two way coupling. Thirdly, the

current Simplex program can add more subroutine to include more models of viscoelastic material to widen its application. Fourthly, the rheological properties of the rubber should be identified to give proper prediction of the rubber bushing′s serving life.

LIST OF REFERENCES

LIST OF REFERENCES

Ali, A., Hosseini, M., & Sahari, B. (2010). A review of constitutive models for rubber-like materials. *American Journal of Engineering and Applied Sciences*, *3*(1), 232.

Andrews, G., & Kesavan, H. (1978). Simulation of multibody systems using the vector-network model. In *Dynamics of multibody systems* (pp. 1–13). Springer.

Arruda, E. M., & Boyce, M. C. (1993). A three-dimensional constitutive model for the large stretch behavior of rubber elastic materials. *Journal of the Mechanics and Physics of Solids*, *41*(2), 389–412.

Austrell, P.-E., Olsson, A., & Jonsson, M. (2001). A method to analyse the non-linear dynamic behaviour of carbon-black-filled rubber components using standard fe-codes. *CONSTITUTIVE MODELS FOR RUBBER*, *2*, 231–236.

Barenblatt, G., & Joseph, D. (1997). Collected papers of rs rivlin, vol. vols. *I and II*.

Batra, R., & Yu, J. (2000). Torsion of a viscoelastic cylinder. *TRANSACTIONS-AMERICAN SOCIETY OF MECHANICAL ENGINEERS JOURNAL OF APPLIED MECHANICS*, *67*(2), 424–426.

Batra, R., & Yu, J.-H. (1999). Linear constitutive relations in isotropic finite viscoelasticity. *Journal of elasticity*, *55*(1), 73–77.

Beatty, J. (1964). Fatigue of rubber. *Rubber Chemistry and Technology*, *37*(5), 1341–1364.

Becker, A., Dorsch, V., Kaliske, M., & Rothert, H. (1998). A material model for simulating the hysteretic behavior of filled rubber for rolling tires. *Tire Science and Technology*, *26*(3), 132–148.

Berg, M. (1997). A model for rubber springs in the dynamic analysis of rail vehicles. *Proceedings of the Institution of Mechanical Engineers, Part F: Journal of Rail and Rapid Transit*, *211*(2), 95–108.

Berg, M. (1998). A non-linear rubber spring model for rail vehicle dynamics analysis. *Vehicle system dynamics*, *30*(3-4), 197–212.

Bischoff, J., Arruda, E., & Grosh, K. (2002). A microstructurally based orthotropic hyperelastic constitutive law. *Journal of applied mechanics*, *69*(5), 570–579.

Blaurock, E. E. E. (1955, May 24). *Resilient bushing and method of.* Google Patents. (US Patent 2,709,096)

Blundell, M., Harty, D., et al. (2004). *The multibody systems approach to vehicle dynamics*. Elsevier.

Boyce, M. C., & Arruda, E. M. (2000). Constitutive models of rubber elasticity: a review. *Rubber chemistry and technology*, *73*(3), 504–523.

Browne, A., & Wickliffe, L. (1980). Parametric study of convective heat transfer coefficients at the tire surface. *Tire Science and Technology*, *8*(3), 37–67.

Chace, M. A. (1984). Methods and experience in computer aided design of large-displacement mechanical systems. In *Computer aided analysis and optimization of mechanical system dynamics* (pp. 233–259). Springer.

Chagnon, G., Marckmann, G., & Verron, E. (2004). A comparison of the hart-smith model with arruda-boyce and gent formulations for rubber elasticity. *Rubber chemistry and technology*, *77*(4), 724–735.

Choi, J.-H., Kang, H. J., Jeong, H.-Y., Lee, T.-S., & Yoon, S.-J. (2005). Heat aging effects on the material property and the fatigue life of vulcanized natural rubber, and fatigue life prediction equations. *Journal of mechanical science and technology*, *19*(6), 1229–1242.

Clark, J., & Schuring, D. (1988). Load, speed and inflation pressure effects on rolling loss distribution in automobile tires. *Tire Science and Technology*, *16*(2), 78–95.

Clark, S. K. (1976). Temperature rise times in pneumatic tires. *Tire Science and Technology*, *4*(3), 181–189.

Cooper, M., Mikic, B., & Yovanovich, M. (1969). Thermal contact conductance. *International Journal of heat and mass transfer*, *12*(3), 279–300.

Dannenberg, E. (1975). The effects of surface chemical interactions on the properties of filler-reinforced rubbers. *Rubber Chemistry and Technology*, *48*(3), 410–444.

Diani, J., Fayolle, B., & Gilormini, P. (2009). A review on the mullins effect. *European Polymer Journal*, *45*(3), 601–612.

Doyle, J. F. (1989). *Wave propagation in structures*. Springer.

Doyle, J. F. (2009). *Guided explorations of the mechanics of solids and structures* (No. 26). Cambridge University Press.

Doyle, J. F. (2014). *Nonlinear structural dynamics using fe methods*. Cambridge University Press.

Dzierzek, S. (2000). Experiment-based modeling of cylindrical rubber bushings for the simulation of wheel suspension dynamic behavior. *Training*, *2014*, 05–05.

Ebbott, T., Hohman, R., Jeusette, J.-P., & Kerchman, V. (1999). Tire temperature and rolling resistance prediction with finite element analysis. *Tire Science and Technology*, *27*(1), 2–21.

Feng, W. W., Hung, T.-K., & Chang, G.-L. (1992). Extension and torsion of hyperviscoelastic cylinders. *International journal of non-linear mechanics*, *27*(3), 329–335.

Ferry, J. D. (1980). Viscoelastic properties of polymers.

Forni, M., Martelli, A., & Dusi, A. (1999). Implementation and validation of hyperelastic finite element models of high damping rubber bearings.

Fujiwara, Y., Tanuma, S., & Yoda, N. (1992, January 14). *Structure of vibration-proof rubber bushing.* Google Patents. (US Patent 5,080,332)

Gabbott, P. (2008). *Principles and applications of thermal analysis.* John Wiley & Sons.

García Tárrago, M.-J., Kari, L., Vinolas, J., & Gil-Negrete, N. (2007). Frequency and amplitude dependence of the axial and radial stiffness of carbon-black filled rubber bushings. *Polymer testing*, *26*(5), 629–638.

Gehman, S. (1967). Heat transfer in processing and use of rubber. *Rubber chemistry and technology*, *40*(1), 36–99.

Halvorsen, W. G., & Brown, D. L. (1977). Impulse technique for structural frequency response testing. *Sound and Vibration*, *11*(11), 8–21.

Harold, G. (1933, July 25). *Method and means for adhering rubber to metal.* Google Patents. (US Patent 1,919,718)

Harper, C. A. (2006). *Handbook of plastics technologies: the complete guide to properties and performance.* McGraw-Hill New York.

Haug, E. J. (1984). Computer aided analysis and optimization of mechanical system dynamics.

Haug, E. J. (1989). *Computer aided kinematics and dynamics of mechanical systems* (Vol. 1). Allyn and Bacon Boston.

Hausler, K., & Sayir, M. (1995). Nonlinear viscoelastic response of carbon black reinforced rubber derived from moderately large deformations in torsion. *Journal of the Mechanics and Physics of Solids*, *43*(2), 295–318.

Heinrich, G., & Klüppel, M. (2002). Recent advances in the theory of filler networking in elastomers. In *Filled elastomers drug delivery systems* (pp. 1–44). Springer.

Heldt, P. M. (1948). *The automotive chassis (without powerplant).* PM Heldt.

Hooker, W., & Margulies, G. (1965). The dynamical attitude equations for n-body satellite. *Journal of the Astronautical Sciences*, *12*, 123.

Johnson, A. R., & Chen, T.-K. (2005). Approximating thermo-viscoelastic heating of largely strained solid rubber components. *Computer methods in applied mechanics and engineering*, *194*(2), 313–325.

Jones, D. I. (2001). *Handbook of viscoelastic vibration damping.* Wiley.

Kadlowec, J., Wineman, A., & Hulbert, G. (2003). Elastomer bushing response: experiments and finite element modeling. *Acta mechanica*, *163*(1-2), 25–38.

Kalfayan, S., Silver, R., & Mazzeo, A. (1975). Accelerated heat-aging studies on fluorosilicone rubber. *Rubber Chemistry and Technology*, *48*(5), 944–952.

Kaliske, M., & Rothert, H. (1998). Constitutive approach to rate-independent properties of filled elastomers. *International Journal of Solids and Structures*, *35*(17), 2057–2071.

Kane, T. R., & Levinson, D. A. (1985). *Dynamics, theory and applications*. McGraw Hill.

Kane, T. R., Likins, P. W., & Levinson, D. A. (1983). Spacecraft dynamics. *New York, McGraw-Hill Book Co, 1983, 445 p.*, *1*.

Knothe, K., & Grassie, S. (1993). Modelling of railway track and vehicle/track interaction at high frequencies. *Vehicle system dynamics*, *22*(3-4), 209–262.

Kraus, G. (1971). Reinforcement of elastomers by carbon black. In *Fortschritte der hochpolymeren-forschung* (pp. 155–237). Springer.

Kraus, G. (1978). Reinforcement of elastomers by particulate fillers. *Science and technology of rubber*, 387–416.

Kreith, F. (1968). Convection heat transfer in rotating systems. *Advances in heat transfer*, *5*, 129–251.

Kreith, F., & Black, W. Z. (1980). Basic heat transfer.

Kuhn, W., & Grün, F. (1946). Statistical behavior of the single chain molecule and its relation to the statistical behavior of assemblies consisting of many chain molecules. *Journal of polymer science*, *1*(3), 183–199.

LaClair, T. J., & Zarak, C. (2005). Truck tire operating temperatures on flat and curved test surfaces. *Tire Science and Technology*, *33*(3), 156–178.

Lewitzke, C., & Lee, P. (2001). Application of elastomeric components for noise and vibration isolation in the automotive industry. *Technology*, *2013*, 07–22.

Lin, R. (2001). On a nonlinear viscoelastic material law at finite strain for polymers. *Mechanics Research Communications*, *28*(4), 363–372.

Lin, Y.-J., & Hwang, S.-J. (2004). Temperature prediction of rolling tires by computer simulation. *Mathematics and Computers in Simulation*, *67*(3), 235–249.

Luchini, J., Peters, J., & Arthur, R. (1994). Tire rolling loss computation with the finite element method. *Tire Science and Technology*, *22*(4), 206–222.

Mark, J. E., Erman, B., & Roland, M. (2013). *The science and technology of rubber*. Academic Press.

Mars, W., & Fatemi, A. (2004). Factors that affect the fatigue life of rubber: a literature survey. *Rubber Chemistry and Technology*, *77*(3), 391–412.

Mc Allen, J., Cuitino, A., & Sernas, V. (1996). Numerical investigation of the deformation characteristics and heat generation in pneumatic aircraft tires: Part ii. thermal modeling. *Finite Elements in Analysis and Design*, *23*(2), 265–290.

McKenna, G., & Zapas, L. (1979). Nonlinear viscoelastic behavior of poly (methyl methacrylate) in torsion. *Journal of Rheology (1978-present)*, *23*(2), 151–166.

Medalia, A. (1978). Effect of carbon black on dynamic properties of rubber vulcanizates. *Rubber Chemistry and Technology*, *51*(3), 437–523.

Meyers, M., & Chawla, K. (1991). Mechanical behavior of materials, 1999. *Prentice-Hall, Englewood Cliffs (NJ), see also Kallend JS, Kocks UF, Rollett AD, Wenk HR. Operational texture analysis. Mater Sci Eng*, *132*, 1–11.

Mikić, B. (1974). Thermal contact conductance; theoretical considerations. *International Journal of Heat and Mass Transfer*, *17*(2), 205–214.

Mooney, M. (2004). A theory of large elastic deformation. *Journal of applied physics*, *11*(9), 582–592.

Mullins, L. (1969). Softening of rubber by deformation. *Rubber Chemistry and Technology*, *42*(1), 339–362.

Ogden, R. (1972). Large deformation isotropic elasticity-on the correlation of theory and experiment for incompressible rubberlike solids. *Proceedings of the Royal Society of London. A. Mathematical and Physical Sciences*, *326*(1567), 565–584.

Oh, B., Kim, Y., Kim, N., Moon, H., & Park, H. (1995). Internal temperature distribution in a rolling tire. *Tire Science and Technology*, *23*(1), 11–25.

Olsson, A. K., & Austrell, P. E. (2003). Finite element analysis of a rubber bushing considering rate and amplitude dependent effects. *CONSTITUTIVE MODELS FOR RUBBER*, 133–140.

Park, D. M., Hong, W. H., Kim, S. G., & Kim, H. J. (2000). Heat generation of filled rubber vulcanizates and its relationship with vulcanizate network structures. *European polymer journal*, *36*(11), 2429–2436.

Payne, A., & Whittaker, R. (1971). Low strain dynamic properties of filled rubbers. *Rubber Chemistry and Technology*, *44*(2), 440–478.

Payne, A. R. (1962). The dynamic properties of carbon black-loaded natural rubber vulcanizates. part i. *Journal of Applied Polymer Science*, *6*(19), 57–63.

Peeters, F., & Kussner, M. (1999). Material law selection in the finite element simulation of rubber-like materials and its practical application in the industrial design process. In *Constitutive models for rubber: Proceedings of the first european conference on constitutive models for rubber, vienna, austria, dorfmund and muhr (eds), rotterdam: Aa balkema* (pp. 29–36).

Popiel, C. O., & Bogusławski, L. (1975). Local heat-transfer coefficients on the rotating disk in still air. *International Journal of Heat and Mass Transfer*, *18*(1), 167–170.

Rivlin, R. (1948). Large elastic deformations of isotropic materials. iv. further developments of the general theory. *Philosophical Transactions of the Royal Society of London. Series A, Mathematical and Physical Sciences*, *241*(835), 379–397.

Rivlin, R. S. (2004). Torsion of a rubber cylinder. *Journal of Applied Physics*, *18*(5), 444–449.

Roberson, R. E., & Wittenburg, J. (1966). A dynamical formalism for an arbitrary number of interconnected rigid bodies, with reference to the problem of satellite attitude control.

Roland, C. (1989). Network recovery from uniaxial extension: I. elastic equilibrium. *Rubber chemistry and technology*, *62*(5), 863–879.

Rosen, S. L. (1982). *Fundamental principles of polymeric materials*. Wiley.

Roylance, D. (2001). Engineering viscoelasticity. *Department of Materials Science and Engineering–Massachusetts Institute of Technology, Cambridge MA*, *2139*, 1–37.

Schuring, D. (1980). The rolling loss of pneumatic tires. *Rubber Chemistry and Technology*, *53*(3), 600–727.

Song, K., Chen, X.-k., Lin, Y., & Ma, Z.-D. (2012). Functional analysis of bushing in four-link suspension on k&c characteristics using multibody dynamics method. In *Asme 2012 international mechanical engineering congress and exposition* (pp. 1115–1122).

Stein, E., Zhang, G., & Huang, Y. (1993). Modeling and computation of shakedown problems for nonlinear hardening materials. *Computer methods in applied mechanics and engineering*, *103*(1), 247–272.

Stein, E., Zhang, G., & König, J. A. (1992). Shakedown with nonlinear strain-hardening including structural computation using finite element method. *International Journal of Plasticity*, *8*(1), 1–31.

Sullivan, J. (1990). Creep and physical aging of composites. *Composites Science and Technology*, *39*(3), 207–232.

Tien, C., & Campbell, D. (1963). Heat and mass transfer from rotating cones. *Journal of fluid mechanics*, *17*(01), 105–112.

Treloar, L. R. G. (1975). *The physics of rubber elasticity*. Oxford University Press.

Trivisonno, N. (1972). Nonsteady-state thermal analysis of a rolling aircraft tire. *Training*, *2009*, 08–31.

Ulmer, J. (1996). Strain dependence of dynamic mechanical properties of carbon black-filled rubber compounds. *Rubber Chemistry and Technology*, *69*(1), 15–47.

Whibley, I., Cutts, E., Phillip, M., & Pearce, D. (2005). Mechanical characterisation and modelling of elastomers based on chemical compositions. In *Constitutive models for rubber-proceedings-* (Vol. 4, p. 437).

Whicker, D., Browne, A., Segalman, D., Whicker, D., & Rohde, S. (1981). Modeling tire deformation for power loss calculations. *Training*, *2014*, 07–22.

Whicker, D., Browne, A., Segalman, D., & Wickliffe, L. (1981). A thermomechanical approach to tire power loss modeling. *Tire Science and Technology*, *9*(1), 3–18.

Whicker, D., Browne, A. L., & Segalman, D. J. (1981). The structure and use of the gmr combined thermo-mechanical tire power loss model. *Training*, *2014*, 07–22.

Willett, P. (1973). Hysteretic losses in rolling tires. *Rubber chemistry and Technology*, *46*(2), 425–441.

Wittenburg, J. (2007). *Dynamics of multibody systems*. Springer.

Wittenburg, J., & Schmidt, I. A. (1990). Mesa verdea general-purpose program package for symbolical dynamics simulations of multibody systems. In *Multibody systems handbook* (pp. 341–360). Springer.

Woo, C. S., & Park, H. S. (2011). Useful lifetime prediction of rubber component. *Engineering Failure Analysis*, *18*(7), 1645–1651.

Yavari, B., Tworzydlo, W., & Bass, J. (1993). A thermomechanical model to predict the temperature distribution of steady state rolling tires. *Tire Science and Technology*, *21*(3), 163–178.

Yeoh, O. (1993). Some forms of the strain energy function for rubber. *Rubber Chemistry and technology*, *66*(5), 754–771.

Yeow, S., El-Sherbiny, M., & Newcomb, T. (1978). Thermal analysis of a tyre during rolling or sliding. *Wear*, *48*(1), 157–171.

VITA

VITA

EDUCATION

Mechanical Engineering Technology (**Ph.D.**) May 2015

Purdue University, West Lafayette, IN

Material Science and Engineering (**M.S.**) Mar. 2010

Shanghai Jiaotong University, Shanghai, China

Material Science and Engineering (**B.S.**) June 2007

Central South University, Changsha, China

Her research results are partially reflected in the following publications:

1: Zhengui Zhang, Peixuan Wu, Haiyan H. Zhang, Mechanism and effect of mallet tapping on contact stress distribution between V-band clamp and piping systems, IJIEM, 2014.

2: Zhengui Zhang, Haiyan H. Zhang, Viscoelastic parameter identification based structure-thermal analysis of rubber bushing, GJRE, 2014.

3: Zhengui Zhang, Peixuan Wu, Haiyan H. Zhang, Contact stress analysis of interference fit between V-band clamp and piping systems, IJEIT, 2014.